Experimental study of lateral cavities in open-channel flows

Wei Cai

2015ISAL0062 Année 2015

THÈSE

Etude expérimentale des cavités latérales en écoulements à surface libre (Experimental study of lateral cavities in open-channel flows)

Présentée devant

l'Institut National des Sciences Appliquées de Lyon

pour obtenir

le GRADE DE DOCTEUR

École doctorale :

Mécanique, Énergétique, Génie Civil, Acoustique

Spécialité :

MÉCANIQUE des FLUIDES

par

Wei CAI

Soutenue le 15 Juillet devant la Commission d'examen

Jury

M. BELAUD Gilles	Professeur (UMR G-eau, Montpellier)	Rapporteur
M. CHAMPAGNE Jean-Yves	Professeur (INSA, Lyon)	Examinateur
M. MOULIN Frédéric	Maître de Conférences (Université Paul Sabatier)	Rapporteur
M. MIGNOT Emmanuel	Maître de Conférences (INSA, Lyon)	Co-directeur de thèse
M. PUIJALON Sara	Professeur. (CNR, Lyon)	Examinateur
M. RIVIÈRE Nicolas	Professeur (INSA, Lyon)	Directeur de thèse

LMFA - UMR CNRS 5509 - INSA de Lyon
20, avenue Albert Einstein, 69621 Villeurbanne Cedex (FRANCE)

Contents

Remerciements

J’exprime ma plus profonde reconnaissance à Monsieur Nicolas RIVIERE et Emmanuel MIGNOT qui m’ont accompagné depuis le début de ma formation et ont dirigé mon travail, et dont les encouragements, la connaissance intime des cavités latéral et la passion qu’ils m’ont transmis pour la recherche, m’ont permis de mener à bien cette entreprise de longue haleine.

Je remercie Nicolas RIVIERE pour sa patience, sa disponibilité et l’aide qu’il m’a apportée pour pouvoir avancer et marcher et finir. Il peut proposer des conseil très util quand j'ai rencontré des problèmes. Il peut donner des propes idées quand on discute sur mon projet. Il est un professeur rigoureux en scientifique et très responsable.

Je remercie également Emmanuel MIGNOT qu'il est jeune, travailleur et sympatique, Le plus important est qu'il est mon co- directeur. Grand merci pour sa grande aide durant tout le stage:son conseil dans les discussions et l’aide dans les manips.

Ce travail doit beaucoup aux chercheurs qui ont été mes interlocuteurs réguliers et ont accepté de partager avec moi leur expérience, tout particulièrement: Mathilde BROSSET pour sa aide sur la parti de colorant durant 2013;Cristian ESCAURIAZA pour les simulations sur cavités; Mathilde Pozet pour sa aide sur la parti de seich durant 2014.

INSA-LMFA, est une laboratoire très important pour moi. Merci aux mes doctorant-collègues: Lei HAN, Nicolas SOUZYet Gaby LAUNAY pour partager les expériences partagés et les échanges stimulants.Merci aussi aux mes collègues: Jean-Yves CHAMPAGNE, Valéry BOTTON, Mahmoud El Hajem, Gilbert TRAVIN, Cyril MAUGER,Serge SIMOENS et Daniel HENRY pour leur soutien et leur écoute patiente dans le moment de doute et à tous ceux que je ne peux nommer ici mais qui savent ce que cette thèse leur doit.

Résumé

Les cavités latérales sont des zones mortes à surface libre situées sur le côté d'un écoulement fluvial ou côtier. Les vitesses caractéristiques au sein de la cavité étant beaucoup plus faibles que celles de l'écoulement, une couche de mélange se développe à l'interface entre ces deux régions. Cette couche de mélange peut alors transférer de la quantité de mouvement de l'écoulement vers la cavité et ainsi mettre en mouvement la cavité et peut aussi transférer de la masse entre les deux régions, telle une pollution venant de l'écoulement amont. L'étude de cette thèse a alors consisté à étudier les caractéristiques de la couche de mélange, qui est rendue spécifique par le fait qu'elle se développe entre deux coins géométriques formés par l'intersection entre les parois de la cavité et celles de l'écoulement principal. Nous avons alors pu identifier l'origine et l'alternance des mouvements de fluide dans la direction transverse: de la cavité vers l'écoulement et inversement. Concernant la mise en mouvement de la cavité, le choix a été fait de considérer un écoulement principal fixé et de modifier l'extension de la cavité dans la direction perpendiculaire à l'écoulement, passant ainsi d'une cavité rectangulaire alignée avec l'écoulement principal à une cavité allongée dans le sens opposé. La mesure de champ de vitesse par PIV 2D a alors montré une forte évolution de la forme de l'écoulement à mesure que la géométrie de la cavité évolue : un système avec deux cellules alignées dans le sens de l'écoulement à un système à une seule cellule, puis un système à deux cellules et enfin un système complexe 3D ont ainsi été observés pour une cavité de plus en plus allongée. Ensuite, une modification du dispositif expérimental a permis de mesurer de deux façons différentes le transport de scalaire de l'écoulement principal vers la cavité, de comprendre les processus associés à ce transfert et enfin de quantifier cette capacité de transfert pour différents écoulements principaux et différentes géométries de cavités. Nous avons notamment montré que la géométrie de la cavité a peu d'effet alors que le nombre de Reynolds et la profondeur d'eau normalisée ont un effet majeur sur cette capacité de transfert de masse entre les deux régions.

Mots clés: Cavité latérale, champ de vitesse, recirculation, couche de mélange, transport de scalaire

Abstract

Lateral cavities are free-surface dead-zones located on the side of a fluvial or coastal main flow. As the typical velocities are much larger in the main flow than in the cavity, a mixing layer appears at the interface between both regions. This mixing layer is able to transfer between the main flow and the cavity momentum which then sets the fluid in the cavity in motion and also passive scalar, such as a pollution coming from upstream. The objective of this work was then to investigate the characteristics of the mixing layer, which specificity comes from the fact that it is constrained between the upstream and downstream geometrical corners. It was possible to observe the origin and alternation of the transversal fluid motions: from the cavity towards the main flow and conversely. Regarding the motion in the cavity, the choice was made to keep a constant main flow and to measure the 2D horizontal velocity field using PIV as the extension of the cavity increases. The flow pattern then passes from a 2-cell patterns aligned in the direction of the main flow to a single-cell pattern, then a 2-cells patterns aligned along the direction perpendicular to the main flow and finally a complex 3D pattern for the widest cavity. Then a modification of the experimental set-up permitted to investigate the passive scalar exchanges from the main stream towards the cavity. It was possible to understand the processes responsible for such transfer and to quantify the transfer capacity. The analysis dimensional revealed that in the present subcritical, smooth simplified geometry cavity, the three parameters possible responsible for the modification of the transfer capacity are the geometrical aspect ratio of the cavity, the Reynolds number of the main flow and finally the normalized water depth. It was then shown that the impact of the cavity geometry remains negligible but that the Reynolds number and the normalized water do impact this passive scalar transfer capacity.

Keywords: Lateral cavity, velocity field, recirculation, mixing layer, scalar transport

List of Figures

Figure IV.12: Time evolution every 1/3s of fluctuation velocity field (black arrows) averaged over 4 consecutive times (4/30s) and contours of clockwise (blue color, Γ_1<-0.55) and counter-clockwise (red color, Γ_1>0.55) coherent vortices obtained through POD with the white circle corresponding to the vortex core, that is the maximum local $|\Gamma_1|$. The dashed line represents the mixing interface (y=0).. .. .. .82
Figure IV.13: Time-evolution of the streamwise location of the clockwise (blue) and counter-clockwise (red) vortex centers located near the interface (with $|y|$<50mm). Red arrow corresponds to four periods and equals 6.5s... .. .. .84
Figure IV.14: Statistics of spatial location of both types of vortex centers.. 84
Figure IV.15: Same as Figure IV.12 for other times and other frequency exhibiting vortices L and M originating from the cavity and ending-up in the mixing-layer. 85
Figure IV.16:Mean velocity profiles U/U_m along the transverse direction at x/L=0.83 for series 3 and 4 88
Figure IV.17:Outer velocities U_1/U_m, U_2/U_m and ratio $r(x)$ for all configurations from series 1 and 2 for x/L=0.33 and x/L=0.83 89
Figure IV.18:Outer velocities U_1/U_m, U_2/U_m and ratio $r(x)$ for all configurations from series 3 (as a function of Re) for x/L=0.33 and x/L=0.83 89
Figure IV.19: Outer velocities U_1/U_m, U_2/U_m and ratio $r(x)$ for all configurations from series 4 for x/L=0.33 and x/L=0.83. 89
Figure IV.20: the mixing layer width δ(x) along the transverse direction for series 3 and 4. 90
Figure IV.21: Fit of the linear growth of the mixing layer width. 90
Figure IV.22: Fitted linear growth rate of the mixing layer width for all configurations from series 1 and 2 at x/L=0.33 and 0.83. . . . . .. .91
Figure IV.23: Fitted linear growth rate of the mixing layer width for all configurations from series 3 at x/L=0.33 and 0.83. 91
Figure IV.24: Fitted linear growth rate of the mixing layer width for all configurations from series 4 at x/L=0.33 and 0.83. 92
Figure IV.25:Evolution of the peak frequency normalized by L and U_m as a function of:(a) the aspect ratio of the cavity (W/L) for series 1 (U_m=0.167m/s) and series 2 (U_m=0.119m/s); (b): the velocity of the main stream U_m and Reynolds number Re in series 3; (c): the dimensionless water depth h/L in series 4. . . . .

List of Tables

Notations

Abbreviation

ADV	**A**coustic **D**oppler **V**elocimetry
CCD	**C**harge-**c**oupled **D**evice
LMFA	**L**aboratoire de **M**ecanique des **F**luides et **A**coustique
PIV	**P**article **I**mage **V**elocimetry
POD	**P**roper **O**rthogonal **D**ecomposition
SNR	**S**ignal **N**oise **R**atio
TKE	**T**urbulent **K**inetic **E**nergy
W/L	The aspect ratio of the cavity

Symbols

Symbol	Description	Unit
C	The mean celerity in the mixing layer	[m/s]
f	The recording frequency of the camera	[s^{-1}]
Fr	The froude number	[-]
h	The depth of the main flow	[m]
L	The width of the cavity	[m]
L_d	The total length of the downstream channel	[m]
P	The turbulent production term	[m^2/s^3]
Q	The inlet discharge of the main flow	[m^3/s]
r	the outer velocity ratio	[-]
R	The resolution of the image	[m/pixel]
Re	The Reynolds number	[-]
s	The slopes of the upstream and downstream branches of the main channel	[-]
Stk	The Stokes number	[-]
T	The time during the PIV video	[s]
U_m	The mean velocity of the main stream	[m/s]
U_1	The streamwise velocity measured at the transverse location in the main flow where the velocity gradient becomes negligibly small	[m/s]
U_2	The streamwise velocity measured at the transverse location in the cavity where the velocity gradient becomes negligibly small	[m/s]
U_{ex}	The mean streamwise velocity in the mixing layer	[m/s]
u'	Fluctuation of streamwise velocity u	[m/s]
V_1	The velocity at the mid-points between the center of the first cell and the side wall along X/L=1	[m/s]
V_2	The velocity at the mid-points between the center of the first cell and the cavity interface	[m/s]
V_{c1}	The characteristic velocity of the first cell	[m/s]
v'	Fluctuation of transverse velocity v	[m/s]

W	The length of cavity	[m/s]
x	The position along the streamwise direction	[m]
x_{c1}	The distance from the center of the first cell to downstream side wall of the cavity	[m]
x_{c2}	The distance from the center of the second cell to downstream side wall of the cavity	[m]
x_4	The distance from the stagnation point 4 to the downstream wall of the cavity	[m]
y_{c1}	The distance from the center of the first cell l to the cavity opening	[m]
y_{c2}	The distance from the center of of the second cell to the cavity opening	[m]
y_{3c}	The distance from the stagnation point 3 to the extremity of the cavity	[m]
y	The position along the transverse direction	[m]
z	The position along the vertical direction	[m]
ΔU	The velocity difference	[m/s]
Δt	The time period between the two images.	[s]
α	The coefficient of linear growth rate of the mixing layer width	[-]
θ	Angle between the ADV and the flume reference frames	[°]
θ_U	Rotation angel of principle axis of $\Delta 2u_i$ and u_i	[°]
δ_m	The measured width of mixing layer in section x	[m]
δ_e	The estimated width of mixing layer in section x	[m]

Résumé étendu

Chapitre I: Introduction

Le Chapitre d'introduction a pour objectif de présenter les aspects généraux des cavités latérales. Il révèle que les cavités latérales sont une des singularités engendrant une zone de recirculation dans un écoulement permanent, aussi appelée zone d'eau morte. L'écoulement au sein de cette zone de recirculation est d'au moins un ordre de grandeur plus lent que l'écoulement principal et a un débit net nul. De plus, la grande différence de vitesse entre les deux régions donne naissance à une couche de mélange turbulente à l'interface entre ces deux régions. Cette couche de mélange est alors capable de transférer de la quantité de mouvement de l'écoulement principal à la cavité et ainsi de la mettre en mouvement et est aussi capable de transférer des scalaires (gaz, matières solides) entre les deux régions. Du point de vue biologique, les cavités latérales présentent une importance majeure du fait de l'aspect privilégié de cet habitat de faible vitesse mais de constant renouvellement de gaz et matière du fait de sa connexion avec l'écoulement. Les aspects principaux à étudier dans cette thèse sont donc doubles : 1. étudier la forme d'écoulement qui se met en place au sein de la cavité et 2. étudier la capacité de transport de masse entre les deux régions.

Plusieurs types de cavités latérales peuvent être rencontrés dans un écoulement à surface libre, de type rivière, tels que les espaces entre épis, ou les séries de cavités alignées. Dans notre cas, nous nous focaliserons sur les cavités latérales isolées qui correspondent à un élargissement brusque unique de la largeur du canal suivi d'un rétrécissement unique équivalent et qui peut représenter un bras mort, un ancien méandre, un port fluvial ou une zone ouverte sur le côté de l'écoulement (voir Figure. A).

Figure A: Exemple de cavités latérales,(google earth and Lecoz,2007)

L'approche privilégiée dans la thèse est l'approche expérimentale à échelle réduire considérant une géométrie simplifiée à l'extrême avec une cavité rectangulaire horizontale caractérisée par sa longueur L dans l'axe de l'écoulement et sa largeur W dans la direction perpendiculaire, de la vitesse débitante et de la largeur de l'écoulement principal U_m et b respectivement et enfin de la profondeur d'eau de l'ensemble du domaine h.

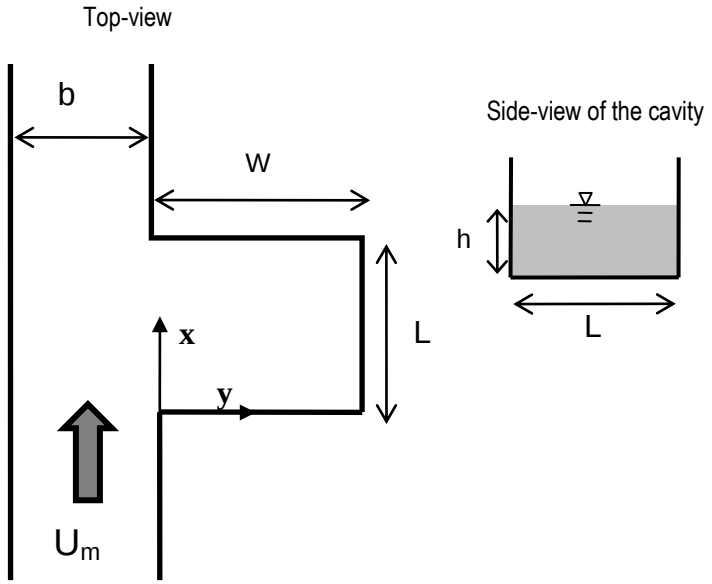

Figure B:Schéma de la cavité latérale expérimentale

La littérature disponible sur de telles cavités latérales comprend des mesures de champ de vitesse et de transport de scalaire à l'interface. Concernant les champs de vitesse, les auteurs ont principalement étudiées des cavités alignées dans le sens de l'écoulement ($W<L$) ou carrées ($W=L$) et ont montré que pour $W<<L$ deux cellules alignées dans l'axe de l'écoulement se développe alors que pour $W=L$ une cellule horizontale occupe l'ensemble de l'espace disponible. Une étude de Booij (1989) a montré que deux cellules alignées dans la direction de W pouvaient être observées pour $W=3L$. Concernant le transport de scalaire passif, les données de la littérature s'avèrent peu nombreuses et ne permettent pas de conclure quant à l'importance des différents paramètres adimensionnels sur cette capacité de transport, ce qui sera l'objet d'un des chapitres.

Chapitre II: Méthode expérimentale

L'approche choisie pour mener à bien ces travaux est une approche expérimentale sur canal. Le chapitre II présente alors les moyens de mesure utilisés pour mesurer le débit de recirculation, la hauteur d'eau dans la cavité et les champs de vitesse et de concentration dans la cavité. Pour les mesures de vitesse, deux techniques sont utilisés, un ADV permettant de mesurer les 3 composantes de la vitesse localement à haute fréquence et la PIV 2D permettant de mesurer 2 composantes de la vitesse sur un plan rectangulaire à haute fréquence. Tout d'abord, des mesures dans le canal amont permettent de renseigner sur l'état de la couche limite latérale en approche de la cavité. Ensuite, la PIV horizontale est mise en place soit centrée sur la couche de mélange, soit centrée sur la cavité. Dans le cas où deux cellules de recirculation ont lieu dans la cavité, deux champs de PIV sont mesurés, centrés chacun sur une des cellules et une méthode de reconstruction du champs complet est utilisée. Enfin, dans les cas pù l'écoulement est fortement 3D, des plans de PIV verticaux sont mesurés et permettent de mieux appréhender la forme de l'écoulement.

Chapitre III: Formes d'écoulement dans la cavité

Pour ce chapitre, une configuration d'écoulement dite « de référence » est définie et les vitesses amont et hauteur d'eau sont conservées fixé tout au long du chapitre. Le seul paramètre que l'on fait alors varier est le rapport d'aspect géométrique horizontal de la cavité W/L. Pour chaque valeur de W/L, une mesure PIV est réalisée à $z/h=0.71$ de la façon détaillée au chapitre II.

-Tout d'abord, pour $0.6<W/L<2$, une cellule unique, appelée 1ère cellule, occupe l'ensemble de l'espace disponible (Figure. C), à l'exception de petites cellules contra-rotatives cantonnées dans les coins. Cette cellule est donc de dimensions proches de $W*L$ et a déjà été observée dans la littérature.

-Pour $2 \leq W/L < 2.3$, une deuxième cellule de plus petite taille prenant naissance au coin ($x=W$, $y=L$) tend à grandir et occuper une plus grande partie de la largeur de la cavité x/L à mesure que W/L augmente (Figure. C). Des mesures additionnelles (voir Figure. D) ont montré que les configurations $W/L=2$ d'une part et 2.3 d'autre part, sont stables dans le temps alors que les configurations intermédiaires $W/L=2.1$ et 2.2 sont instables et oscillent entre i) une configuration d'écoulement où la 2e cellule est confinée au coin (comme pour $W/L=2$) et une configuration où cette 2e cellule occupe l'ensemble de la largeur disponible (comme pour $W/L=2.3$). La valeur de $W/L=2.2$-2.3 est alors définie comme la transition entre zone de recirculation à 1 cellule et à 2 cellules.

-Pour $2.3 \leq W/L \leq 3$, deux cellules prennent place, l'une à côté de l'autre alignées suivant x, confirmant ainsi la mesure de Booij (1989) dans la littérature (Figure. C).

-Enfin, pour $W/L>3$, l'écoulement au-delà de la 1ere cellule devient fortement 3D et beaucoup plus complexe. La méthode de PIV 2D montre alors ses limites pour caractériser l'écoulement.

Maintenant, concernant la dimension des cellules, la Figure. C montre que:
-Pour $W/L<2.2$ l'extension de la 1ère cellule augmente à mesure que W augmente de telle sorte que cette extension reste égale à W.
-Pour W/L passant de 2.1 à 2.2, la dimension de la 1ere cellule diminue subitement de $2.1L$ à $1.7L$ et la 2e cellule grandit et occupe, pour $W/L=2.2$, les $x=0.5L$ restant. Ensuite, pour $2.3 \leq W/L < 3$, l'extension de la 1ère cellule ne varie plus et reste égale à environ $1.7L$ alors que la 2e cellule occupe l'espace disponible et sa dimension augmente donc à mesure que W augmente.
-Enfin pour $W/L>3$, l'écoulement dans la 2e cellule devient fortement 3D et les dimensions telles qu'introduites ci-dessus perdent du sens.

Enfin, concernant la vitesse de l'écoulement au sein de ces cellules, la Figure. C montre qu'au sein de la 1ère cellule, la vitesse de rotation n'évolue que très peu à mesure que W augmente et vaut de l'ordre de 2cm/s soit de la vitesse débitante de l'écoulement principal. Il apparaît ainsi que la zone en noire (correspondant à une vitesse supérieure à 2.75cm/s) est mesurée pour $W/L=0.6$ à 5. En conséquence, les deux vitesses extérieures bordant la couche de mélange restent à peu près identiques. Cela explique le résultat du chapitre 4 où la capacité de transfert de masse ne varie quasiment pas lorsque W varie. Ensuite, la vitesse de la 2e cellule est nettement inférieure à celle de la 1ere, avec une vitesse caractéristique de l'ordre de 0.5cm/s pour $W/L \leq 3$, correspondant à un rapport de vitesse de 1/4 par rapport à la 1ère cellule et de l'ordre de 0.2cm/s (rapport de 1/10) pour $W/L>3$.

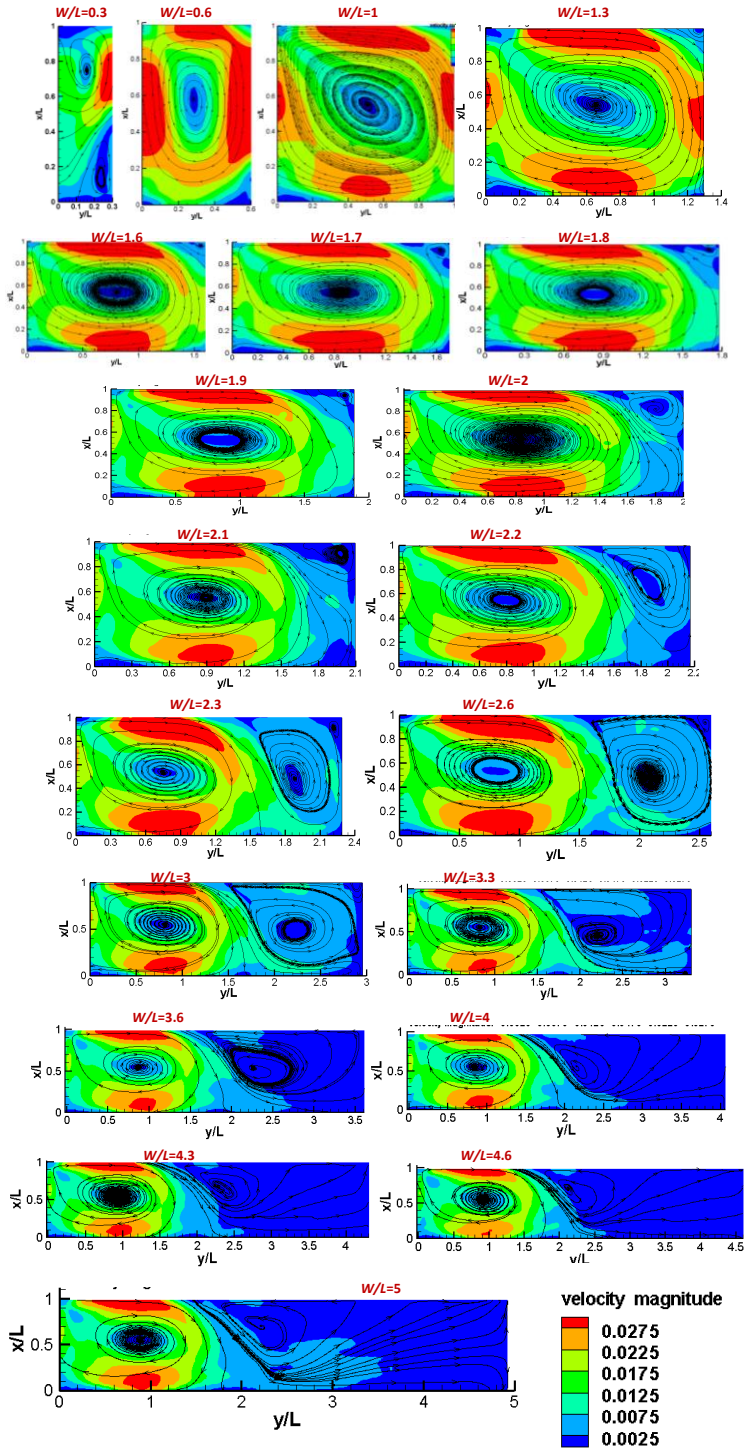

Figure C:Champs de vitesse moyenne 2D horizontal mesuré dans la cavité par PIV à l'élévation 0.71h pour différentes géométries où *W/L* varie.

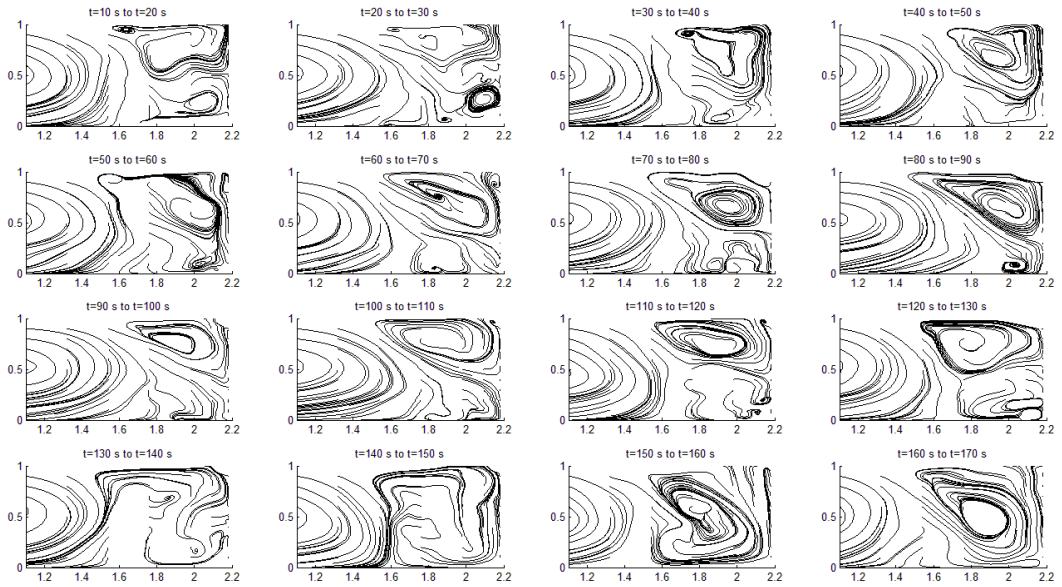

Figure D:Lignes de courant du champ de vitesse 2D horizontal mesuré toutes les 10s et moyenné chacun sur 10s, pour la configuration W/L=2.2

Chapitre IV: Couches de mélange

Le chapitre IV présente le fait qu'à l'interface entre l'écoulement principal et la cavité, une intense couche de mélange a lieu du fait du fort gradient de vitesse entre ces deux régions. Cette couche de mélange (le long de l'axe x comme montré sur la Figure E.a) est contrainte entre les deux arrêtes situées à x=0 et x=b et il apparaît que l'axe de la couche de mélange, défini comme la position de maximum gradient transverse (selon y) de vitesse longitudinal (selon x), suit à peu près le segment reliant ces deux coins (voir Figure E.b et E.c), c'est-à-dire l'axe x lui-même.

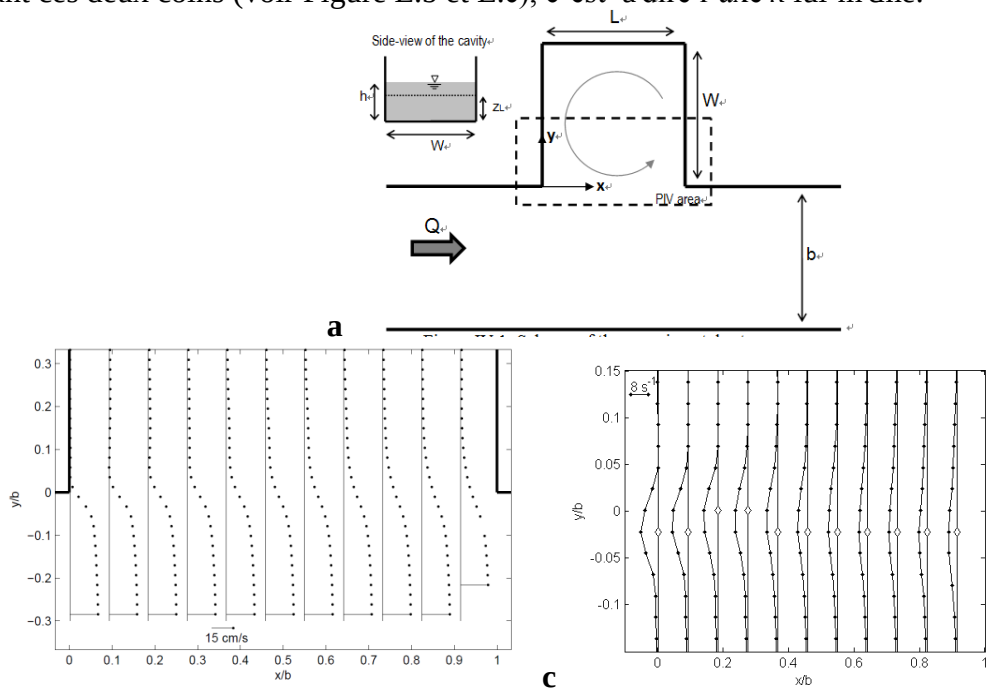

Figure E:Schéma de la cavité latérale carrée à surface libre (y>0) et de l'écoulement principal (y<0) adjacent (a). Evolution longitudinale (selon x) : des profils transverse (selon y) de vitesse moyenne longitudinale (b), de gradient transverse de cette vitesse (c),

Ainsi, l'axe de la couche de mélange est contraint par la configuration géométrique et à son extrémité aval (x/b=1), la couche de mélange impacte le coin aval. Ces deux spécificités associées à

la géométrie de la singularité modifient les caractéristiques de la couche de mélange par rapport à une couche de mélange classique libre de toute paroi, comme détaillé ci-dessous :
-L'épaisseur de la couche de mélange augmente à peu près linéairement jusque vers x/b=0.8 mais diminue soudainement sur sa partie aval (Figure F.a).
-La contrainte de Reynolds de cisaillement horizontal normalisée par la différence des vitesses moyennes externes (U_1 mesurée dans la cavité et U_2 dans l'écoulement principal), augmente d'amont en aval, atteint un maximum vers x/b=0.7 puis diminue en s'étalant transversalement (Figure F.b), en lien avec la réduction soudaine de l'épaisseur de couche de mélange.

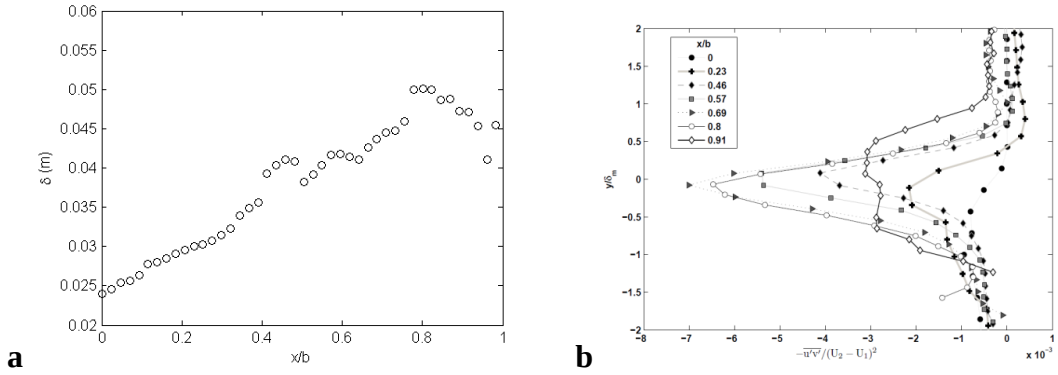

a **b**

Figure F:Evolution longitudinale (selon x) : de l'épaisseur δ de la couche de mélange (a) et des profils de contrainte turbulentes de cisaillement horizontal (b).

-Le spectre d'énergie de la vitesse transverse (selon y) montre (Figure G.a) que sur sa portion amont (x/b<0.5), la bande de fréquence de passage des structures turbulentes est assez étalée alors qu'entre x/b=0.5 et 0.6, cette bande se resserre sur une fréquence pic (égale à 0.58Hz dans le cas présent) ; on peut dire que la couche de mélange « s'organise » le long de son axe de développement. Plus à l'aval, entre x/b=0.6 et 0.8, ce pic de fréquence est maintenu, mais à l'approche du coin aval, la couche de mélange tend à se désorganiser et à perdre toute énergie.

-Ce pic à f=0.6Hz est retrouvé sur la Figure G.b où la vitesse transverse instantanée (v, selon y) est tracée le long de la couche de mélange (x/b, en abscisse) au cours du temps (t, en ordonnées). Cette figure permet de visualiser l'alternance de vitesse dirigée de l'écoulement vers la cavité (v>0 en jaune-orange) et de la cavité vers l'écoulement (v<0 en bleu). Dans la zone organisée (x/b>0.5), cette alternance correspond à l'alternance de passage des structures turbulentes (voir Figure G.b). La flèche rouge couvrant 4 périodes mesure environ 6.5s, ce qui confirme la fréquence de passage de 0.6Hz.

-La Figure G.c présente i) en flèches noires les champs de vitesse instantanés tracés tous les 1/3 de secondes et ii) en couleur les isovaleurs de Γ_1 définit par Graftieux *et al.* (2001), correspondant à la zone centrale des structures de rotation horaire en bleu et anti-horaire en rouge. Il apparaît, de plus, que les zones de forte vitesse transverse sur la Figure G.b correspondent aux zones situées entre ces centres de structures alors que la Figure H présente la position longitudinale de leur centre où il apparaît que le leur célérité est relativement constante et que leur fréquence de passage vaut bien ~0.6 Hz. La Figure G.c montre que les centres de ces structures cohérente ne se trouvent pas sur l'axe de la couche de mélange mais plutôt décalés vers la cavité ou l'écoulement principal et que deux organisations principales sont observées : i. les cellules bleues (sens horaire) dans la cavité et les rouges (sens anti-horaire) dans l'écoulement principal (tel à t=1.9s) ou ii. l'opposé (tel à t=6.2s). Au final, la couche de mélange à l'interface de la cavité révèle une alternance de 4 phases consécutives : 1. une forte vitesse transverse dirigée vers la cavité, 2. une cellule cohérente de sens de rotation horaire, 3. une forte vitesse transverse dirigée vers l'écoulement principal et 4. une cellule cohérente de sens de rotation anti-horaire. Cette organisation très périodique de structures cohérentes et de zones de vitesse transverse permettra de mieux comprendre la capacité de transport de scalaire entre la cavité et l'écoulement principal.

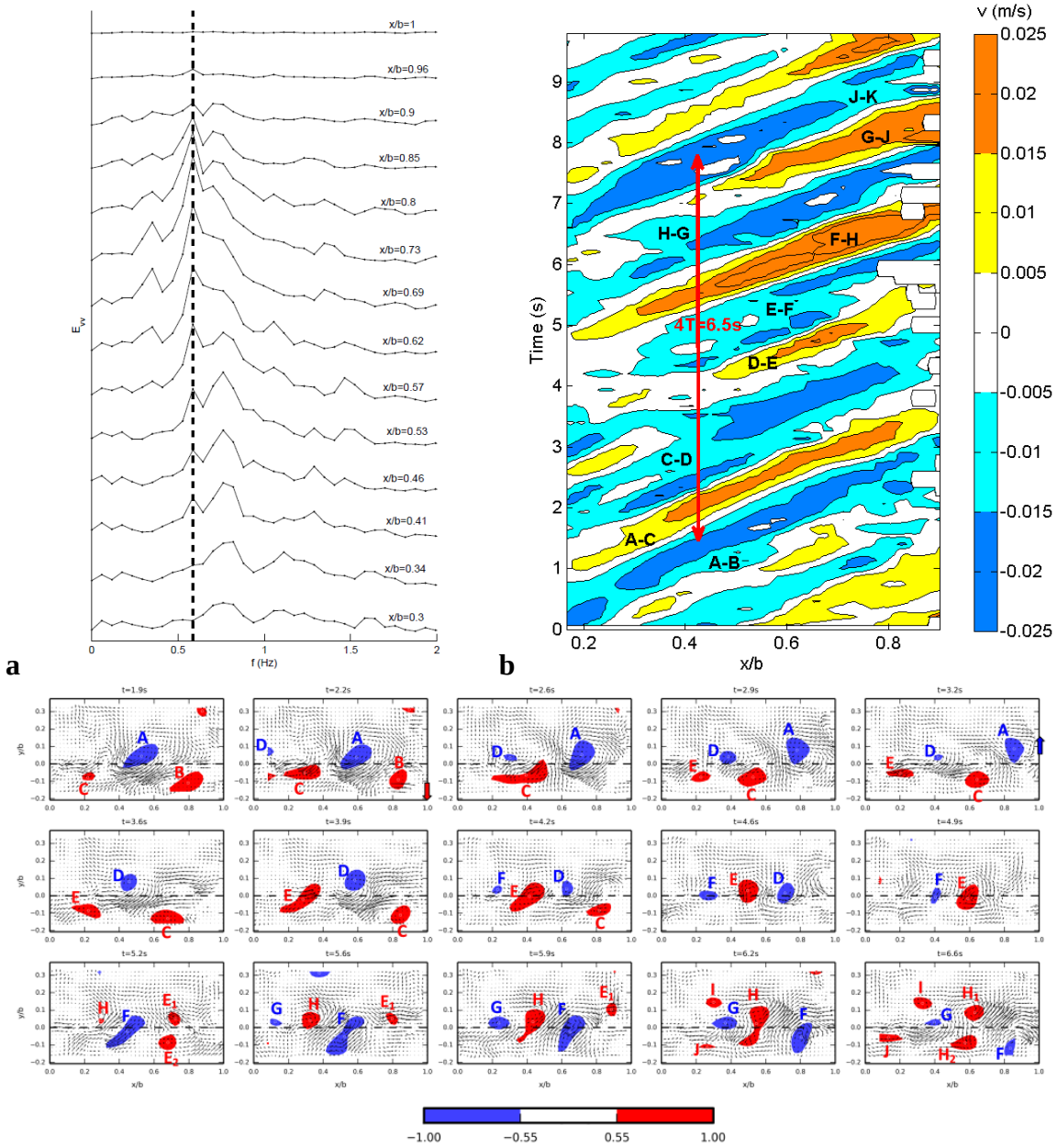

Figure G:Evolution longitudinale des spectres d'énergie de la vitesse transverse (a). Evolution spatio-temporelle de la norme de vitesse transverse instantanée (b). Champs de vitesses chaque 1/3s des champs de vitesse horizontaux et iso-valeurs de Γ_1 (c).

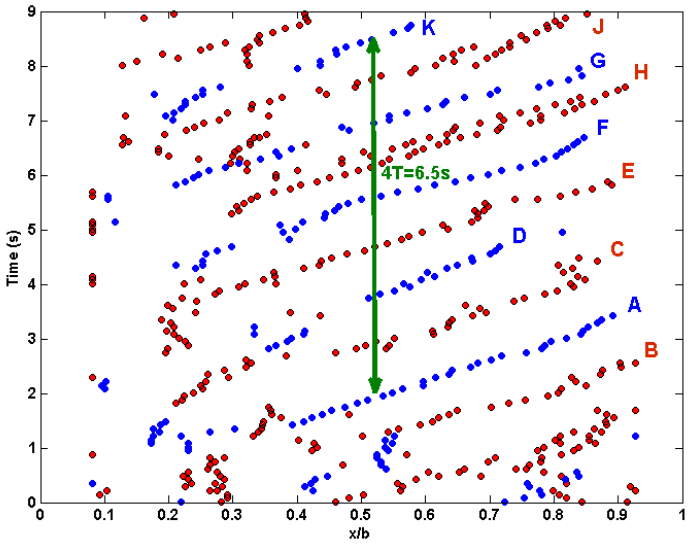

Figure H:Evolution spatio-temporelle de la position longitudinale des centres des cellules cohérentes identifiées sur le graphique h (d).

Chapitre V: Echange de masse entre les deux régions

Dans le chapitre V, le dispositif expérimental est adapté pour l'étude des échanges de scalaire passif entre la cavité et l'écoulement. Dans un premier temps, seul l'eau claire recirculante est utilisée et l'écoulement dans la cavité se met en place. A un instant donné, un débit faible mais très concentré en colorant (alimentaire ici) est injecté à débit constant à l'amont de l'écoulement amont de façon à optimiser son homogénéisation, comme montré sur la Fig. Ia. Lorsque le colorant entre dans la cavité, des photographies sont prise depuis le dessus de la surface libre et grâce à une calibration antérieure, les champs de concentration peuvent être reconstruits, comme présenté sur la Figure I.b pour une cavité carrée (W/L=1) et Ic pour une cavité rectangulaire (W/L=3). Il apparaît que dans un premier temps les processus associés à ce transfert sont identiques. Les structures cohérente présentes dans la couche de mélange permettent un transfert turbulent de colorant tout au long de la couche de mélange de l'écoulement vers la cavité (t~5s sur Figure I.b-c). Ce colorant est alors advecté par la cellule de recirculation vers le coin aval où cette concentration augmente puis le long de la paroi aval de la cavité (t~10s), puis tout le long de la zone externe de la première cellule de recirculation (celle située le plus à gauche au contact avec l'écoulement). Ainsi vers t~20s pour la cavité carrée ou t~35s pour celle rectangulaire, l'ensemble de la couche externe de la première cellule est colorée et le colorant se trouve en contact avec l'écoulement près du coin amont. Le fait que ce temps soit plus court pour la cavité carrée est due au fait que la vitesse est légèrement supérieur et que l'extension de cette cellule est plus faible pour la cavité carrée que pour celle rectangulaire (Figure C). Dans le même temps, la diffusion turbulente permet un transfert de colorant de la couche externe vers le centre de la cellule où la concentration augmente lentement. De plus pour le cas de la cavité rectangulaire, une part du colorant de la première cellule rejoint la deuxième cellule (t~80s sur la Figure I.c), qui met donc beaucoup plus de temps à se polluer, du fait aussi de sa faible vitesse d'advection et faible niveau de turbulence.

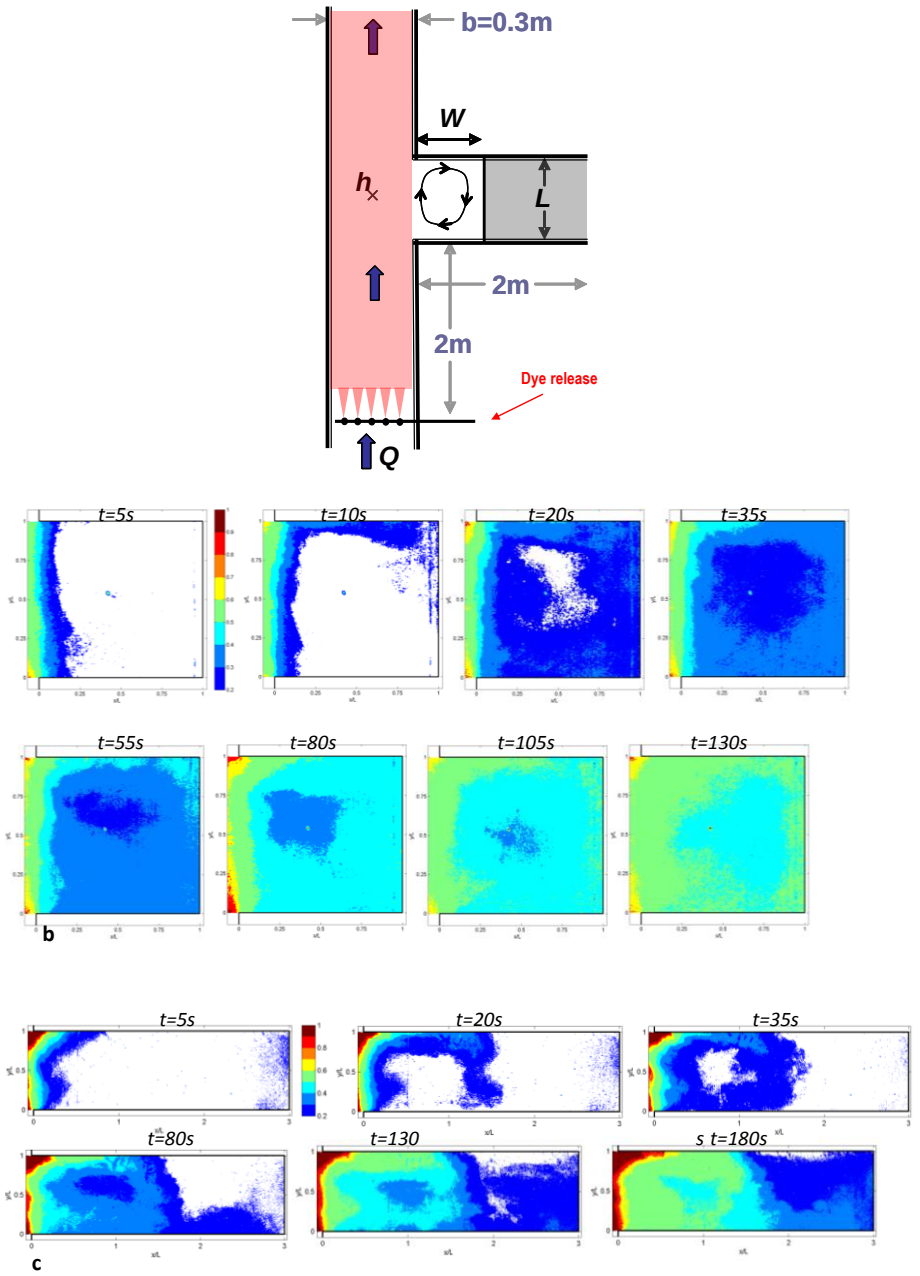

Figure I: Schéma de la cavité modifiée pour étudier le trasnport de scalaire de l'écoulement principal vers la cavité (a). Champs de concentration de scalaire au cours du temps pour la cavité carrée (W/L=1) (b) et la cavité rectangulaire (W/L=3) (c).

Ces travaux permettent enfin de calculer un coefficient de transfert du scalaire de l'écoulement principal (noté k) vers la cavité qui s'avère être identique pour les deux géométries de cavité. L'analyse dimensionnelle révère que dans notre configuration simplifiée, en régime fluvial et lisse, 3 paramètres sont susceptibles d'affecter ce coefficient k : la forme géométrique de la cavité W/L, la hauteur d'eau normalisée h/L et le nombre de Reynolds de l'écoulement amont Re. Tout d'abord il s'avère pour deux écoulements que la géométrie de la cavité W/L n'a que très peu d'effet sur k. De plus, la Figure J.a montre que lorsque Re augmente, k diminue à peu près linéairement, alors que la Figure J.b montre que lorsque h/L augmente (ainsi que Re), k augmente à peu près linéairement. Cela révèle que k tend à augmenter lorsque Re décroit ou h/L augmente et que l'effet de h/L domine celui de Re dans la gamme des paramètres étudiés.

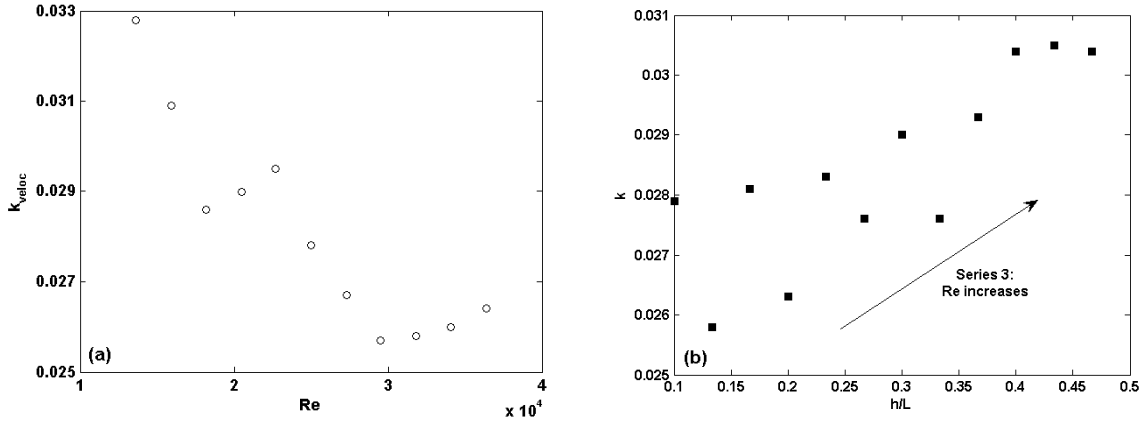

Figure J:Evolution du paramètre *k* en fonction du nombre de Reynolds *Re* (a) et de la hauteur d'eau normalisée *h*/*L* (b, avec *Re* qui augmente lorsque *h*/*L* augmente).

Chapter I: Introduction

The aim of this Chapter is to give an overview of main researches on the open-channel lateral cavities, focusing on the main three aspects considered in this work *i.e.* the studies of flow patterns in the cavity, of the mixing layer at the interface with the main stream and of the mass transfer between the two regions.

1 DEAD ZONES IN RIVER FLOW

A river flow is a complex watercourse including portions where the flow is rapid, almost 1D directed towards downstream parallel to the main axis of the river and zones of complex flow patterns where the flow direction is varying spatially. Among these zones are the so-called "dead zones" that are defined as volumes, either aligned along a vertical or horizontal axis, where the integral of the mean discharge is nil, so that this portion of the river does not participate to the river discharge capacity. These dead zones thus exhibit streamwise velocities oriented towards upstream and towards downstream that cancel each other so that the net discharge is nil. These zones of complex flows are usually created by singularities in the river topography or artificial structures.

These dead zones are either naturally present in the flow, downstream boulder or macro-roughness (see for instance Mignot *et al.*, 2009 or Franca, 2005), downstream islands (see for instance Babarutsi *et al.*, 1989), in a bifurcation (see Mignot *et al.*, 2014 and Figure I.2) or a junction (see Shakibainia *et al.*, 2010 and Figure I.3), downstream a flow enlargement (see Babarutsi *et al.*, 1989 – Figure I.1 below – and Han, 2015), *etc*. They can also be a consequence of an artificial structure added to the river, reviewed by Li and Djilali (1995) in Figure I.4, such as a bridge pier (see for instance Chen and Jirka, 1995 and Figure I.5) a groyne or dike (see Peltier *et al.*, 2013 and Figure I.6), around an obstacle (Hattori and Nagano, 2010 and Figure I.7). Among these dead zones are the cavities, which can be defined as an area connected to a main stream through one face, with a free surface and closed along the 3 other sides and that we will detail in the sequel.

These dead zones are of major importance for the river biology and chemistry activity (see Lecoz, 2007) as they are areas with velocities of about one order of magnitude lower than the main stream but still connected to the main stream. Fauna and Flora can thus encounter there a location to rest where the concentration of gazes, nutriments *etc.* remains high thanks to the exchanges with the adjacent main stream through a turbulent mixing layer. These areas are thus of primary importance for the river restoration programs (see for example Klein *et al.*, 1994 for a French example).

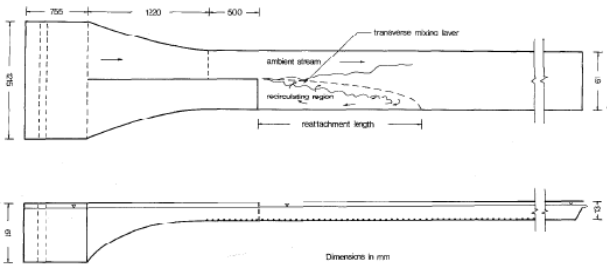

Figure I.1:Shallow Open Channel Flow downstream a sudden Channel Expansion, from Babarutsi et al. (1989)

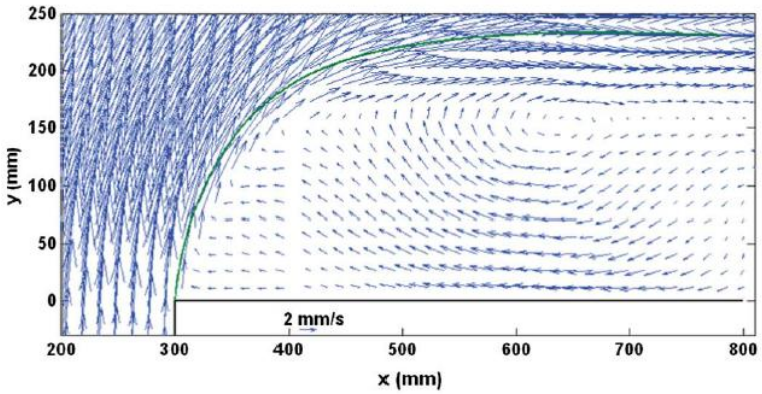

Figure I.2. Velocity magnification to unveil the recirculation region from Mignot *et al*. (2014)

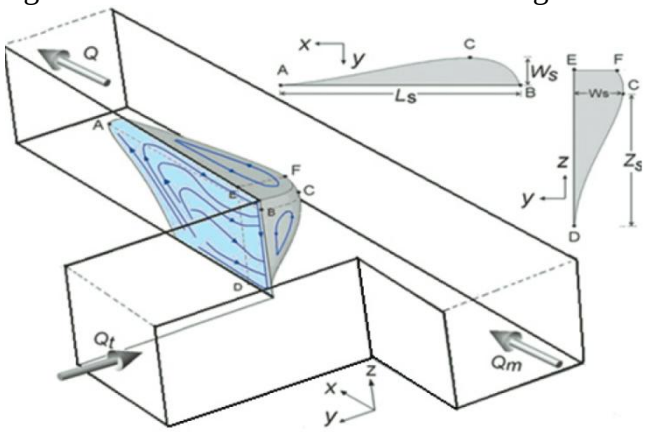

Figure I.3: Conceptual model of separation zone in channel confluences from Shakibainia *et al.* (2010)

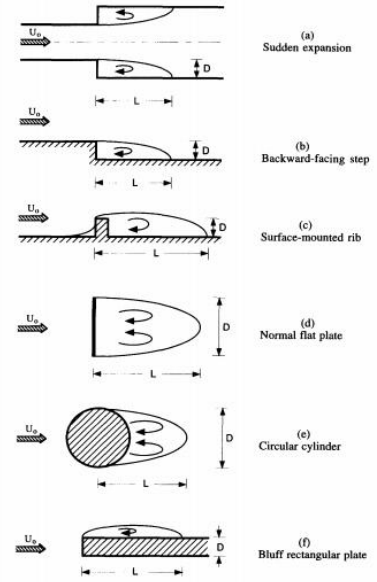

Figure I.4:Schematic view of some reattaching flow geometries, from Li and Djilali (1995)

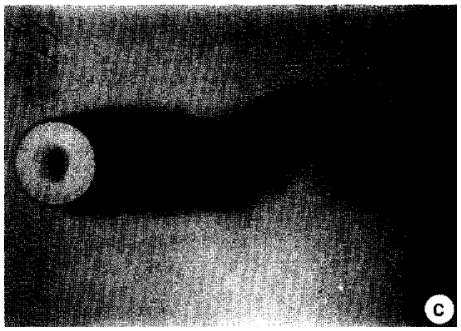

Figure I.5: shallow near-wake flow pattern produced by cylinder: unsteady bubble wake with weaker downstream instabilities, from Chen and Jirka (1995)

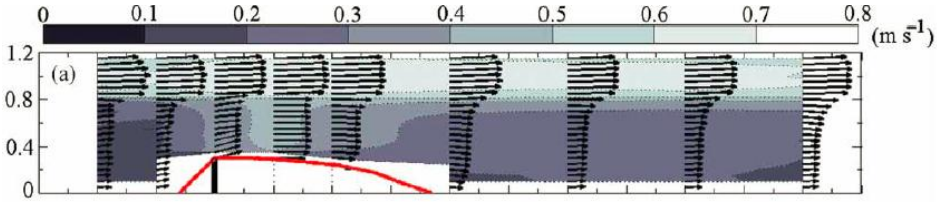

Figure I.6:Two-dimensional depth-averaged velocity fields for flow-cases (Peltier *et al.* ,2013)

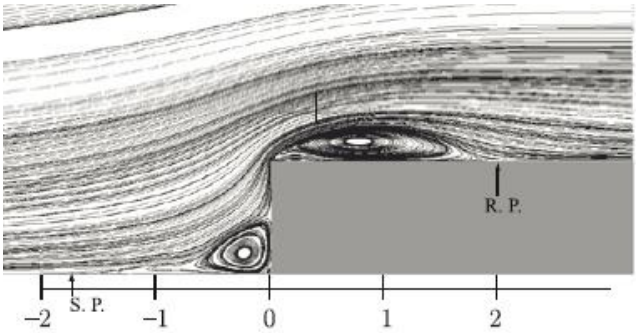

Figure I.7:Streamlines around the step, from Hattori (2010)

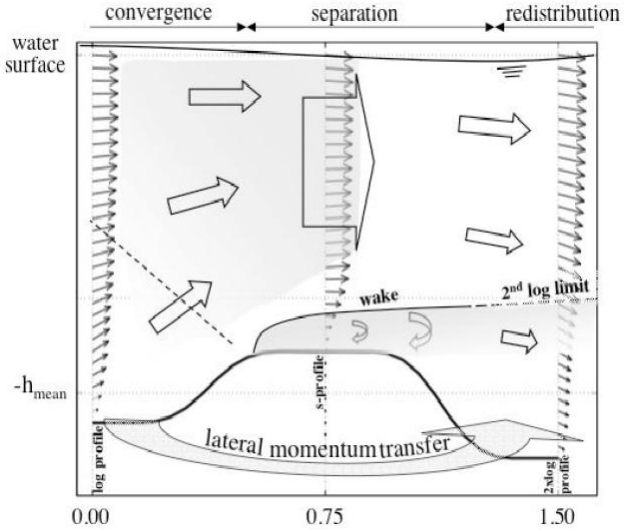

Figure I.8:Interpretation of the investigated flow field, from Franca (2005)

2 LATERAL CAVITIES

Two main types of cavities can be encountered: a) “closed-conduit cavities”, thus without free-surface, bounded by walls and a connection with the main stream; the cavity may be located either on the side, top or underneath the main stream and b) the “open-channel cavities”, thus with a free surface, connected to the main stream through a lateral face, and comprised within three lateral and

a bottom wall plus the free surface above. The main difference between both types lies in the existence or not of a free surface and thus of a vertical confinement of the cavity flow. "Open-channel cavities" are generally referred to as "lateral cavities" or "side cavities".

Lateral cavities consist of a relatively large volume of water initially located on the side of a main flow of relatively high speed. These lateral cavities can themselves be divided into: A. the isolated cavities (as in the present case), B. the cavities located between two consecutive groins (see Uijttewaal *et al.*, 2001 and Figure I.9) and C. the series of lateral cavities (see Erpicum *et al.*, 2009 and Figure I.10). Differences between these configurations mainly lie in the direction of the main stream velocity as reaching the upstream limit of the cavity. Unlike case A, in cases B and C the transverse velocity of the main stream is not nil when reaching the studied cavity ; it is directed towards the main stream as it is influenced by the flow leaving the upstream cavity. Moreover, coherent turbulent structures originating from upstream cavities or groynes influence the flow. Literature on groyne fields focuses more on the number of recirculation cells and the exchanges between the main stream and the cavity. Such experiments are proposed by Langendoen *et al.* (1994), Uijtewaal *et al.* (2001), Weitbrecht *et al.* (2008, see Figure I.11). They show that, compared to a single cavity, the groyne fields are characterized by the interaction between the successive cavities. Recent numerical contributions are the ones of Hinterberger *et al.* (2007) and McCoy *et al.* (2008), the latter emphasizing on the three-dimensionality of the flow in the cavity.

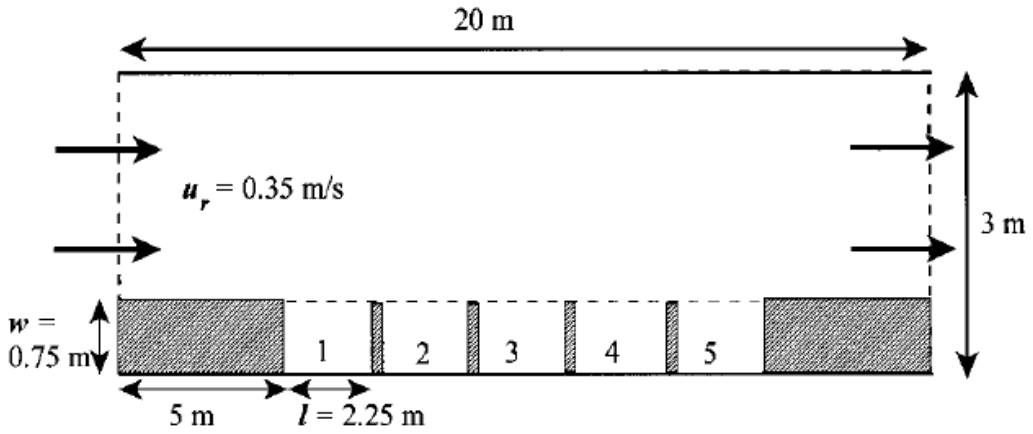

Figure I.9:Schematized Top View of Shallow Flume with Five Groyne Fields Adjacent to Main Stream, from Uijttewaal *et al.* (2001)

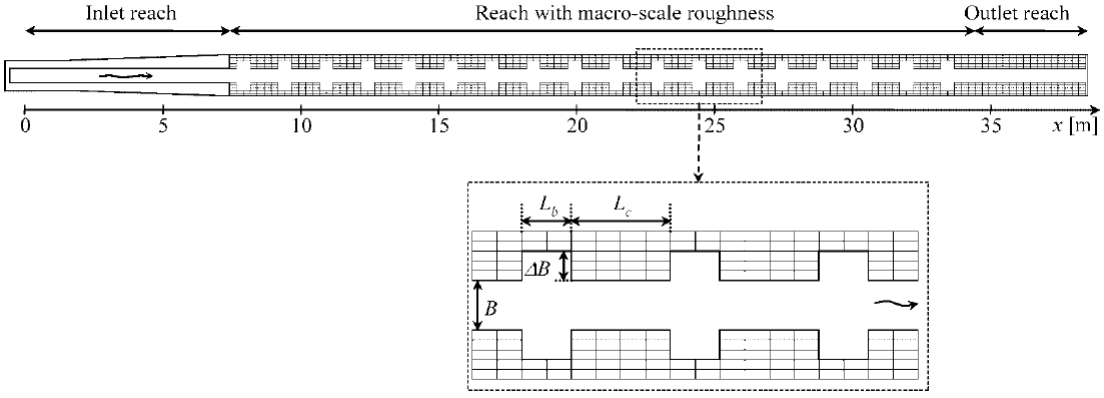

Figure I.10:Plane view of the test flume (above) and definition of the parameters of the macro-rough geometrical configurations (below), from Erpicum *et al.* (2009)

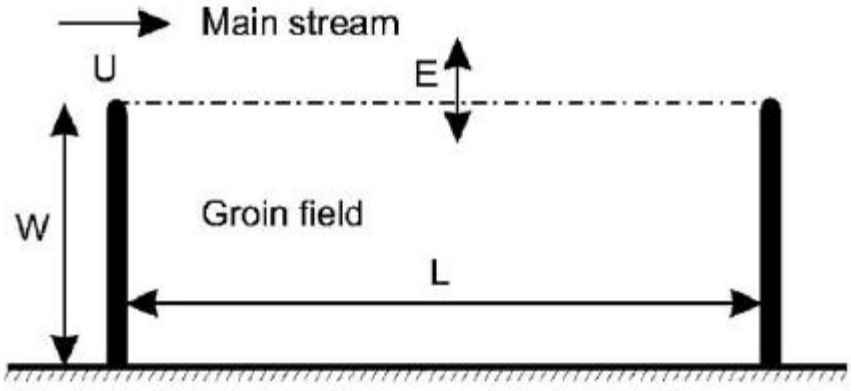

Figure I.11. Schematic of the idealized groin field model, from Weitbrecht *et al.* (2008)

The present paper is dedicated to lateral cavities of type A, which are encountered in various open channel flow hydrodynamics situations. Oxbows, cut-off meanders are natural isolated lateral cavities connected to rivers while harbors connected to a river or sea streams are typical artificial isolated lateral cavities. In the fluvial environment, these situations correspond to meanders (Figure I.12a); to old dead rivers channels (Figure I.12b) or spacing ears positioned perpendicularly to the banks; to river ports (Figure I.12d) where the artificial socket is then connected to the adjacent stream. In the coastal environment, the cavity is generally a port (Figure I.12c), connected to the sea in which a coastal current parallel to the coast develops.

Figure I.12. Lateral cavities,from google earth and Lecoz (2007)

Contributions concerning lateral cavities mix experimental (based on PIV measurements) and numerical approaches (Kimura and Hosoda, 1997; Nezu *et al.*, 2002 ; Mizumura and Yamasaka, 2002). Kodotani *et al.* (2008) measured simultaneously the velocity field at the surface and surface level oscillations to correlate seiching and streamwise velocity in the main stream.

When focusing on the recirculation cells (often referred to as “recirculations” throughout manuscript) that develop in the cavity, the main parameter emerging from literature is the aspect ratio W/L of the cavity with W the cavity width (along the crosswise direction, perpendicularly to the main stream direction) and L its transverse dimension. Most studies in the literature consider a low aspect ratio ($W/L \leq 1$)

1. For $W/L << 1$, two cells are observed, aligned in the streamwise direction, as for instance in Sanjou and Nezu (2013).

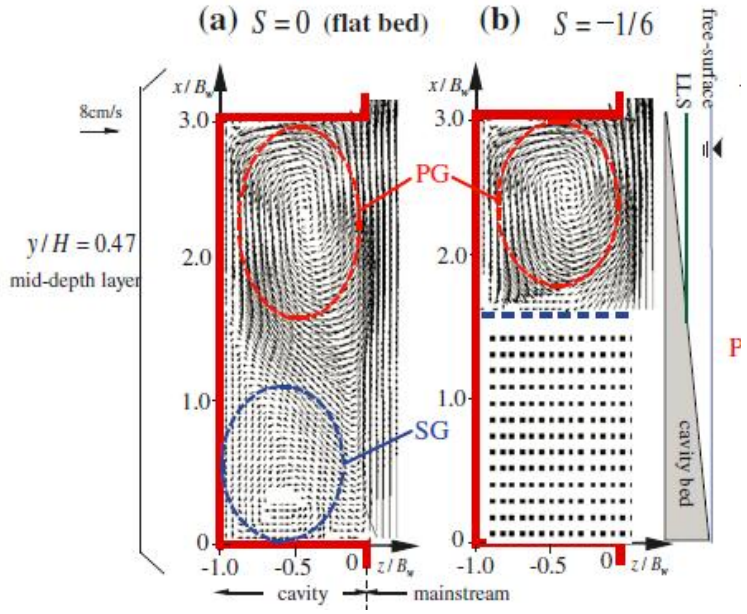

Figure I.13:Comparison of time-averaged horizontal velocity components among different bed configurations, from Sanjou and Nezu (2013)

2. For $W/L \approx 1$, a single quasi 2D recirculation cell occupies the whole cavity, as for instance in Mizumura and Kimura (2002)

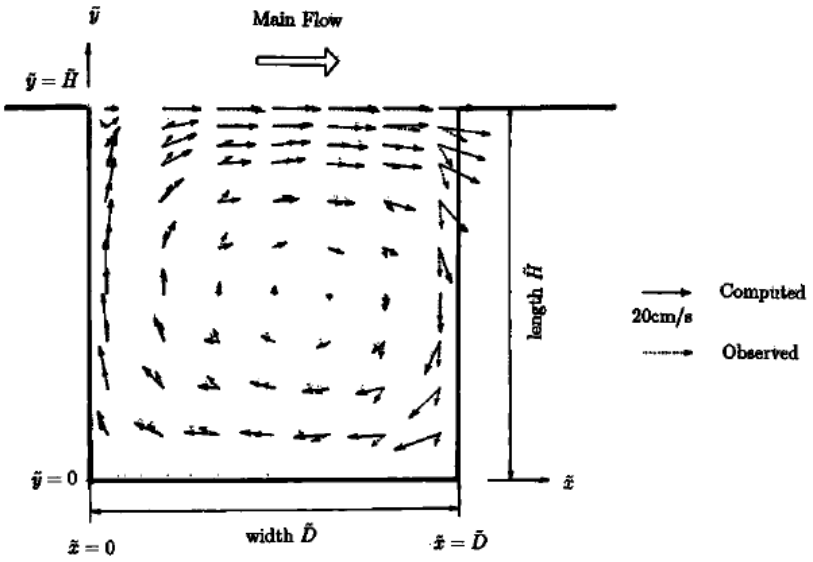

Figure I.14:Time-Averaged Velocity Vectors:Definition sketch of coordinate system and computed and observed flow velocity in square embayment. From Mizumura and Kimura (2002)

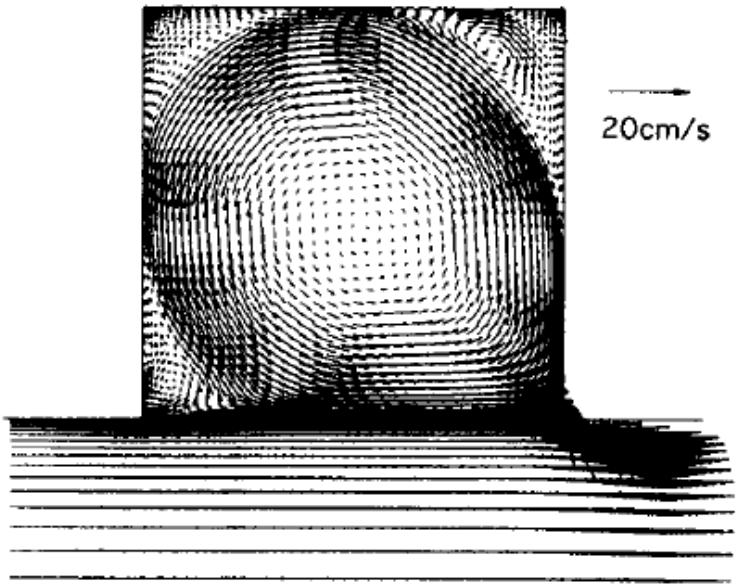

Figure I.15. Time-Averaged Velocity Vectors, from Kimura and Hosoda (1997)

3. For *W/L*>1, only one contribution was encountered: the work by Booij (1989) where two cells are observed. Note that for a groyne field, Weitbrecht *et al.* (2008)'s experiments, with *W/L* reaching 2, also obtained a second recirculation.

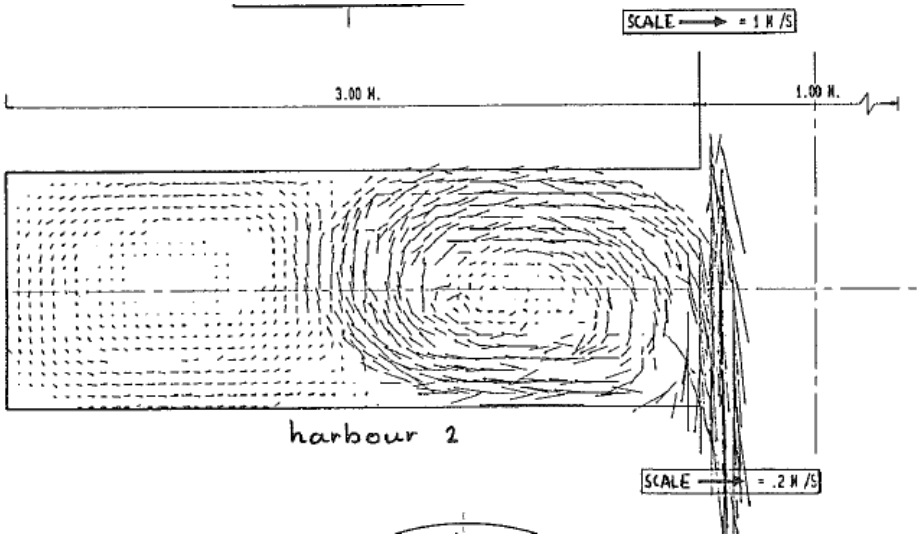

Figure I.16:Measured depth-averaged velocity field, from Booij (1989)

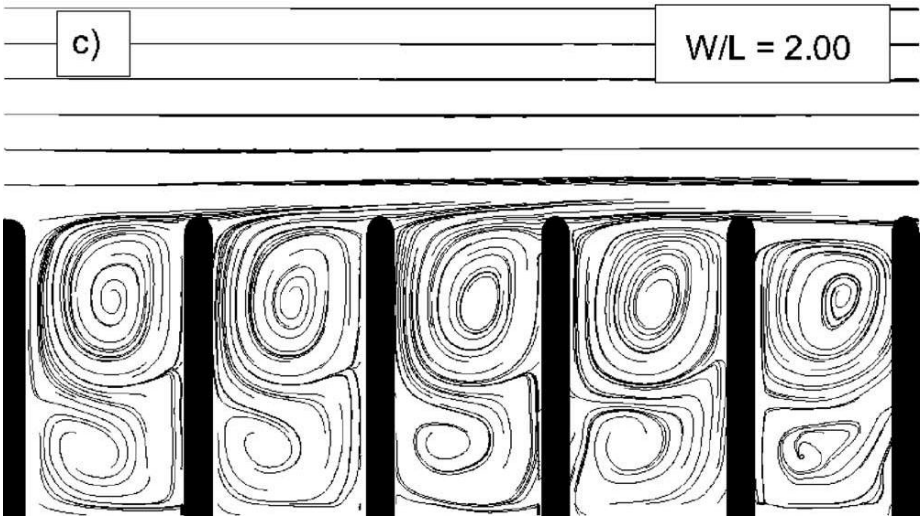

Figure I.17: Mean flow properties in groin field flows with aspect ratios *W/L*=2, where the 2-gyre systems are visible, from Weitbrecht *et al.* (2008)

Table I.1 summarizes the papers encountered for Groyne fields and lateral cavities in the literature where it appears that the dimensions are always so that *W/L*<1.5 except for Booij (1989) where *W/L* reaches 3.

Table I.1. Range of parameters in previous works

	Case	*L(cm)*	*W/L*	*Fr*	*Mass transfer*
Uijttewaal *et al.*, 2001	Groin fields	107-225	0.3-0.7	0.3	
Uijttewaal, 2005	Groin fields	450	0.4	0.2	
Hinterberger *et al.*, 2007	Groin fields	125	0.4	0.2	
Weitbrecht *et al.*, 2008	Groin fields	15-145	0.3-3.3	0.1	*yes*
McCoy *et al.*, 2008	Groin fields	107.5	0.7	0.6	
Booij, 1989	Lateral cavities	100, 300	1, 3	0.2	*yes*
Kimura & Hosoda, 1997	Lateral cavities	15-22.5	0.7-1	0.8	
Altai and Chu, 1997	Lateral cavities	32,89	1		*yes*
Muto, 2000	Lateral cavities	16,48	0.33, 1		
Mizumura & Yamasaka, 2001	Lateral cavities	8-16	0.5-1	0.2-0.8	
Nezu & Onitsuka, 2002	Lateral cavities	20	0.2	0.5	
Nezu & Onitsuka, 2002	Lateral cavities	0.15-0.2	0.1-0.33	0.5	
Booij, 2004	Lateral cavities	100-300	1	0.2	
LeCoz *et al.*, 2006	Lateral cavities	10	0.5	0.4	
Kadotani *et al.*, 2008	Lateral cavities	25-35	0.2-0.3	0.6-0.8	
Tominaga, 2011	Lateral cavities	30	0.5		
Wolfinger, 2012	Lateral cavities	30	1.5		
Tuna *et al.*, 2013	Lateral cavities	30.5	1.5		*yes*
Sanjou *et al.*, 2012 & 2013	Lateral cavities	30	0.33	0.17	*yes*
Present work	**Lateral cavities**	**30**	**0-5**	**0.2**	***yes***

3 MIXING LAYER

At the connection between the main stream with uniform velocity and the cavity at rest, a large velocity gradient forms. This velocity gradient leads to a horizontal mixing layer which extends from the upstream corner to the downstream corner of the interface. This mixing layer transfers mass and momentum from the main flow to the cavity. It is thus of primary importance for cavity performance, exchange of nutrients and gases influencing the ecological equilibrium of oxbows, or exchange of fine sediments influencing the geo-morphological efficiency of groyne fields. Moreover, the coherent vortices shed from the upstream corner to the downstream corner of the junction induce the excitation of the cavity resulting (for specific conditions, out of scope of the present work) in large standing waves: this is the so-called "seiche" phenomenon (*e.g.* the recent contribution by Tuna *et al.*, 2013).

Mixing layers are very common in the field or in the literature. Different types of mixing layers exist depending on their specificities. To start with, authors such as Wygnanski and Fiedler(1970), Bell and Mehta(1990, and Figure I.18) and Loucks and Wallace(2012) studied the simple configuration for a mixing layer with two parallel flows of different velocities suddenly released one next to the other. These measurements agree that the width of the mixing layer increases linearly along its development length. The maximum turbulent intensities and Reynolds shear stress across the mixing layer occur at its centerline. After an initial increase, they tend to decrease in magnitude with distance from the upstream boundary condition. Moreover, for high velocity gradients, the inflection of the transverse profiles of mean streamwise velocity leads to Kelvin-Helmholtz instabilities that give birth to coherent turbulent structures that are shed from the upstream end and advected along the mixing layer with increasing typical size and time-scale.

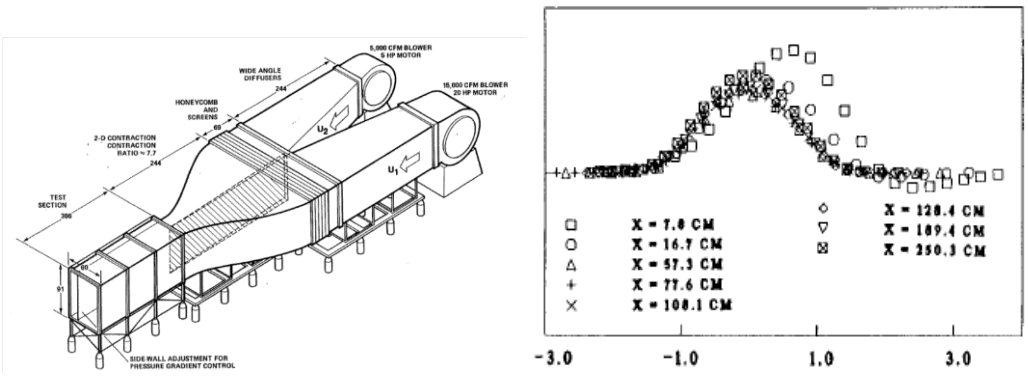

Figure I.18:Schematic view of mixing-layer wind tunnel and profiles of turbulence products in similarity coordinates, at different streamwise stations, from Bell and Mehta (1990)

Authors studied mixing layers in other configurations, among others are: mixing layers in accelerated (Fiedler *et al.*, 1991) or curved flows (Margolis and Lumley, 1965; Gibson and Younis, 1983; Plesniak *et al.*, 1996 and Figure I.19), or in much more complex situations such as a sudden lateral expansion (Babarutsi *et al.*,1989 and Figure I.20).

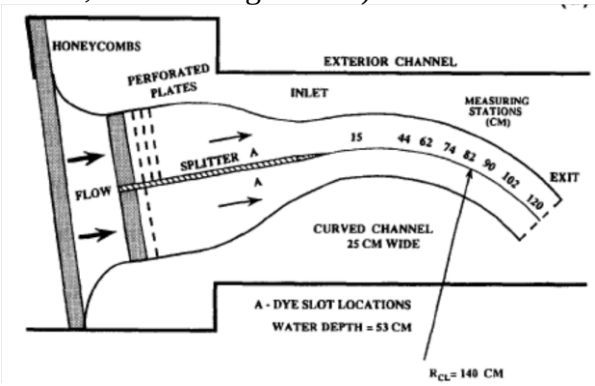

Figure I.19:Schematic view of curved test sections for water facility, from Plesniak (1996).

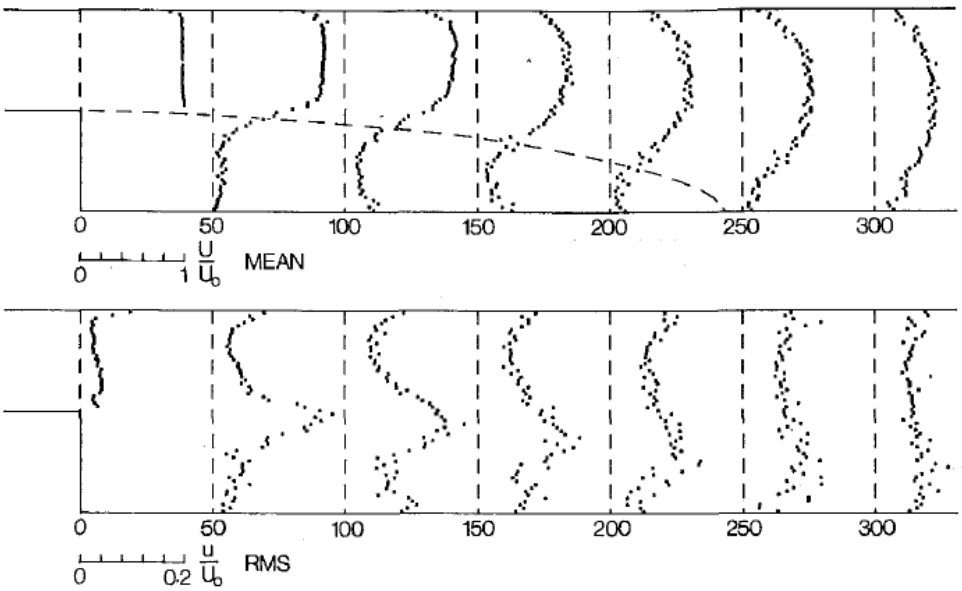

Figure I.20. Experimental transverse profiles of mean velocity and mean velocity r.m.s., from Babarutsi *et al.* (1989)

Moreover, apart from the specific geometry in which the mixing layer is observed, the mixing layer may be confined, either laterally due to the side walls located close enough from the mixing layer to impact it (Chandrsuda and Bradshaw, 1981 and Figure I.21) or vertically due to the limited depth for a liquid flow or channel height for a gas flow (Biancofiore, 2014; Sukhodolov *et al.*, 2010; Uijttewaal and Booij, 2000; Van Prooijen and Uijttewaal, 2002 and Figure I.22).

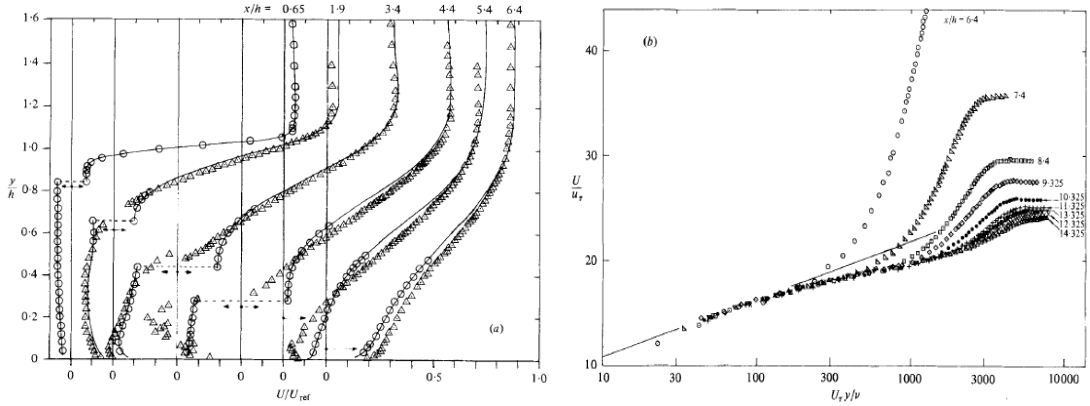

Figure I.21. Mean velocity profiles： upstream of reattachment and downstream of reattachment, from Chandrsuda and Bradshaw (1981)

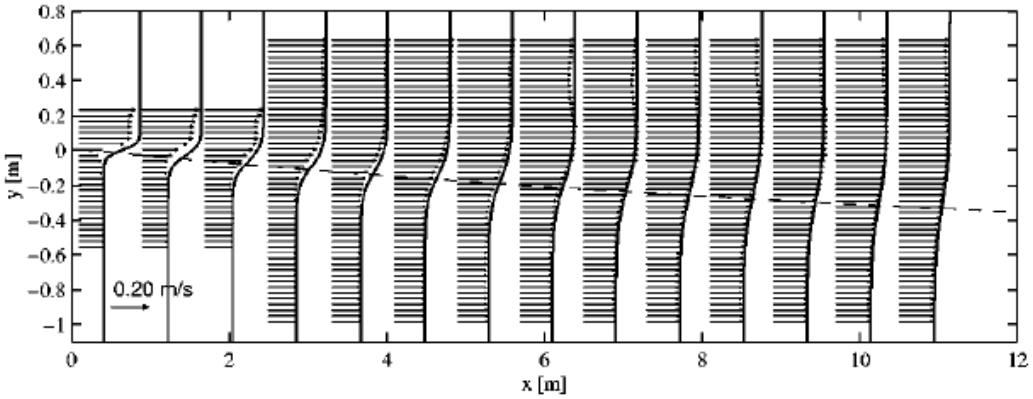

Figure I.22. Velocity vectors (measurements) and profiles (model) of the mean velocity field where the dashed line indicates the position of the center of the mixing layer (Van Prooijen and Uijttewaal, 2002)

In most mixing layers, this centerline is free to develop and its localization is one of the important results (see Uijttewall & Booij, 2000 and the previous figures). The specificity of the mixing layer at the interface with the lateral cavity is that its centerline is constrained by both corners of the cavity (see Tuna *et al.*, 2013 and Figure I.23). Mixing layers with such a constrained centerline correspond to several filed cases, such as compound channel flows where the mixing layer remains aligned with the bank-step (see the scheme from Bousmar and Zech, 1999 and Figure I.24), composite channels with longitudinal zones of different roughness (see scheme by Vermaas *et al.* (2011) and Figure I.25) or finally the canopies where the mixing layer remains located at the crest (Raupach,1996).

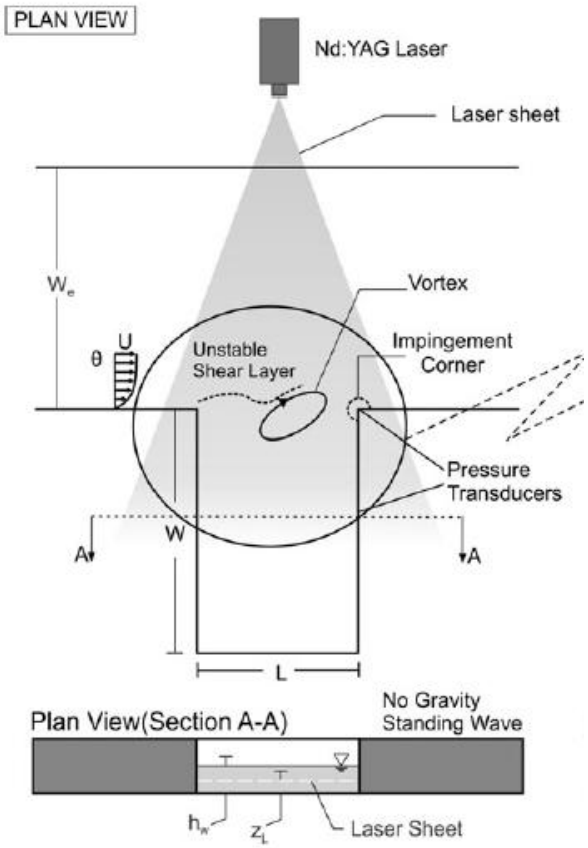

Figure I.23:Schematic of experimental test section and quantitative imaging system, from Tuna *et al.* (2013)

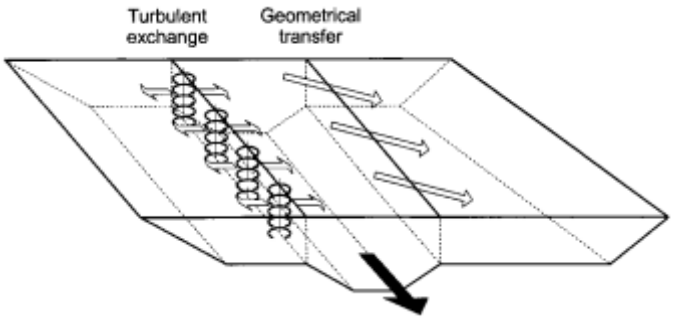

Figure I.24: Flow exchange at interfaces between main channel and floodplains, from Bousmar and Zech (1999)

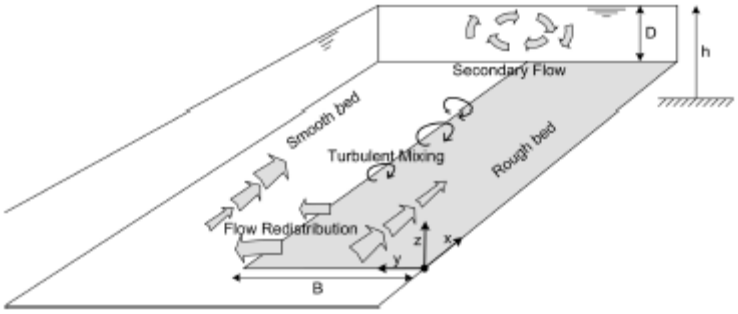

Figure I.25:Schematization of a mixing layer between two parallel flows subject to different bed rough roughnesses, as it develops after an initially uniform situation, from Vermaas *et al.* (2011)

Figure I.26 :Large coherent structures are visualized by dye injection in the center of the mixing layer just downstream of the splitter plate. The arrows indicate the velocities in the two undisturbed streams, from Van Prooijen and Uijttewaal (2002)

4 MASS TRANSFER

The exchange between a river and adjacent flow domains like harbors, groyne fields, and flood plains is motivated by questions from the practice of civil engineering. These processes indeed govern the balance of bio-habitat (maximum speeds, volumes of sediment available, exchange of nutrients, oxygen, pollutants) and industrial activity especially for harbors (maximum oscillation, strong sediment deposition, pollutions).

Assuming a steady flow in the main stream, the connection with the lateral cavity studied in the literature correspond to a transfer from the main stream to the cavity of i) passive scalar (see Booij, 1989, Tuna *et al.*, 2013) or ii) particles (see Mizumura and Yamasaka, 2002 or Jamieson and Gaskin 2014). The governing process for these transfers is the occurrence of coherent turbulent structures advected along the mixing-layer. The probability of the deposition of sediment and silt in a river reach and the retention time for biological material like algae, are also highly determined by the details of the flow field in the stagnant zones and the intermediate mixing layer (Brinke *et al.*, 1999).

Experimental research on the effects of dead zones for passive scalar transport in rivers has been done by Valentine and Wood (1977, 1979), who performed model experiments with artificially created dead zones in the bottom of a channel. Their experimental data suggest that the effect of

dead zones on longitudinal dispersion can be covered by a description in terms of a first-order exchange process with a constant exchange coefficient.

Substantial experimental work on exchange processes has been performed on model harbors, clearly because of its relevance regarding dredging problems (*e.g.* Westrich and Clad, 1979; Booij, 1989; Langendoen *et al.*, 1994; Altai and Chu, 1997). In most cases, this concerns simple geometries from which the bulk exchange properties are determined along with a rough indication of flow patterns. For approximately square harbors, the exchange process appears to be governed by the single time constant of a first-order system (Booij, 1989; Altai and Chu, 1997). The shape of the harbor gives birth to a single large gyre that completely fills the harbor. The exchange between the harbor and the river is then mediated by two processes: the exchange of momentum and matter through the mixing layer, and the turbulent transport from the center of the gyre toward the interface with the mixing layer. The latter process is slower, thereby dominating the characteristic time of the exchange.

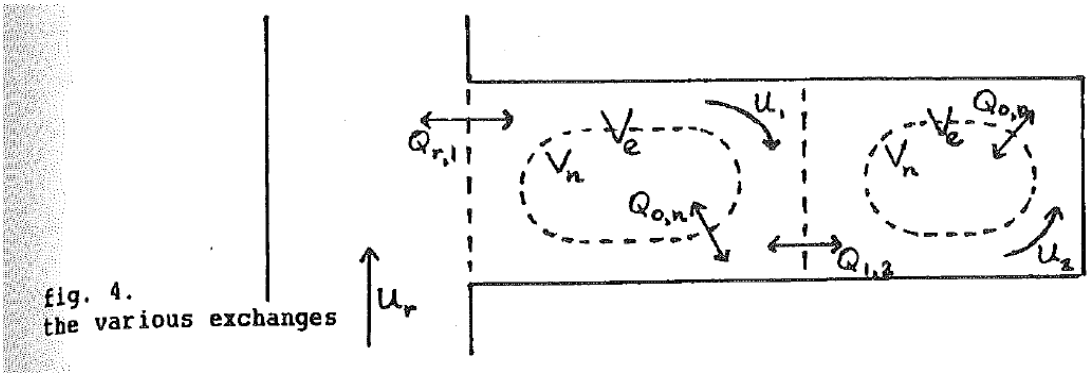

Figure I.27: The various exchanges in harbours. (Booij, 1989)

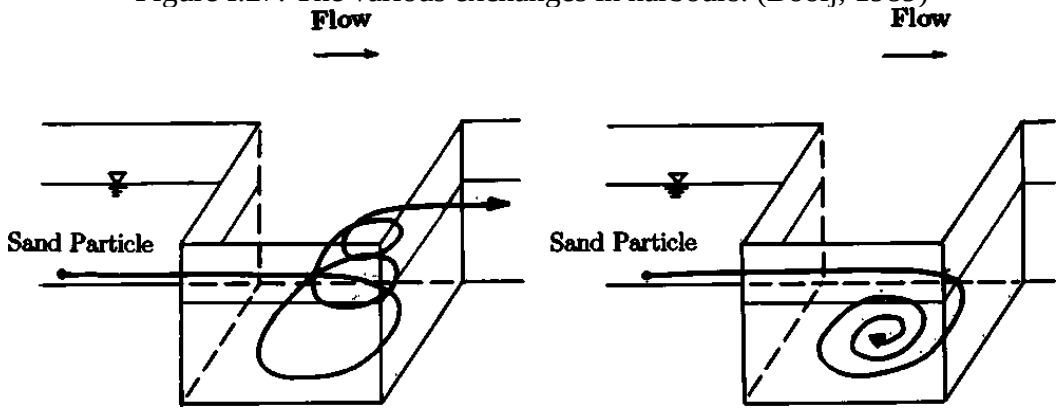

Figure I.28: Left-hand side shows sketch of sand particle movement which goes back to main channel and right-hand side gives sketch of sand particle movement which accumulates in embayment. (Mizumura,2002)

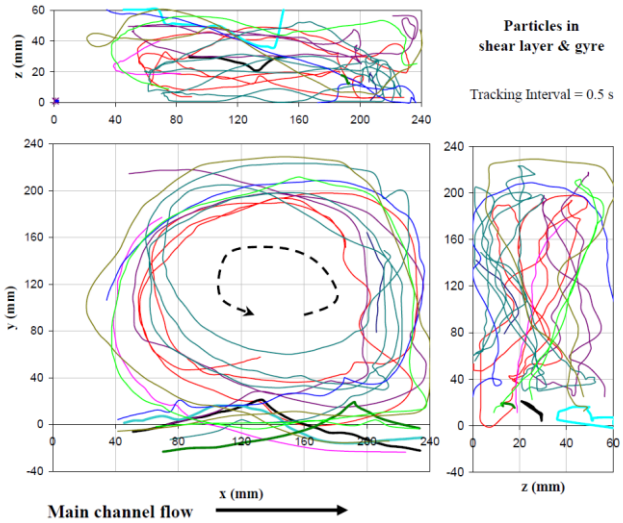

Figure I.29: Particle paths indicating the dynamically active regions of the shear layer and the gyre. (Jamieson and Gaskin,2007)

5 SCIENTIFIC ISSUE AND ORGANIZATION OF THE MANUSCRIPT

The preceding literature review indicates that recirculations of different characteristics (size, number, crosswise or streamwise alignment, etc.) form in the cavity. In these past studies, the cavity aspect ratio varied in a limited range (please to Table I.1). Yet, it seems to be the main parameter ruling the characteristics of the recirculations and no evidence existed, at the beginning of this work, of the existence of a third or even additional recirculations within extremely wide cavities, corresponding to oxbows. Additionally, the appearance of recirculations is also influenced by the momentum exchange with the mainstream, which is ensured through the mixing layer at the cavity/main stream interface; a feedback effect from the recirculations structures on the mixing layer is expected at the beginning of the work. Finally, exchanges processes are ruled by a characteristic time imposed by the slowest parts of the flow. The effect of the recirculations structures on the validity of Fickian processes and on their intensity was worth seeing.

To get answers to these different questions, an experimental approach is selected herein and the work was divided in three parts. Chapter II describes the experimental set-up and measuring techniques used to characterize the recirculations structures. Compared to previous experiments reported in the literature (Table I.1), our work takes advantage of an experimental facility with comparable dimensions but which allows an aspect ratio reaching W/L up to 5. Chapter III is devoted to the study of the mixing layer at the interface, with a hydraulic point of view (flow pattern, vortex shedding, etc.). Chapter IV then focuses on the role of this mixing layer on passive scalar transfer. Finally, general conclusions and prospects are proposed in chapter V.

Chapter II: Experimental set-up and methodS

The aim of this Chapter is to introduce the experimental set-up that is intensively used for the present work (section 1), and to present the main measuring techniques used to quantify velocities and mass exchanges (section 2). The velocity measurement in the cavity and within the mixing layer are mostly performed using PIV (section 2.1) and partly with ADV (section 2.2). The objective is to verify the accuracy of the other measuring method.

1 EXPERIMENTAL SET-UP AND FLOW CONFIGURATION

1.1 *Experimental facility*

The experiments are performed in the open-channel intersection facility that was available in the laboratory (described in Rivière *et al.*, 2011, here with a sealed up branch as in Mignot *et al.*, 2012). It consists of a 90° junction of three identical channels, all horizontal, made from glass, 2 m long and 0.3 m wide (Figure II.1). The flow enters through the upstream channel and mix in the cavity. A pump located in the downstream tank produces the flow that is measured by electromagnetic flowmeters.

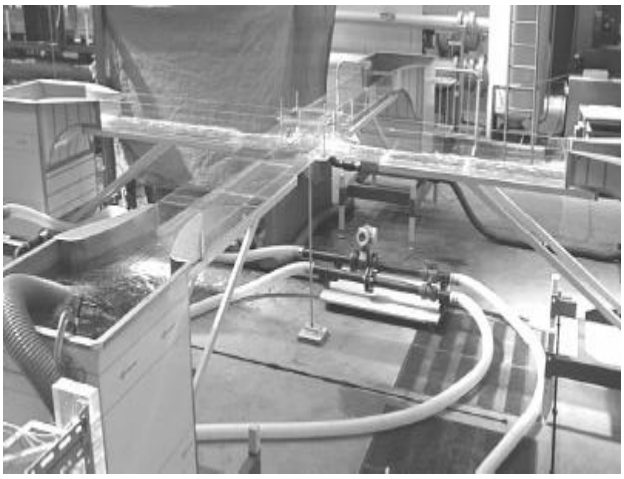

Figure II.1. Photographs of the intersection facility at LMFA

The facility was modified for our purposes: the upstream branch of the main channel provides the inlet flow, the downstream branch of this channel acts as outlet channels and the side channel is closed with no inflow or outflow. A honeycomb at the inlet of the upstream branch serves to stabilize and straighten the inlet flow. A PVC channel (length 60 cm) is added to the end of the downstream channel which total length is then L_d=2.6m, and the flow depth is imposed using a vertical sharp crest weir. The inlet discharge Q varies in the range 1-5 L/s. Corresponding hydraulic radius based Reynolds number range is 9000-36000.

1.2 *Adjustment of the flow geometry and parameters*

The length of cavity (noted W herein) is easily modified by fixing an end wall in the side channel at a given distance from the junction. This wall is made by a sheet of polyurethane with a flat glass gasket ensuring its tightness, to have the same roughness as the channel walls (and same wave reflection capacity in case of seiching phenomenon, which is out of scope of our work). Conversely, the width of the cavity (noted L) remains constant, equal to the width of the main channel (L=b=30 cm). The aspect ratio of the cavity (W/L) can vary from 0 up to 5 as L varies from 0 to 1.5m. This was shown to be a considerable advantage compared to the available literature, where this ratio is usually fixed, in the introduction

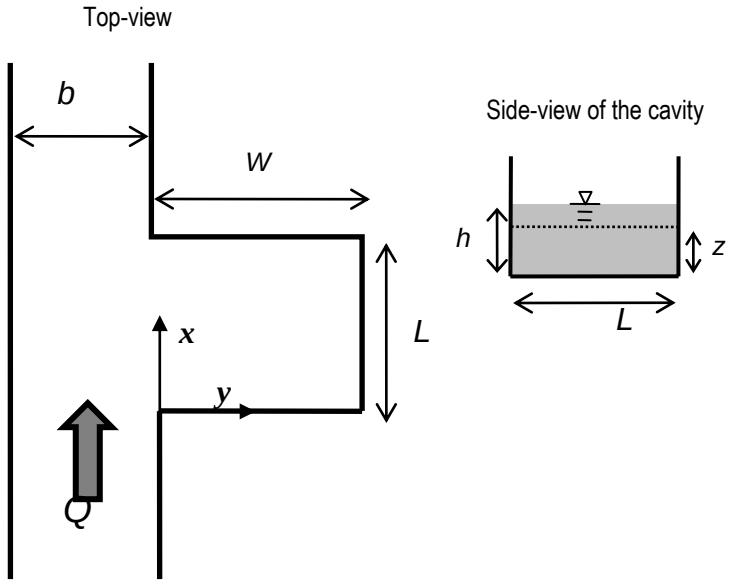

Figure II.2. Sketch of the cavity geometry: top-view (left) and side-view (right)

A continuously adjustable sharp crested weir is used to fix the water depth at the outlet section of the downstream branch. The water depth in the junction *h* is measured in the centre of the junction using a moveable point gauge with an uncertainty of ±0.15 mm. Additional measurements used wave probes (three resistive probed from Churchill Inst. and two ultrasonic probed from Hyde Park, Daniel Wood head Company) with comparable uncertainty: in the cavity, the depth of four other positions are measured at the same time, shown as the red points in the following figure. At each point, the water depth during 1 minute is recorded: both variations (at a given point) and deviation (from one point to another) are smaller ±0.1 cm. This confirms that no seiching occurs during our experiments and that the flow depth can be considered as constant within the whole flow.

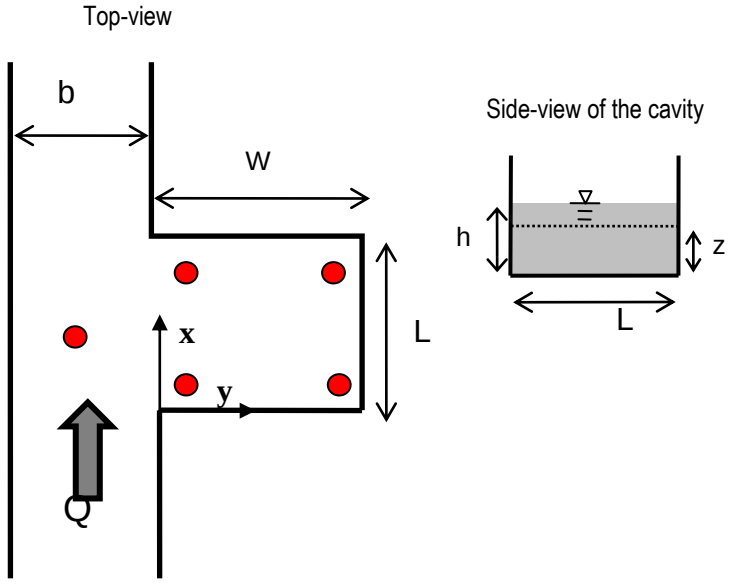

Figure II.3:The schema for measuring depth

A pump located in the downstream tank produces the flow that is measured by electromagnetic flowmeters (Promag 50 from Endress Hauser) shown in the Figure II.21. The uncertainty of the measured flowrate is ±0.05L/s.

Figure II.4: Electromagnetic flowmeters

For both cavity experiments (chapter III) and mixing layer experiments (chapter IV), a reference flow configuration is defined, notably for analyzing the influence of different flow parameters. The hydraulic conditions of this reference flow are sum-upped in table II.1.

Table II.1:Hydraulic conditions used as a reference flow

W(m)	L(m)	*h* (cm)	*Q* (L/s)	*U* (cm/s)	*Fr*	*Re*
0.3	0.3	7	3.5	1.67	0.02	69000

1.3 *Conclusion*

The modified experimental facility allows to adjust continuously and easily the width *W* of the cavity. Flow parameters are controlled using point gauges and electromagnetic flowmeters. A reference configuration was defined, used to study the influence of these flow parameters on the behavior of the cavity. The measurement techniques used to characterize this behavior are described in the following.

2 MEASURING TECHNIQUES USED TO CHARACTERIZE THE FLOW

2.1 *Particle Imaging velocimetry*

2.1.1 *Operating principle*

The fluid is seeded with tracer particles which, for sufficiently small particles, are assumed to faithfully follow the flow dynamics. The fluid with entrained particles is illuminated so that particles are visible. The motion of the seeding particles is used to calculate speed and direction (the velocity field) of the flow being studied.

Typical PIV apparatus consists of a camera (normally a digital camera with a CCD chip), a strobe or continuous laser with an optical arrangement to limit the physical region illuminated (normally a cylindrical lens to convert a light beam to a sheet, the seeding particles and the fluid under investigation. Velocities are obtained after a post-processing of the optical images.

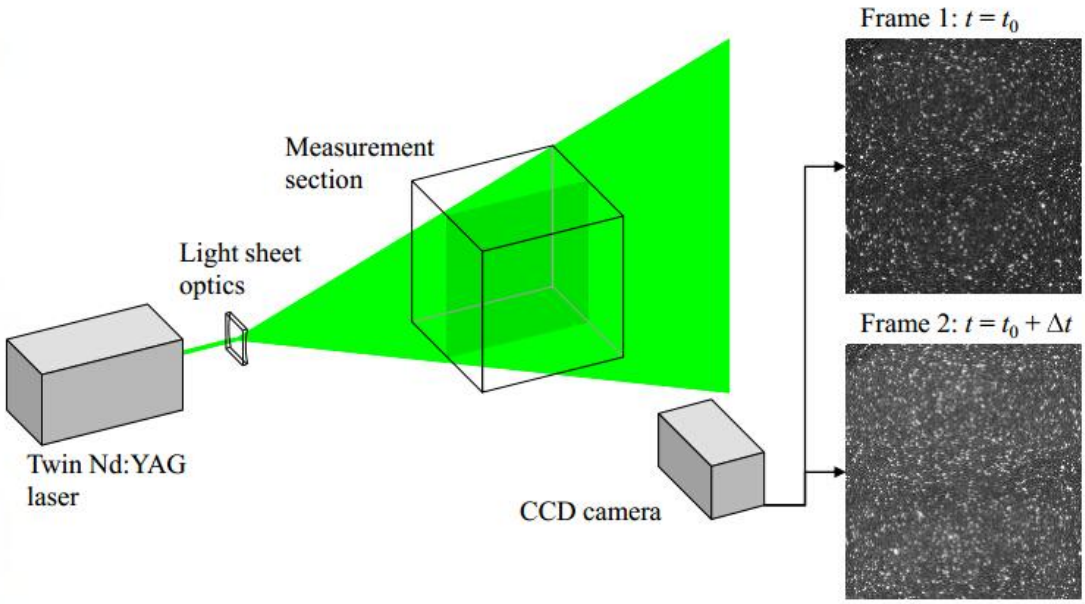

Figure II.5:Classical PIV system, from Brossard (2009)

Most measurements in the following chapters are performed using 2D horizontal PIV. A 40mW laser (Z-Laser Germany) coupled with a cylindrical lens generates a 1mm horizontal light layer at the elevation: z=5cm (z/h=0.71). Polyamid particles (diameter 50 μm, Dantec) are added to the water. Finally, a video camera (Allied Vision Technologies) is located above the cavity in order to record the particle motion over 3000 consecutive images of 1280x960 pixels each, with an average spatial resolution of 0.6mm per pixel for cavity PIV and with an average spatial resolution of 0.3mm per pixel for mixing layer PIV, at a frequency equal to 30Hz. Finally, the commercial software Davis (from La vision) permits to correct image distortions, subtract the background and finally compute the velocity fields.

2.1.2 .*Estimation of the PIV uncertainties*

- Uncertainty from tracers (seeding particles)

The Stokes number *St* is a dimensionless number corresponding to the behavior of particles suspended in a fluid flow. It is defined as the ratio of the characteristic time of a particle (or droplet) to a characteristic time of the flow or of an obstacle, namely:

$$St = \frac{t_0 u_0}{l_0} \quad (1)$$

where t_0 is the relaxation time of the particle (the time constant in the exponential decay of the particle velocity due to drag), u_0 is the fluid velocity of the flow well away from the obstacle and l_0 is the characteristic dimension of the obstacle (typically its diameter). Particles with low Stokes number follow fluid streamlines (perfect advection) whereas for large Stokes number, the particle's inertia dominates so that the particle will continue along its initial trajectory.

In case of Stokes flow, which is when the particle (or droplet) Reynolds number is low enough that the particle drag coefficient is inversely proportional to the Reynolds number itself the characteristic time of the particle can be defined as

$$t_0 = \frac{\rho_d d_d^2}{18\mu_g} \quad (2)$$

where ρ_d is the particle density, d_d is the particle diameter and μ_g is the gas dynamic viscosity (Brennen, 2005).

In experimental fluid dynamics, the Stokes number is a measure of flow tracer fidelity in particle image velocimetry (PIV) experiments where very small particles are entrained in turbulent flows and optically observed to determine the speed and direction of fluid movement (also known as the velocity field of the fluid). For acceptable tracing accuracy, the particle response time should be faster than the smallest time scale of the flow. Smaller Stokes numbers represent better tracing accuracy; for *St* >>1, particles will detach from a flow especially where the flow decelerates abruptly. For *St*<<1, particles follow fluid streamlines closely. If *St*<<0.1, tracing accuracy errors are below 1% (Tropea, 2007).

For our work, the Polyamid seeding particles have a diameter with 50 μm and a density 1100 kg/m^3. This corresponds to St=0.5, which means the particle herein will bring an accuracy error which can be ignored.

- Uncertainty from calibration

Calibration here is defined as the process for correcting image distortions by the commercial software Davis (from La vision). According to the software, the treatments for the calibration will bring an accuracy error with $\Delta s_{calib} = 1.4$ pixel.

- Uncertainty from correlation

Cross-correlation involves the shifting windows. The basic theory of the cross-correlation is the development of cross-correlation between two singly exposed images which is explained in figure II.6. The interrogation window size is also progressively reduced to reach a final size of 32x32 or 16x16 pixels in practice, depending upon the density of particle images.

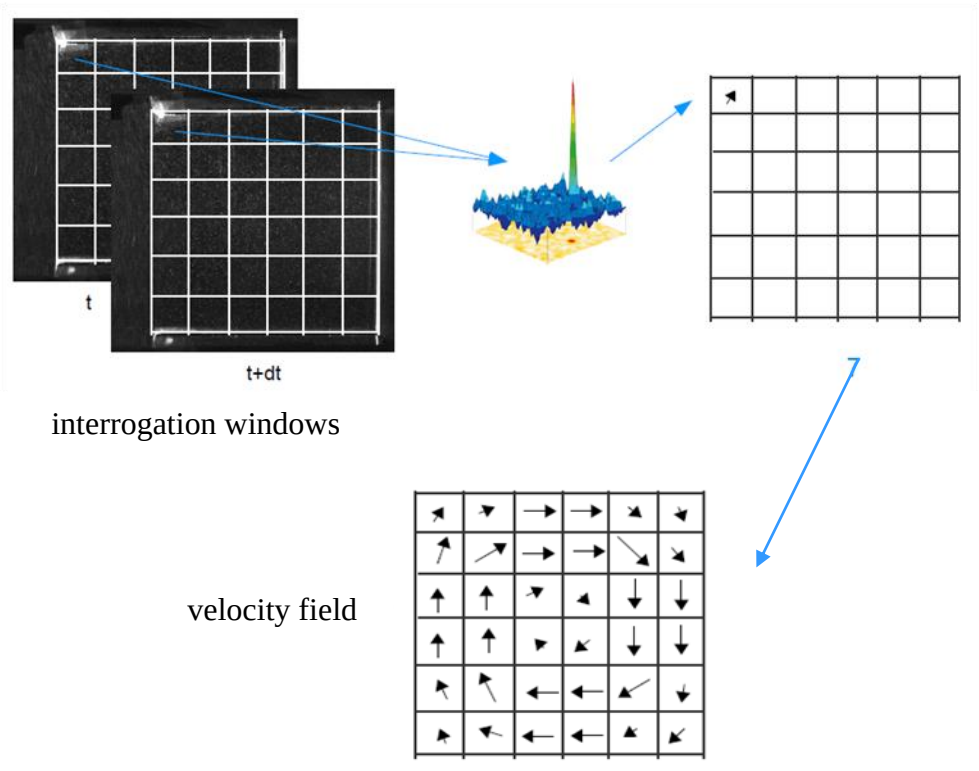

Figure II.6. Cross-correction(Brossard,2009)

The minimum treatment unit between the two exposed images is 1 pixel, so the estimated error is defined:

$$\Delta v_{corr} = \frac{0.1\ R}{\Delta t} \quad (3)$$

where *R* is the resolution of the image, and Δ*t* is the time period between the two images (Mignot *et al.*,2014). For cavities PIV, the average spatial resolution is 0.6mm per pixel at a frequency equal to 12.2Hz. The estimated error for 1 pixel for the velocity is 0.7 mm/s, which is about $\Delta v_{corr} = 0.42\%$ of the mean flow velocity. For mixing layer PIV, the average spatial resolution is 0.3mm per pixel at a frequency equal to 30Hz. The estimated error for 1 pixel for the velocity is 0.9 mm/s, where $\Delta v_{corr} = 0.54\%$ of the mean flow velocity.

Another possible approach to estimate the uncertainties related to the PIV measuring method is to analyze, a posteriori, the obtained data and evaluate their coherency or consistency, or oppositely their chaotic aspects. An attempt to this method is proposed in Appendix A and seems to indicate that the level of uncertainty of the PIV measuring tool remains limited.

2.2 *Acoustic Doppler Velocimetry*

Though PIV was mainly used to characterize both flow velocities and fluctuations, some experiments used ADV. The ADV (Acoustic Doppler Velocimetry) can indeed be easily and rapidly implemented for measuring local mean and fluctuating velocities. rapid and practical. The ADV was the main measuring techniques for two recent Ph.D. in the laboratory (Peltier, 2012 ; Han, 2015) from which we reproduce the following principles and methods.

2.2.1 *Operating principle*

The Vectrino probe we use (Nortek, Vectrino+, *Fs* = 1-200 Hz) is a high-resolution acoustic velocimeter used to measure 3D water velocity in a wide variety of applications from the laboratory to the ocean. The basis measurement technology is the coherent Doppler processing, which is characterized by accurate data with no appreciable zero offset (Nortek, website). There are many types of ADV instruments such as the down-looking /side-looking and with/without the rigid stem. For this thesis, we use the Vectrino side looking fixed probe (Figure II.7, red frame) especially adapted for shallow flows. As displayed in this Figure II.7, the probe (part 4) is mounted on a fixed stem (part 3) connected to the main housing (part 2) through the probe end bell. It uses the Doppler effect to measure flow velocity by transmitting a short pulse of sound, receiving its echo and measuring the change in pitch or frequency of the echo. Different from the standard Doppler profilers, the Vectrino seperates the sender part and the receiver part as shown in the Figure II.7. It transmits the signals through the central beam and receives them through four beams displaced in one side. All the four beams focus on the same sampling volume which forms at a 5cm distance from the center of the sending beam. The sampling volume is cylinder with a fixed diameter of 6mm. The height can be adjusted from 3mm-15mm. And so the receiver will ‘listen’ the data in this sampling volume and then give out the instantaneous velocity. The velocity fluctuations can be measured at a maximal frequency of 200 Hz, which is useful for having a well described turbulent spectrum.

1.Underwater meatable connector

2.Intergrated shape zinc anode and main housing

3.Rigid stem

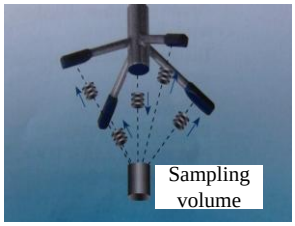

4.Miniature 4 beam stainless steel prob with temperature sensor 5cm to the sampling volume

Figure II.7: different probes and working principle of the side looking probe (Nortek)

2.2.2 *Measuring characteristics*

During the measurement process, SNR (Signal noise ratio) is surveyed, which is defined as $20log_{10}(\frac{Amplitude_{signal}}{Amplitude_{noise}})$ according to Nortek user guide. It influences the precision apparently. As the method used by Hurther (2001), the data is too complex for our experiment. So, the noise correction was generally not performed here. However, according to the study of Strom and Papanicolaou (2007), the noise has a negligible effect on the mean velocities, and Reynolds normal stress τ_{yy} and Reynolds shear stress τ_{xy}. Only τ_{xx} is noised, but according to McLelland and Nicholas(2000), when the SNR is bigger than 20 db, the noise influences very little. Notably thanks to the use of appropriate particles, this SNR was always higher than 20 db in all our experiments (see below).

For measuring the turbulence characteristics in the mixing layer, the frequency is fixed to 30 Hz. For testing the average velocity, a longtime data acquisition is in the Figure 8. For finding the end of the recirculation, only the direction of the mean velocity is required so the time-average velocity is used so 120 s is enough. However, for the measurement of turbulence characteristics, 3 minutes is used get a good convergence of the cross-power spectrum densities in the most productive zone of turbulence in the flume.

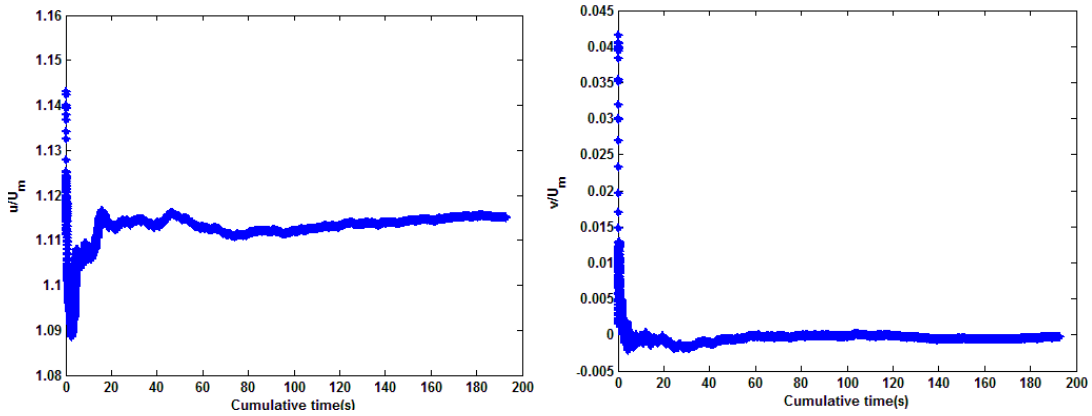

Figure II.8: Cumulative mean velocity in streamwise and transverse direction

2.2.3 *Despiking the ADV data*

However, it presents two main disadvantages. The first one is aliasing of the signal emitted by the ADV. That appears as the phase-shift between the outgoing and incoming pulse lies outside the range between+180° and -180°.And so the ambiguity will introduce a spike in the recording data (Goring and Nikora, 2002). A spike also occurs when the flow velocity range exceeds the preset velocity range or there exits an contamination by the complex boundary geometry in the channel and also when a large bubble passes.

The spikes are removed using a correction of the method developed by Goring and Nikora (2002). This method is called "Phase-Space Thresholding Method" and is widely used by most of the ADV users, at least by the last two Ph.D. in our team.
The basic thought is simple which includes two parts: (1) detecting the spikes and (2) replacing the spikes with corrected data.

(1) Detecting. The threshold arises from a theoretical result from normal probability distribution theory which says that for n independent, identically distributed, standard, normal, random variables ξ_i the expected absolute maximum is $E(|\xi_i|_{max}) = \sqrt{2lnN} = \lambda_U$ where λ_U is called the Universal threshold. For a normal, random variable whose standard deviation is estimated by $\hat{\sigma}$ and the mean is 0, the expected absolute maximum is $\lambda_U\hat{\sigma} = \sqrt{2lnN}\hat{\sigma}$. In the figure NN, it is apparent that most of the data points are enclosed in the ellipsoid cloud and the spikes are outside. So, the points spiked are found out.

(2) Replacing. For Goring and Nikora (2002), they have tried many method for replacing the holes. It's said that a third-order polynomial through 12 points on either side of the spike is the best choice which can be adopted for the sampling rate changes from 25Hz to 100Hz.

However, there is a disadvantage in the algorithm: If more than 10 % of the time series is spiked, the series is simply invalidated. So in this thesis, we use the methodology introduced by Peltier (2012), which improves the equation of Goring and Nikora (2002), for calculating $\lambda_U\hat{\sigma}$ as shown below.

$$\theta_U = tan^{-1}(\sum u_i \Delta^2 u_i / \sum {u_i}^2) \quad (4)$$

θ_U is the angle of rotation of principle axis of $\Delta^2 u_i$ versus u_i.
When the second derivative $\Delta^2 u_i$ is one order smaller (or even more) than the variable u_i, the angle becomes very small and it is impossible to follow the real slope of the cloud ,so Peltier(2012) improved the equation for $\bar{u_i}$ which can ba written as below:

$$\theta_U = tan^{-1}[\sum((u_i - \bar{u}_i)(\Delta^2 u_i - \overline{\Delta^2 u_i}))/\sum(u_i - \bar{u}_i)^2] \quad (5)$$

This despiking method is less restrictive than the original method. So, the despiked data signal is obtained in the Figure 9.

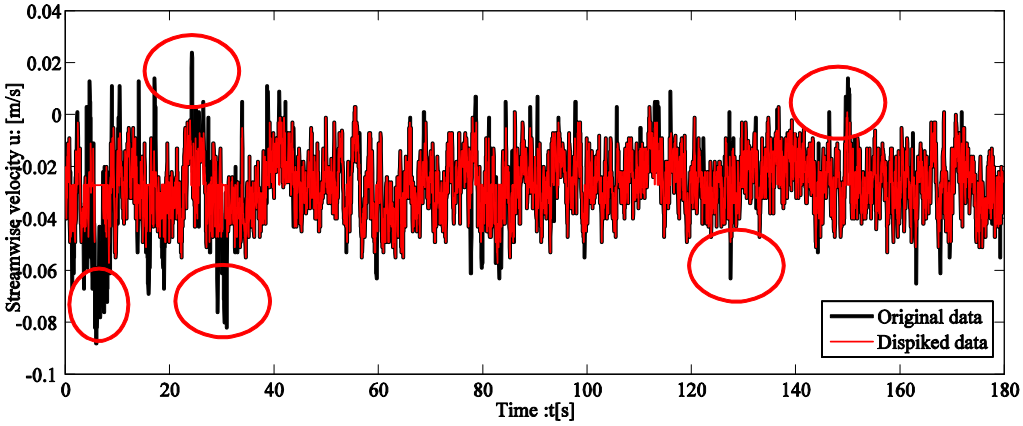

Figure II.9: Application of the Phase-Space Thresholding Method (from Han,2015)

The Figure II.9 illustrates that most of the peaks seen on the original data are removed by the despiking method and are replaced with the interpolated data.

2.3 *Comparison of ADV and PIV*

The uncertainties reported on the PIV appear discouraging, somehow. In order to check its relevance, it is compared to the results obtained using ADV. Here, the comparison focuses on the crosswise velocity signal $v(t)$, acquired with PIV and ADV in the mixing layer of the cavity at x/L=0.7, y/L=0(see Figure II. 10).

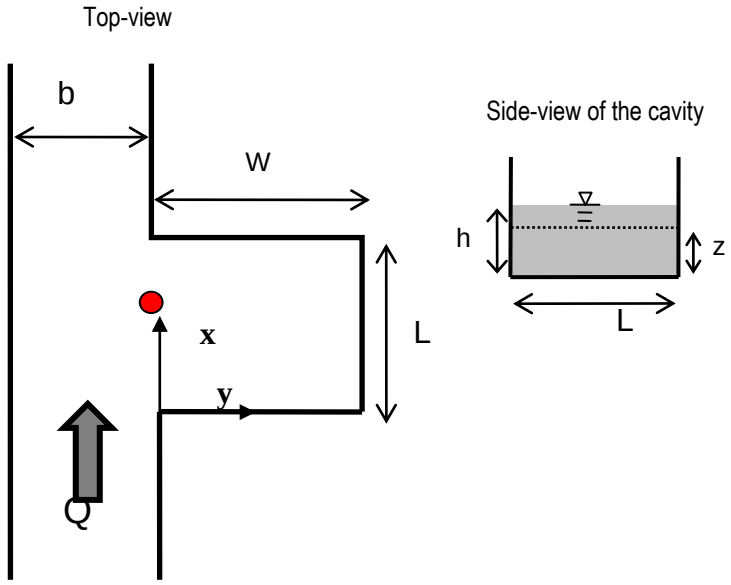

Figure II.10: The location for the comparison of ADV and PIV

Figure II.11 shows the comparison of the signals associated to the crosswise velocity fluctuations *v* (not at the same time – indeed at different days – so no phasing is expected). It appears that the std(standard deviations) standard deviations values are similar (1.3 & 1.5 cm/s) and that the amplitude of variation are also similar (crest to crest of 6cm/s).

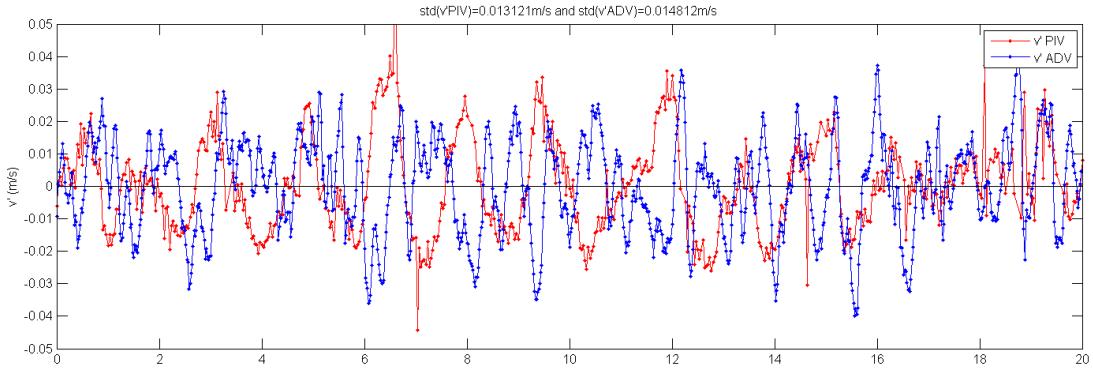

Figure II.11: The comparison of v oscillation signals

Figure II.12 shows the comparison of the *v* fluctuations spectrum: the peak is similar (0.6Hz), the ADV spectrum may be affected by intrusivity (already observed in seiching measurements).

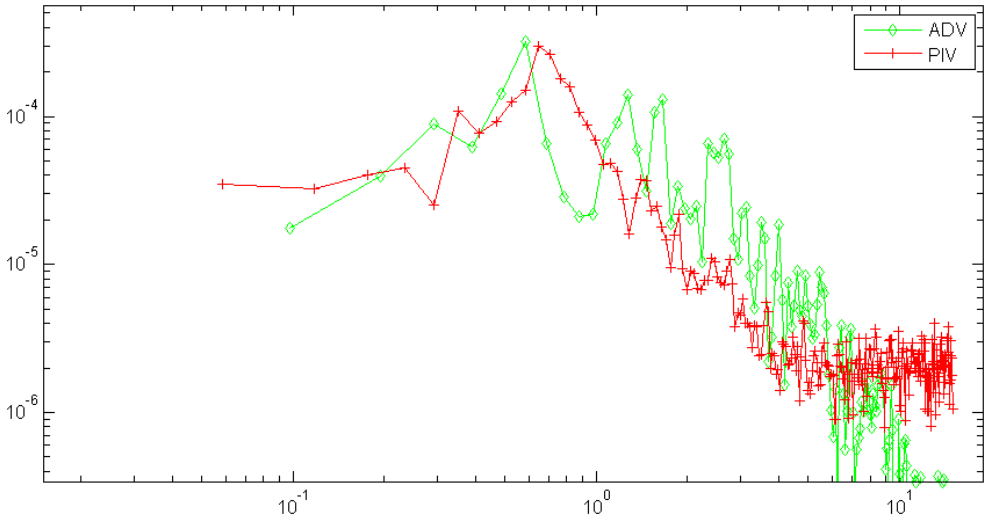

Figure II.12. The comparison of *v* oscillation spectrum

Above all, ADV and PIV compare quite well at the desired uncertainty level. For the following work, the ADV is then used to:
--measure the mean velocity components *u* and *v*
--measure the fluctuating velocities *u'*, *v'* and the associated shear *u'v'*
--decrease the noise of the experimental data

PIV will be the main measuring method of flow used in our research for:
-- characterizing the flow field in lateral cavities (chapter III)
-- characterizing the flow field in the mixing layer (chapter IV)
-- characterize mass transfer (chapter V)

Dye concentration measurements devoted for mass transfers through the mixing layer will be described in the corresponding chapter, namely chapter V.

3 CONCLUSION

The experimental set-up and measuring techniques have been described in this chapter. They will be used in next chapters to describe the flow patterns in the cavity (chapter III), the properties of the mixing layer (chapter IV) and finally the mass transfer (chapter V).

Chapter III: Measurements in cavities

The aim of this Chapter is to investigate the main characteristics of the velocity fields in the open-channel single lateral cavities. The hydrodynamics of the cavities is deeply analyzed based on horizontal planes(section 4), and on the vertical planes(section 5). Then the transition from 1 cell to 2 cells (section 6) and the temporary stability of the velocity (section 7) are investigated.

1 LITERATURE REVIEW

The aim of this section, is to investigate the main characteristics of the flows in open-channel cavities studied in the literature. At the connection between the main stream with uniform velocity and the cavity at rest, a large velocity gradient forms. This velocity gradient leads to a horizontal mixing layer which extends from the upstream corner to the downstream corner of the junction. This mixing layer transfers momentum from the main flow to the cavity, which sets the cavity flow in motion. Nevertheless, the literature shows that depending on the geometry of the cavity, the number and the nature of the recirculation cells (2D or 3D) varies.

Indeed, several authors have measured the recirculation cells in an open-channel lateral cavity. Nevertheless, for most of them, the width to length ratio *W/L* remained low (lower or equal 1).

- For a very narrow cavity, namely of about *W/L*<1/2, past studies observe 2 cells, aligned streamwise, *i.e.* along the direction of the main stream (see Nezu, 2002 ; Lecoz *et al.*, 2006 ; Tominaga and Jong, 2011 ; Sanjou *et al.*, 2012; Sanjou and Nezu, 2013). Sanjou and Nezu (2013) recently analyzed this flow in details, as can be seen on the Figure below. The most upstream cell is of smaller extension than the downstream one, and is more confined near the upstream extreme corner.

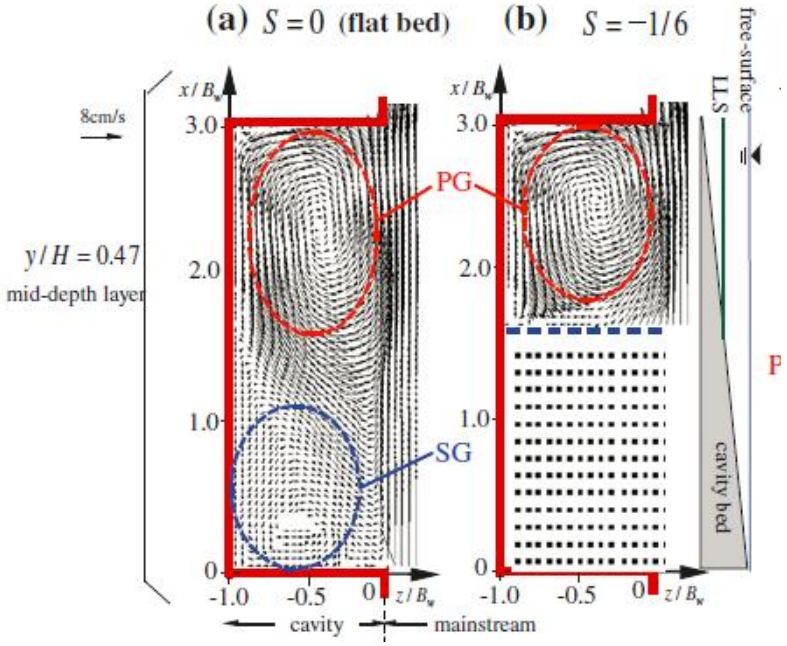

Figure III.1. Comparison of time-averaged horizontal velocitycomponents among different bed configurations, from Sanjou (2013).

- For a square cavity (*W/L*~1), authors such as Kimura (1997), Mizumura and Hasatani(2001), Nezu and Onitsuka (2002), Booij (1989) observe that a unique cell of vertical axis occupies most of the available space, and that the center of this cell is located at about the center of the cavity.

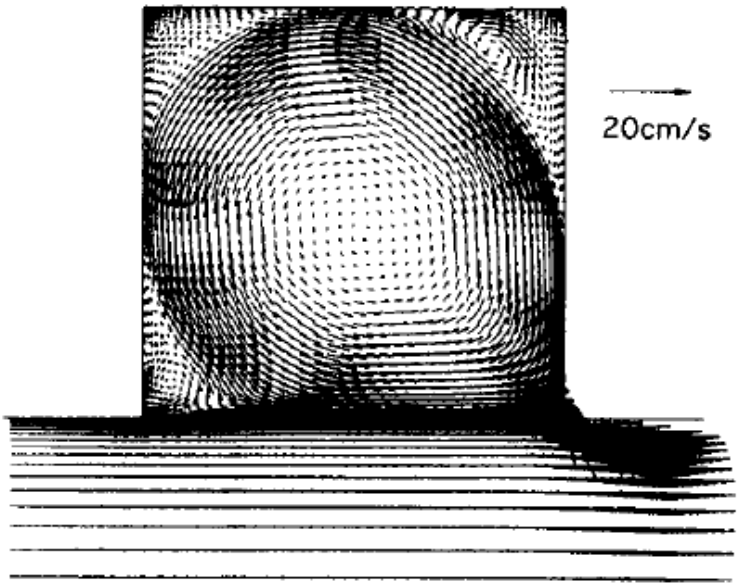

Figure III.2:Time-Averaged Velocity Vectors, from Kimura (1997)

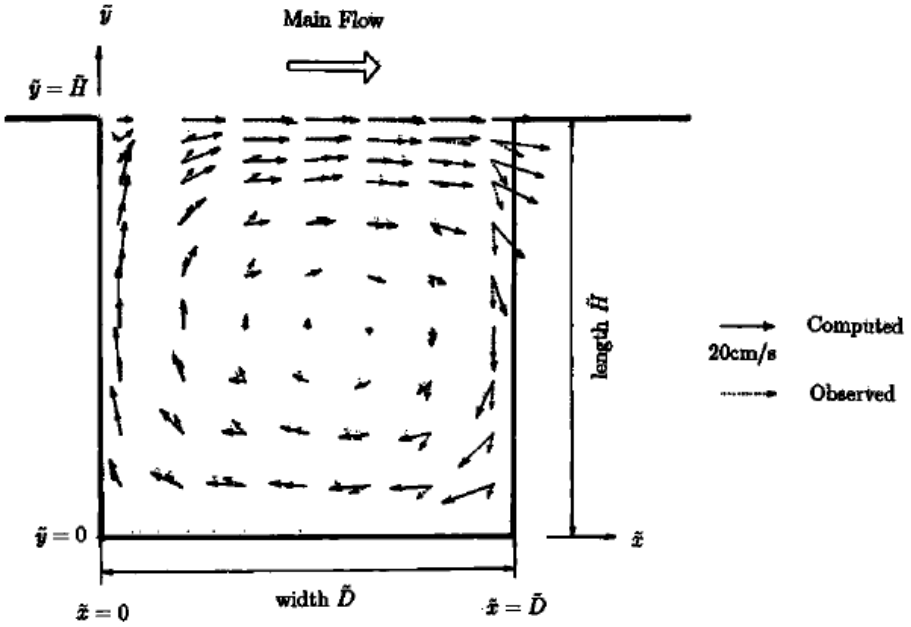

Figure III.3:Definition sketch of coordinate system and computed and observed flow velocity in square embayment from Mizumura and Hasatani (2002)

For wider cavities (W/L>>1), the only reference we could find is the preliminary work by Booij (1989) (see below) who observed and measured two adjacent cells of vertical axis, aligned crosswise, *i.e.* along the width (W) of the cavity for a configuration with W/L=3. It appears from this figure that:
- the typical velocity of the first cell highly exceeds that of the second cell,
- the size of the first cell exceeds that of the second cell
- the center of both cells are aligned along the centerline of the cavity.

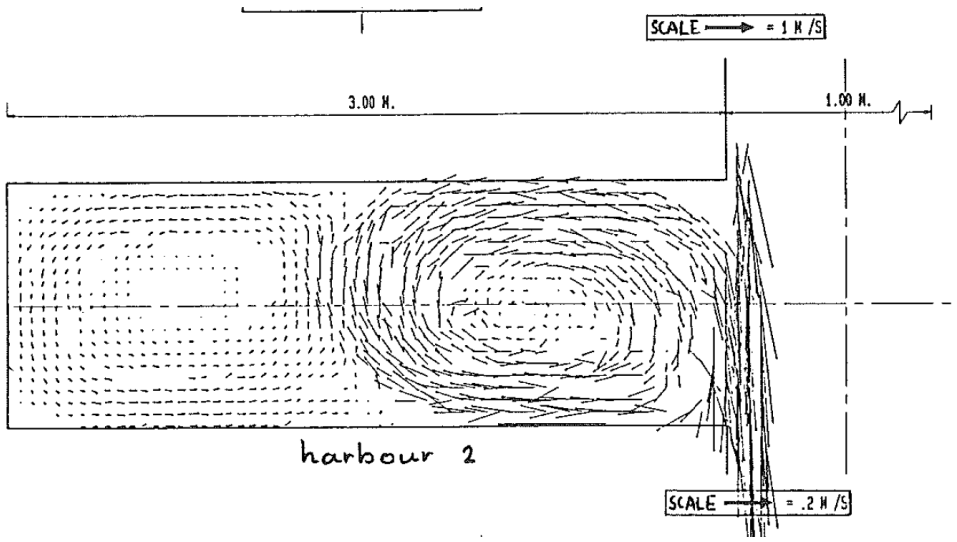

Figure III.4:Figure I.9: Measured depth-averaged velocity field, from Booij (1989)

The aim of the present chapter is to investigate the evolution of the main characteristics of the recirculation cells, for a fixed main stream flow configuration, taking benefit of the modifiable geometry of the LMFA experimental facility
- by slowly varying the cavity width and observing the transition between the various flow patterns.
- by increasing the maximum available aspect ratio *W/L* to values up to 5.
- by measuring the velocity field at different elevations.

2 EXPERIMENTAL SET-UP

The experiments are performed in the open-channel intersection facility of LMFA, Lyon (described by Rivière *et al.*, 2011, here with a sealed up branch as presented by Mignot *et al.*, 2012). The facility consists of three glass channels of rectangular shape sections, 0.3m wide and 2m long, which intersect at 90 ° (see Figure III.5). The bed of cavity and channel were horizontal for all experiments.

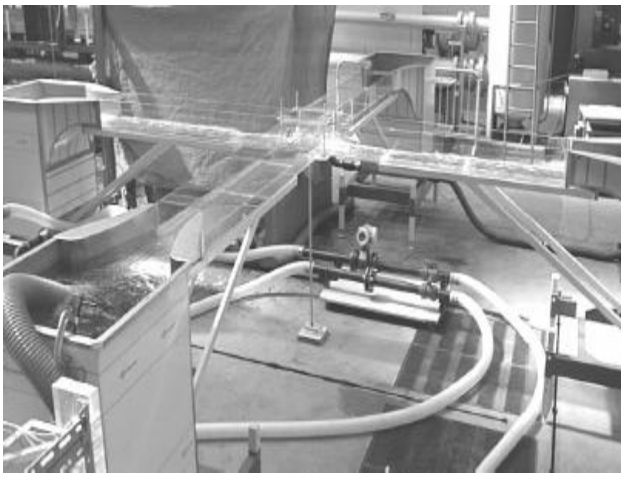

Figure III.5:The channels of LMFA

The length of cavity (*W*) is easily modified by placing an end wall (moveable cap) in the side channel at a given distance from the junction. This cap is made by a sheet of polyurethane with a stick glass plate, ensuring the same roughness as the channel walls, and a flat gasket, ensuring its imperviousness. Oppositely, the width of the cavity (noted *L*) remains constant, equal to the width of the main channel (*L*=*b*=30 cm). The aspect ratio of the cavity (*W/L*) can then vary from 0 up to 5 as *W* varies from 0 to 1.5m.

The inlet discharge in the channel is measured using a Promag 50 flowmeter (from Endress Hauser; accuracy 0.05 L/s). A honeycomb at the inlet of the channel serves to stabilize and straighten the inflow and a sharp crested weir at the outlet is used to fix the water depth at the entrance of the cavity. It was verified that the maximum free-surface oscillations in the cavity remained negligibly small (lower than a percent of the flow depth h).

In the present chapter only one flow configuration is considered with Q=3.5L/s and h = 7 cm (±0.15 mm) so that U_m=0.167m/s, Fr=0.02, Re=69000.

Most measurements in this chapter are performed using 2D horizontal PIV. A 40mW laser coupled with a cylindrical lens generates a 1mm horizontal laser sheet at the elevation: z=5cm (z/h=0.71). Polyamid particles (diameter 50 μm) are added to the water. Finally, a video camera is located above the cavity in order to record the particle motion over 3000 consecutive images of 1280x960 pixels each, with an average spatial resolution of 0.3mm per pixel, at a frequency equal to 30Hz. Finally, the commercial software Davis (from La vision) permits to correct image distortions, subtract the background and finally compute the velocity fields.

2.1 *Upstream measurements*

It seems reasonable to assume that the transverse profile of streamwise velocity of the approaching flow impacts the flow characteristics in the cavity. The present section thus aims at measuring this profile.
To do so, the PIV measurement method is applied in the so-called upstream zone as shown on fig III.6. This zone is located just upstream of the cavity opening, which is from x/L=-0.5 to x/L= -1.5. Additionally, ADV measurements are performed along two streamwise profiles with 10 points to be tested are chosen as y/L=-0.5 (ADV-line, shown in Figure III.7). The measurement elevation is 40% of the total depth of the flow. For every point, the signal is collected by 200 Hz in 3 minutes.

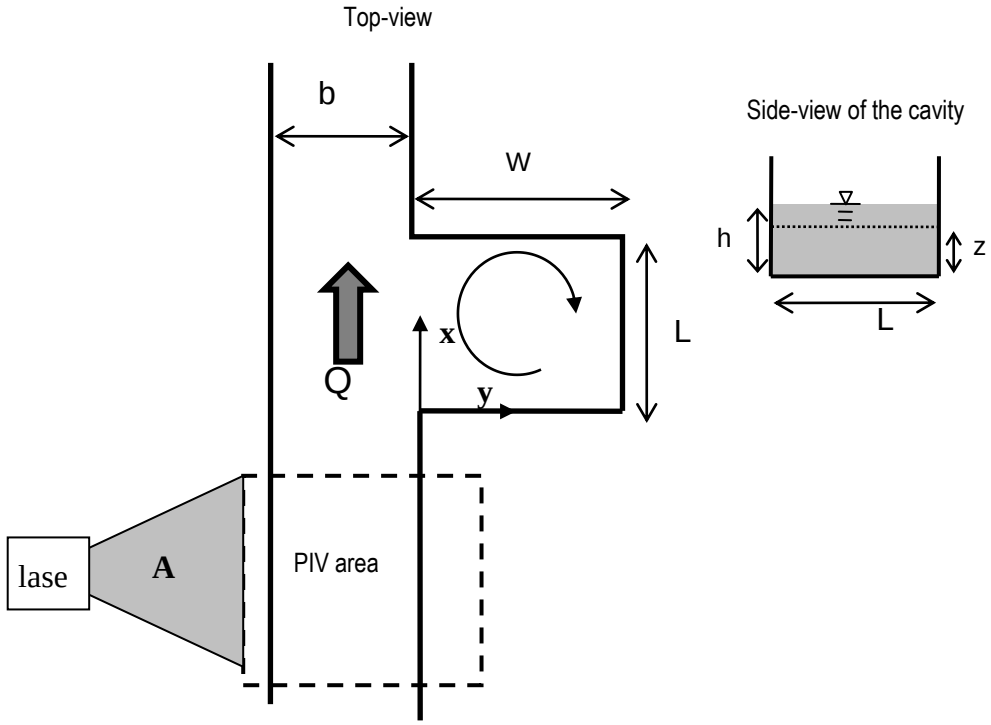

Figure III.6. Horizontal PIV for upstream flow

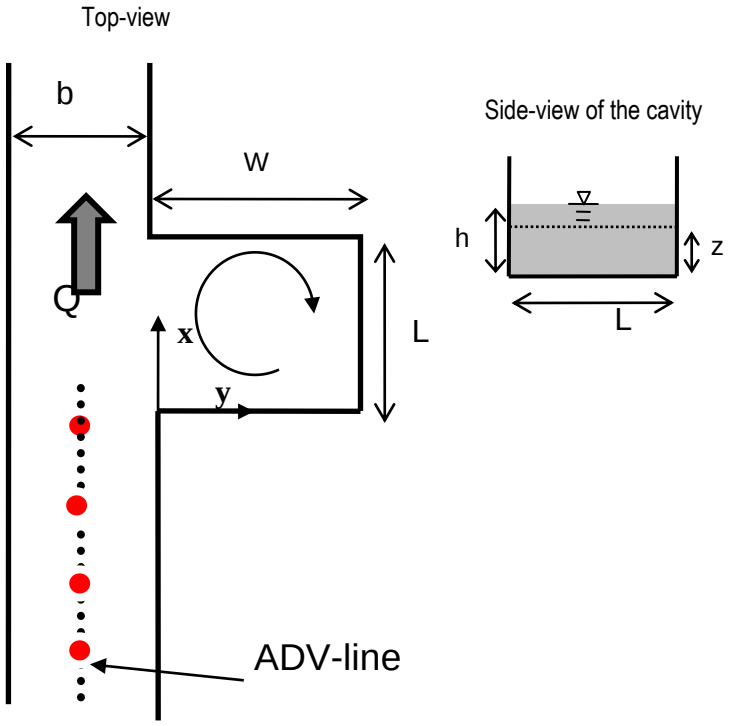

Figure III.7:Horizontal PIV for upstream flow

The mean PIV velocity field is shown in fig III.8. It reveals that:
- the velocity magnitude is larger in the middle on the channel than on the side. Also the transversal location of the peak velocity is a little off-center to the side wall of the cavity (y/L=0). This asymmetric profile is obviously impacted by the cavity located further downstream. This influence is so strong in the measured zone that it seems reasonable to assume that the whole upstream flow is influenced by the presence of the cavity.
- the transverse profile of mean streamwise velocity does not evolve much along the streamwise direction, the flow is then about established in the upstream zone.

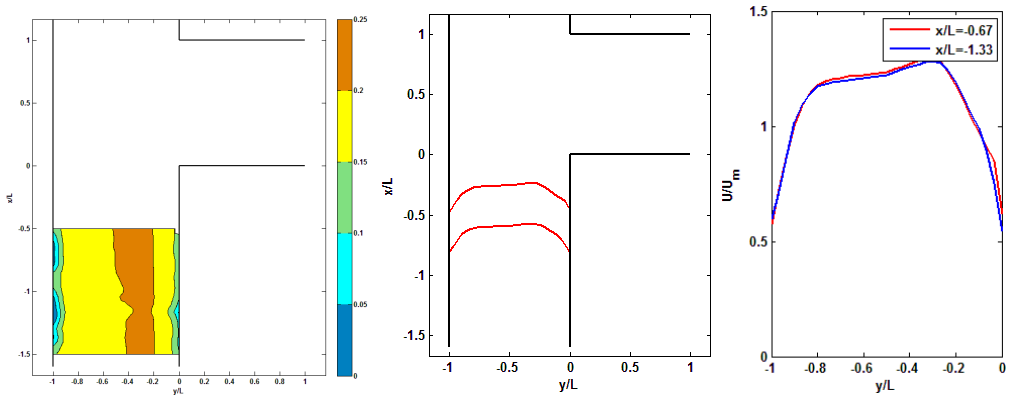

Figure III.8:Upstream velocity field (the zone from x/L=-0.5 to -1.5)

In order to verify this asymmetry is induced by the cavity and not some imperfection of the experimental set-up, a similar PIV measurement was performed by closing the cavity. The velocity profiles at the same locations are exhibited on Fig.III.9 and reveal a more symmetrical profile. The asymmetry in Figure III.8 is thus mostly caused by the cavity

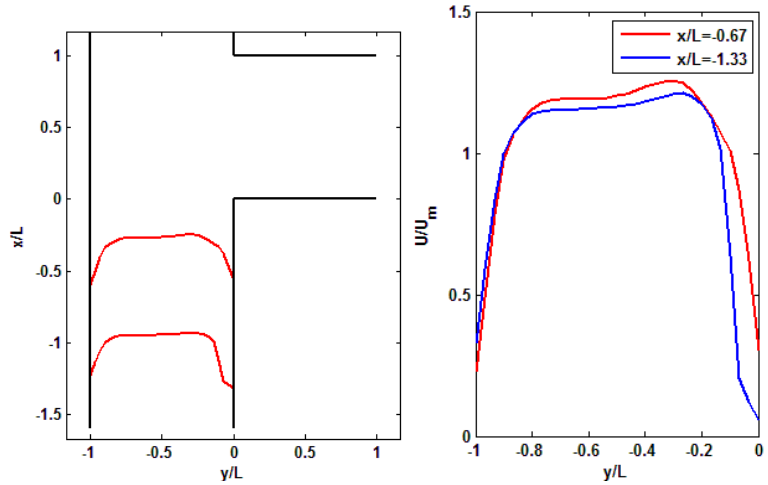

Figure III.9: Upstream velocity field by closing the cavity (the zone from *x/L*=-0.5 to -1.5)

The ADV measurements along the streamwise profile in Figure III.10 appear to be in fair agreement with the PIV data (U/U_m~1.1 along the centerline of the upstream section). ADV data confirm that the flow is established in this region as the velocity does not evolve along the streamwise direction. Moreover, the transversal component *v* is negligibly small.

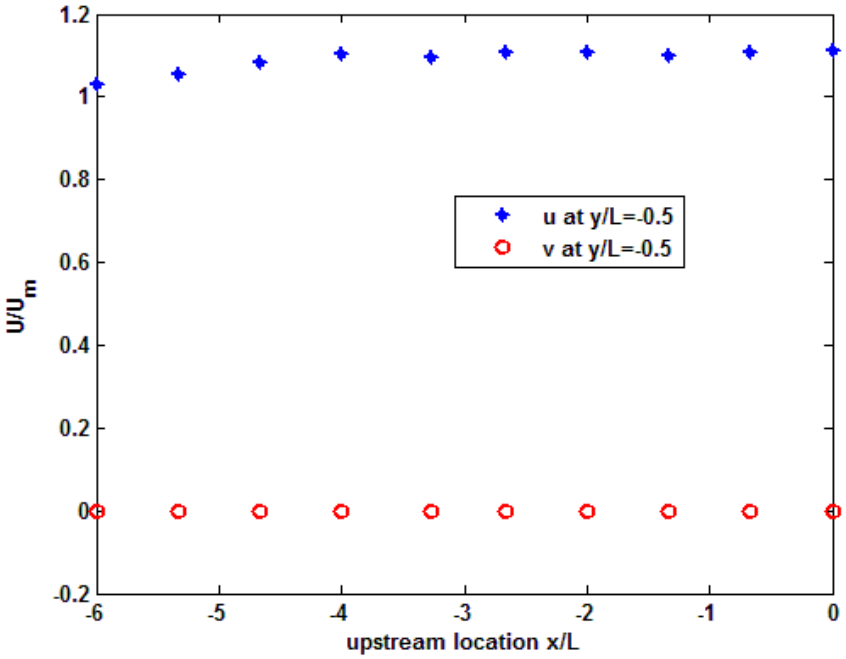

Figure III.10:Mean velocity along streamwise direction

2.2 *Horizontal PIV methodology in the cavity*

As observed in the literature (see Booij, 1989), two or more consecutive horizontal recirculation cells, with significantly different velocities, can occur in the cavity as its aspect ratio *W/L* increases. Two methodologies for the velocity measurements using 2D horizontal PIV are thus considered:
1. For the narrow cavities (*W/L*<3) in which the extension of the second cell (when it is present) remains limited, a single video is taken at a frequency equal to 12.2Hz. The laser is located on the main stream side (see Figure III.11). The camera located above the free-surface is centered above the center of the cavity.

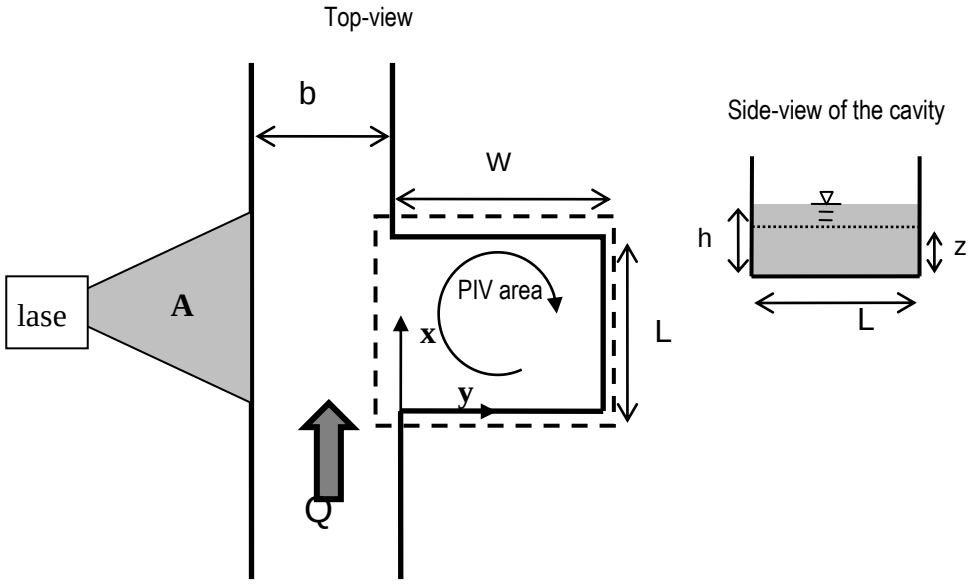

Figure III.11:Horizontal PIV for small cavities

2. For longer cavities (*W/L*>3), the extension of the cavity is so high that:
- the spatial resolution of the camera decreases too much if the whole flow is filmed at once.
- the light intensity within the laser sheet at the extremity of the cavity becomes too low.

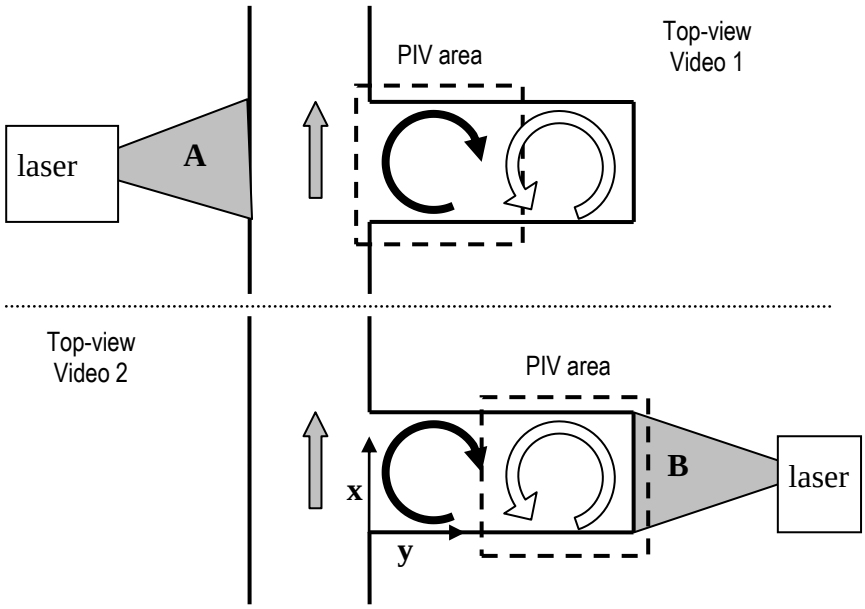

Figure III.12:Horizontal PIV for larger cavities

Consequently, the following methodology is employed: two videos are recorded, one after the other (with the same flow and geometry parameters), as sketched on Figure III.12. The first video is performed as detailed above for small cavities with the camera centered above the first cell of the flow. For the second video, the laser is moved to the other extremity of the cavity and in this case, the camera is located above the second cell of the flow and the recording frequency is much reduced as the velocity of the second cell is much lower than that of the first cell: *f*=12.2Hz. These two videos are analyzed using the PIV method described above.

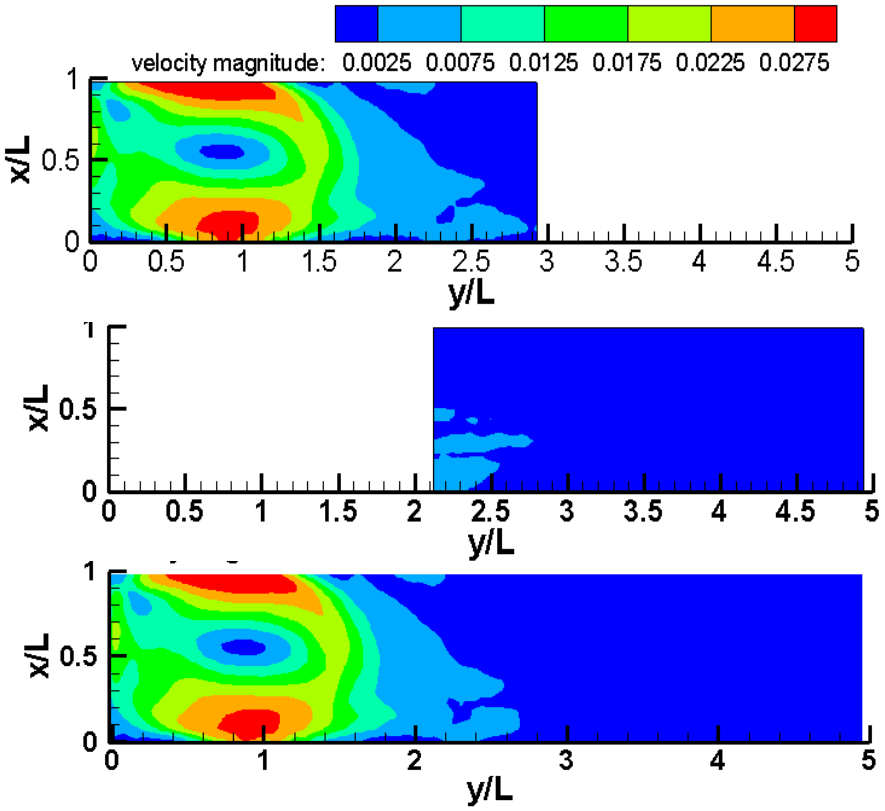

Figure III.13: Horizontal PIV combination for lager cavities

Now, the difficulty is to combine the information from both PIV measurements. Considering the configuration with W/L=5 as an example, the PIV measurement at an elevation of z=5cm (z/h=0.71) was divided into two videos as shown in Figure III.13, video 1 from y/L=0 to y/L=3 and video 2 from y/L=2 to y/L=5. Obviously, the velocity magnitude of the first cell is much larger than that of the second cell. The overlap zone for from y/L=2 to y/L=3, the final velocity is taken as the average of both PIV data and both PIV can then be combined into a single one by using a linear method.

2.3 *Vertical PIV methodology in the cavity*

It will appear in this chapter that for the long cavities (W/L>3), the second cell cannot be deeply understood from only the horizontal PIV data. So, additional information is brought by measurements of vertical planes using PIV, as shown in Figure III.14. The camera is now located on the side of the cavity and the laser is rotated to generate the laser sheet in a (y, z) plane over the second cell. Three vertical planes are considered here: at x/L=0.5 (center plane) and near both walls, that is x/L=0.17 and 0.83 (see Table III.2) for the configurations with W/L=3, 4 and 5.

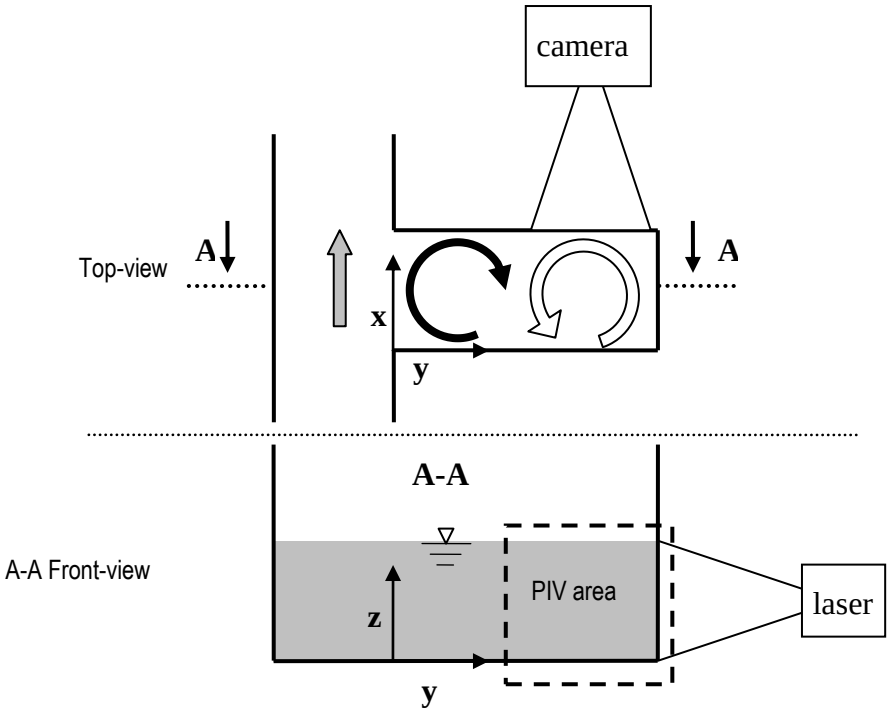

Figure III.14:Vertical PIV for lager cavities

2.4 *List of the tested configurations and available data*

As exposed above, the aim of the present chapter is to measure the velocity characteristics of the recirculation cells for configurations with slowly varying aspect ratios *W/L*. The selected configurations are then *W/L*=0.3, 0.6, 1, 1.3, 1.6, 1.7, 1.8, 1.9, 2, 2.1, 2.2, 2.3, 2.6, 3, 3.3, 3.6, 4, 4.3, 4.6 and 5.

As shown in Table III.1 and III.2, all the cavity configurations are measured by horizontal PIV while only three with a high aspect ratio *W/L* have additional measurements with vertical planes.

Table III.1: PIV configurations

W/L	Number of cells	Position of laser	Camera located above the cell number	Image acquisition frequency(Hz)
0.3,0.6,1,1.3	1	A	1	12.2
1.6,1.7,1.8,1.9,2,2.1,2.2,2.3,2.6,3	2	A	1	12.2
3.3,3.6,4,4.3,4.6,5	2	A	1	12.2
		B	2	3.75

Table III.2:Vertical PIV configurations for different sections

x/L	*W/L*
0.17	3,4,5
0.5	3,4,5
0.83	3,4,5

Finally, in order to check the 2D or 3D aspect of the flow pattern in the cavity, additional horizontal PIV measurements are performed at additional elevations (other than *z*=5cm) for a few configurations (*W/L*=3, 4 and 5). These additional elevations are indicated in Table III.3.

Table III.3:PIV configurations for different elevation

Elevations for PIV *z/h*	*W/L* cavity cases
0.07	3
0.21	3,4,5
0.71	0.3,0.6,1,1.3, 1.6,1.7,1.8,1.9,2,2.1,2.2,2.3,2.6,3, 3.3,3.6,4,4.3,4.6,5
0.93	3,4,5

3 DATA OF THE LATERAL CAVITY FLOW PATTERNS CHARACTERIZED FOR *Z/H*=0.71

This section is dedicated to the analysis of the velocity fields measured in the cavity with fixed, main stream, flow conditions and *W/L* increasing from 0.3 to 5.

3.1 *Description of the recirculation cell patterns*

The main transformations of the flow pattern in the cavity are described herein based on selected configurations. All measured horizontal PIV at *z/h*=0.71 data are shown on Figure III.56 at the end of the present chapter.

For a narrow cavity (small *W/L* ratio), two recirculation cells are aligned along the transverse direction of the cavity, as already predicted by the literature. The main cell is rotating clockwise and the secondary cell located upstream and shifted away from the main stream is rotating counter-clockwise. Figure III.15 shows the flow pattern for *W/L*=0.3. Please be aware of the main stream that is located on the left of the cavity, contrary to some figures from literature such as Fig. III.1.

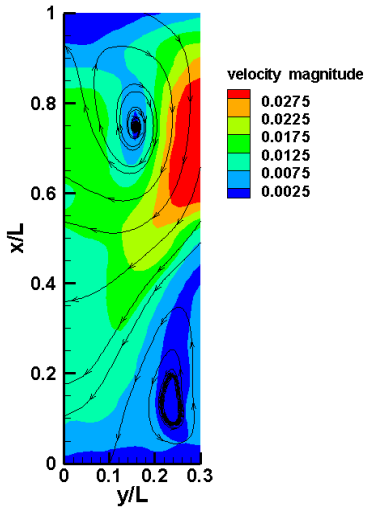

Figure III.15:Measured velocity field in a narrow cavity with two cells for *W/L*=0.3

For a small cavity (1/3<*W/L*<1), the secondary cell on the upstream region becomes smaller and then disappears gradually. Finally a single clockwise recirculation develops, which occupies the whole cavity area.

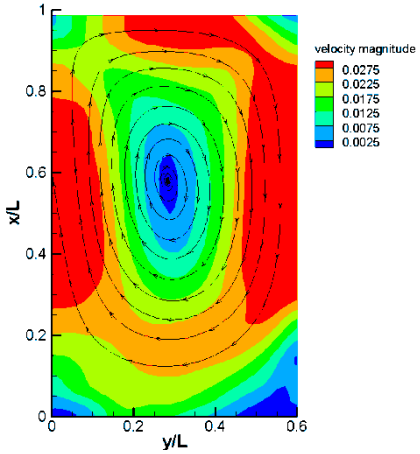

Figure III.16:Measured velocity field in for *W/L*=0.6

For a slightly wider cavity, a single clockwise recirculation develops, which occupies the whole cavity area. Figure III.17 shows the flow pattern for *W/L*=1. Note that a region of high velocity is located along all lateral walls and in the center of the mixing layer. Moreover, an asymmetry is observed for *x/L* lower or larger than 0.5: a region of low velocity takes place along the diagonal starting from the center of the cell towards the downstream corner of the cavity (*y*=0 and *x/L*=1).

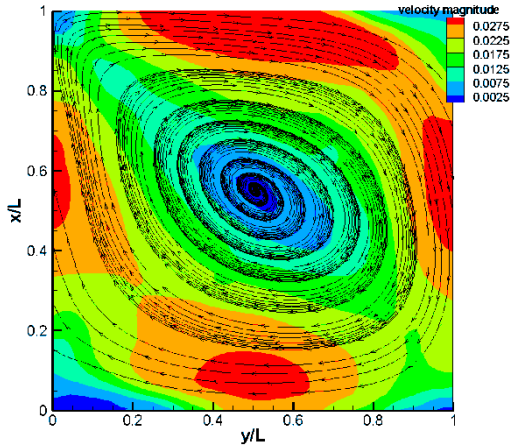

Figure III.17:Measured velocity field in the square cavity with one complete cell for *W/L*=1

When increasing the cavity length, the single cell pattern is replaced by a two-cell pattern. For *W/L*=1.3 the center of secondary cell is clearly recognized. But the main cell is only slightly modified and occupies the whole length of the cavity (see Figure III.18).

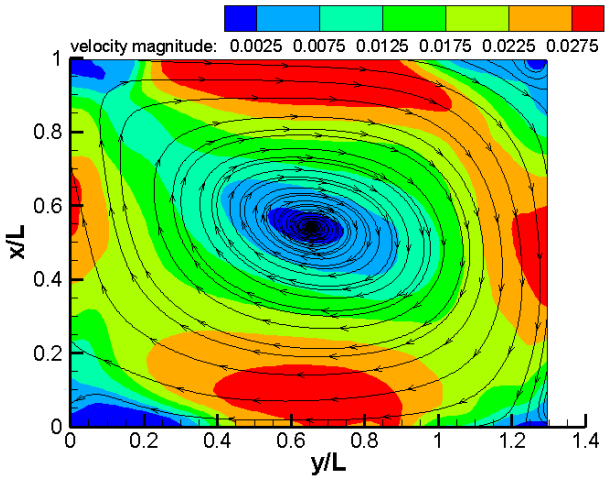

Figure III.18:Measured velocity field for *W/L*=1.3

For larger *W/L*, the size of the second cell increases and limits the growth of the first cell (see Figure III.19).

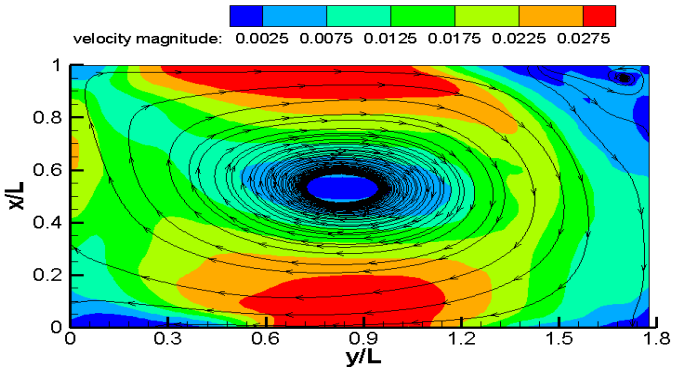

Figure III.19:Measured velocity field for *W/L*=1.7

The second recirculation cell (anti-clockwise) starts to occupy the whole length *L* when the cavity length exceeds *W/L*=2.6. Both cells occupy the whole length L but the second cell is confined at the extremity of the cavity (see Figure III.20).

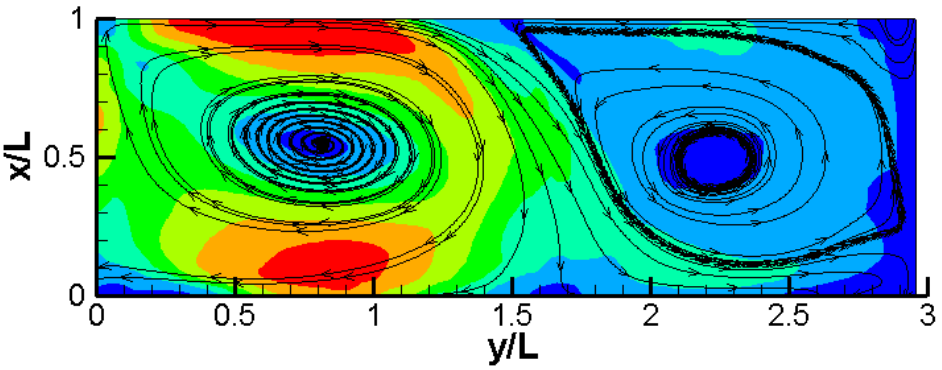

Figure III.20:Cavity with two main cells for *W/L*=3

For a very wide cavities, the second cell area becomes complex and, at least partially, 3D. A slow motion region (from *y/L*=4 to *y/L*=5) is measured with a strongly three- dimensional flow (see section 4.3 the vertical measurements).

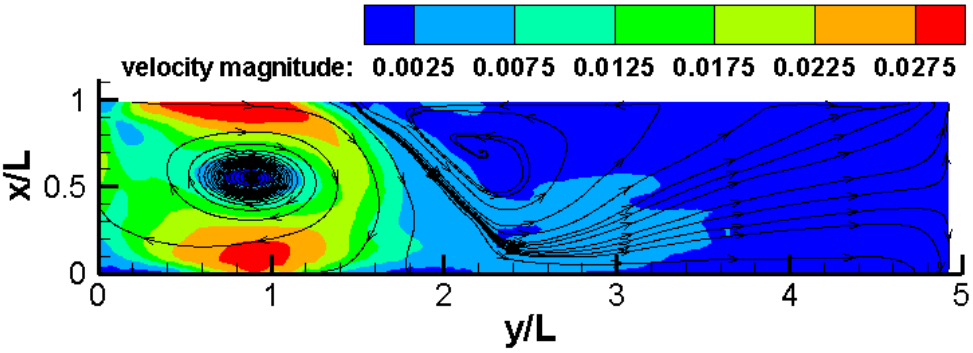

Figure III.21:Large cavity with two cells

3.2 *Definition of the specific points in the cavity*

In order to describe more quantitatively the evolution of the flow pattern as *W/L* increases, specific points are introduced and detected on each flow configuration:

Point 1 refers to the center of the first main cell, which is the point of minimum velocity magnitude. X_{c1} is the distance to downstream side wall and Y_{c1} the distance to the cavity opening (see Figure III.22).

Point 2 refers to the center of the second main cell, when it exists. X_{c2} is the distance to downstream side wall of and Y_{c2} the distance to the extremity of the cavity (see Figure III.22).

Point 3 is defined as the separation point separating the two cells along the *x/L*=1 wall. It is precisely defined as the point where the velocity along y changes sign and thus equals 0 (see Figure III.22).

Point 4 (4') is defined as the re-attachment point of the first and second cells, either along the extremity wall (*y*=*W*) where it is noted point 4 (see Figure III.22) or along the *x/L*=0 wall where it is noted 4' (see Figure III.23). Indeed, for *W/L*>2.1, the second cell occupies the whole cavity length *L*, Point 4 thus is displaced towards point 4'. Then Point 4 is precisely defined as the location where the velocity along *x* changes sign and thus equals 0, point 4' is the location where the velocity along *y* changes sign and equals 0.

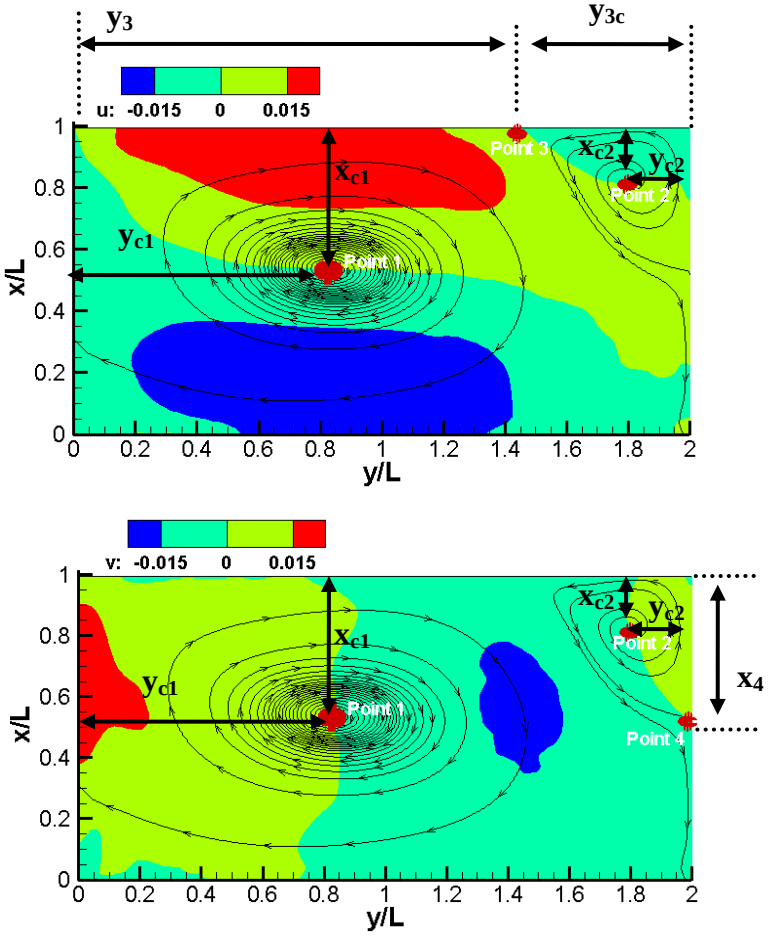

Figure III.22:Definition of Point 3 and Point 4

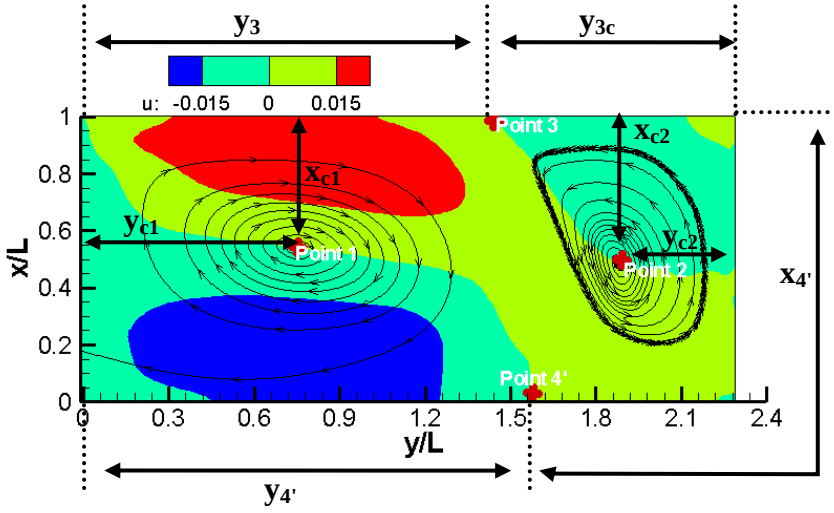

Figure III.23:Definition of Point 3 and Point 4'

Point 5 refers to a focus point at the center of a swirl near the upstream corner (see figure III.24) for *W/L*=3 measured at *z/h*=0.93).

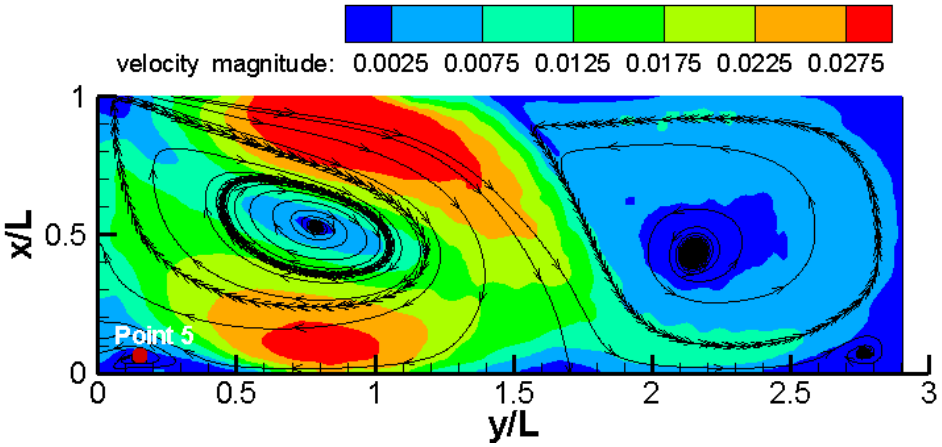

Figure III.24:Definition of Point5

Point 6 refers to a saddle point which occurs on the leading (upstream) wall of the cavity at a small elevation (see figure III.25). Consider the case of the cavity with *W/L*=3 measured at the *z/h*=0.15 for example.

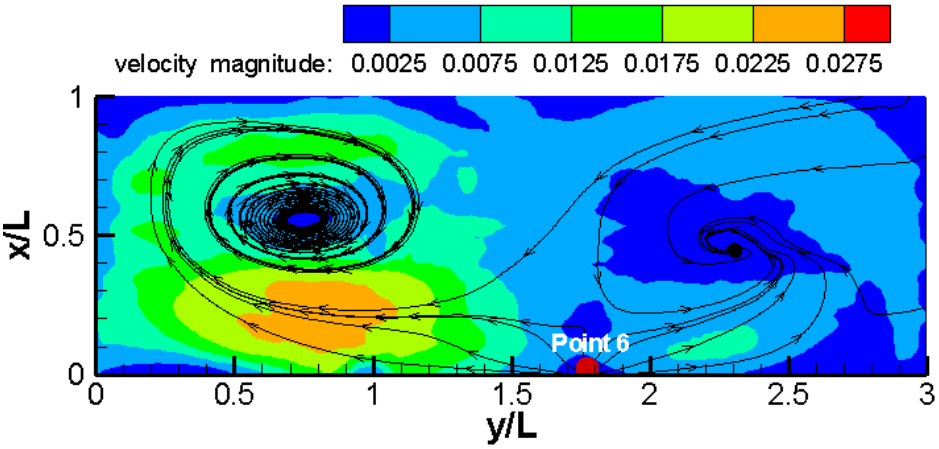

Figure III.25:Definition of Point6

3.3 *Definition of the characteristic velocity of the first cell*

In addition to specific points, some velocities are defined herein:

-V_1 is defined as the velocity at the mid-points between the center of the first cell (point 1) and the side wall along *x/L*=1 (see figure III.27).
-V_2 is defined as the velocity at the mid-points between the center of the first cell and the cavity interface, as shown on figure III.27.
-The characteristic velocity of the first cell, noted V_{c1}, is taken as the average of both velocities V_1 and V_2 as: $V_{c1}=(V_1+ V_2)/2$.

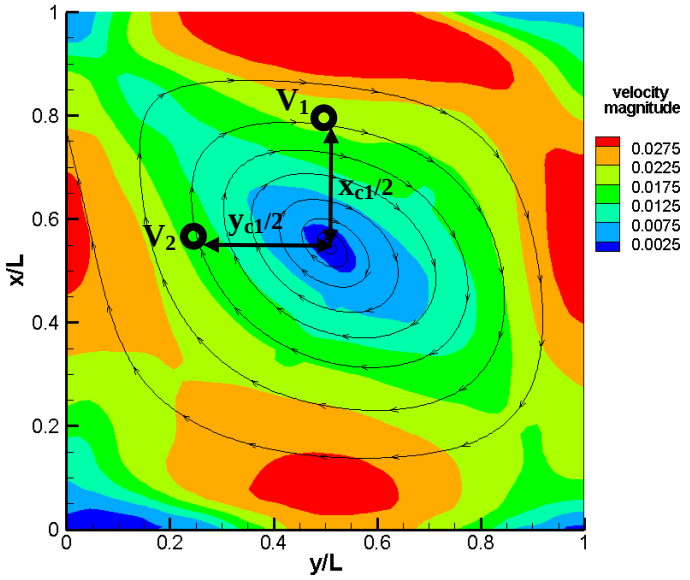

Figure III.27:Characteristic velocity of main cell

3.4 *3 Evolution of the specific points and velocity*

The values of points 1, 2, 3 and 4 and velocity V_{c1}, measured at z/h=0.71 are given in Table III.4 and plotted in Figure III.28 and29 and 30.

Table III.4: The parameters of specific points 1, 2, 3, 4 measured at z/h=0.71

W/L	x_{c1}/L	y_{c1}/L	V_{C1} (m/s)	x_{c2}/L	y_{c2}/L	y_4/L	y_{3c}/L	x_4/L
0.3	0.25	0.15	0.018					
0.6	0.42	0.28	0.0185					
1	0.45	0.51	0.0175					
1.3	0.47	0.66	0.0145				0.06	0.09
1.6	0.46	0.80	0.015	0.05	0.04		0.12	0.13
1.7	0.46	0.86	0.0145	0.08	0.07		0.35	0.19
1.8	0.47	0.84	0.0145	0.05	0.1		0.19	0.22
1.9	0.46	0.85	0.0145	0.06	0.09		0.2	0.25
2	0.47	0.82	0.0135	0.17	0.07		0.54	0.47
2.1	0.44	0.89	0.016	0.1	0.12		0.56	0.3
2.2	0.46	0.8	0.017	0.15	0.25	1.62	0.75	
2.3	0.47	0.75	0.0175	0.51	0.42	1.59	0.85	
2.6	0.47	0.8	0.017	0.5	0.5	1.68	1.04	
3	0.46	0.8	0.016	0.52	0.76	1.64	1.51	
3.3	0.45	0.82	0.0155	0.54	1.1	1.70	1.77	
3.6	0.47	0.87	0.015	0.45	1.35	1.8	1.93	
4	0.54	0.83	0.0145	0.44	2.25	1.74	2.34	
4.3	0.46	0.92	0.0145	0.32	2.04	1.90	2.63	
4.6	0.46	0.91	0.0145	0.3	2.47	1.80	1.77	
5	0.44	0.89	0.015	0.31	2.79	1.72	1.73	

- characteristic velocity

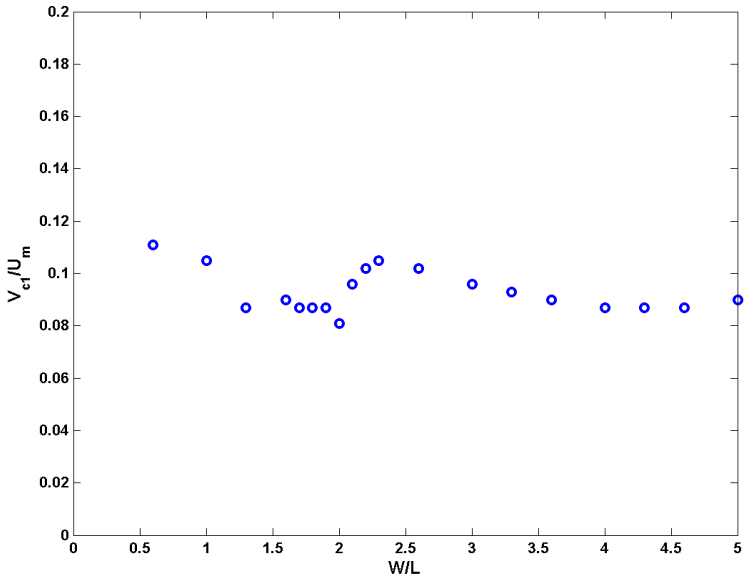

Figure III.28:Characteristic velocity of the first cell V_{c1}/U_m for all configurations

Figure III.28 shows the evolution of the characteristic velocity of the first cell when increasing the aspect ratio *W/L*. This velocity equals about 10% of the bulk velocity of the main stream and appears not to vary much as a function of *W/L*. When only one cell exists (*W/L*<1), the characteristic velocity is the maximum. When a secondary cell appears downstream (*W/L*=1.3), this velocity decreases. When the second main cell develops completely (*W/L*=2.3), it increases a little and finally tends to decrease.

- the positions of the centers of the cells

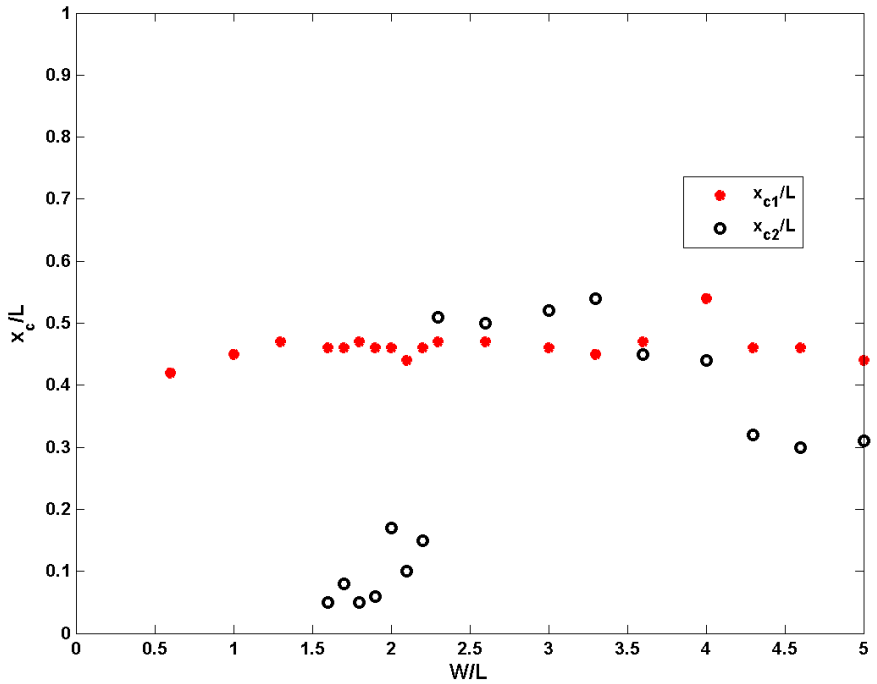

Figure III.29:*x*-position of the center of the cells for all configurations

Figure III.29 shows the *x*-position of the center of both main cells. It appears that the center of the first cell moves only slightly along the streamwise direction and remains near the center line of the cavity (*x/L*=0.5). The second cell initiates from the trailing (downstream) wall for *W/L*=1.5 and then reaches the center line of the cavity (*x/L*=0.5). As the aspect ratio *W/L* exceeds 3.6, the center of the second cell moves towards the downstream wall (x_{C2} decreases).

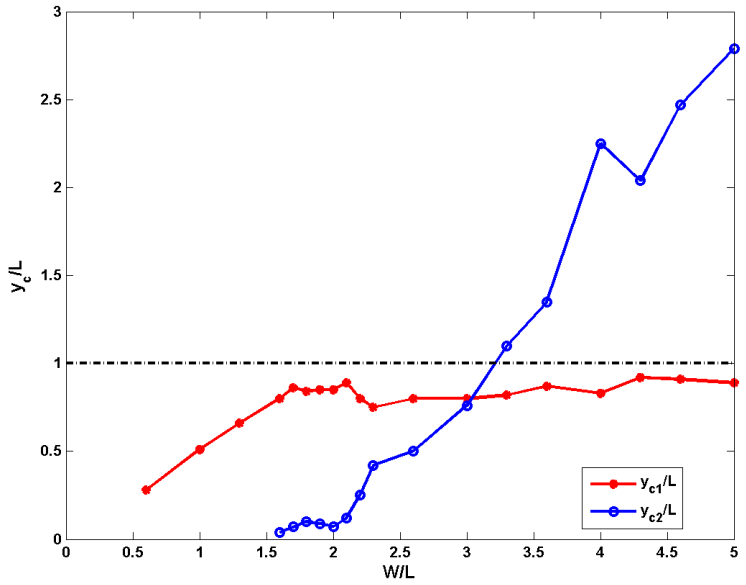

Figure III.30:*y*-position of the center of main cell for all configurations

Figure III.30 shows the y-position of the center of these two main cells. As long as only one cell exists (W/L<1.6), y_{C1}~$W/2$. When the secondary cell appears, the center of the first cell doesn't move further as it remains nearly at y/L=0.9. The center of the second cell moves away from the extremity of the cavity as W/L increases and as the extension of this second cell increases: y_{C2} keeps on increasing.

- the detachment and reattachment points

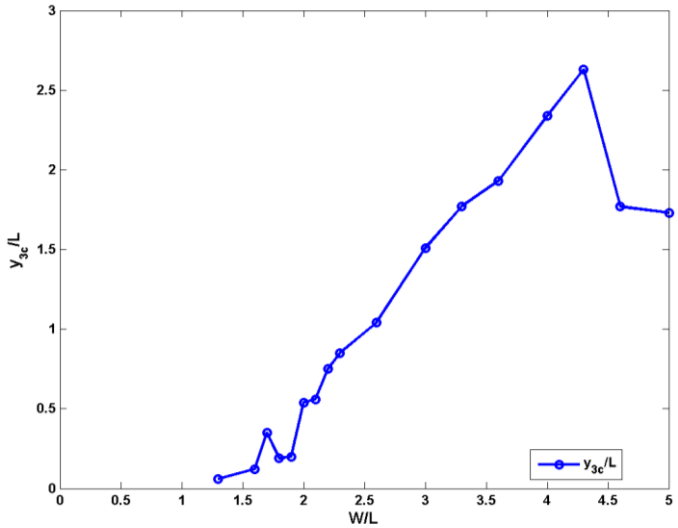

Figure III.31:*y*-position of stagnation point for all configurations

Figure III.31 shows the *y*-position of points 3, which are relevant only when two cells exist.

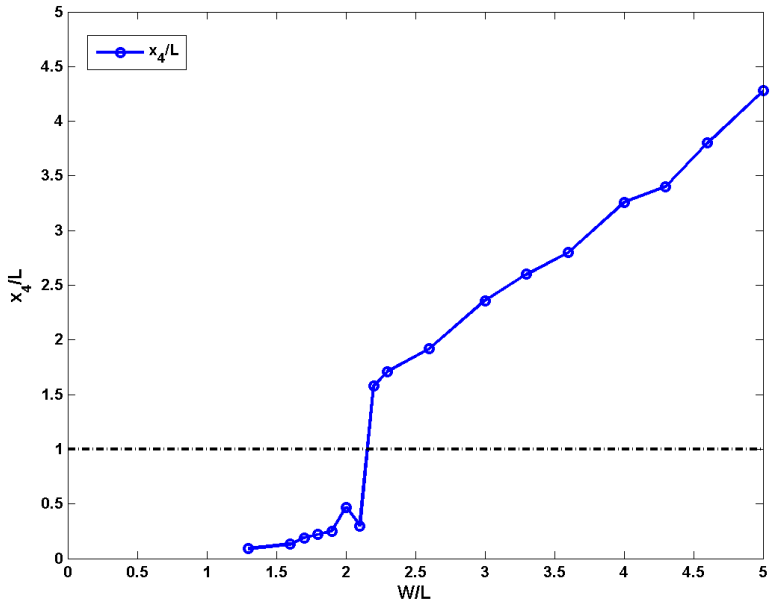

Figure III.32:*x*-position of stagnation point for all configurations

Figure III.32 shows the *x*-position of point 4. It is interesting to note that for W/L=1.2 to 2.2, x_4/L<1 meaning that the second cell remains confined near the downstream upper corner of the cavity. Then x_4 suddenly increases and x_4/L exceeds 1 for W/L=2.3 as the second cell occupies the whole width of the cavity. x_4 then keeps on increasing as the extension of the 2nd cell increases. The transition from one to two cells, aligned and occupying the whole cavity length L, is caused by the merging of the corner secondary cells. This will be emphasized in section 6.

4 MEASUREMENTS AT DIFFERENT ELEVATIONS

Literature showed that, for one-cell patterns, that the flow experiences negligible variations along the flow depth, except very close to the bed. For instance Tuna *et al.*, (2013) report no variation as long as $z/h \geq 0.167$. In order to investigate the evolution along the depth of the velocity fields, measurements were performed at different elevations. The four elevations at which horizontal PIV is measured are z/h=0.07,0.21,0.71 and 0.93, including the measurements at z/h=0.71 were already presented above.

4.1 *Configuration with W/L=3*

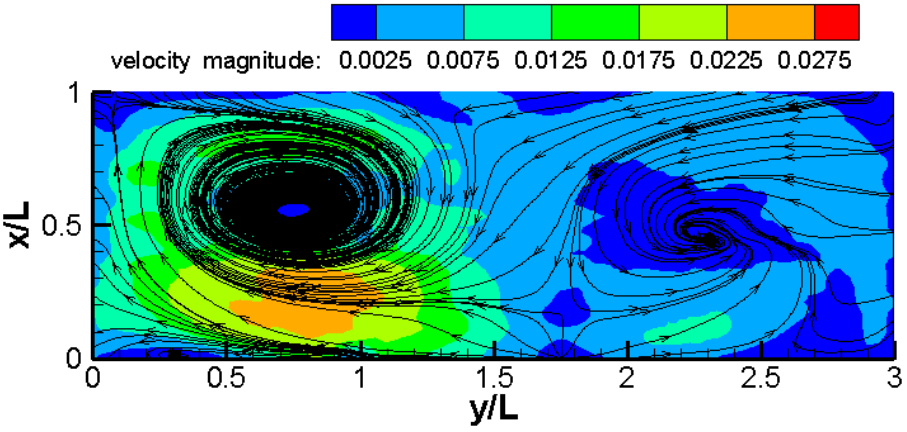

z/h=0.07

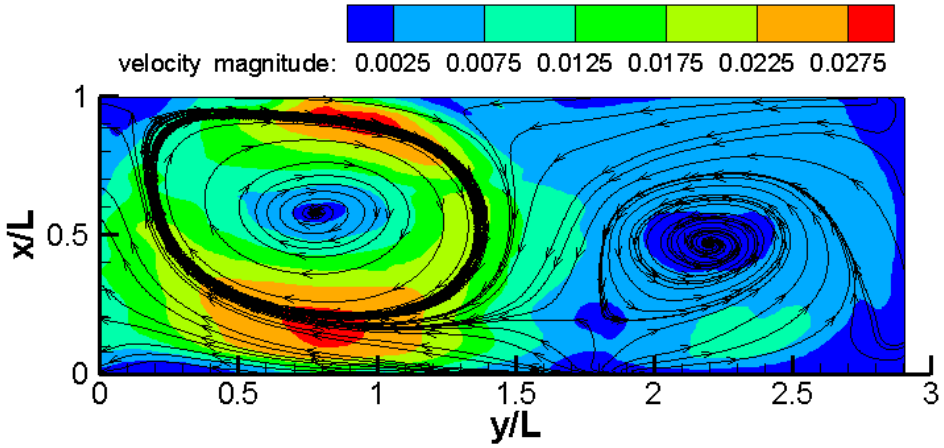

z/h =0.21

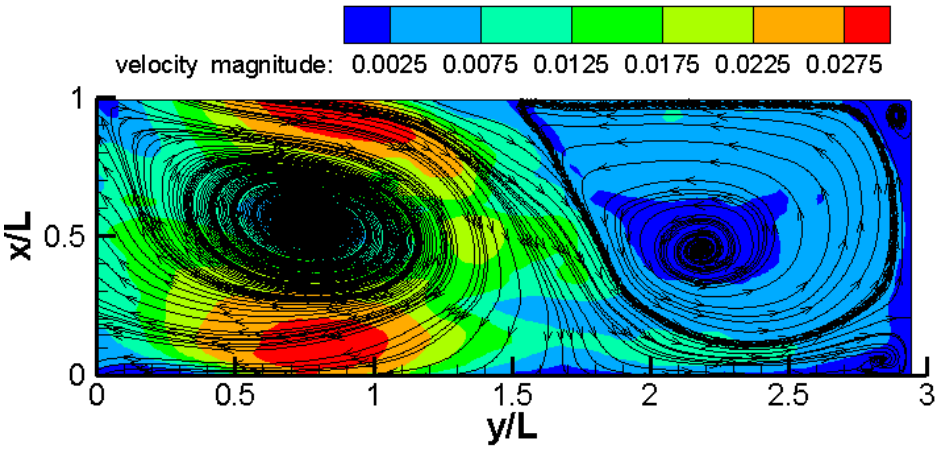

z/h=0.71

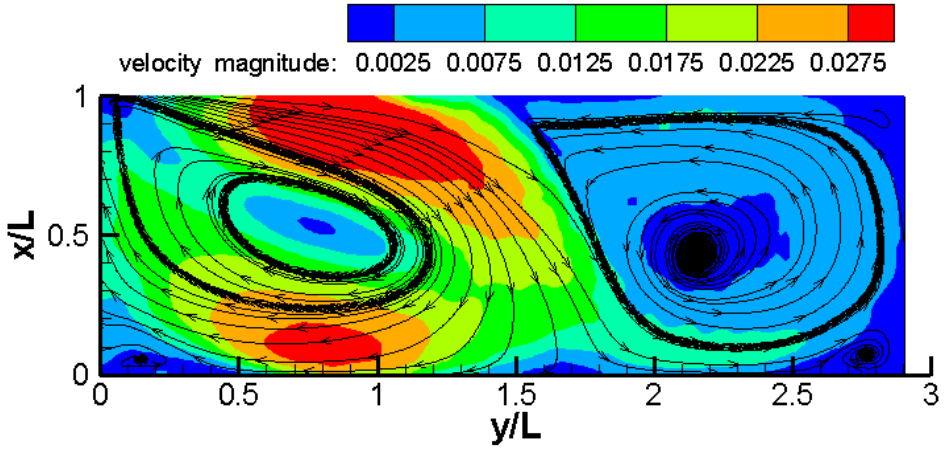

z/h=0.93

Figure III.33:Velocity fields at different elevations for *W/L*=3

Figure III.33 shows patterns of time-averaged velocity fields at the four elevations for *W/L*=3. The velocity magnitude obviously appears to be reduced in the near-bed region, mostly for the first cell. Nevertheless, this velocity does not evolve much from *z/h*=0.21 to 0.93. The global pattern of the first cell is hardly changing over the depth. A focus (Point 5, see section 3.2) occurs near the leading corner, which is the center of a swirl pattern of the streamlines.

Regarding the second cell: at an elevation close to the bed *z/h*=0.07 and 0.21, there exists a saddle point (Point 6, see section 3.2) between the two cells at the leading wall of the cavity. This point disappears higher in the water column.

4.2 *Configuration with W/L=4*

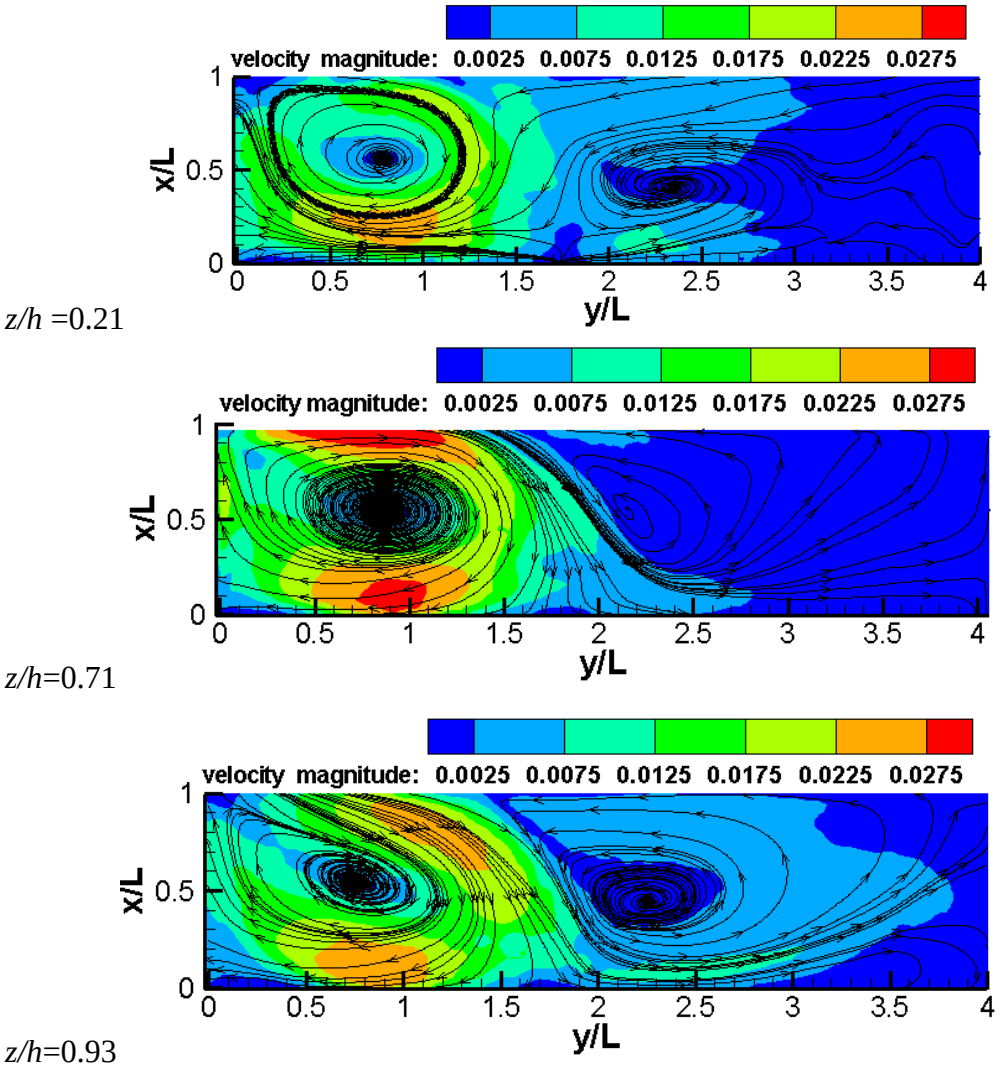

Figure III.34:Velocity fields at different elevations for *W/L*=4

Figure III.34 shows patterns of time-averaged velocity fields at different elevations for *W/L*=4. For the first cell, the mean velocity does not change a lot in an elevation closer to the free surface *z/h*=0.93 to that in an elevation closer to the bed *z/h*=0.21. For the second cell, the flow pattern changes very much at different elevations. Especially in an elevation closer to the bed *z/h*=0.21, the flow pattern at the second cell region seems to be complex. There exists a saddle point (Point 6, see section 3.3) at *z/h*=0.21 between the two cells at the leading wall of the cavity.

It is interesting to observe that a region with very limited vertical axis vorticity is measured for *y/L*>3-3.5. This flow goes towards the end wall (*y*=*W*) in the top half of the water column and back towards the main stream (*y*=0) near the bed.

4.3 *Configuration with W/L=5*

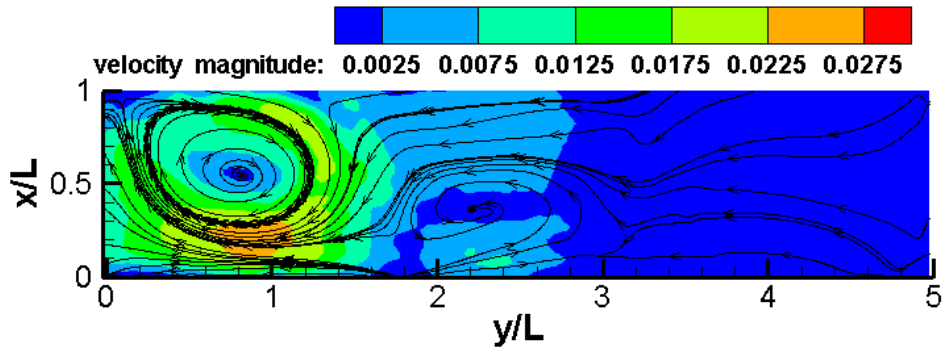

z/h =0.21

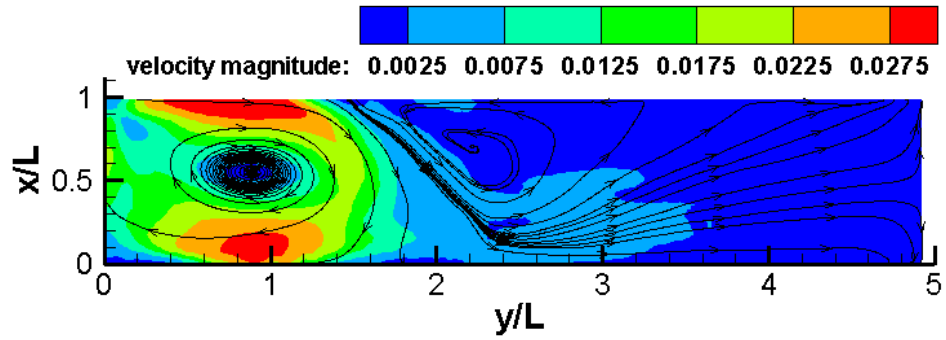

z/h=0.71

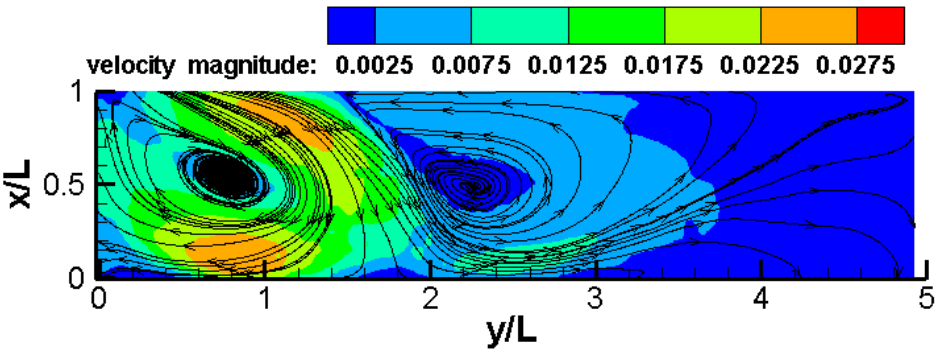

z/h=0.93

Figure III.35. Velocity fields at different elevations for *W/L*=5

Figure III.35 shows the patterns of time-averaged velocity fields at different elevations for *W/L*=5. The first cell does not change much along the vertical axis, both in terms of velocity magnitude and flow pattern.

For the second cell, the flow pattern changes very much at different elevations. As for *W/L*=4, a region with very limited vertical axis vorticity is measured for *y/L*>3-3.5. This flow goes towards the end wall in the top half of the water column and back towards the main stream near the bed. Nevertheless, very close to the *y/L*=1 wall, the flow goes back towards the main stream.

4.4 *Comparison with the literature*

The appearance of three-dimensional vortex systems in the presence of groynes in river flows has been computed by McCoy *et al.*(2007). They showed a horseshoe-like vortex can be present at the base of a groyne.

In the present experiment, the flow patterns under different elevations show the same features as the experiments without a gravity standing wave of Tuna *et al.* (2013 shown in Figure III.36.).

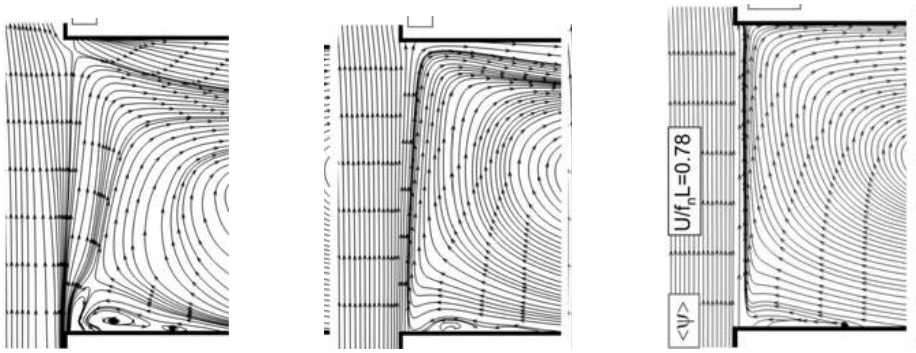

z/h=0.033 *z/h*=0.167 *z/h*=0.833

Figure III.36:Data from Tuna *et al.* (2013)

For all configurations, at an elevation close to the bed *z/h* =0.07 and 0.21, there exists a saddle point (Point 6, see section 3.3) between the two cells at the leading wall of the cavity. This point disappears higher in the water column. Also, the scale of the separation bubble adjacent to the leading wall of the cavity is generally larger at the elevations closest to the surface such as *z/h* =0.93 and *z/h* =0.71. It is also evident that there exists a region of focus which occurs near the leading corner, which is the center of a swirl pattern of the streamlines.

5 MEASUREMENTS ALONG VERTICAL PLANES

The horizontal PIV measurements at different elevations indicate that a three-dimensional vortical structure seems to exist within the second cell for wide cavities. For more detail, vertical PIV are measured at three transversal locations in the cavity, upstream plane *x/L*=0.17 (*x*=5cm), center plane *x/L*=0.5 (*x*=15cm), and downstream plane *x/L*=0.83 (*x*=25cm). The streamlines are indicated as black lines and the color represents the vertical velocity magnitude.

5.1 *Configuration with W/L=3*

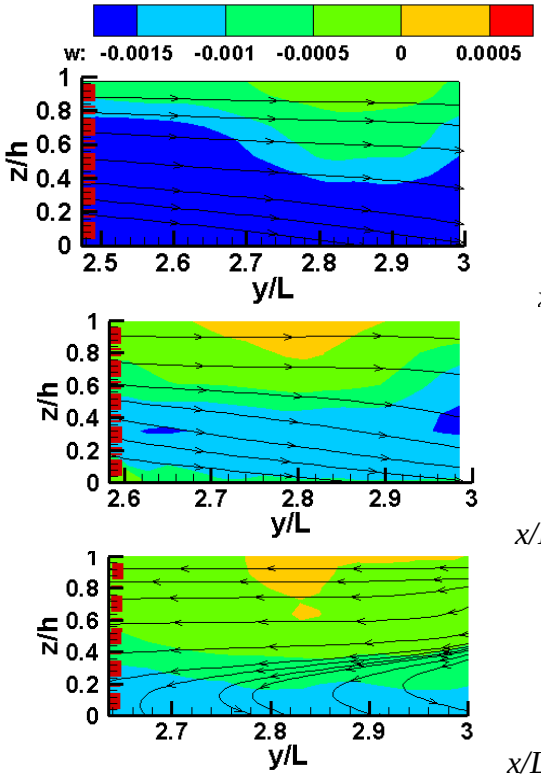

Figure III.37: Velocity fields of second cell region at different transversal locations for *W/L*=3

Figure III.37 shows the vertical velocity fields of the second cell region at different transversal locations for *W/L*=3. The mean vertical velocity is oriented towards the bed in the three measured planes with a more rapid vertical velocity in the upstream plane *x/L*=0.17 than the downstream one *x/L*=0.83.

5.2 *Configuration with W/L=4*

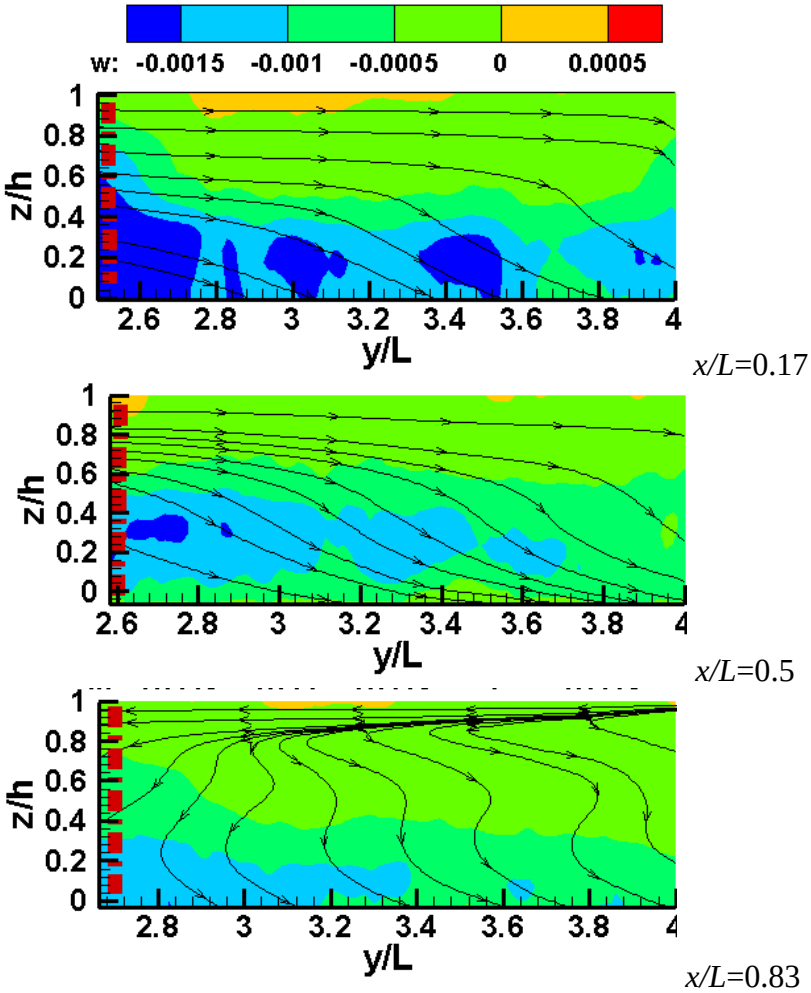

Figure III.38: Velocity fields of second cell region at different transversal locations for *W/L*=4

Figure III.38 shows the velocity fields of second cell region at different transversal locations for *W/L*=4.

It is interesting to note that at *x/L*=0.17 the whole flow is oriented towards the end wall (*y/L*=4), in agreement with the horizontal PIV measurements.
At *x/L*=0.83, the flow near the free surface (*z/h*=0.93) goes towards the main stream for *y/L*<3.5 and towards the end wall for *y/L*>3.5 (in agreement with the horizontal PIV figures); at *z/h*=0.71 this separation takes place at *y/L*=3 (in agreement with horizontal PIV data) and finally at *z/h*=0.21, the flow is very slow for *y/L*>3, in agreement with the horizontal PIV data.

It was observed in the horizontal PIV data that "a region with very limited vertical axis vorticity is measured for y/L>3-3.5. This flow goes towards the end wall (y=W) in the top half of the water column and back towards the main stream (y=0) near the bed.

5.3 *Configuration with W/L=5*

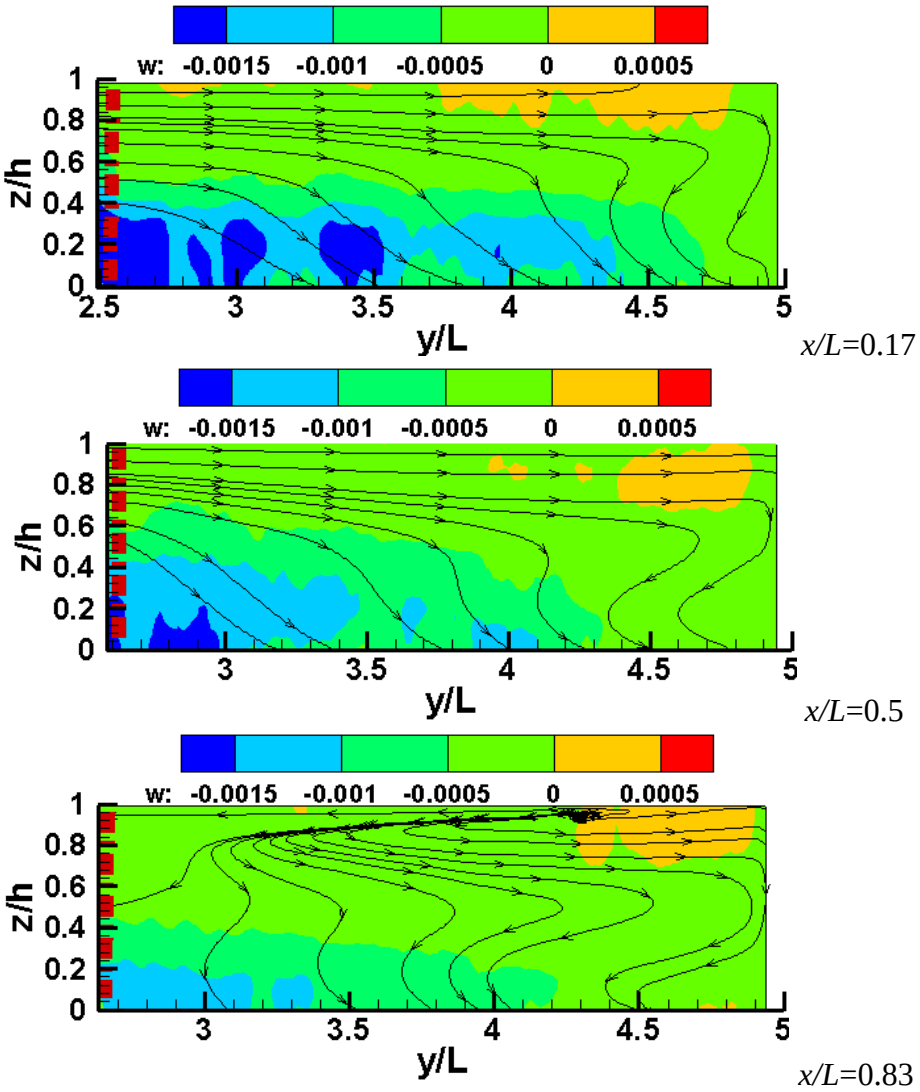

Figure III.39. Velocity fields of second cell region at different transversal locations for *W/L*=5

Figure III.39 shows the velocity fields of second cell region at different transversal locations for *W/L*=5.

At *x/L*=0.83 an interesting feature is observed : near the free surface, the flow goes towards the main stream (as observed in horizontal PIV at *z/h*=0.93) while below (*z/h*=0.71) it separates: it goes towards the main stream for *y/L*<3 and to the end wall for *y/L*>3 (in agreement with the horizontal PIV), finally near the bottom (*z/h*=0.21), the flow component along y is very limited (in agreement with the horizontal PIV).

6 DETAILED ANALYSIS OF THE FLOW

6.1 *The evolution of the first cell for increasing W/L*

As described in section 4, the typical velocity of the first cell does not evolve much as *W/L* increases (for *W/L*>1). At the same time, the location y_{c1} of the center of the first cell increases as the cavity width increases (for *W/L*=1 to 2).

This section proposes a zoom on the first cell for selected measured configurations: *W/L*=1-2-3-4-5 in Figure III.40. This figure confirms that the shape of the streamlines and the spatial distribution of the velocity magnitude remain very similar: the zones with larger velocity are mostly at the same position near the downstream wall and upstream wall.

The fact that the characteristics of the first cell do not evolve much as *W/L* increases will be of high importance when analyzing the characteristics of the mixing layer as *W/L* increases (please refer to next chapter).

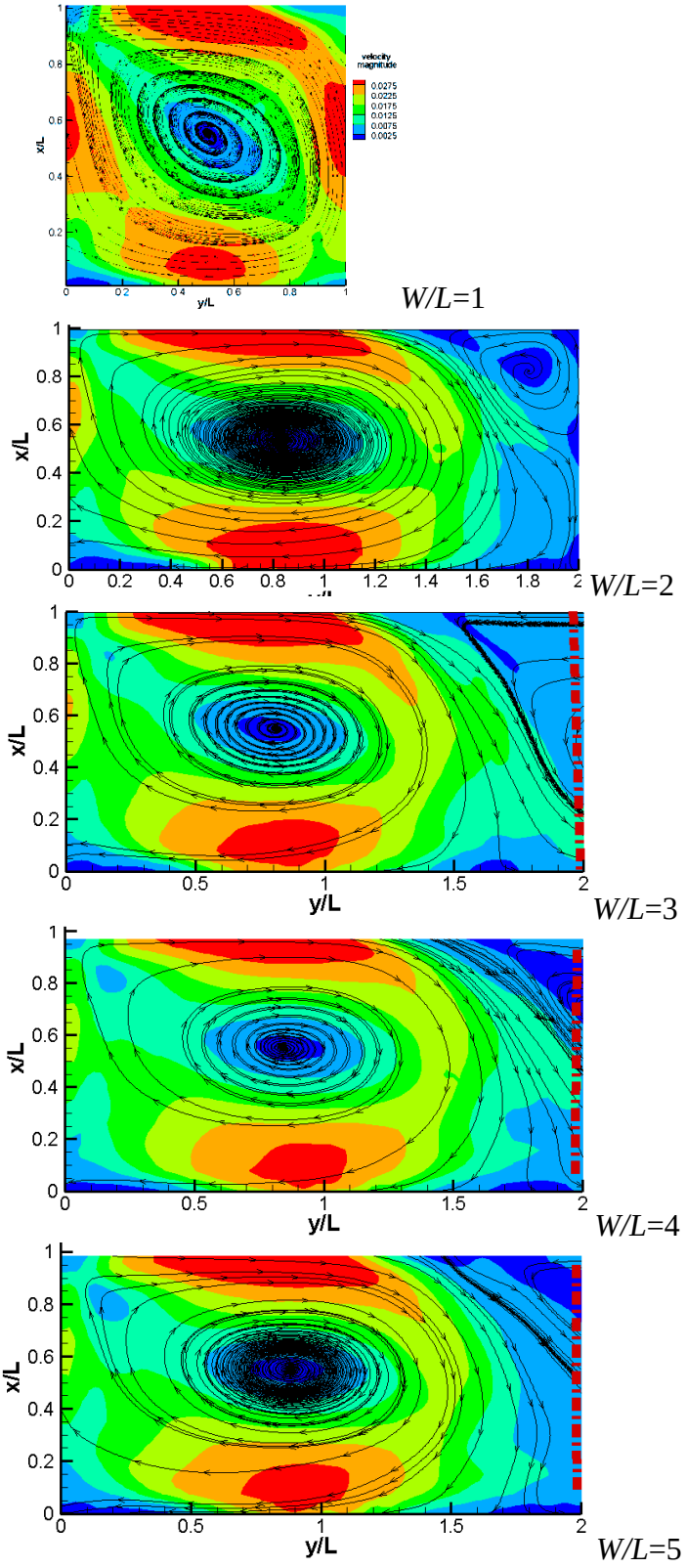

Figure III.40:First cells for different geometries with *W/L* from 1 to 5

Moreover, Figure III.41 shows the first cell at different elevations (z/h=0.07, 0.14, 0.71 and 0.93) for case W/L=3. The general pattern of the first cell doesn't evolve much but the characteristic velocity decreases when approaching the bed (z/h=0.07) as already mentioned by Tuna *et al.*, 2013. As a result, in most cases (for W/L>1), the first cell is considered to be quasi-2D.

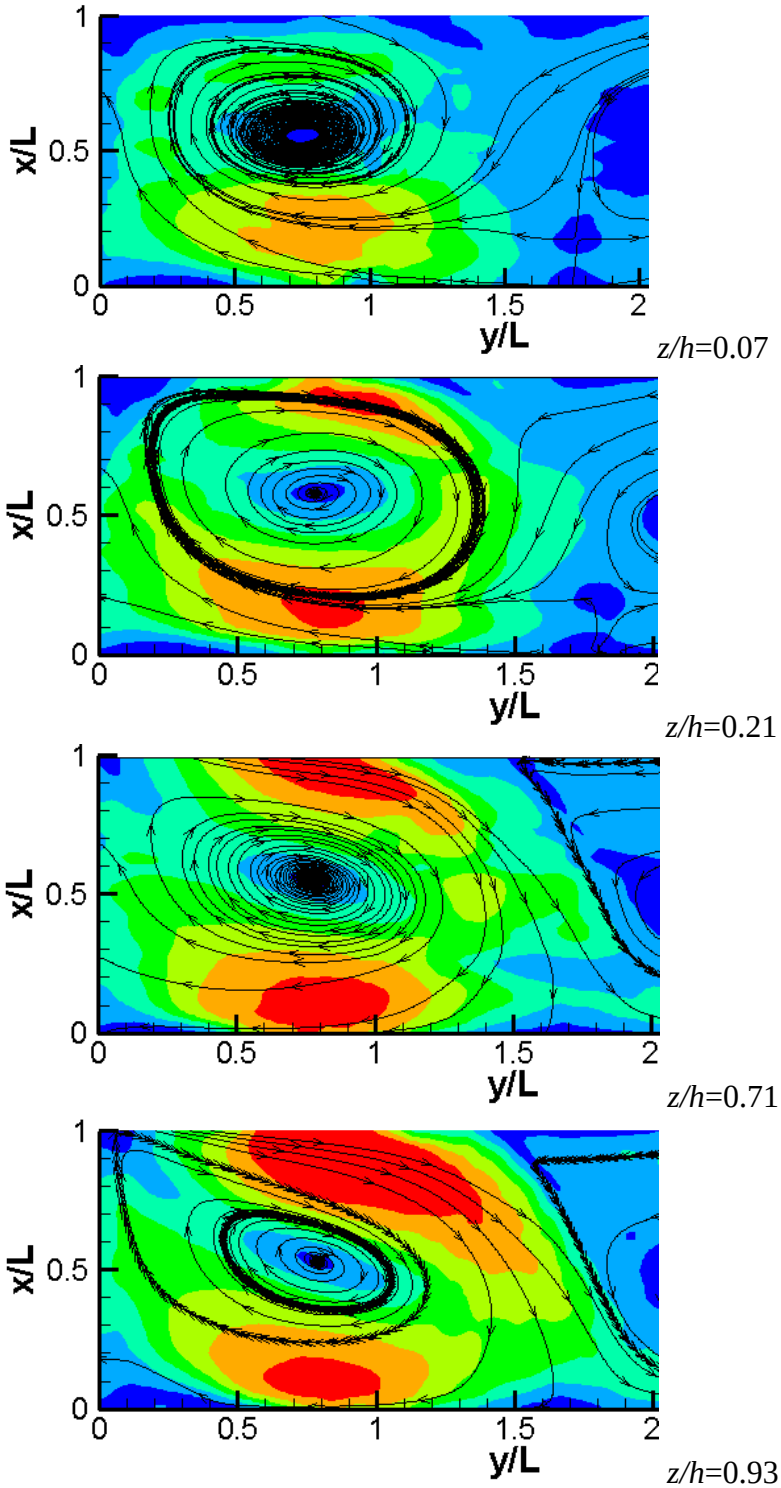

Figure III.41:First cells at different elevations for W/L=3

6.2 *Transition from a one-cell to a two-cell pattern*

In order to detect the appearance of the second cell as W/L increases, flow patterns for W/L=2, 2.1, 2.2, 2.3 are analyzed in details. The mean velocity field of the transition zone from y/L=1 to y/L=2

is plotted, as successive averages performed over 10 seconds periods, in the following figures. This allows notably to investigate the temporal stability of the flow pattern.

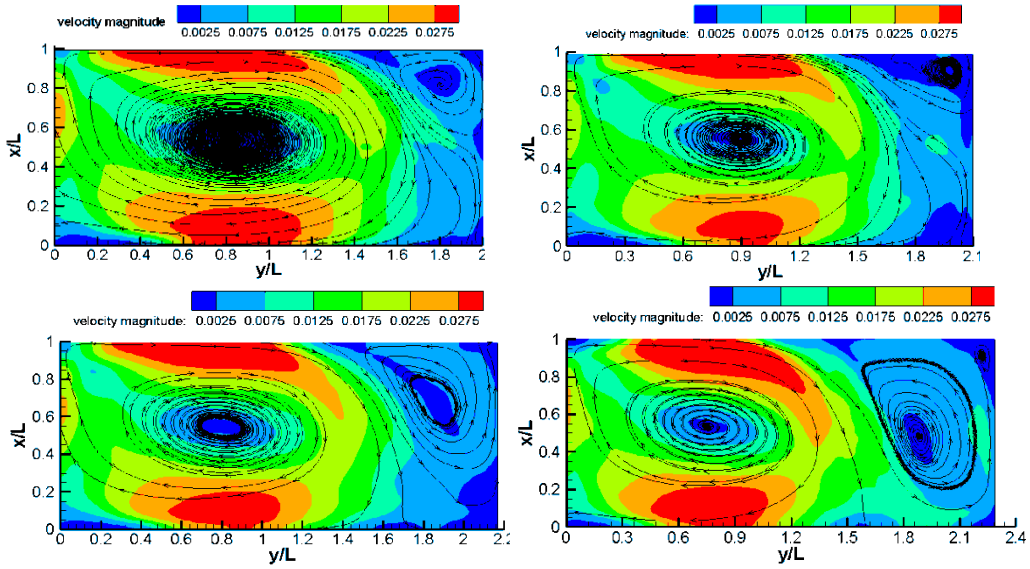

Figure III.42:Transition for configurations *W/L*=2, 2.1, 2.2, 2.3

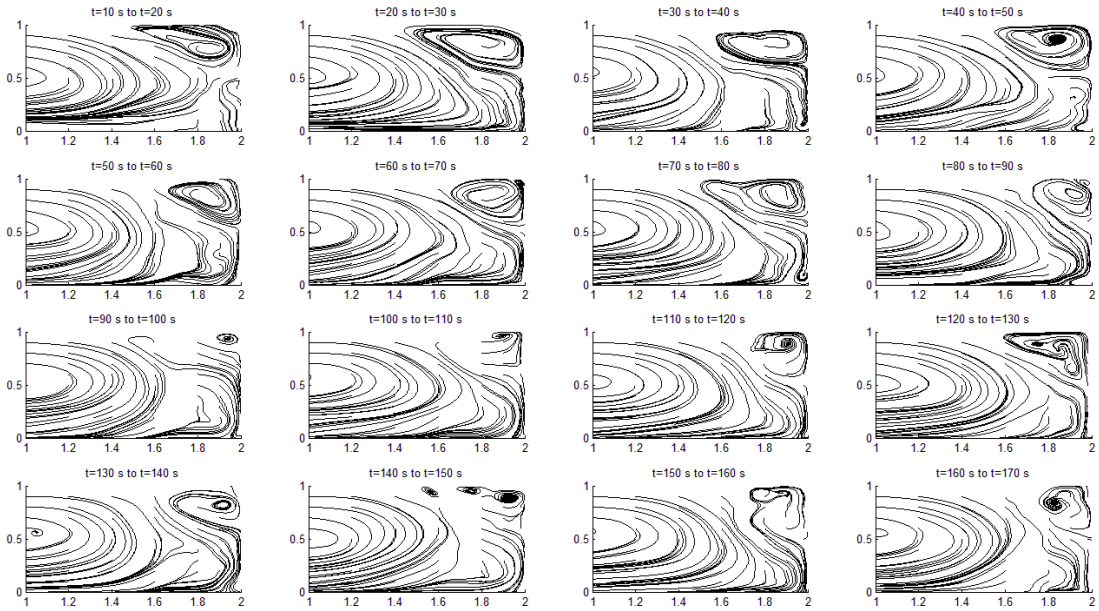

Figure III.43:Streamlines of the flow averaged over 10 seconds, and plotted every 10 seconds for *W/L*=2

For *W/L*=2, a small second cell is observed in the extreme downstream corner of the cavity (see Figure III.43.). The streamlines corresponding to both cells keep the same during the whole measurements. This flow is thus timely-stable and it is classified here as a "1-cell pattern with 1 secondary cell".

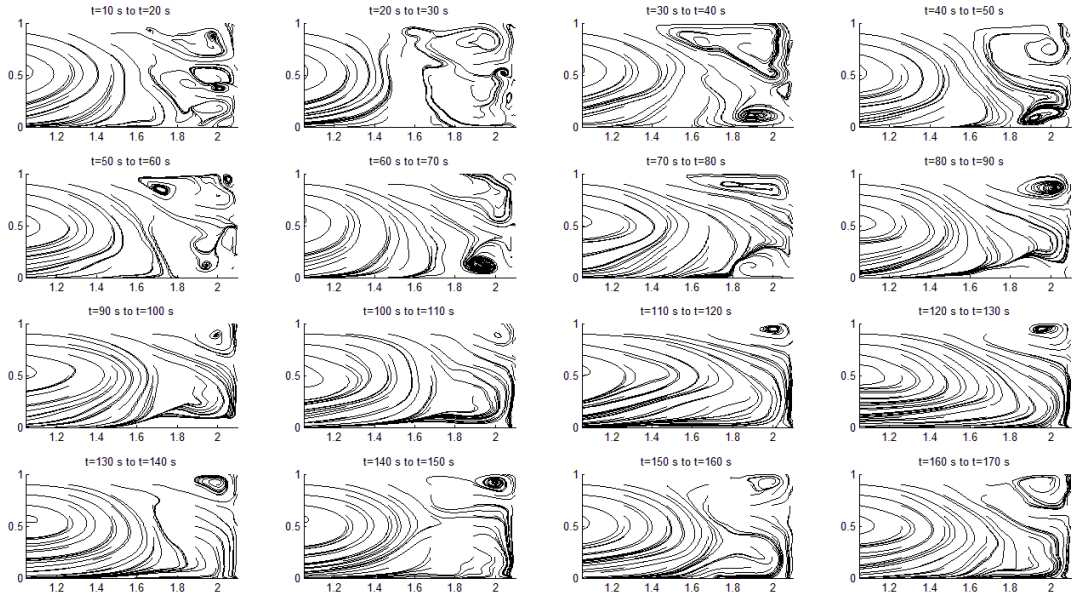

Figure III.44: Streamlines of the flow averaged over 10 seconds, and plotted every 10 seconds for *W/L*=2.1

For *W/L*=2.1, the streamlines belonging to the first cell remain quite stable but near the opposite wall (*y/L*=2.1), the flow pattern evolves with time: two cells can be seen, on both corners of this wall. Nevertheless, the cell located near *x/L*=0 sometimes disappears, its presence is unstable. This flow is thus slightly timely-unstable and it is classified here as a "1-cell pattern with 2 secondary cells".

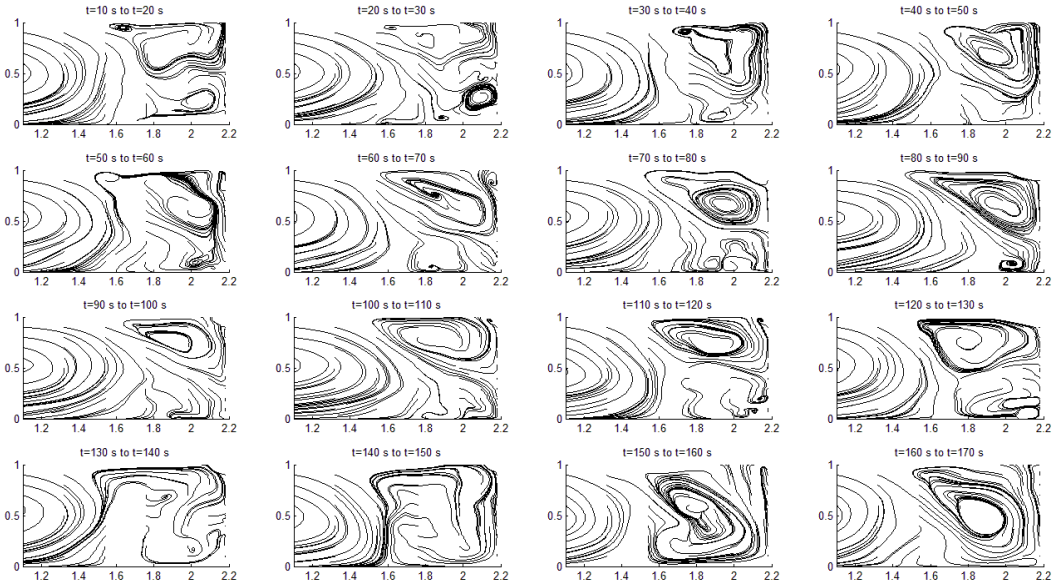

Figure III.45: Streamlines of the flow averaged over 10 seconds, and plotted every 10 seconds for *W/L*=2.2

For *W/L*=2.2, we sometimes observe two cells as for *W/L*=2.1 (as at time *T*=0-100 s on Figure.III.44) and sometimes one large second cell as at time *T*=160-170s. This flow is highly unstable and is classified here as: intermediate between a "1-cell pattern with 2 secondary cells" (as for *W/L*=2.1) and a "2-cell pattern" (as for *W/L*=2.3).

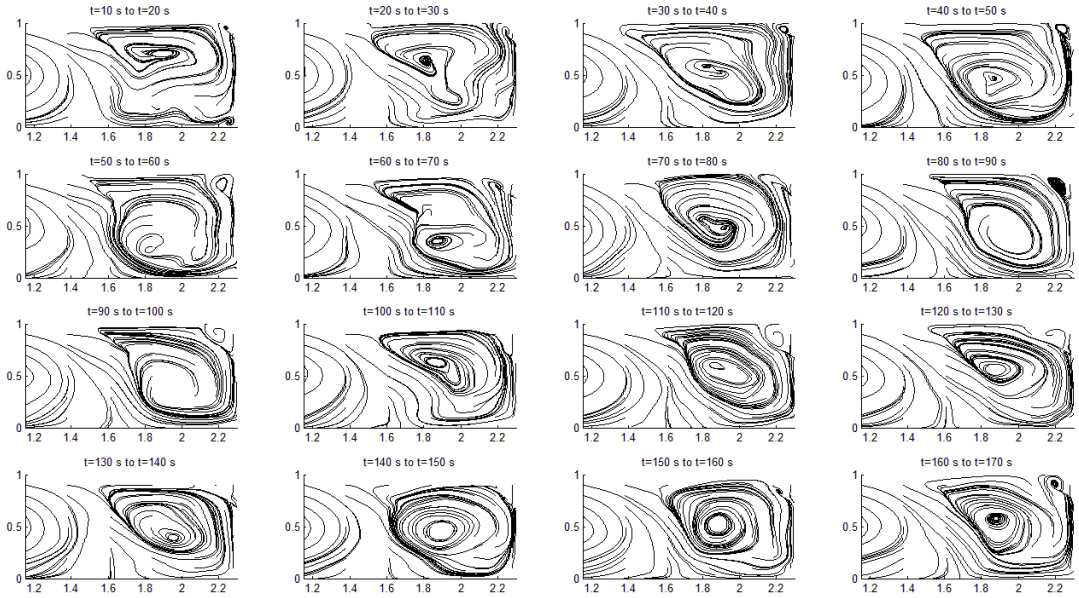

Figure III.46: Streamlines of the flow averaged over 10 seconds, and plotted every 10 seconds for *W/L*=2.3

For *W/L*=2.3, the second cell is quite stable and occupies the whole available space, it ranges from *x/L*=0 to 1. This flow is classified as a stable "2-cells" pattern.

The transition from a 1-cell to a 2-cell pattern thus occurs at *W/L*=2.2.

7 TEMPORAL STABILITY OF VELOCITY FIELD

In order to investigate the temporal stability of the flow pattern, velocity fields for different configurations are timely-averaged over an increasing time.

First, Figure III.47 shows the mean flow field for *W/L*=1 averaged over the first 24 seconds, 49 seconds etc… The general flow pattern appears to be already stable after 24 seconds, even though the exact velocity contours do not change after about 100s.

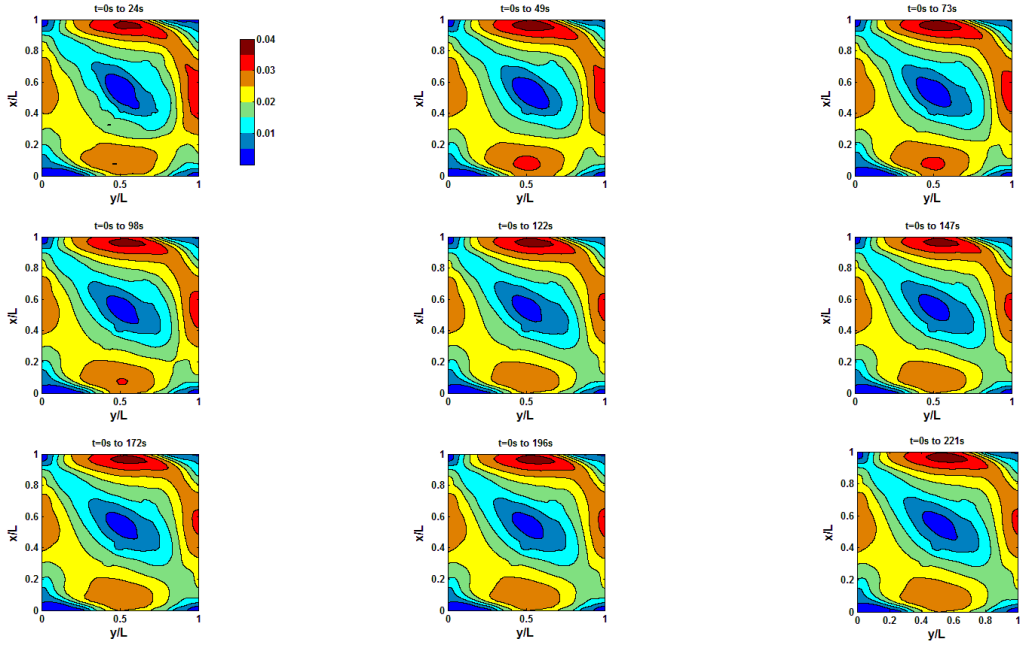

Figure III.47:Flow field averaged over increasing time for *W/L*=1

Second, the same process is applied to the *W/L*=2 configuration, focusing on the first cell. As for *W/L*=1, a 24s time is enough to reach a quite converged flow pattern for this case.

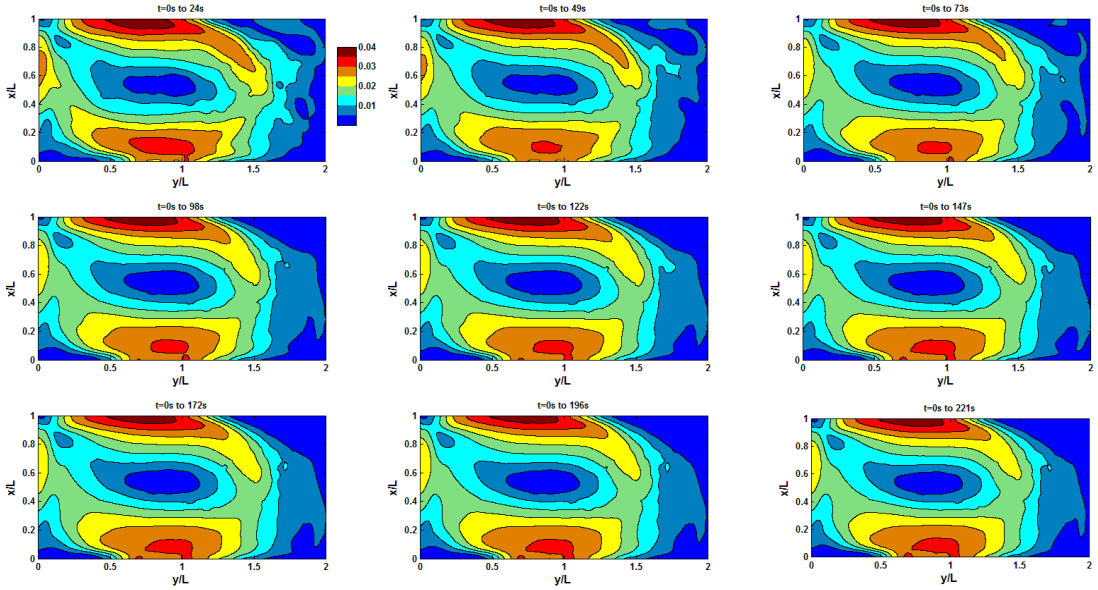

Figure III.48:Flow field averaged over increasing time for *W/L*=2

Still for *W/L*=2, we focus on the second cell on Figure.III.49. It appears that it takes more time to reach a converged flow pattern: after about 100s the flow has converged.

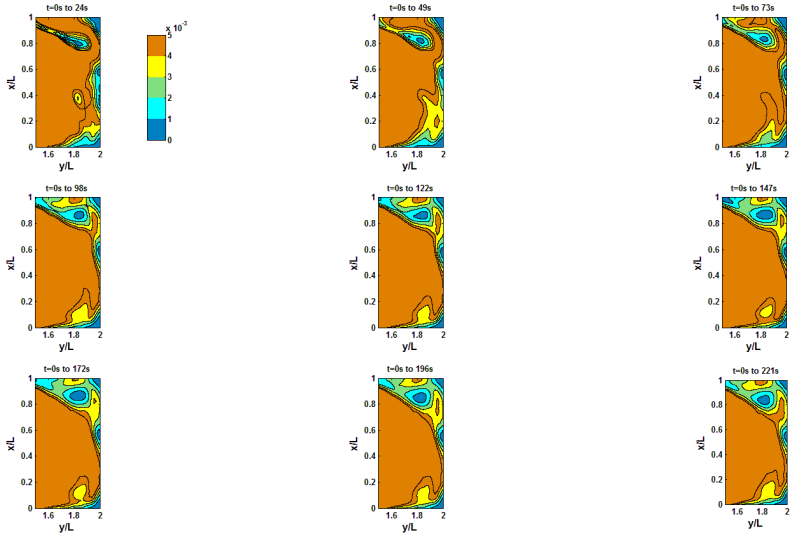

Figure III.49:Flow field of the second cell averaged over increasing time for *W/L*=2

Third, for the first cell of *W/L*=3, 24 seconds appears not to be enough to reach a stabilized flow pattern. The time for converge is estimated at about 40 seconds.

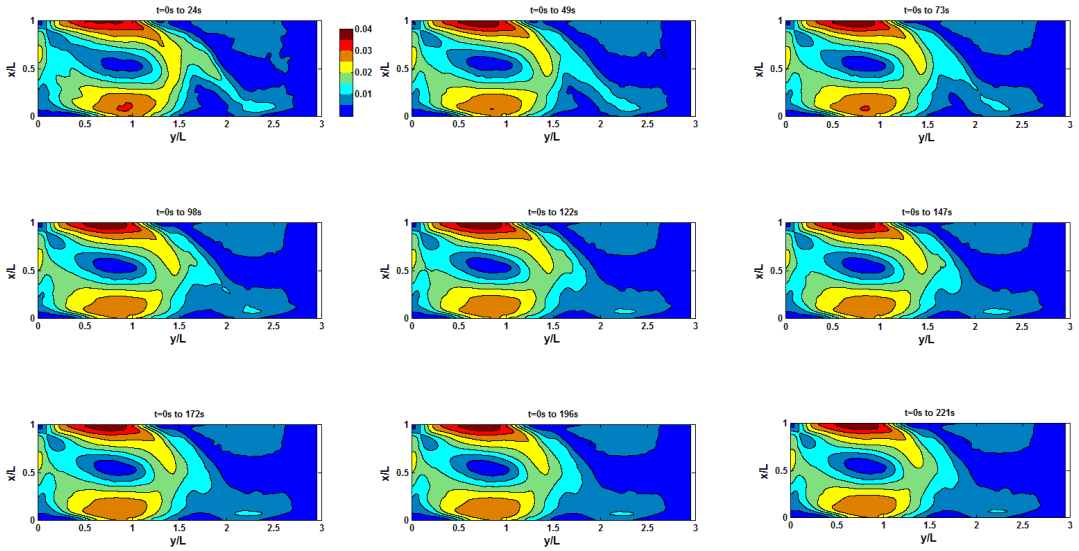

Figure III.50:Flow field averaged over increasing time for *W/L*=3

As for *W/L*=2, we now focus on the second cell of the *W/L*=3 configuration. About 100s is required to reach convergence.

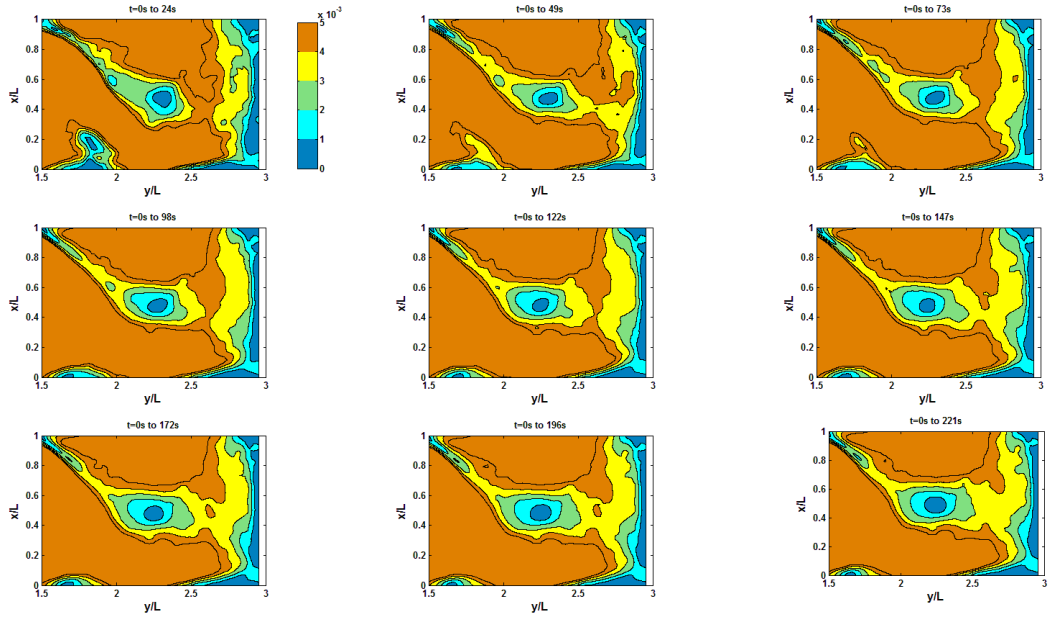

Figure III.51:Flow field of the second cell averaged over increasing time for *W/L*=3

Fourth, for the first cell of *W/L*=4, a converged flow is obtained after about 50 seconds.

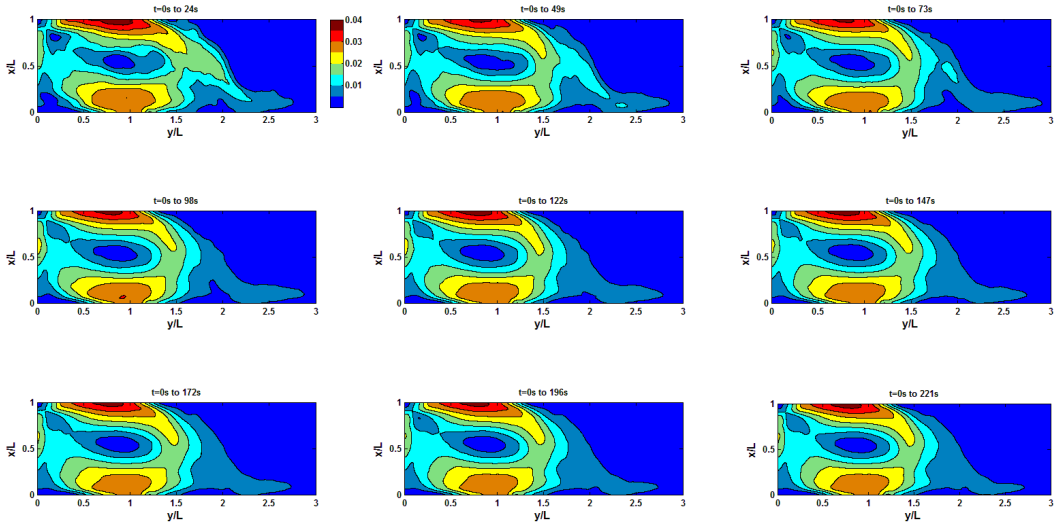

Figure III.52:Flow field averaged over increasing time for *W/L*=4

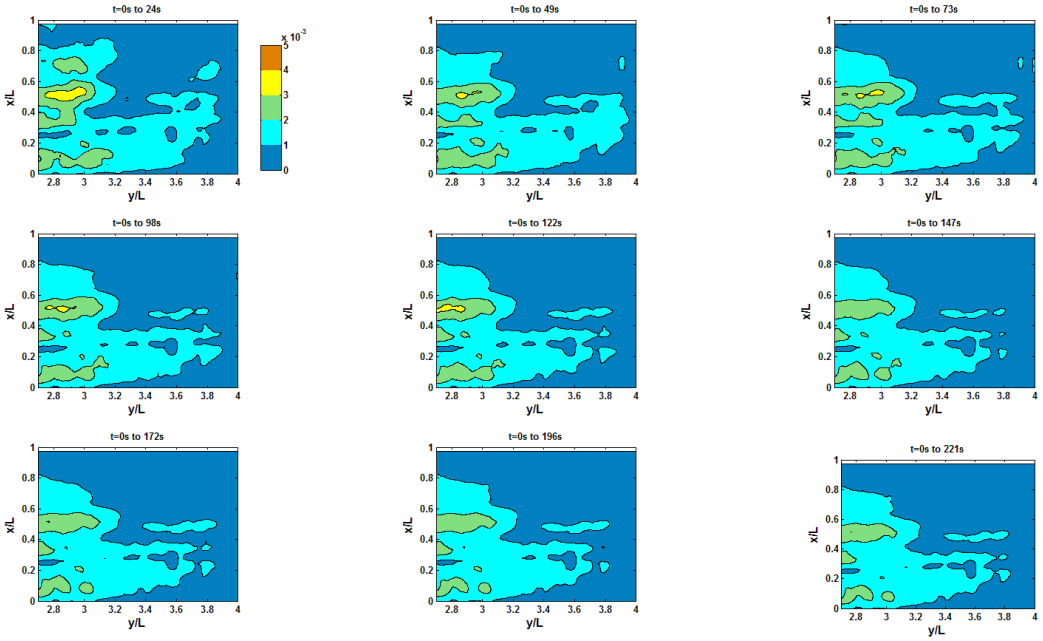

Figure III.53:Mean flow field of second cell in every 24 seconds for *W/L*=4

Fifth, for the *W/L*=5 case, Figure III.54 shows that the first cell becomes stable after about 50s.

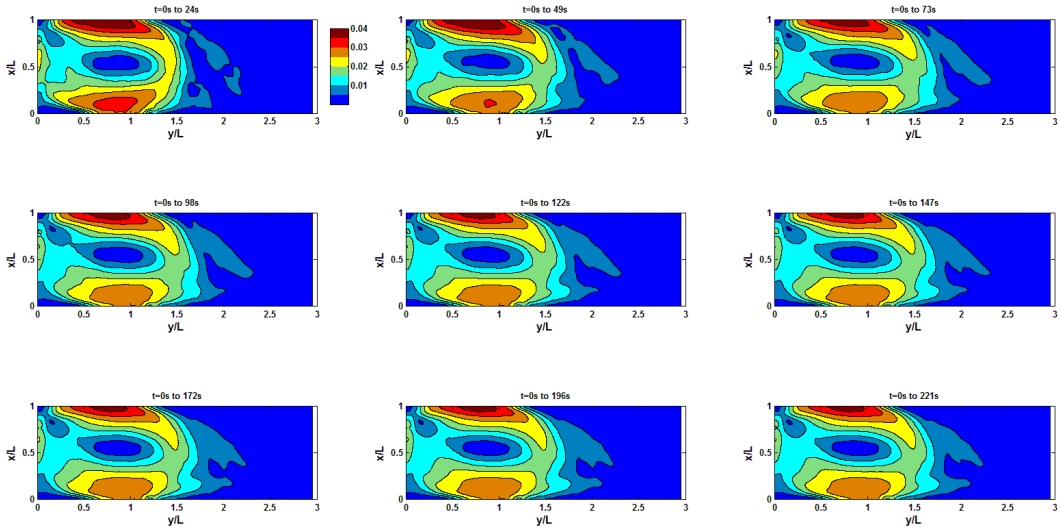

Figure III.54:Mean flow field in every 24 seconds for *W/L*=5

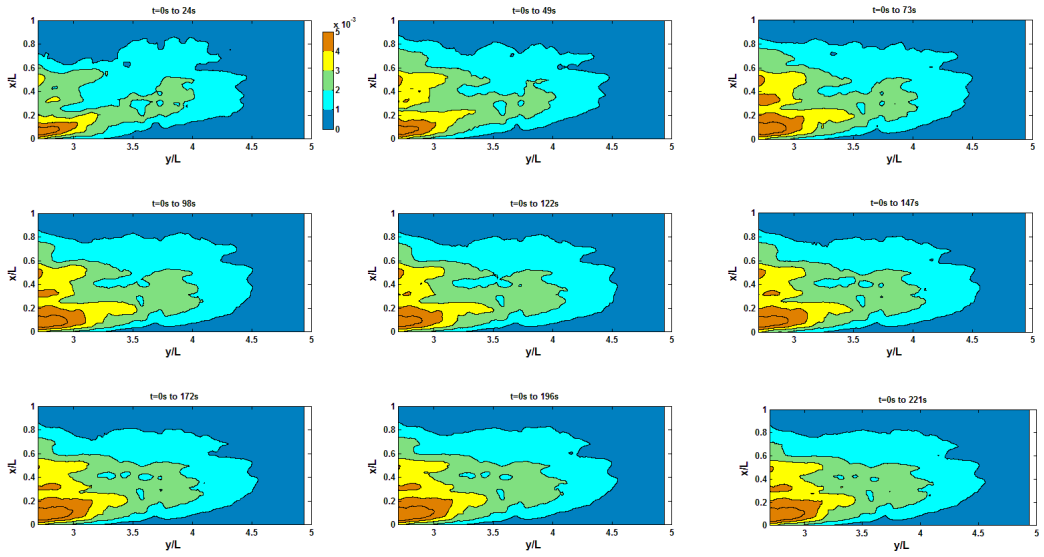

Figure III.55 Mean flow field of second cell in every 24 seconds for *W/L*=5

Table III.5:The estimation time for the stability of the cells

W/L	An estimation time for the stability of the first cell(s)	An estimation time for the stability of the second cell(s)
1	24	
2	24	100
3	40	100
4	50	110
5	50	110

To conclude, the first cell is stable after 30 seconds for all configurations, the second cell is stable after 100 seconds. That makes sense, the characteristic velocity of the second cell is just 10% of that of the first cell. In addition, the required time for time-convergence thus increases as *W/L* increases.

8 CONCLUSIONS OF CHAPTER III

8.1 *Sum-up of all horizontal PIV data obtained for z/h=0.71*

As a help before emitting conclusions for this chapter, all flow patterns observed for the different aspect ratios, *W/L*=0.3-5, are put together herein.

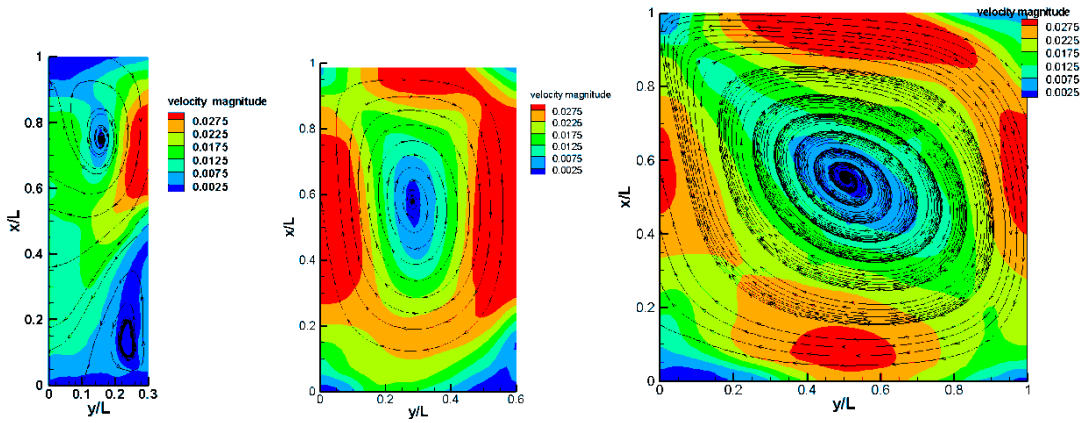

W/L=0.3 *W/L*=0.6 *W/L*=1

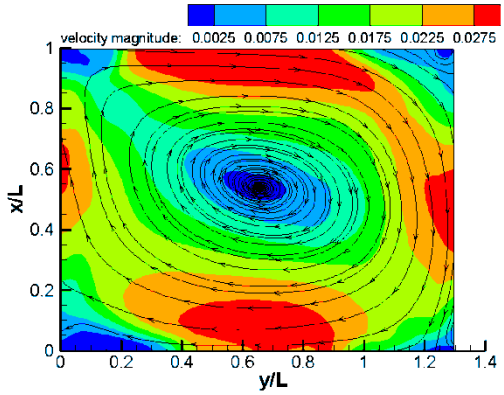

W/L=1.3

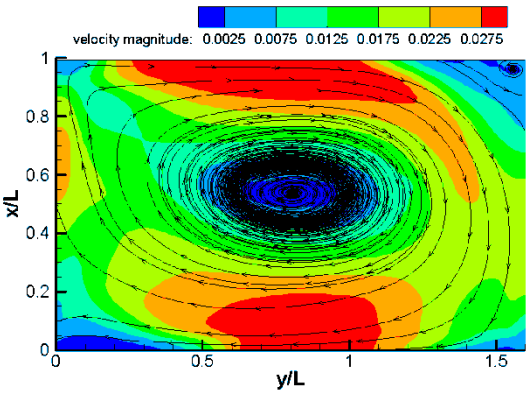

W/L=1.7

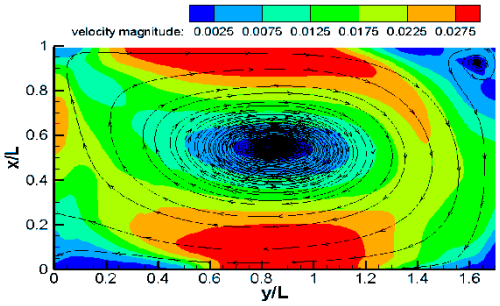

W/L=1.7

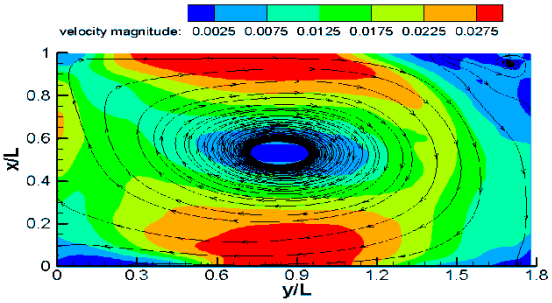

W/L=1.8

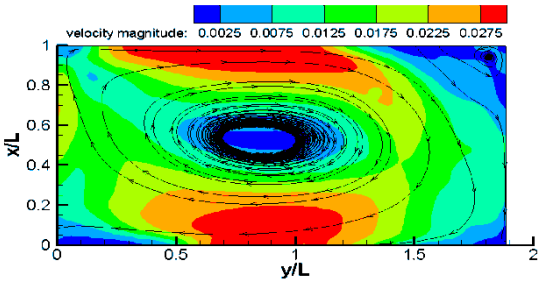

W/L=1.9

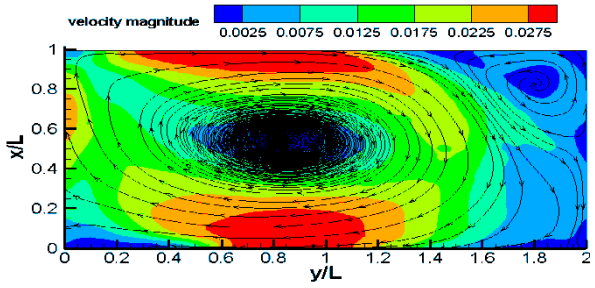

W/L=2

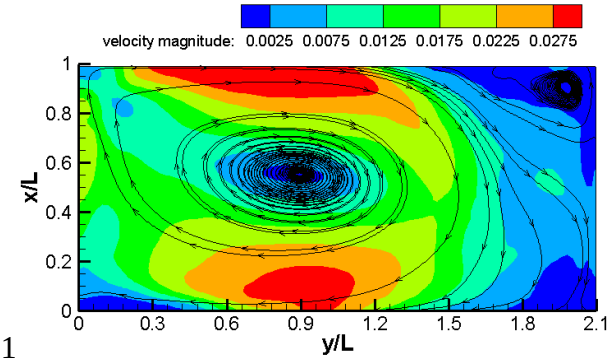

W/L=2.1

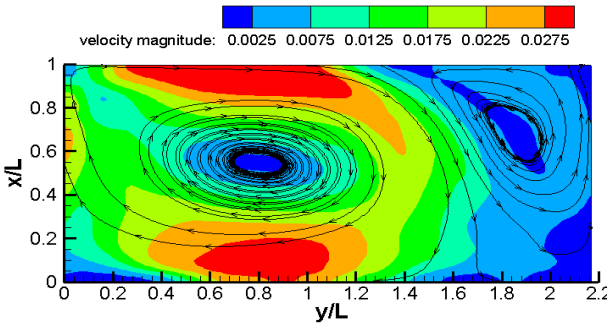

W/L=2.2

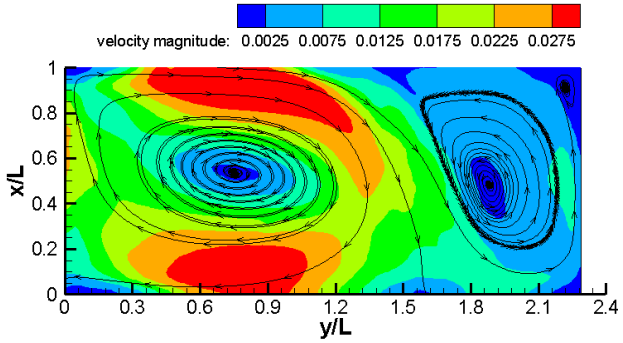

W/L=2.3

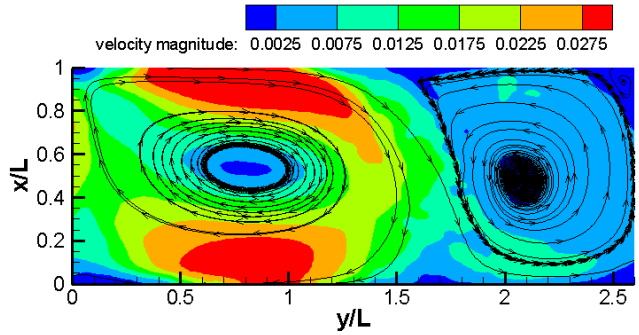

W/L=2.6

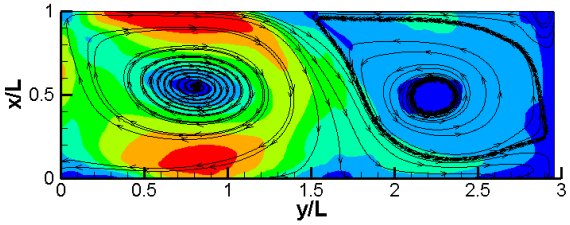

W/L=3

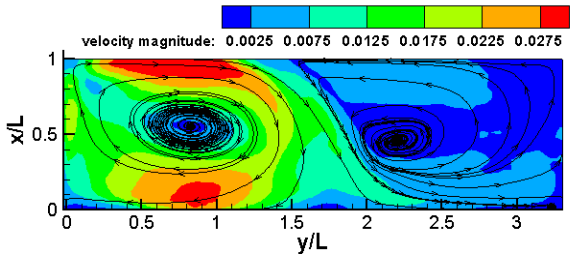

W/L=3.3

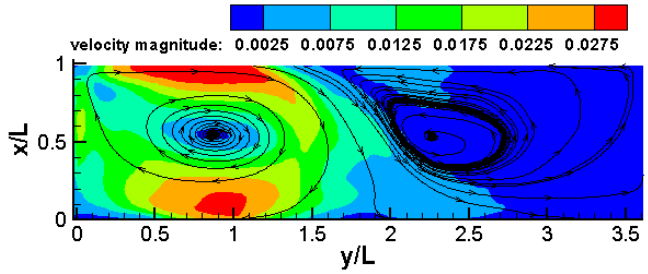

W/L=3.6

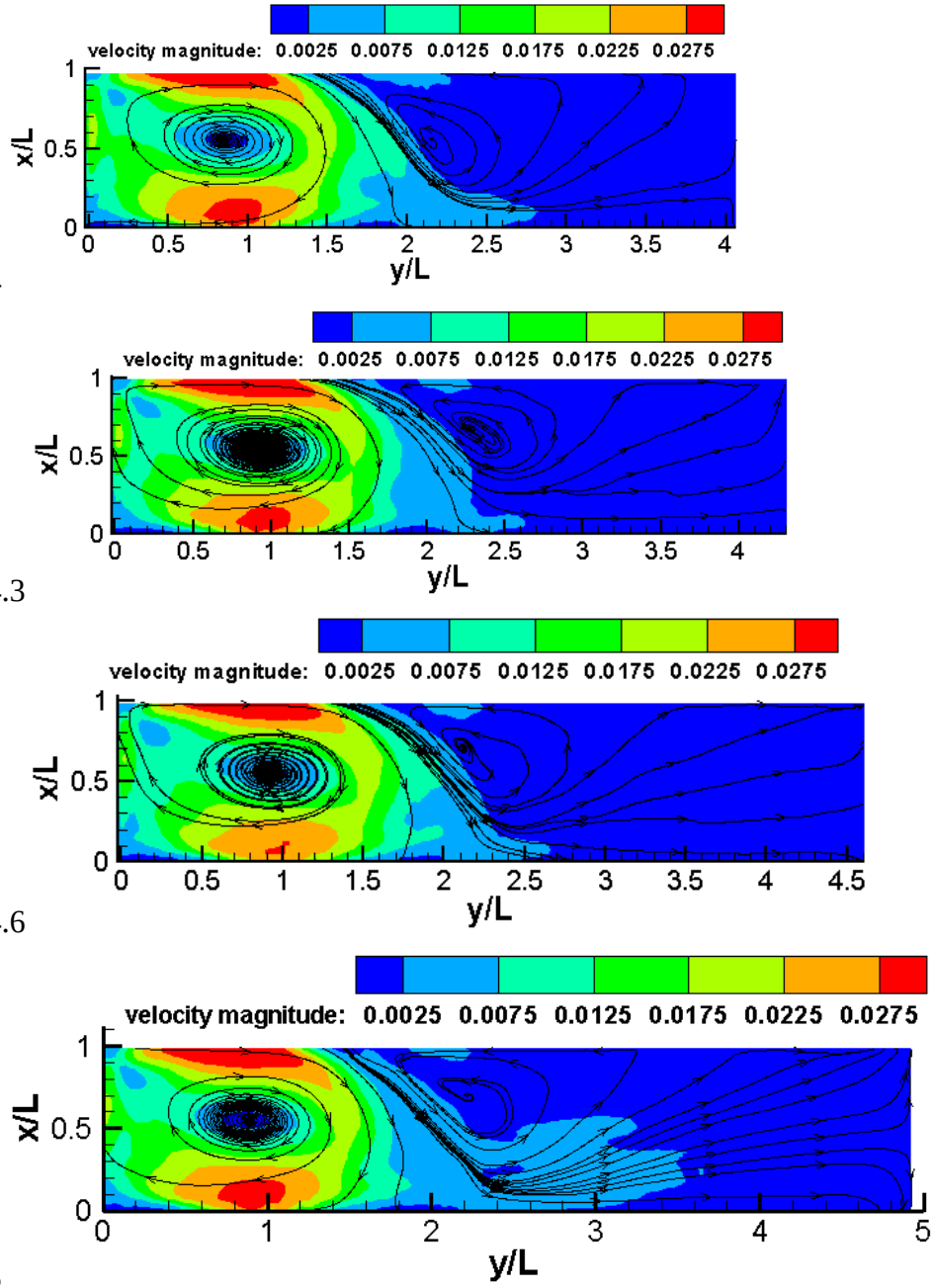

Figure III.56. Velocity field for all configurations

For *W/L*=0.3, the pattern reported in, say, half of the literature is retrieved: two cells aligned in the streamwise direction. Higher aspect ratios, *W/L*=0.6-2.0, correspond to the situation reported in, say, the other half of the available literature, where one cell occupies the whole cavity. The cell size and the position of the cell center both follow the evolution of the cavity aspect ratio. Secondary cells develop in the two corners at the back of the cavity with sizes increasing with *W/L*. For *W/L*=2.1-2.3, these secondary cells exhibit unstable behavior and sizes. They merge for *W/L*=2.3, corresponding to the appearance of a second main cell in the crosswise direction, with new secondary cells in the corners at the cavity back. For *W/L*>4, the streamlines indicate that, instead of a third cell aligned with the two preceding ones, a 3D flow develops in the back of the cavity, with recirculation zones of horizontal axis.

8.2 *Conclusions*

In this chapter, we have studied in detail the evolution of the flow pattern within a lateral cavity of variable width and connected to a main stream of fixed characteristics. Our work takes benefits from the available experimental set-up which allows adjusting continuously the aspect ratio and reaching values really higher than in the existing literature.

The patterns reported till then – *i.e.* two cells aligned in the streamwise direction, and then one cell occupying the whole cavity – were reproduced. The pattern with two cells aligned in the crosswise direction was observed for different aspect ratio. Finally, the development of a third zone where the flow is three-dimensional was observed for the highest aspect ratios.

The transition from one to two cells aligned in the crosswise direction was explained. It is due both to the increasing size and the unstable behavior of the secondary cells located in the back corners that merge to form the second main cell.

The first cell characteristics are hardly modified by the appearance of the second cell and so by the increase of the cavity aspect ratio. The motion in the cavity is due to momentum exchange with the mainstream. These exchanges are operated through the mixing layer located at the cavity/main stream interface: this mixing layer is studied in detail in next chapter.

Finally, velocity measurements show that the characteristic velocities decrease considerably from one cell to another. The characteristic time of advection thus increases considerably in the cells located at the back: the implications of these results on the scalar transfers within the cavity are studied in the last chapter.

Chapter IV: Mixing layer analysis at the interface between the main stream and the cavity

The aim of Chapter IV is to investigate in detail the main characteristics of the mixing layer taking place between the main stream and the cavity. The hydrodynamics of the mixing layer is deeply analyzed based on flow statistics (section 3) and eddy identification (section 4) for one reference flow configuration. The impact of the flow and geometrical parameters on these issues is studied in section 5.

1 LITERATURE REVIEW

The aim of this *Chapter IV* is to investigate in detail the main characteristics of the mixing layer taking place between the main stream and the cavity. An overview of the literature dealing with open-channel mixing layers is thus included is the present section.

1.1 *Generalities*

As described by Riviere et al. (2010), at the connection between the main stream and the cavity, a large velocity gradient forms. This velocity gradient leads to a transverse mixing layer which extends from the upstream to the downstream corner of the cavity. This mixing layer permits to transfer mass and momentum between the main flow and the cavity. This region is thus of primary importance for cavity performance: exchange of nutrients and gases influencing the ecological equilibrium of oxbows, or exchange of fine sediments influencing the geo-morphological budget.

For high velocity gradients, the inflection of the transverse profiles of mean streamwise velocity leads to Kelvin-Helmholtz instabilities that give birth to coherent turbulent structures that are shed from the upstream end and advected along the mixing layer with increasing typical size and time-scale. Many experimental studies have measured the flow characteristics in straight free mixing-layers (Wygnanski and Fiedler, 1970 or Bell and Mehta, 1990). These measurements agree that the width of the mixing layer increases linearly along its development length. The maximum turbulent intensities and Reynolds shear stress across the mixing layer occur at its centerline. After an initial increase, they tend to decrease in magnitude with distance from the upstream boundary condition.

A review of more complex mixing layer configurations in open-channel flows under deep conditions was established by Mignot *et* al. (2014a and b). All these configurations reveal the same behavior as for the straight mixing layers discussed above: the width of the mixing layer increases along the streamwise axis from up- to downstream with the occurrence of turbulent eddies and a maximum turbulence production occurs along this mixing layer due to the increased shear and velocity gradient, so that: i) all these terms are maximum along the centerline of the mixing layer and rapidly decrease on both sides, and ii) their magnitude first increases from the upstream limit towards downstream, reach a maximum value and decrease again towards downstream.

1.2 *Impact of the shallowness*

In all mixing layers, the dimensions of the eddies generated in the upstream region of the mixing layer tend to increase towards downstream; nevertheless, for shallow mixing layers, Uijttewaal and Booij (2000) showed that the shallowness tends to limit the growth of the large scale eddies in the vertical direction (due to the limited water depth, also referred to as “vertical confinement”) so that the eddies become quasi-2D (the maximum vertical extension obviously equals the water depth). Moreover, bottom friction tends to decrease the velocity difference between outer velocities on both sides due to friction. As a consequence, the shallowness causes a limitation of the growth of the mixing layer width along its development: while this growth rate is constant along the streamwise axis for a mixing layer in deep conditions, in shallow conditions the initial growth rate equals that of the deep conditions but it then decreases when advancing towards downstream.

1.3 *Constrained mixing layers*

The straight mixing layer is free to develop and thus the location of its centerline is not fixed and depends mostly on the velocity gradient between both layers. Oppositely many mixing layers are so called “constrained”, that is that the location of their centerline follows a geometrical singularity. For instance, for a fully-developed flow in a compound channel, the centerline of the mixing layer

follows the bank-step. In the present case, it is expected that the presence of two corners at the intersection of the main stream with the cavity will constrain the mixing layer.

1.4 *Mixing layer in the case of a lateral cavity*

Regarding open-channel lateral cavities, in a flow configuration without seiching, Sanju and Nezu (2013) observe that peaks of instantaneous Reynolds shear stress measured within coherent turbulent vortices are advected along the mixing layer periodically. The authors also observe events of transverse velocity from the cavity towards the main stream, which they name 'sweep motion', followed by events of velocity from the main stream towards the cavity which they name 'ejection'. They report that this triple structure: a sweep followed by a vortex and then by an ejection is generated periodically and once generated travels towards downstream along the interface. Sanjou et al. (2012) perform statistics regarding these motions based on a quadrant analysis. They report complex relative probabilities depending on the vertical elevation and streamwise location in the mixing layer. The coherent vortices shed and advected along a mixing layer are also reported by Weitbrecht et al. (2008) for a quite similar flow configuration: the flow between consecutive groynes. The authors observe coherent horizontal cells referred to as 2DLCS (2-dimensional large coherent structures) periodically shed from the extremity of the upstream groyne and advected towards the following groyne. They note that the coherent structures are not located along the mixing-layer axis but rather displaced on both sides: on the main stream or on the dead zone sides. They also notice that when reaching the downstream groyne, the vorticies either end up within the dead zone where they are advected by the recirculating flow or remain in the main stream where they are transported towards downstream. However, the frequency, location and statistics of these structures remain unclear.

This chapter is organized in 6 sections. After this introduction, section 1 gives additional details concerning the experimental set-up. In section 2, the hydrodynamics of one flow within one configuration is studied in detail. It corresponds to the flow studied in Chapter 2 within the L/b=1 geometry. Section 3 focuses on the turbulent coherent structures in the mixing layer. Then in section 5, we investigate the influence of the different dimensionless parameters of the problem on the mixing layer characteristics. Section 6 finally proposes the conclusions for this chapter.

1.5 *Experimental set-up*

The time-resolved horizontal velocity field u (along x axis) and v (along y axis) is measured using the 2D-horizontal PIV system used in Chapter 2 but with a focus on the mixing layer region. Measurements are performed at the elevation z_L=5cm indicated in Figure IV.1. Polyamid particles (diameter 50 μm) are added to the water; the 40mW laser coupled with the cylindrical lens generates a 1mm horizontal light layer at the elevation z_L; and finally a video camera located above the mixing layer records the particle motion over about 3000 consecutive images of 1280*960 pixels each, with an average spatial resolution of 0.3mm per pixel, at a frequency equal to 30Hz over the dashed-line area in Figure IV.1. Finally, the commercial software Davis (from Lavision) permits to correct image distortions, subtract the background and compute the instantaneous velocity fields.

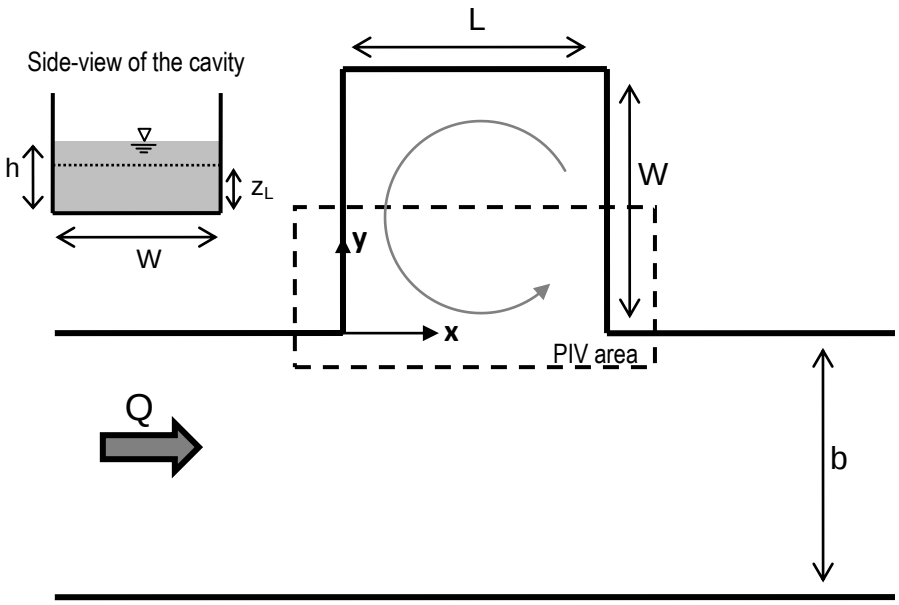

Figure IV.1: Scheme of the experimental set-up

2 STATISTICS OF THE MIXING LAYER

This section is dedicated to the complete analysis of the mixing layer which occurs at the interface between the main stream and the cavity for a reference flow configuration:
L=W=30cm, Q=3.5L/s, U_m=0.167m/s, h=7cm.

2.1 *Mean flow description*

For a square open-channel cavity, a single main horizontal recirculation cell occupies the whole available space (as shown in Chapter 2 and previously shown by Booij, 1989, Kimura and Hosoda, 1997, Mizumura and Yamasaka, 2002, Riviere et al., 2010 and Cai et al., 2014). Only two small size contra-rotative cells are observed in both outer corners at y/L=1. For the present flow, Figure IV.2 shows that the typical velocity of the recirculation cell in the cavity equals about 0.025m/s, that is 0.15U_m (as for Tuna *et al.*, 2013 for a longer cavity along y axis) with some higher and lower velocity regions distributed over the cavity (see chapter 2). Note that a region of high velocity takes place along both lateral walls of the cavity, but this velocity remains much lower than the velocity of the main stream.

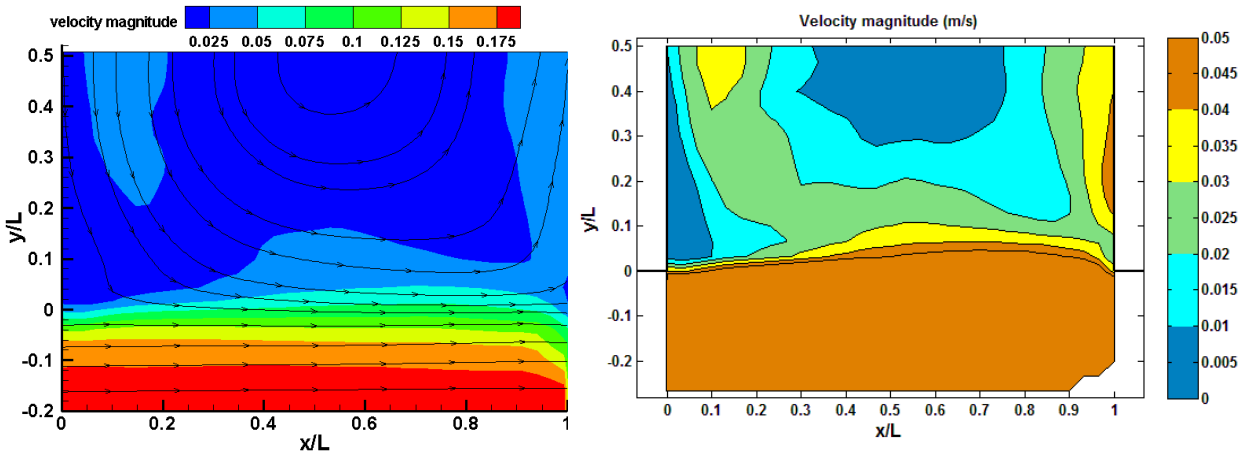

Figure IV.2: Mean velocity field in the mixing layer along with a few streamlines

Figure IV.3 confirms that the interface between the main stream and the cavity (y=0) is the region of maximum streamwise velocity gradient. The transverse profiles of mean streamwise velocity appear to be similar to most simple mixing layers (see for instance Pope, 2008) with a quite constant outer velocity in the main stream U_2 about equal to the bulk velocity (U_2~U_m) and a very limited outer velocity in the cavity U_1~0.15U_m. The shape of the transverse gradient of mean streamwise velocity between these two outer velocity regions also appears to be similar to most mixing layers with a maximum value located along the interface (y~0), slightly deflected towards the main stream (y<0) and with the region of large gradient spreading laterally and a decreasing maximum value for increasing x. This maximum ranges from more than 7.5s^{-1} near the upstream corner and about 3.5 to 4 s^{-1} near the downstream corner.

The present mixing layer exhibits strong similarities with developing self-sustained mixing-layers from which the axis of the mixing layer is geometrically constrained: in compound channels where the axis is constrained along the bank-step or over canopies where the axis is constrained along the crest.

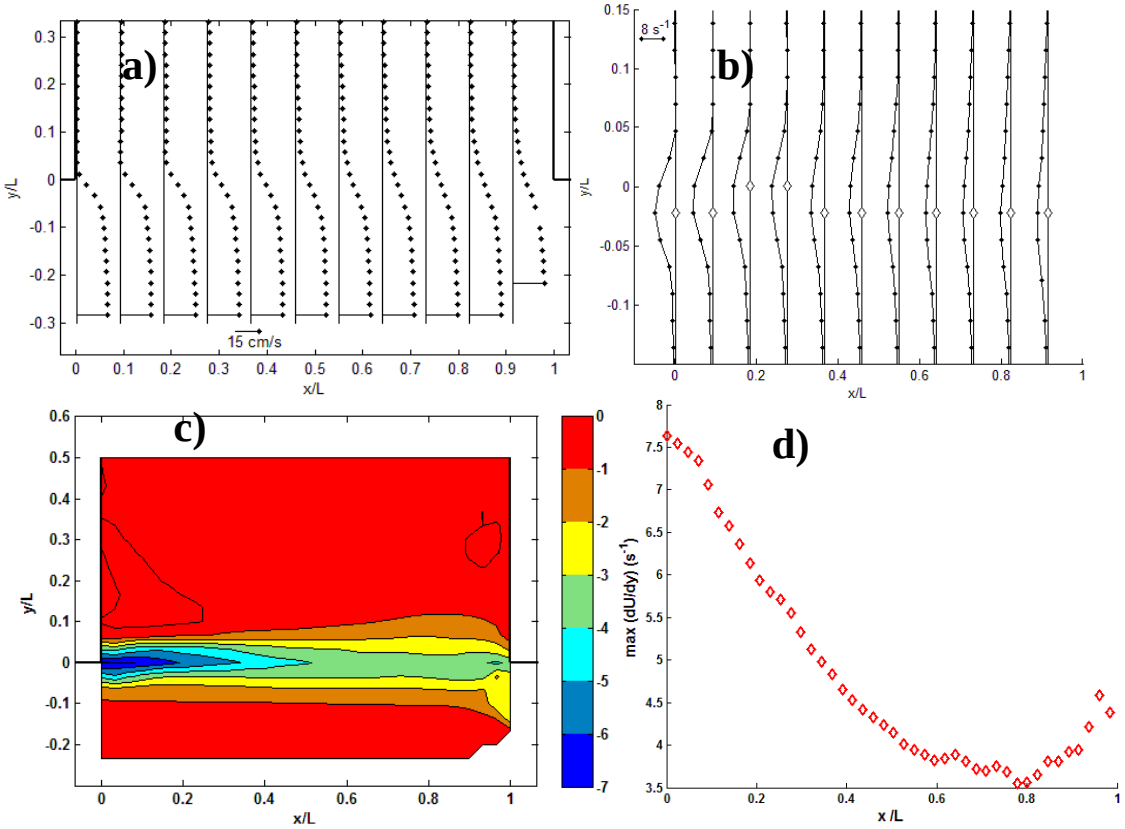

Figure IV.3: (a): Transverse profiles of mean streamwise velocity, (b) and (c): transverse gradient of mean streamwise velocity with white symbols indicating the location of maximum gradient (the spatial resolution is reduced on the right graph for better reading); (d) magnitude of the maximum transverse gradient of mean streamwise velocity.

2.2 *Width of the mixing-layer*

$U_1(x)$ and $U_2(x)$ are actually defined, for each streamwise location, as the streamwise velocity measured at the transverse location where the velocity gradient becomes negligibly small (lower than 0.05s^{-1}). The streamwise evolution of these outer velocities is given in Figure IV.4. It appears that U_2 remains quite constant, slightly larger than the main stream bulk velocity (0.1667 m/s), and that U_1 remains negligible. The velocity difference $\Delta U=U_2-U_1$ thus remains constant almost equal to U_2.

The mixing layer thickness $\delta_m(x)$ is defined as

$$\delta_m(x) = \frac{U_2(x) - U_1(x)}{\left| \partial U(x) / \partial y \right|_{max}} \quad (1)$$

and is plotted in Figure IV.4. As expected, this thickness increases from upstream to downstream. It also exhibits an interesting feature near the downstream corner ($0.8<x/L<1$, $y=0$) where δ decreases suddenly, corresponding to a sudden increase of the velocity gradient. This is connected to the motion of coherent structures around the downstream corner, which is studied in section 4. In most studied flow configurations reported in the literature, the evolution of the free mixing layer estimated width δ_e fits the following evolution curve:

$$\frac{d\delta_e}{dx} = \alpha \frac{(U_2 - U_1)}{(U_1 + U_2)/2} \quad (2)$$

with α~0.06-0.11 (see Pope, 2008) or 0.085 (see Lesieur, 1997). In the present case, considering δ_0=0.024m (according to Figure IV.4) measured at x~0m, a best fit leads to α=0.075, which in fair agreement with estimations from the literature. Figure IV.4 compares the streamwise evolution of measured (δ_m) and estimated (δ_e) mixing layer widths. Overall agreement is fair up to x/L=0.8. Moreover, Figure IV.4(c) shows the transverse profiles of non-dimensional streamwise velocities revealing that the velocity profiles are self-similar along the mixing layer.

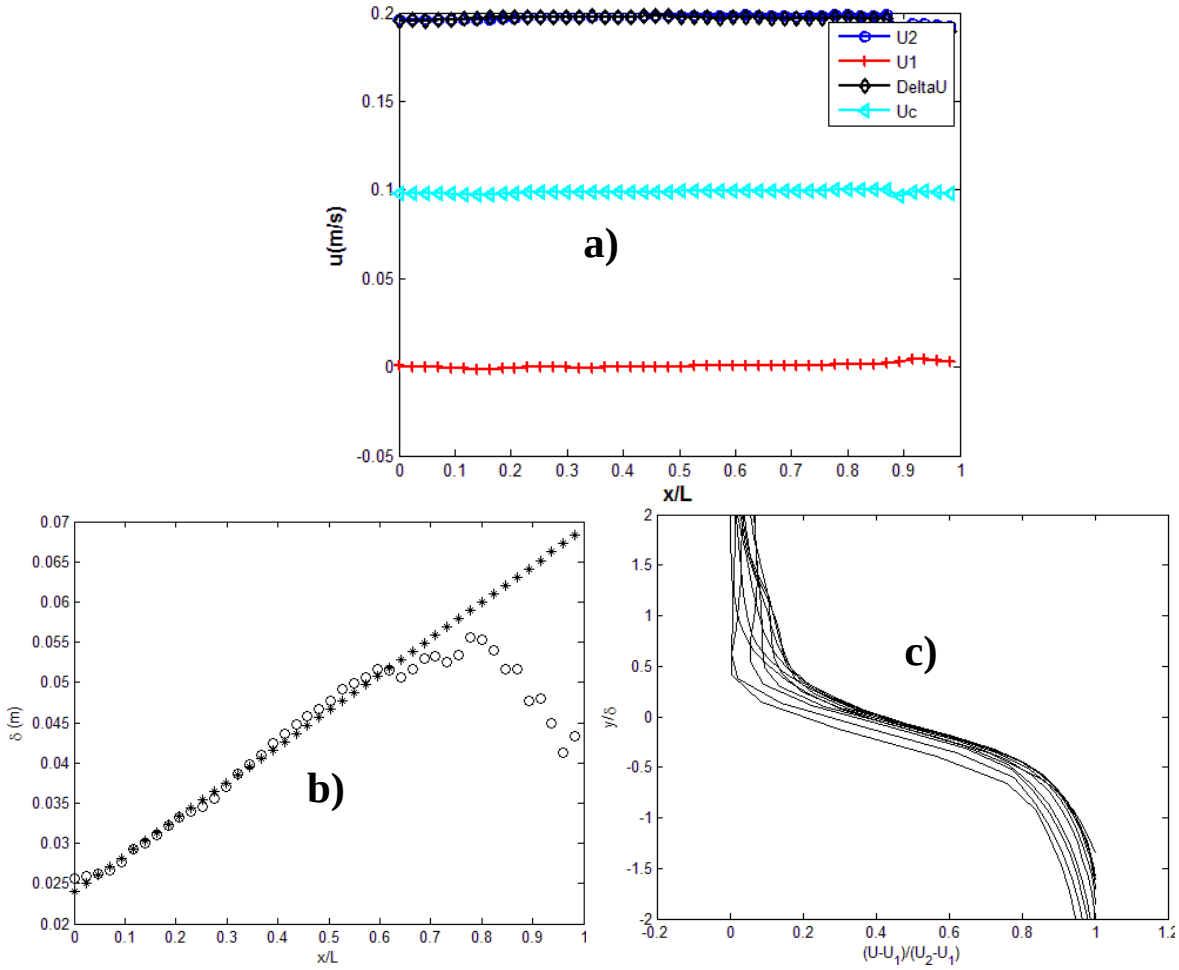

Figure IV.4: (a): streamwise evolution for the outer velocity, the velocity difference and the velocity average. (b): Streamwise evolution of the measured (o) and estimated (*) mixing-layer widths and (c) non-dimensional transverse profiles from (Figure IV.3) of streamwise velocity across the mixing layer

2.3 *Reynolds stress tensor*

Figure IV.5 shows the spatial distribution of the Reynolds shear stress in the mixing layer and the cavity. A change of sign of the intense Reynolds shear stress occurs between the cavity, where the Reynolds shear stress is positive, and the mixing layer, where it is negative.
Figure IV.5 reveals that at each selected streamwise location, the Reynolds shear stress term -<u'v'> is maximum along the centerline of the mixing layer (y~0) and rapidly vanishes on both sides at a distance equal to about δ_m except near the downstream end of the mixing layer (x/L=1) where it spreads further away as δ_m suddenly decreases (see Figure IV.4). Figure 5 also reveals that the magnitude of the maximum Reynolds shear stress increases from the upstream corner of the mixing layer (x~0) towards downstream, reaches a maxima near x/L=0.7-0.8 and decreases again towards the downstream corner.

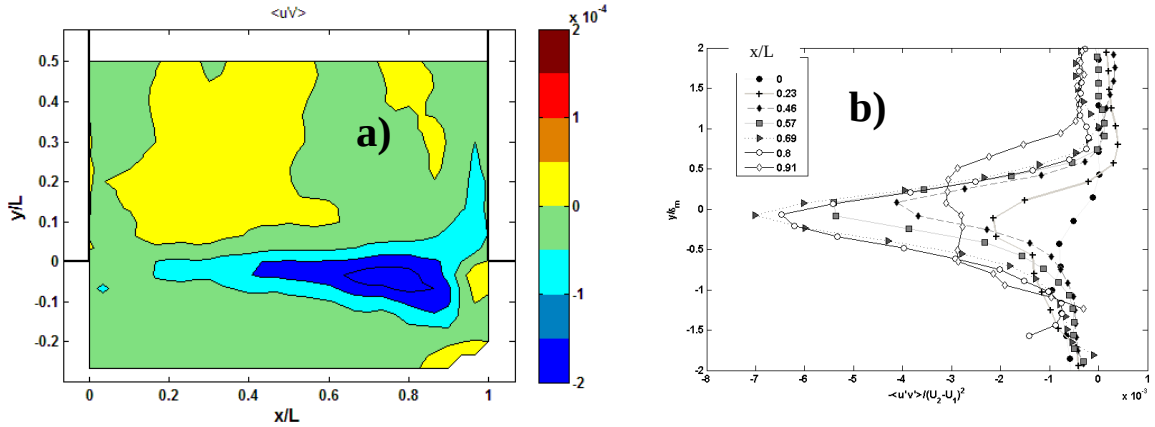

Figure IV.5:(a) spatial distribution of Reynolds shear stress and (b) Transverse profiles of dimensionless Reynolds shear stress at several streamwise locations along the mixing layer.

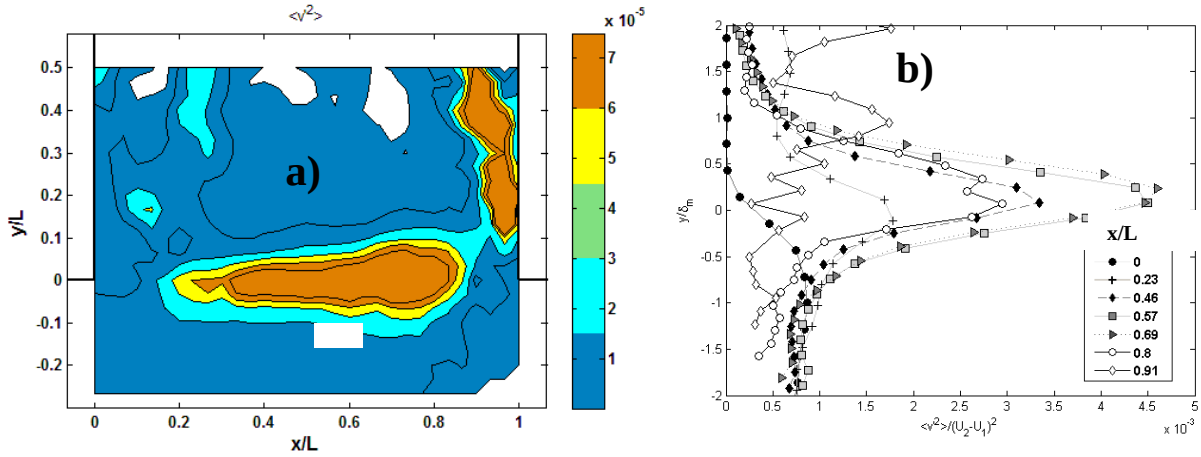

Figure IV.6:(a) spatial distribution of transverse Reynolds stress and (b) Transverse profiles of dimensionless transverse Reynolds stress at several streamwise locations along the mixing layer.

Figure IV.6(a) shows the spatial distribution of the transverse normal Reynolds stress (corrected using a Voulgaris and Throwbridge approach) in the mixing layer and the cavity. Two regions of intense transverse Reynolds stress can be observed: near the downstream wall of the cavity where the flow is oriented along the y axis and is rapid (thus with a high v velocity) and in the mixing layer.

Figure IV.6(b) reveals that at each selected streamwise location the maximum transverse normal Reynolds stress is measured along the centerline of the mixing layer (y~0) and rapidly vanishes on both sides at a distance equal to about δ_m except near the downstream end of the mixing layer (x/L=1) where it becomes complex. This last result is again connected to the coherent structures motion around the downstream corner.

2.4 *Other characteristics of the mixing-layer*

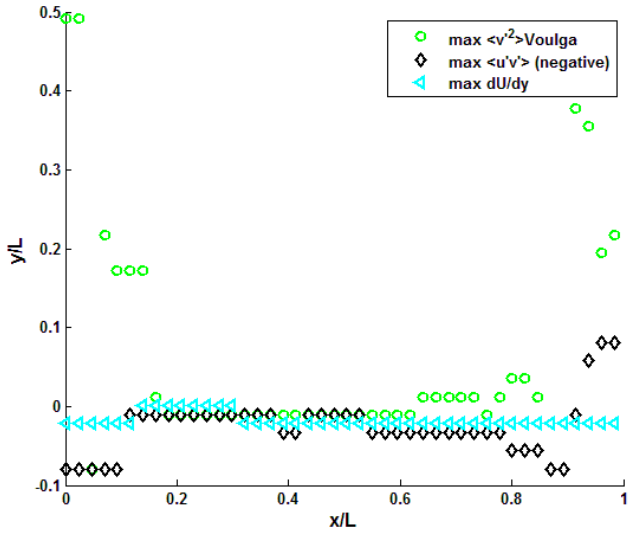

Figure IV.7: Location of the maximum transverse velocity gradient, Reynolds shear stress and transverse shear stress along the mixing layer.

Figure IV.7 reveals that away from the upstream and downstream corners of the mixing layer, the maximum magnitude of the three tested parameters: velocity gradient, Reynolds shear stress and transverse Reynolds stress is located along the mixing layer, as for most self-sustained mixing layers. Near both corners, the behavior is more complex.

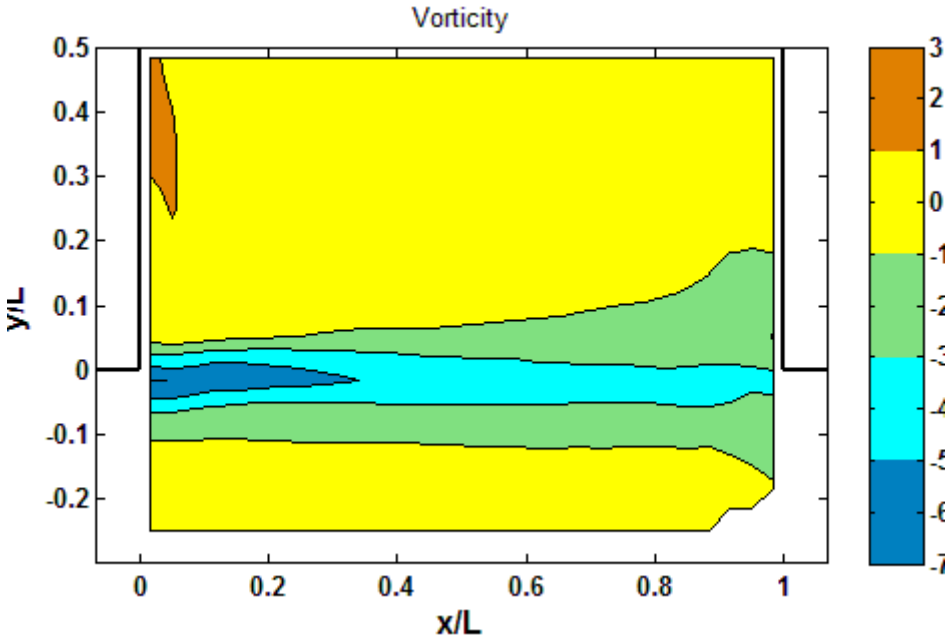

Figure IV.8:Spatial distribution of vorticity in the mixing layer and the cavity.

Figure IV.8 plots the spatial distribution of vorticity in the mixing layer and the cavity: $\frac{\partial U}{\partial y}-\frac{\partial V}{\partial x}$.

It appears that the maximum vorticity magnitude is measured along the mixing layer and rapidly vanishes on both sides; moreover, the maximum magnitude is measured near the upstream corner of the cavity and slightly decreases towards downstream.

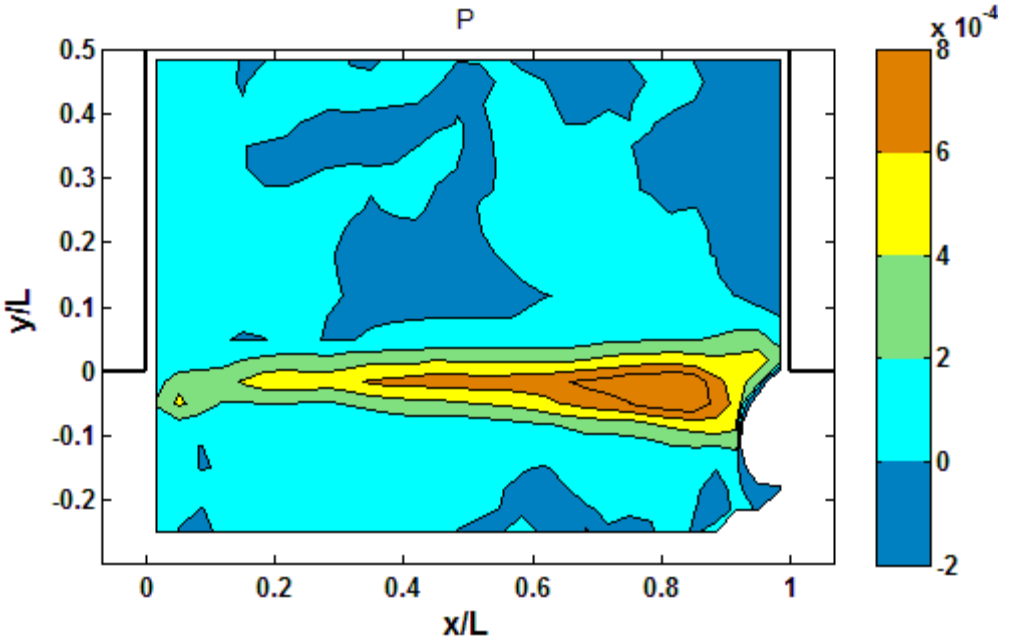

Figure IV.9. Spatial distribution of turbulence production in the mixing layer and the cavity.

The 2D turbulent production term reads:

$$P = \overline{u'^2}\frac{\partial \bar{u}}{\partial x} + \overline{v'^2}\frac{\partial \bar{v}}{\partial y} + \overline{u'v'}\frac{\partial \bar{u}}{\partial y} + \overline{u'v'}\frac{\partial \bar{v}}{\partial x} \quad (3)$$

Figure IV.9 shows its spatial distribution and reveals that the maximum magnitude is measured along the mixing layer, where both the Reynolds stresses and the velocity gradients are maximum.

To summarize, the flow at the interface between the main stream and the cavity exhibits characteristics that are typical of developing constrained mixing layers: the maximum velocity gradient and turbulent shear stress are located along the interface and decrease towards downstream. The main specificity of the present mixing layer is the sudden decrease of width and of maximum Reynolds shear stress when approaching the downstream corner, connected to the phenomena studied in next section.

3 TURBULENT STRUCTURES IN THE MIXING-LAYER

The objective of the present section is to measure the characteristics of the turbulent structures taking place in the mixing layer.

3.1 *Streamwise evolution of transverse velocity spectrum*

Firstly, the power spectral density of the transverse velocity signals is plotted for increasing streamwise axis in Figure 10. It appears that the frequency of maximum energy varies from f~0.8Hz in the upstream region (x/L<0.6) to f~0.6Hz in the downstream region where it remains constant. This behavior is in agreement with other developing mixing layers such as the one between a mean flow and a porous media, as revealed in Figure IV.9, by White and Nepf (2007). Moreover, the maximum peak is measured at x/b~0.7 where the transverse velocity fluctuation coherency is thus maximum.

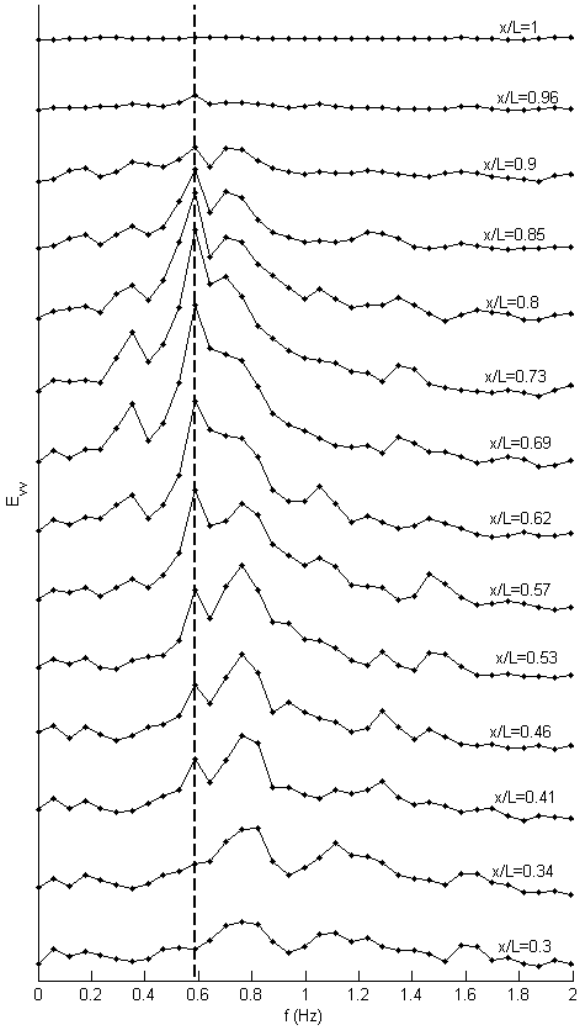

Figure IV.10: Power spectral density for $v(t)$ plotted for different streamwise locations. A similar scaling is used for all spectrum.

3.2 *Spatio-temporal transverse motion*

The so-called flapping coherent transverse velocity motion is exhibited on the graph of spatio-temporal evolution of the transverse velocity component in Figure IV.11. This figure shows the streamwise and temporal evolution of transverse velocity v (averaged over 0.133s that is over 4 consecutive values) along the mixing interface during the 10 first seconds of measurement. Positive v regions indicated in yellow/orange correspond to a flow directed along the y axis towards the cavity while negative v region in blue correspond to a flow directed towards the main stream. Note that when the time-averaged v value is negligibly small, both processes compensate each other. It appears that:

- the alternation of transverse velocity between positive and negative values gains in self-organization along the streamwise axis: for $x/L<0.5$, this alternation is somewhat disorganized and becomes more periodic (with time) further downstream, at least up to $x/L=0.9$. This self-organization when advancing along the mixing layer is in agreement with conclusions from Figure IV.10. The oscillation frequency of the transverse velocity component in the downstream half of the mixing layer ($x/L>0.5$) equals $f=0.6$ Hz, in agreement with the peak frequency of the power spectrum in Figure 10.
- the maximum magnitude of transverse velocity increases when advancing towards downstream until x/L~0.7-0.8mm, where it reaches a maximum amplitude of about ±0.025m/s, that is about

0.15U_m (about equal to the recirculation velocity in the cavity) and then decreases again towards downstream. The streamwise location of this maxima is in agreement with the maximum spectrum amplitude observed for x/L=0.7 in Figure IV.10.

This flapping (*i.e.* alternation of extremely intense positive and negative transverse velocity events) is responsible for the relatively rapid passive scalar and particulate exchanges between the main stream and the cavity (studied in next chapter).

Moreover, estimating (through standard image analysis processes) the slope of the centerline of each intense positive and negative transverse velocity contours in Figure IV.11 permits to estimate the celerity C and subsequently the wavelength λ (along x axis) of these structures of high transverse velocity magnitudes along the mixing interface. As these zones in Figure IV.11 are quite parallel to each other, the celerity is very stable. The mean celerity equals C=dx/dt=0.094m/s=0.56U_m and λ=C/f=0.16m=0.53L (with f=0.6Hz at x/L>0.5). The celerity thus exceeds the mean flow locally: C/U~1.3. Shaw *et al.* (1995) and Raupach *et al.* (1996) observed coherent structure at the crest of a vegetation canopy advected at a celerity equal to about 2 times the mean local velocity. Zhang *et al.* (1992) estimated the ratio C/U through measurements and obtained 1.6, in fair agreement with our result.

In order to identify whether both fluctuation velocities are mostly of same sign, a quadrant analysis is performed at this location (x/L=0.7 and y=0) and reveals that as v'>0, u'>0 during 71% of time (and u'<0 during the remaining 29%) while for v'<0, u'<0 during 74% of time (and u'>0 during the remaining 26%). This relatively high sign concordance confirms the negative time-averaged Reynolds shear stress -<$u'v'$> exhibited in Figure 5. Moreover, the maximum u' and v' amplitudes reported for x/L=0.7 is in agreement with the maximum Reynolds shear stress at this location in Figure IV.5.

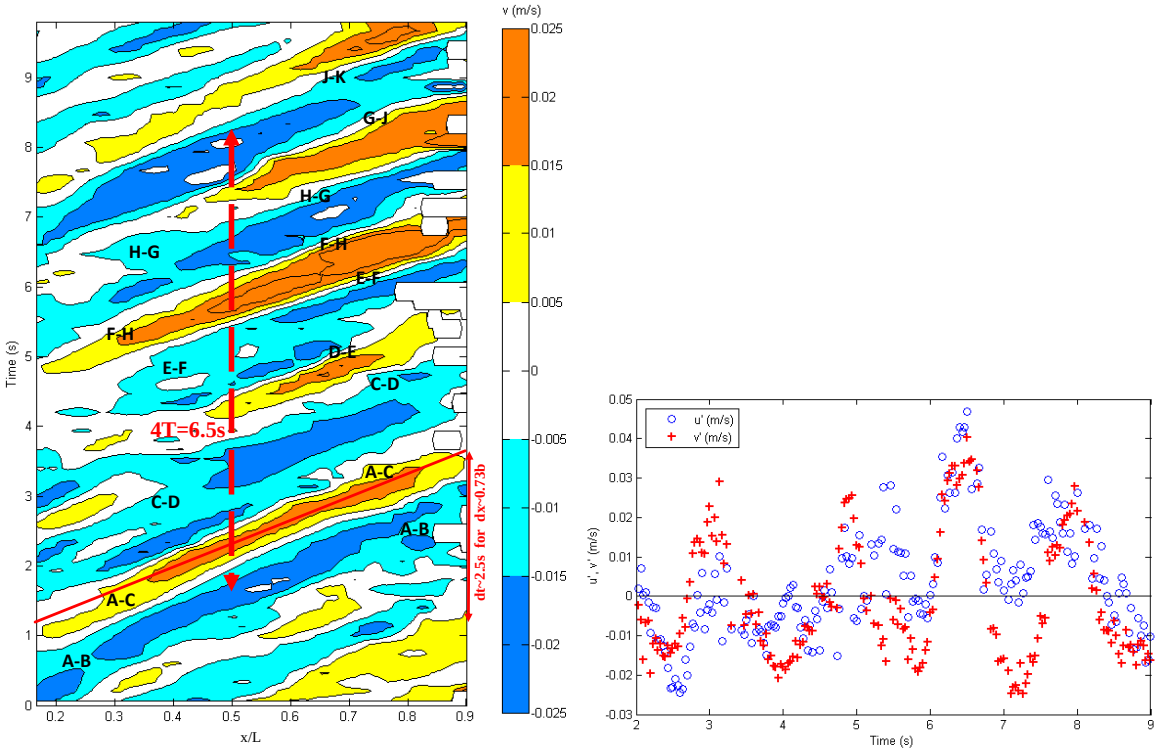

(a) **(b)**

Figure IV.11: (a) Streamwise and time evolution of the transverse velocity component along the mixing layer. The capital letters refer to the structures from Figures IV.12 and IV.15. (b) time evolution of u' and v' values at y=0 and x/L=0.7.

3.3 *Vortex identification*

Figure IV.12 presents data at 15 consecutive times including: 1) the fluctuation velocity field averaged over 4 consecutive times, reducing the sampling frequency from 30Hz to 30/4=7.5Hz and 2) clockwise (blue) and counterclockwise (red) large scale intense vortex contours. These vortex contours are obtained as follows:

- First, a POD (Proper Orthogonal Decomposition) is applied on the fluctuation velocity fields (obtained after applying a Reynolds decomposition) over 133s at the sampling frequency of 30 Hz to identify the eigenmodes (see Graftieux et al., 2001 for more details on the methodology). The 10 first eigenmodes are used to filter and reconstruct the fluctuation velocity fields through a linear combination of modes (keeping 90% of the kinetic energy and 40% of the turbulent kinetic energy).

- Second, the spatial distribution of dimensionless scalar function Γ_1 is computed over the velocity field at each time step using the methodology proposed by Graftieux et al. (2001). This function was precisely developed to "identify the location of the center of vortices on the basis of [a] velocity field". It consists, for each point of the grid, of integrating over a surrounding area the sine of the angle between the local velocity vector and each other velocity vector in the area. $|\Gamma_1|$ is bounded by 1. In the present case, a circle of radius equal to 30mm is used as surrounding integration area (about the size of the turbulent structures along the mixing layer in Figures IV.12).

- Third, a threshold of $|\Gamma_1|=0.55$ is selected for the detection of the energetic vortices. Contours of counter-clockwise (with red color referring to $\Gamma_1>0.55$) and clockwise (with blue color referring to $\Gamma_1<-0.55$) vortices are plotted on the figures. The vortices observed over the 8 first seconds are individually indicated by a letter between A and H which permits to analyze their trajectory along the mixing layer.

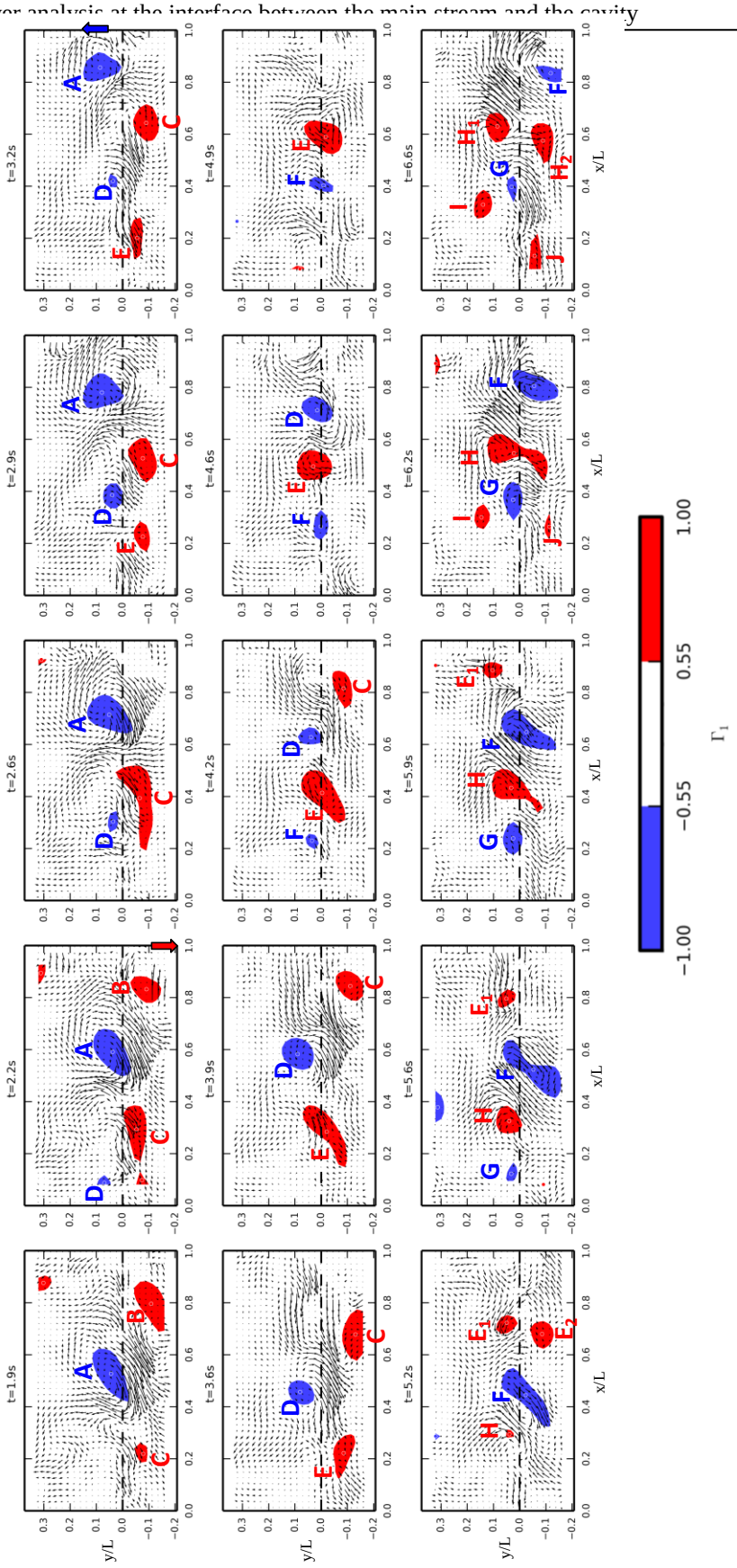

Figure IV.12: Time evolution every 1/3s of fluctuation velocity field (black arrows) averaged over 4 consecutive times (4/30s) and contours of clockwise (blue color, Γ_1<-0.55) and counter-clockwise (red color, Γ_1>0.55) coherent vortices obtained through POD with the white circle corresponding to the vortex core, that is the maximum local $|\Gamma_1|$. The dashed line represents the mixing interface (y=0)

Figure IV.12 shows three main vortex configurations:

- Configuration noted "A", for which a clockwise (blue) vortex is located on the cavity side (y>0) and the consecutive counter-clockwise (red) vortex is on the main stream side (y<0), takes place from time t=2.2s to t=4.2s. In such configuration, two intense transverse velocity regions take place along the interface (y=0):
i) region A1 upstream from the clockwise vortices with v'>0 and u'~0 as upstream from vortex A at x/L=0.7 at t=2.9-3.2s (see also Fig.11a).
ii) region A2 downstream from the clockwise vortices with v'<0 and u'<0, as downstream from vortex A at x/b=0.7 and t=2.2-2.6s (see also Fig.11a).

- Configuration noted "B", for which a clockwise (blue) vortex is located on the main stream side (y<0) and the consecutive counter-clockwise (red) vortex is on the cavity side (y>0), takes place from time t=5.9s to t=6.6s. The opposite from configuration A takes place along the interface with two regions:
i) region B1 upstream from the clockwise vortices with v'>0 and u'>0 as upstream from vortex F at x/b=0.7 and t=6.2-6.6s (see also Figure.11a).
ii) region B2 downstream from the clockwise vortices with v'<0 and u'~0 as downstream from vortex F at x/b=0.7 and t=5.9s (see also Figure.11a).

- Configuration noted "C", for which all vortex cores are located near the interface (y~0), takes place between vortices F-E-D at time t=4.6-4.9s and between vortices G-H-F at time t=5.2-5.6s. In such configuration, v' oscillates between positive and negative value depending on the location with regards to the vortices of both signs and u' exhibits a complex pattern (as at x/L=0.7 at times 4.9-5.6s (see also Figure IV.11a).

The location of the vortices cores with regards to the interface thus permits to explain the behavior of the transverse and streamwise fluctuation velocity components obtained in Figure 11b where both fluctuation velocity components u' and v' are sometimes together strongly positive or negative and sometimes v' is strongly positive or negative while absolute value of u' remains very small.

Consequently, positive and negative v periods alternate and this alternation is not affected by the change of configuration between A, B and C. This explains the coherent v alteration frequency in Figure 6 and the fact that u' alternation is less coherent. Moreover, this confirms that u' and v' are most of the time (but not at all time) of same sign leading to two dominant motions: u' and v' positive (with the flow entering the cavity), named "ejection" by Sanjou and Nezu (2013) and u' and v' negative (with the flow leaving the cavity towards the main stream), named "sweep" by these authors.

Figure IV.12 also reveals that:
- some vortices such as H tend to separate into two cells located on either side of the interface.
- as the coherent vortices reach the downstream corner (x/L=1), they either leave towards the cavity (y>0) or towards the main stream (y<0), mostly depending on their location (with regards to the interface) before reaching the downstream corner. For instance, A and H_1 located at y>0 finish up within the cavity while B, C, F, H_2 located at y<0 finish up in the main stream.

3.4 *Vortex center statistics*

In a forward analysis, the location of the center of the vortices is defined as the location with maximum $|\Gamma_1|$. Figures IV.13- IV.14 then show trajectories and statistics regarding the trajectories of these centers of vortices.

Figure IV.13 shows the evolution with time (for the 9 first seconds of measurement) of the streamwise abscise (x) of the vortex centers located near the interface ($|y|$<50mm). All curves appear to be quite straight, confirming the quite constant streamwise advection celerity reported before. The period defined as typical time between two cells of same rotation sign passing at the same abscise equals 1.62s (f=0.61Hz) as already observed in Figures IV.10 and IV.11.

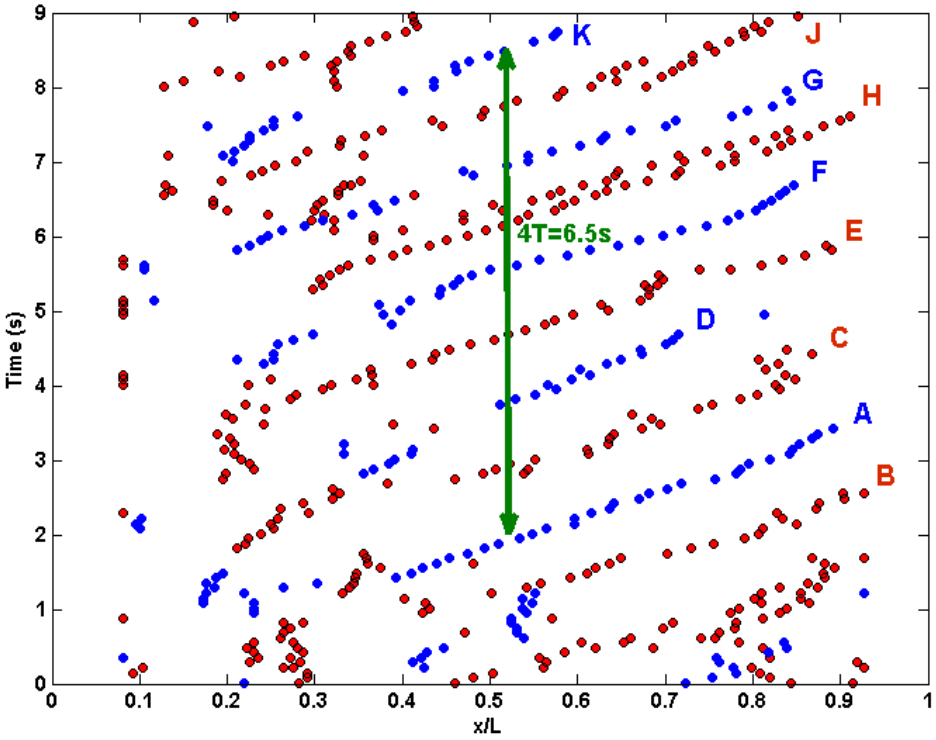

Figure IV.13: Time-evolution of the streamwise location of the clockwise (blue) and counter-clockwise (red) vortex centers located near the interface (with $|y|$<50mm). Red arrow corresponds to four periods and equals 6.5s.

Figure IV.14 shows the location of the vortex centers recorded during about 100s of measurement (that is 1500 frames). It appears that:
- in the upstream region (x/L<0.3), most vortex centers are located within the cavity at y/L>0.1 (as L or M in Figure 11) or near the interface (as most vortices in Figure 8). Further downstream (0.3<x/L<0.7), the vortices are mostly located near the interface and this region spreads from y/L=0 to 0.1 near x/L=0.4 to y/L=-0.1 to 0.1 at x/L=0.6.
- in the downstream region (x/L>0.65), the vortices either move towards the cavity (y>0) or towards the main stream (y<0) and two maximum probability regions are then observed in Figure 14 for y/L~-0.1 and +0.1. This separation between cells ending up in the dead-zone or in the main stream is in agreement with data from Weitbrecht *et al.* (2008) for the flow between two groins.
- the statistics of spatial location do not reveal major differences between the clockwise and contra-clockwise rotating vortices (see Figure IV.14).

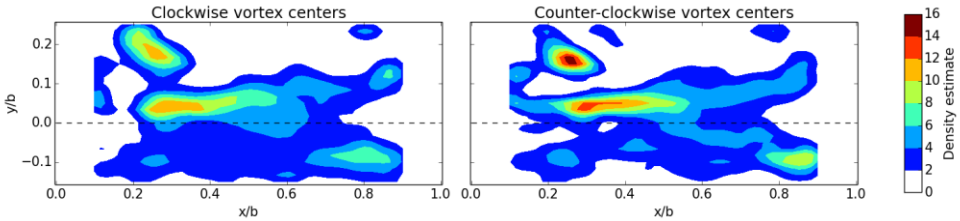

Figure IV.14: Statistics of spatial location of both types of vortex centers.

Consequently, regarding the origin of the vortices observed in the mixing layer, two cases are observed:

- Most vortices appear in the upstream part of the mixing layer itself (x/b~0-0.3 and $|y/b|$<0.1) such as vortices A to K in Figure IV.12.
- A few vortices, such as L (clockwise) and M (counter-clockwise) in Figure 15 already exist in the cavity (y/L>0.15 at 0.2<x/L<0.3) but they are quite rare (only 2 vortices of each rotation sign were clearly identified over 100s, that is over about 61 periods). These vortices are stretched and separate as: (i) a large scale vortex (L or M in Figure IV.15) is located in the cavity near x/L~0.16 – y/L~0.2, (ii) this vortex stretches in an oblique direction towards positive x and negative y direction, (IV) the vortex separates in two sub-vortices, one (L1 & M1) staying at the initial location and the second one (L2 & M2) being advected within the mixing layer where it becomes equivalent to the other vortices.

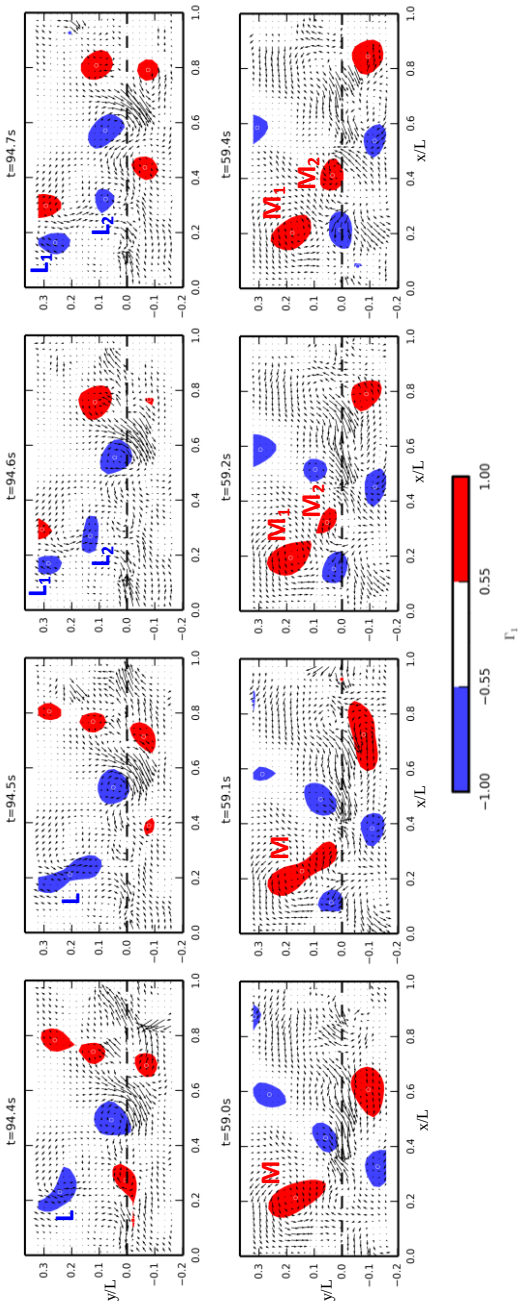

Figure IV.15: Same as Figure IV.12 for other times and other frequency exhibiting vortices L and M originating from the cavity and ending-up in the mixing-layer.

To conclude, the present section aimed at investigating the dynamics and organization of the coherent vortices and intense transverse motions in the mixing-layer at the interface between a main stream and a lateral cavity. They are indeed responsible for most processes regarding exchanges (of momentum, passive scalar, sediments…) between the two regions and are also responsible for the seiching processes in the cavity. Present data revealed that:

- the mixing layer is similar to most constrained mixing-layer for which the centerline is defined by the geometry (by the two corners in the present case).
- The organization of the mixing layer can be simplified as an alternation of: 1) a clockwise (blue) rotation vortex followed by 2) an intense transverse motion from the main stream towards the cavity, 3) a counter-clockwise rotation vortex (red) and 4) an intense transverse motion from the cavity towards the main stream. Note, however, that vortices are not located along the centerline of the mixing layer but are either slightly below (y<0) or above (y>0) this centerline.
- the mixing layer tends to gain in self-organization from up-to downstream along the mixing-layer: (1) the periodicity of the transverse velocity motion and vortices alternations and (2) the transverse velocity magnitude increase in the downstream part of the mixing layer and decrease again near the downstream corner.
- most vortices originate from the upstream region of the mixing layer but a few of them come from the cavity itself. They all end up either in the cavity or in the main stream. No major difference of location statistics is reported between the clockwise and contra-clockwise rotating vortices. This jection of vortices from the mixing layer, due to the downstream corner, explains the drastic decrease of the velocity gradient observed in figure IV.3.

4 IMPACT OF THE FLOW AND GEOMETRY PARAMETERS ON THE CHARACTERISTICS OF THE MIXING LAYER

In the previous sections, one flow configuration associated with one cavity geometry was analyzed in details. Later on, we observed that changing the characteristics of the main stream and of the geometry only slightly modifies these characteristics; the present section aims at investigating and reporting these changes. The flow is described by its geometry: cavity length L and width W, flow depth h, flow velocity U_m, gravity g, fluid properties *i.e.* density ρ and dynamic viscosity μ. Dimensional analysis indicates that the flow is described by 4 dimensionless parameters:

- the cavity aspect ratio : W/L
- the relative water depth : h/L
- the (upstream flow) Reynolds number $Re=4\rho U_m R_h/\mu$ with $R_h=Lh/(2h+L)$ the hydraulic radius
- the (upstream flow) Froude number : $Fr=U_m/(gh)^{1/2}$

In order to investigate the influence of these parameters, 4 series of flow configuration are tested and presented in Table 1. In these series, the flow parameters are chosen so that Fr is always smaller than 0.3 (namely 0.23) and should not influence the flow. The flow behavior is finally only connected to the triplet (W/L, h/L, Re).

It appears (not shown here) that for cavities of aspect ratios larger or equal to W/L=1, the behavior of the mixing layer changes very little from one configuration to the other. Indeed, in all cases:

- the streamwise velocity in the cavity is much smaller than in the main stream,
- the recirculation pattern in the first cell of the cavity is always similar: it occupies the whole length L of the cavity (see chapter II).
- the centerline of the mixing layer lies along the x axis (between both corners of the cavity).

Oppositely, for very thin cavities (W/L<0.6), the occurrence of two cells aligned along the x axis in the cavity (as shown in Chapter II) should dramatically change the mixing layer behavior, but this aspect is out of scope of the present work.

Thus the present analysis is mainly dedicated to investigate the limited differences between the mixing-layers detailed in Table1, with $W/L \geq 1$. For each flow configuration from Table 1, the following characteristics are plotted and discussed:

- the characteristics of the velocity profiles (section 4.1)
- the width of the mixing layer (section 4.2)
- the peak frequency in the transverse velocity spectrum (section 4.3)
- the vortex celerity (section 4.4)
- the wave length in the mixing layer (section 4.5)

Table IV.1: Flow and geometry characteristics, corresponding values of the dimensionless parameters z_{meas} the altitude at which the velocity profile is measured using the 2D PIV.

	$W(m)$	$L(m)$	$h(cm)$	$U_m(m/s)$	W/L	h/L	Re	Fr	z_{meas}/h
Series 1	0.3	0.3	7	0.167	1	0.23	9.71E+04	0.20	0.71
	0.6	0.3	7	0.167	2	0.23	9.71E+04	0.20	0.71
	0.9	0.3	7	0.167	3	0.23	9.71E+04	0.20	0.71
	1.2	0.3	7	0.167	4	0.23	9.71E+04	0.20	0.71
	1.5	0.3	7	0.167	5	0.23	9.71E+04	0.20	0.71
Series 2	0.3	0.3	7	0.119	1	0.23	6.98E+04	0.14	0.71
	0.6	0.3	7	0.119	2	0.23	6.98E+04	0.14	0.71
	0.9	0.3	7	0.119	3	0.23	6.98E+04	0.14	0.71
	1.2	0.3	7	0.119	4	0.23	6.98E+04	0.14	0.71
	1.5	0.3	7	0.119	5	0.23	6.98E+04	0.14	0.71
Series 3	0.3	0.3	7	0.048	1	0.23	2.77E+04	0.06	0.71
	0.3	0.3	7	0.060	1	0.23	3.46E+04	0.07	0.71
	0.3	0.3	7	0.071	1	0.23	4.14E+04	0.09	0.71
	0.3	0.3	7	0.083	1	0.23	4.84E+04	0.10	0.71
	0.3	0.3	7	0.095	1	0.23	5.53E+04	0.11	0.71
	0.3	0.3	7	0.107	1	0.23	6.23E+04	0.13	0.71
	0.3	0.3	7	0.119	1	0.23	6.92E+04	0.14	0.71
	0.3	0.3	7	0.131	1	0.23	7.62E+04	0.16	0.71
	0.3	0.3	7	0.143	1	0.23	8.31E+04	0.17	0.71
	0.3	0.3	7	0.155	1	0.23	9E+04	0.19	0.71
	0.3	0.3	7	0.167	1	0.23	9.7E+04	0.20	0.71
	0.3	0.3	7	0.179	1	0.23	10.4E+04	0.22	0.71
	0.3	0.3	7	0.190	1	0.23	11.1E+04	0.23	0.71
Series 4	0.3	0.3	3	0.119	1	0.10	67350	0.22	0.71
	0.3	0.3	4	0.119	1	0.13	68170	0.19	0.71
	0.3	0.3	5	0.119	1	0.17	68660	0.17	0.71
	0.3	0.3	6	0.119	1	0.20	69000	0.16	0.71
	0.3	0.3	7	0.119	1	0.23	69240	0.14	0.71
	0.3	0.3	8	0.119	1	0.27	69420	0.13	0.71
	0.3	0.3	9	0.119	1	0.30	69560	0.13	0.71
	0.3	0.3	10	0.119	1	0.33	69680	0.12	0.71
	0.3	0.3	11	0.119	1	0.37	69770	0.11	0.71
	0.3	0.3	12	0.119	1	0.40	69850	0.11	0.71
	0.3	0.3	13	0.119	1	0.43	69910	0.11	0.71
	0.3	0.3	14	0.119	1	0.47	69970	0.10	0.71

4.1 *Impact on the mean velocity field*

Figure IV.16 shows the mean velocity profiles across the mixing layer for series 3 and 4 and reveals

that all profiles are very much alike with a maximum velocity in the main stream and a negligible velocity in the cavity. A tendency appears on Figure IV.16 as a function of Re and *h*/*L* but no conclusion can be easily sorted.

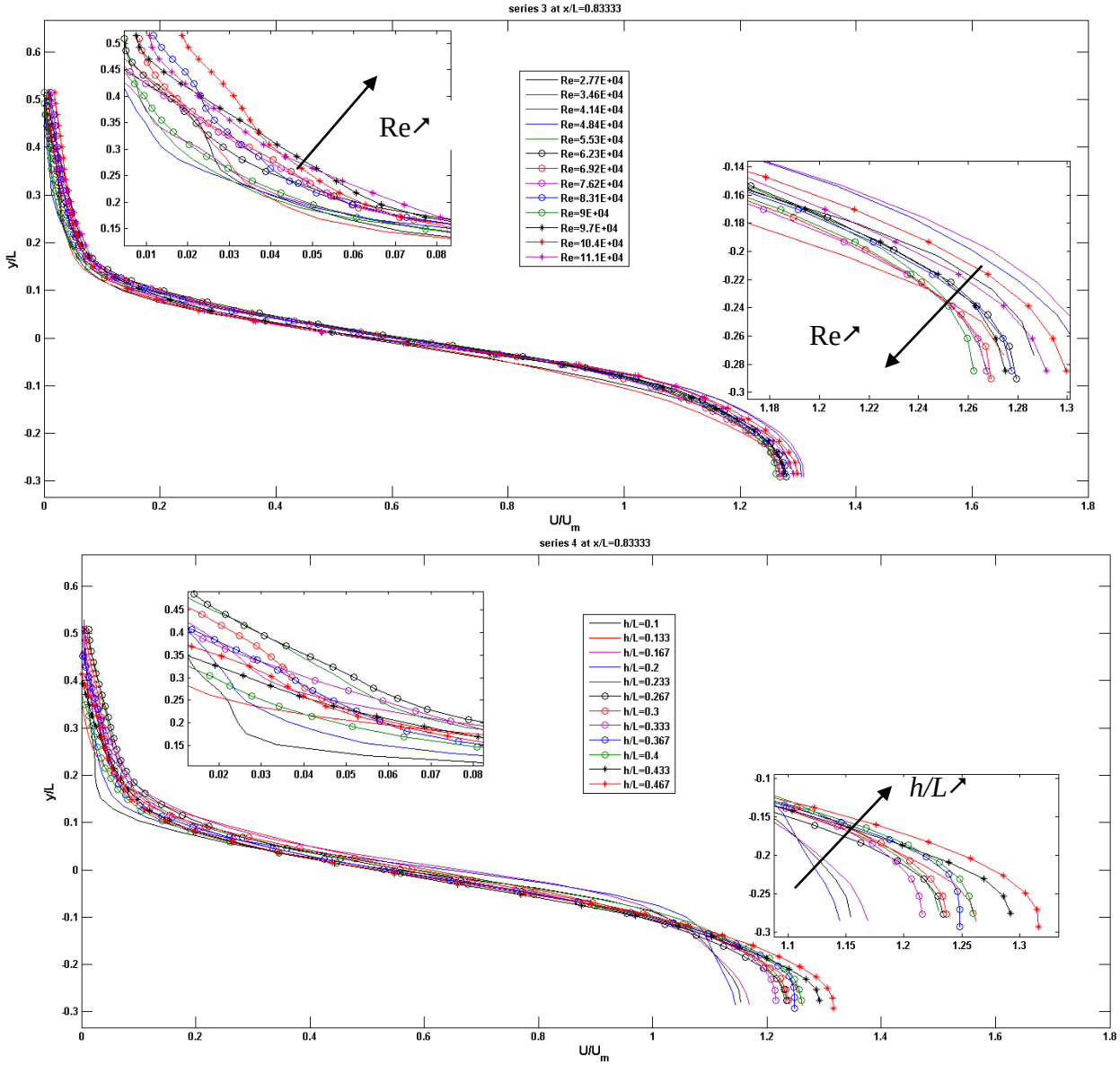

Figure IV.16. Mean velocity profiles U/U_m along the transverse direction at x/L=0.83 for series 3 and 4.

We now define herein the outer velocity ratio r as $r(x)=U_1(x)/U_2(x)$ with U_1 and U_2 defined in section 3.2. This parameter is of major importance as it represents the outer velocity gradient that is the forcing of the mixing layer. This ratio is estimated at two streamwise positions along the mixing layer: x/L=0.33 and x/L=0.83. In the following figures, we start by plotting U_1/U_m, then U_2/U_m and finally $r=U_1/U_2$.

- Series 1 and 2: in case of W/L changing for series 1 and 2, U_2/U_m remains constant as the main stream is not changed, but U_1/U_m increases as W/L increases (Figure IV.17). As a consequence, r also increases.

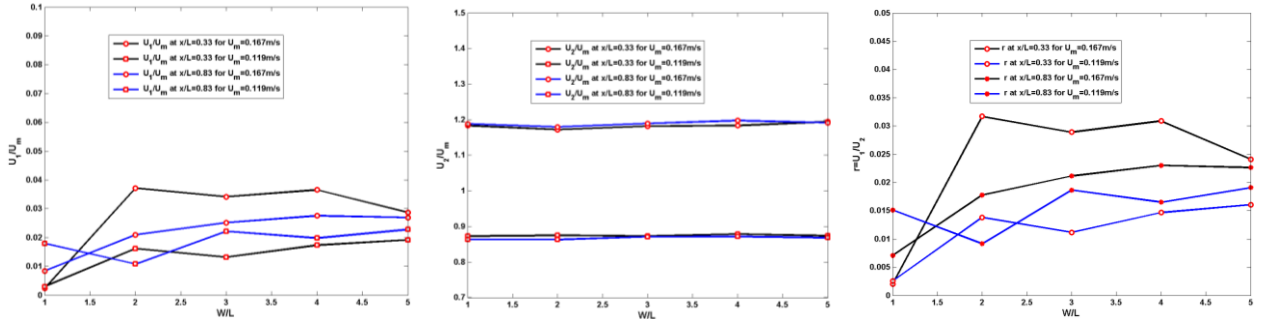

Figure IV.17: Outer velocities U_1/U_m, U_2/U_m and ratio $r(x)$ for all configurations from series 1 and 2 for x/L=0.33 and x/L=0.83 as a function of W/L.

- Series 3: in case of U_m changing for series 3, it appears U_2/U_m is hardly affected, while U_1/U_m decreases gradually with U_m or Re. This indicates a decreasing ratio for r as a function of Re.

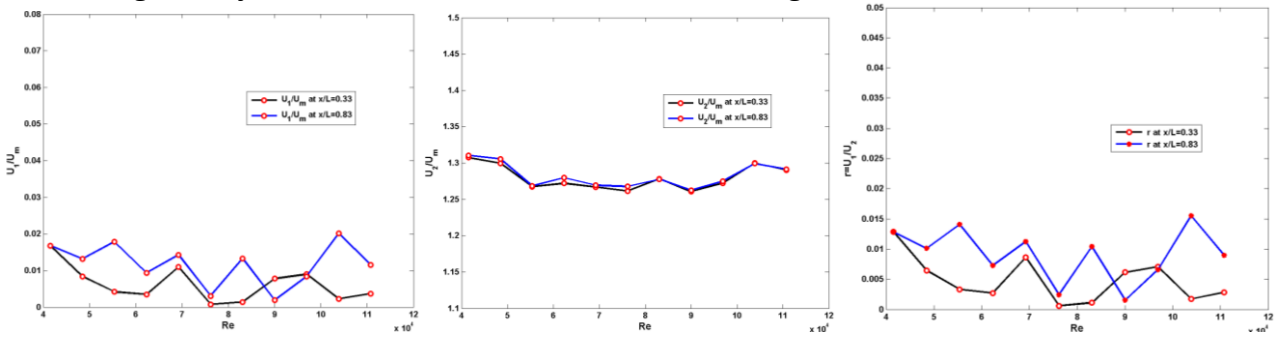

Figure IV.18: Outer velocities U_1/U_m, U_2/U_m and ratio $r(x)$ for all configurations from series 3 (as a function of Re) for x/L=0.33 and x/L=0.83.

- Series 4: in case of h/L changing for series 4, Figure IV.19 shows that U_1/U_m remains quite constant while U_2/U_m increases with an increasing h/L which means a complex and unpredictable trend for r.

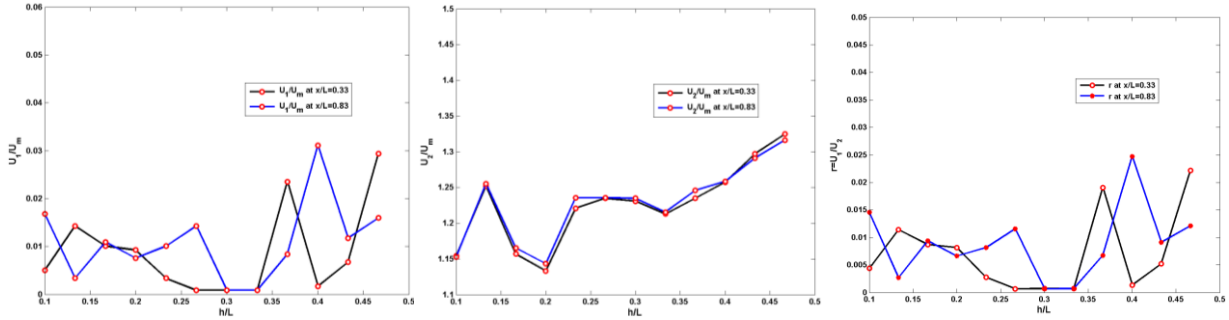

Figure IV.19: Outer velocities U_1/U_m, U_2/U_m and ratio $r(x)$ for all configurations from series 4 for x/L=0.33 and x/L=0.83.

In conclusion, it appears that modifying the flow and geometrical parameters hardly modify the outer velocities . As the velocity inside the cavity remains stable, the estimation of the outer velocities is not so simple: the inaccuracy on the estimation of U_1 is probably responsible of the variations observed. No clear influence of the parameter can be seen.

4.2 *Impact on the width of the mixing layer $\delta(x)$*

Figure IV.20 shows the mixing layer width streamwise profiles for series 3 and 4 and reveals that all profiles are very much alike with a linear trend in the region x/L=0.1 to x/L=0.8 and that the corresponding slope decreases as Re increases or as h/L decreases.

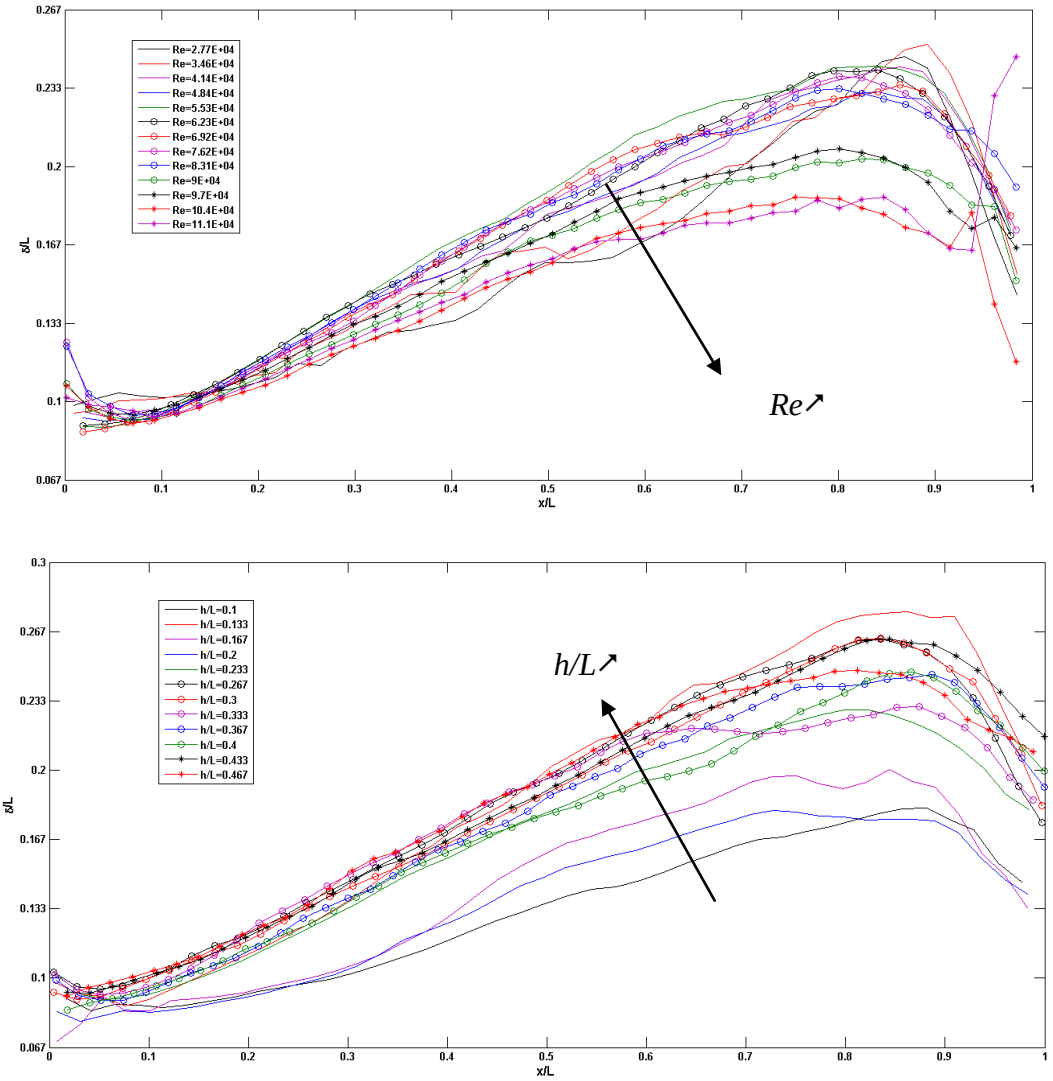

Figure IV.20: the mixing layer width δ(x) along the transverse direction for series 3 and 4.

In order to investigate the effect of the flow and geometrical parameters on the mixing layer width, we define the parameter P_{fit} as the slope of the linear fit of the measured mixing-layer along the mixing layer, in the region x/L=0.17 to x/L=0.83, that is the slope of the red line in Figure IV.21 (analogous to Figure IV.4c). The equation for the red line thus writes:

$$\delta = P_{fit} x + \delta_0 \tag{3}$$

where δ_0 is the extrapolated mixing layer width at the upstream corner of the cavity x=0.

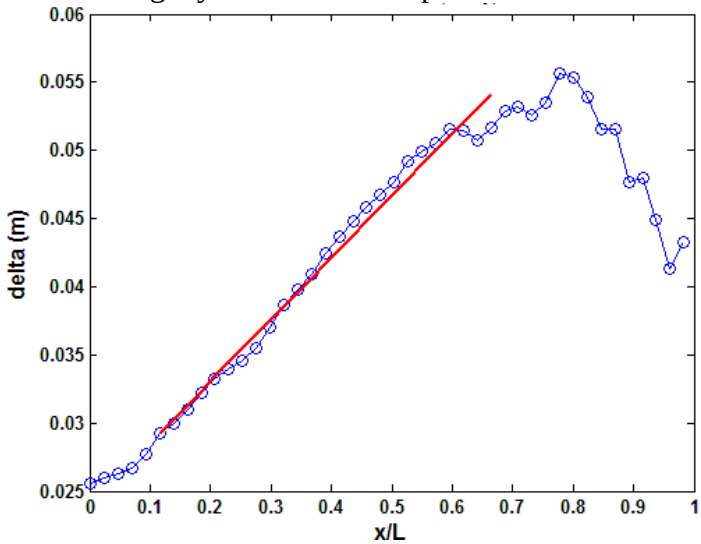

Figure IV.21: Fit of the linear growth of the mixing layer width.

On the other hand, considering the theoretical growth rate equation given in section 3.2 (of the present Part 1), we define α_{fit} as

$$\frac{d\delta}{dx} = \alpha_{fit}\frac{\Delta U(x)}{U_c(x)} = 2\alpha_{fit}\frac{U_2(x)-U_1(x)}{U_2(x)+U_1(x)} = 2\alpha_{fit}\frac{1-r(x)}{1+r(x)} = P_{fit} \qquad (4)$$

As proposed by Pope(2000), ranges from α_{min}=0.06 to α_{max}=0.11. Lesieur(1997) found that α=0.09 applies to most cases. α_{fit} is thus computed from $r(x)$ for our measurements at x/L=0.33 and 0.83 as plotted in section 5.2. We can thus compare α_{fit} with Pope(2000) values for the 4 series:

- Series 1 and 2: in case of W/L changing for series 1 and 2, α_{fit} doesn't changes much, The agreement is quite fair with Lesieur(1997) and Pope(2000) values.

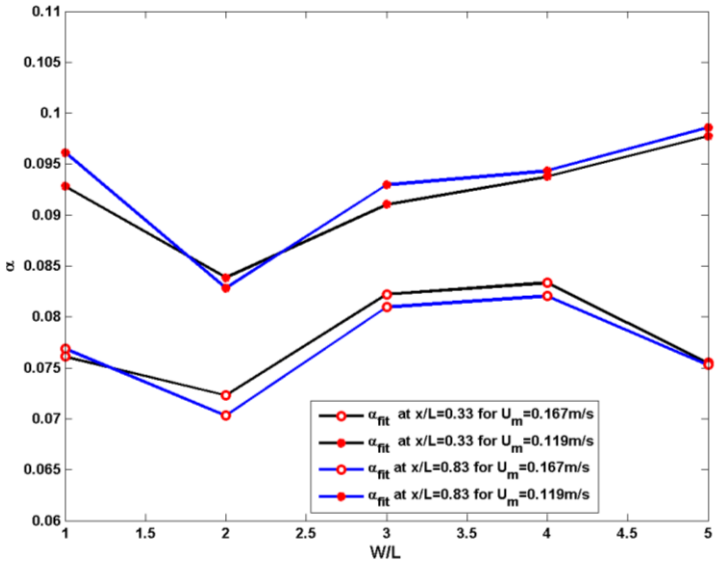

Figure IV.22: Fitted linear growth rate of the mixing layer width for all configurations from series 1 and 2 at x/L=0.33 and 0.83.

- Series 3: in case of U_m changing for series 3, as U_m (and Re) increase, α_{fit} remains between 0.06 and 0.11. In addition , α_{fit} decreases for the highest Reynolds values. This tendency may be related to an increased friction (Figure IV.23) ,as observed for instance by Han (2015).

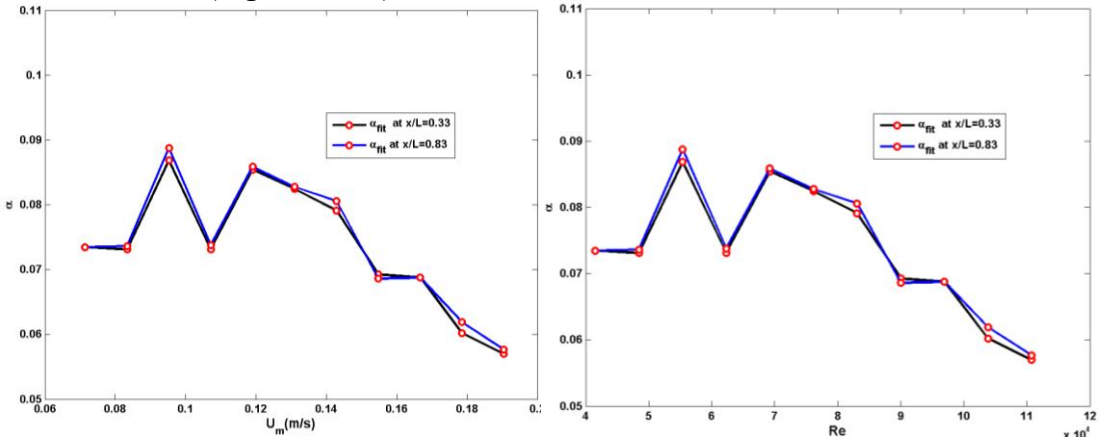

Figure IV.23: Fitted linear growth rate of the mixing layer width for all configurations from series 3 at x/L=0.33 and 0.83.

- Series 4: as h/L changes in Figure IV.24, α_{fit} changes very much but with no clear tendency, and reaches a maximum value of 0.15, and more than a half of fitted data are beyond 0.11.In this case, the fitted data is different from Pope(2000) or Lesieur(1997) proposed values. In such case, α

should no longer be considered as constant but should be a function of the friction parameter as proposed by Chu and Babarutsi (1988).

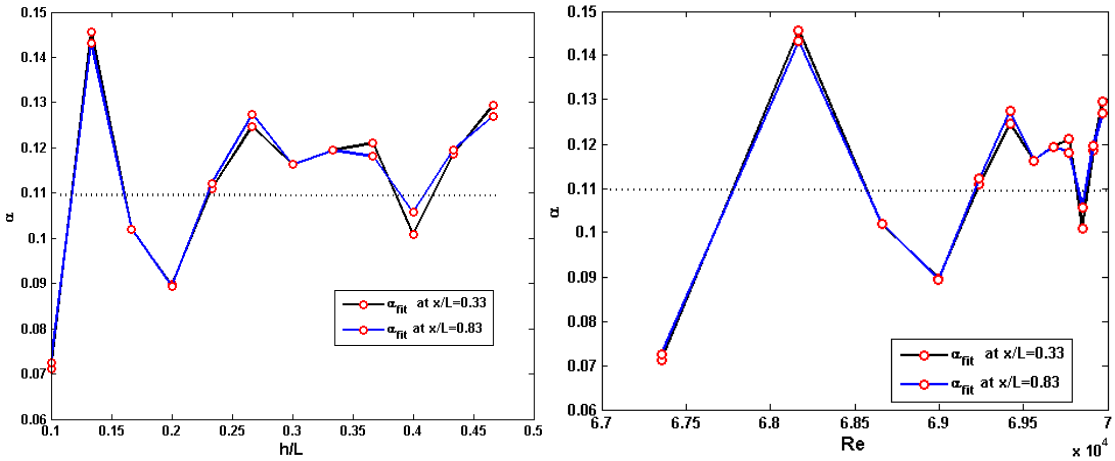

Figure IV.24: Fitted linear growth rate of the mixing layer width for all configurations from series 4 at x/L=0.33 and 0.83.

The error bars associated to the estimation of α is not established due to a lack of time: The criss-cross aspect of the curves provides an estimate. It thus can be concluded that *W/L* and *Re* hardly affect the growth rate of the mixing layer . The influence of *h/L* seems more pronounced.

4.3 *Impact on the peak frequency of the transverse velocity spectrum*

We showed that the peak frequency of the transverse velocity spectrum in Figure IV.10 equals the peak frequency f_{max} of the vortex shedding in Figure IV.13. In Figure IV.10, this peak frequency evolves along the mixing interface from x/L=0 to x/L~0.6 and for x/L>0.6 this peak frequency does not change until x/L~0.9. The aim of the present section is to evaluate the impact of the main stream and cavity parameters in Table 1 on the peak frequency measured in the downstream portion of the mixing-layer (y=0, x/L=0.83), where the mixing layer is assumed to be organized and the peak frequency does not vary along the streamwise direction.

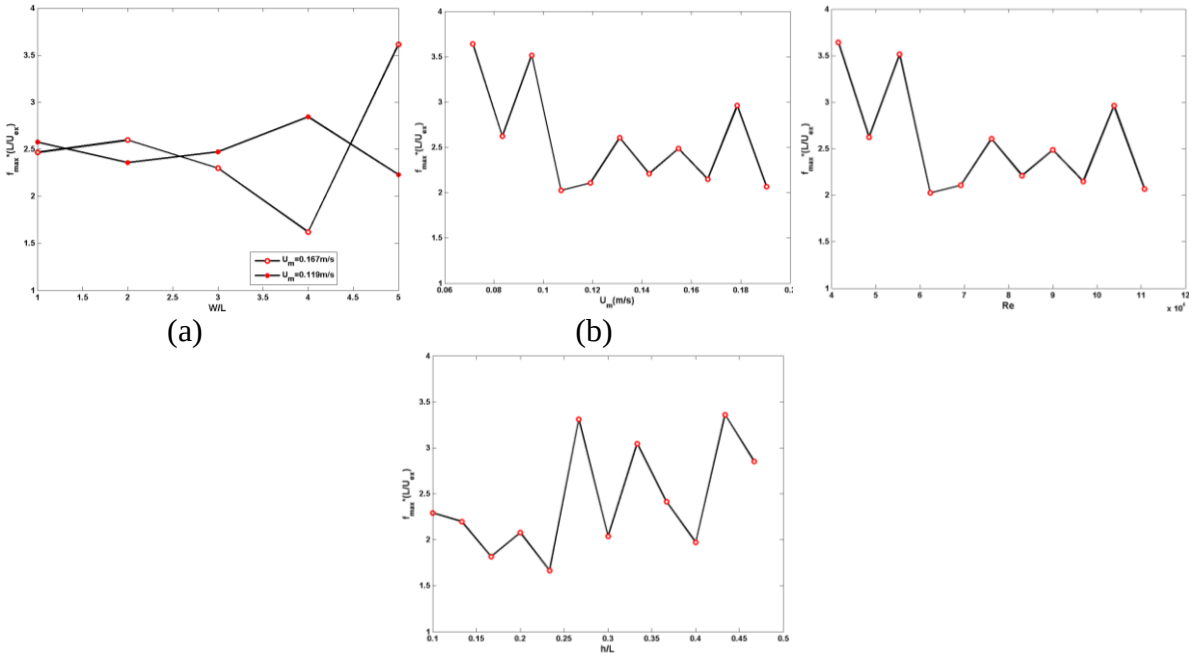

(a) (b)

(c)

Figure IV.25:Evolution of the peak frequency normalized by L and U_m as a function of:(a) the aspect ratio of the cavity (W/L) for series 1 (U_m=0.167m/s) and series 2 (U_m=0.119m/s); (b): the velocity of the main stream U_m and Reynolds number Re in series 3; (c): the dimensionless water depth h/L in series 4.

Figure IV.25 reveals that the aspect ratio of the cavity, the Reynolds number of the main stream and the water depth of the main stream do not impact significantly the normalized peak frequency of the mixing layer.

4.4 *Impact on the vortex celerity C*

The aim of the present section is to investigate the impact of the flow and geometry parameters from Table 1 on the mean celerity of the vortices in the mixing layer C (m/s), normalized by the mean streamwise velocity in the mixing layer U_{ex} (averaged from x/L=0 to 1 at y=0). C is derived as explained in section 4.2 and figure IV.11.

- Series 1 and 2: in case of W/L changing for series 1 and 2, the dimensionless celerity of the vortices slightly decreases from 1.32 to 1.23 as W/L increases from 1 to 5 (Figure IV.26)

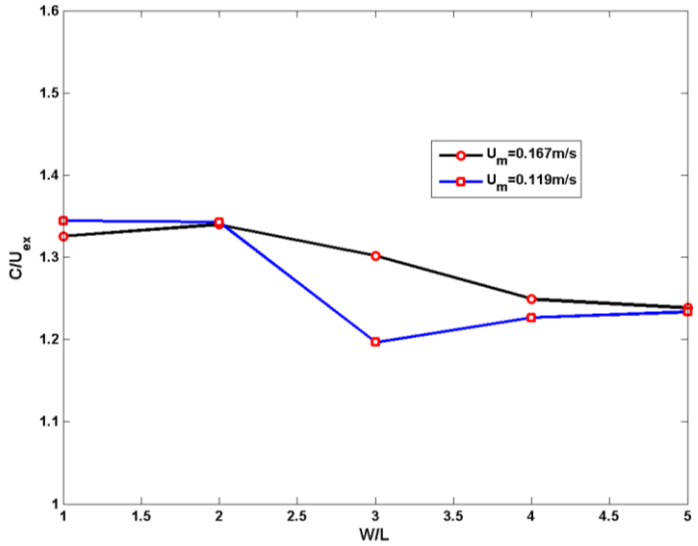

Figure IV.26: Mean non-dimensional celerity of the vortices in the mixing layer for all configurations from series 1 and 2.

- Series 3: in case of U_m changing for series 3, as U_m (and Re) increases, the dimensionless celerity of the vortices also slightly increases (Figure IV.27) ,even though this increases remains much limited..

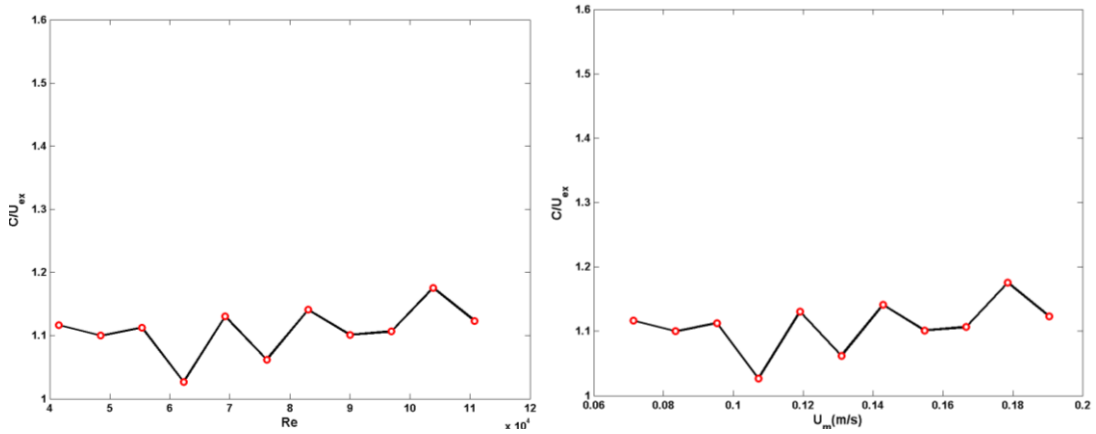

Figure IV.27: Mean non-dimensional celerity of the vortices in the mixing layer for all configurations from series 3.

- Series 4: in case of h/L changing for series 4, as h/L (and Re) increases, the dimensionless celerity of the vortices first slightly decreases and then increases with higher slope (Figure IV. 28). The minimum C/U_{ex} equals about 1.1 for h/L=0.2-0.3.

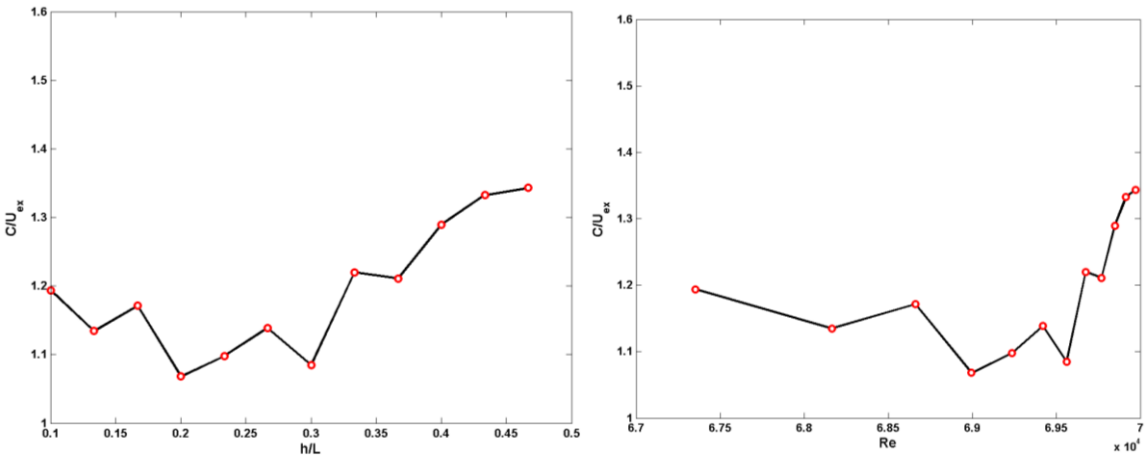

Figure IV.28: Mean non-dimensional celerity of the vortices in the mixing layer for all configurations from series 4.

To conclude, the dimensionless celerity of the vortices remains quite constant for all configurations, with no clear influence of the dimensionless parameters, considering the measurement uncertainties.

4.5 *Impact on the wave length in the mixing layer*

The aim of the present section is to investigate the impact of the flow and geometry parameters on the mean dimensionless wave length of the mixing layer λ/L. λ is derived as explained in section 4.2.

- Series 1 and 2: in case of W/L changing for series 1 and 2 in Figure IV. 29, the mean wave length in the mixing layer remains quite constant, λ/L~0.5

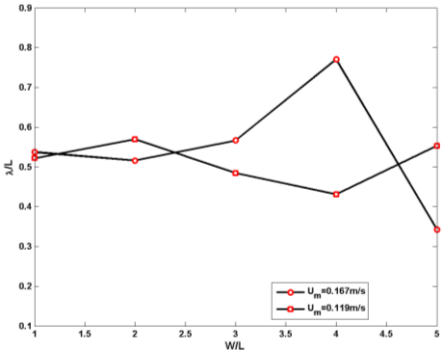

Figure IV.29: Mean non-dimensional wave length in the mixing layerfor all configurations from series 1 and 2.

- Series 3: in case of U_m (and Re)changing for series 3 in Figure IV.30, the mean wave length in the mixing layer remains quite constant, λ/L~0.5

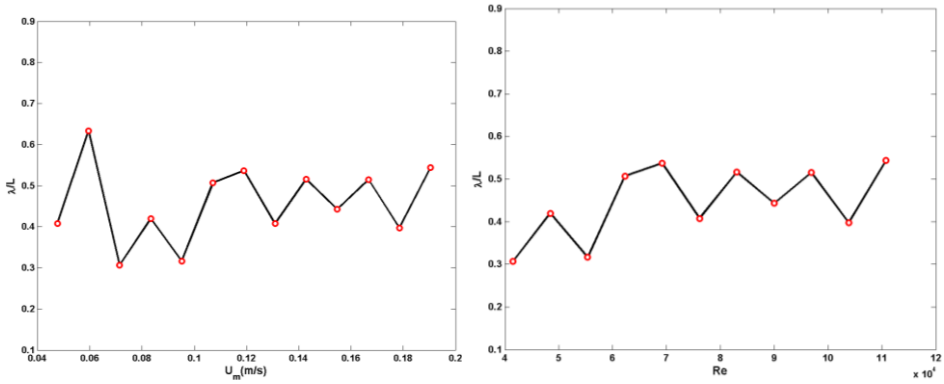

Figure IV.30: Mean non-dimensional wave length in the mixing layer for all configurations from series 3.

- Series 4: in case of *h/L* changing for series 4 in Figure IV.31, the mean wave length in the mixing layer remains quite constant, λ/L~0.5

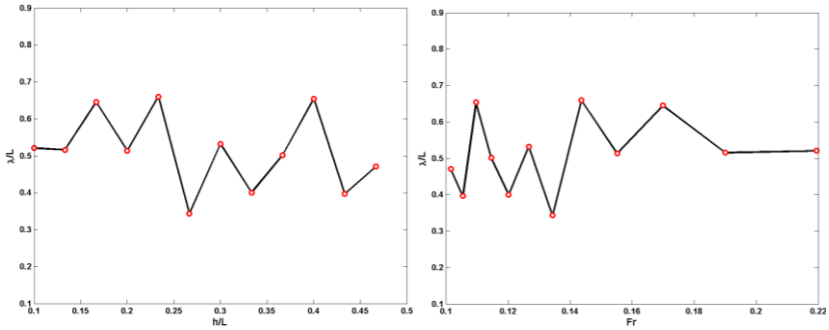

Figure IV.31: Mean non-dimensional wave length in the mixing layer for all configurations from series 4.

As a consequence, as for the vortices celerity *C*, no dimensionless parameter significantly affects the dimensionless wave length of the mixing layer.

4.6 *Concluding remarks, including remarks concerning uncertainties*

Adding error bars on figure IV.16 to IV.31 would have been necessary to improve our conclusions. However, defining the impact of uncertainties is not a simple task. Indeed, measurement uncertainties using PIV were defined in chapter II, but they are not the main source of uncertainty in our results, far from it. The main source is in fact the estimation of the local mainstream $U_1(x)$ and cavity $U_2(x)$ outer velocities. Yet, these $U_1(x)$ and $U_2(x)$ values are used to compute parameters such as the outer velocity ratio *r*, the mixing layer width δ, and the mixing layer growth rate α. $U_1(x)$ and $U_2(x)$ are defined using a criteria on the streamwise velocity gradient that becomes negligibly small. A first try of sensitivity analysis to this criteria gave no convincing conclusions. More work should be devoted to this point as it was not possible in the time available for the Ph.D.

The general conclusion for section 5 is that within the range of the 3 parameter variations in Table 1, the mixing layer at the interface between the main stream and the cavity remains quite similar. Only small changes in terms of outer velocity gradient, or celerity of the vortices and corresponding wave length were reported with no major tendency. The only real observed tendency seems to be that the growth rate coefficient of the mixing layer width (α) decreases as the Reynolds number of the main stream increases.

5 CONCLUSION OF CHAPTER IV.

We have shown that the cavity is connected to the main stream by a mixing layer that presents the classical features of mixing layers, in terms of velocity profiles, velocity gradient, mixing layer width. On the other hand, we showed that this is a “constrained” mixing layer as the mixing layer centerline is located at the interface, as it is at canopies crests or compound channels bank-steps. The impact of the dimensionless parameters that rule the flow was studied through several data series. Formerly, special post-processing tools were implemented, namely proper orthogonal decomposition (POD) and identification of the vortices center based on the scalar function G, to analyze the coherent structure dynamics within the mixing layer. The results can be connected to the role of the mixing layer on the mass transfers from the mainstream to the cavity studied in the next chapter.

Chapter V: Mass exchange between the main stream and the cavity

The aim of *Chapter V* is to measure the capacity of passive scalar exchanges between the main flow and the cavity. The characteristics of the scalar exchange is studied for the reference configuration in section 2 and then impact of the flow and geometrical parameters on these issues is studied in section 3.

1 LITERATURE REVIEW ON EXCHANGE COEFFICIENTS

The aim of *Chapter V* is to measure the capacity of passive scalar exchanges between the main stream and the cavity and to relate this capacity with the characteristics of the flow pattern in the cavity (as presented in Chapter II). An overview of the literature dealing with scalar exchanges between an open-channel main stream and a connected dead zone is first included and measurement and results are detailed afterwards.

1.1 *Theoretical background*

In order to measure the mass transfer between a main stream and a dead-zone, Valentine & Wood (1977) state that the mass conservation within the cavity is related to the exchanges at the interface between the main stream and the cavity. This relation reads:

$$\frac{dM}{dt} = S_{ex} V_{ex} \left(C_{MS} - C_C(t) \right) \tag{1}$$

where M is the mass of pollutant within the cavity at time t, $S_{ex}=Lh$ is the interface section between the main stream and the cavity (L being the length and h the depth of the interface), V_{ex} is the typical time-averaged exchange velocity across the interface, C_{MS} is the main stream concentration (assumed to be uniform and constant with time) and C_C the spatially averaged scalar concentration in the cavity. Moreover, Valentine & Wood (1977) propose to relate V_{ex} to the bulk velocity of the main stream U_m as $V_{ex}=kU_m$, where k is a non-dimensional variable named "exchange coefficient". Then, the mass in the cavity reads:

$$M(t) = C_C(t).WLh \tag{2}$$

where W is the cavity width (as in previous sections) and thus WLh is the cavity volume (constant with time). Inserting Eq. 2 within Eq. 1 leads to Eq.3:

$$\frac{dC_C(t)}{dt} = \frac{kU_m}{W} \left(C_{MS} - C_C(t) \right) \tag{3}$$

k coefficient can then be estimated using two methodologies:

- First methodology consists in measuring or computing the time-evolution of the mean concentration in the cavity C_C(t). Integrating Eq. 3 leads to:

$$C_C(t) = Ae^{-\frac{kU_m}{W}t} + C_{MS} \tag{4}$$

with A being a constant. If (as in present case) the initial concentration in the cavity is null $C_C(t=0)=0$, then $A=-C_{MS}$ then Eq. 4 reads:

$$\frac{C_{MS} - C_C(t)}{C_{MS}} = e^{-\frac{kU_m}{W}t} \tag{5}$$

that is,

$$\log_{10}\left(\frac{C_{MS} - C_C(t)}{C_{MS}} \right) = \frac{-kU_m}{\ln(10).W} t \tag{6}$$

The next step is thus to plot the time evolution of the left-hand-side term (obtained by calculations or measurements) of Eq. 6 and identifying the slope of the curve, equal to $-k.U_m/(W.\ln(10))$ to obtain k. This k is noted k_{conc} for "concentration measurement" in the sequel.

- Second methodology for estimating k coefficient, described by Weitbrecht *et al*. (2008), is based on the measurement of the transverse velocity along the main stream-cavity interface v so that v_{ex} equals:

$$v_{ex}(t) = \frac{1}{2S_{ex}} \int_{S_{ex}} |v(x,z,t)| dS \quad (7)$$

and then time-averaging v_{ex} to obtain V_{ex} from Eq.1, where $v(x,z,t)$ is the instantaneous transverse velocity component (perpendicular to the main stream direction). The value "2" relates the fact that the absolute value in Eq. 7 corresponds to the exchanges from the main stream to the cavity plus the ones from the cavity towards the main stream, that is twice the exchanges referred to in Eq.1. Using the relation between V_{ex} and U_m proposed by Valentine & Wood (1977), k can then directly be obtained as $k_{veloc} = V_{ex} / U_m$, where k_{veloc} stands for "velocity measurement".

1.2 *Data from the literature*

In the literature, the exchange coefficient k was measured in various cavity configurations such as in a groyne field (Uijttewaal *et al*., 2001 and Weitbrecht *et al*., 2008), a cavity located below the main flow (as for Caton *et al*., 2003), a serie of cavities below (street canyons as Salizzoni *et al*., 2009 or Markides *et al*., 2010) and finally a single lateral cavity (as in the present case, see below for references).

In 18 groyne field configurations in an open channel flow, Weitbrecht *et al* (2008) measured and compared both estimated coefficients k_{conc} and k_{veloc}. They report a fair agreement between results from both approaches (about 17% difference). Moreover, they propose to relate the coefficient k (including additional data from the literature) to a so-called "morphometric parameter" R_D which reveals a linear trend.

For the lateral cavities adjacent to an open channel main stream, various configurations are investigated which complicate the comparison: Li & Ip (1999) and Li & Gu (2001) respectively measured and computed the k coefficients for a single lateral cavity with an entrance length limited by a partial wall. Langendoen *et al*. (1994) studied an oscillating flow (corresponding to the entrance of a harbor), Muto *et al*. (2000) considered a step at the entrance of the lateral cavity, Jackson *et al*. (2013) summarized residence times (related to exchange coefficients) of lateral cavities in field conditions available in the literature, that is cavities with complex shapes bathymetries.

Finally, regarding the ideal lateral cavity configuration studied herein (horizontal open-channel lateral-cavity, with established main stream and no wall at the cavity entrance), only 4 papers were encountered. First, Booij (1989) used temperature as indicator to estimate k_{conc} but measurements were limited to a single location in the cavity. This author obtained k_{conc}=0.02 for W/L=1 while for W/L=3, two values are reported: k=0.014 and 0.02 (as two sensors are used, at different locations). C_C is thus not spatially averaged within the cavity so that these data present a limited accuracy. Second, Altai & Chu (1997) estimated 9 dye exchange coefficients k_{conc} for 2 square cavity dimensions with W/L=1 (see Table 1). In one of them, they increased the main stream velocity while in the other cavity they modified both the main stream velocity and depth. However, the authors encounter no clear tendency of k coefficient with these parameter modifications. They obtain k_{conc} values comprised between 0.013 and 0.028. However, these values strongly depend on the number of samples considered, preventing to emit definite conclusions. Thirdly, Sanju & Nezu (2013) considered positive, null and negative longitudinal slopes in a lateral cavity with W/L=1/3. For the null slope configuration (corresponding to the present configuration), they obtain k_{conc}=0.014 using LIF method. Finally, Tuna *et al*. (2013) applied a PIV technic to measure the k_{veloc} methodology at 6 elevations from the bed to the free surface for two flows: one without and one

with seiching. They obtained two different k_{veloc} values: i) from 0.026 (near the surface) to 0.03 (near the bed) without seiching and ii) from 0.034 (near the surface) to 0.042 (at mid-elevation) with seiching. This collected data are summarized in Table 1.

Table V.1:Flow and geometrical configurations along with *k* estimated from the literature.

	W/L	W (m)	L (m)	h (m)	Um (m/s)	k veloc	k conc
Tuna et al. (2013) :							
near bed region PIV	1.50	0.457	0.305	0.0381	0.24	0.03	
surface region PIV	1.50	0.457	0.305	0.0381	0.24	0.026	
surface region - seiching - PIV	1.50	0.457	0.305	0.0381	0.43	0.035	
Altai et Chu (1997) Concentration	1	0.89	0.89	0.029	0.29		0.028
	1	0.89	0.89	0.05	0.16		0.014
	1	0.89	0.89	0.027	0.30		0.025
	1	0.89	0.89	0.06	0.13		0.019
	1	0.32	0.32	0.025	0.34		0.028
	1	0.32	0.32	0.025	0.30		0.014
	1	0.32	0.32	0.025	0.21		0.019
	1	0.32	0.32	0.025	0.14		0.013
	1	0.32	0.32	0.025	0.07		0.020
Booij (1989) Concentration at single point	1	1	1	0.11	0.5		0.020
	3	3	1	0.11	0.5		0.020
	3	3	1	0.11	0.5		0.014
Sanjou & Nezu (2013) Concentration	0.33	0.1	0.3	0.053	0.12		0.014

Data from the literature then seem to indicate that:
- increasing *W* does not impact *k* coefficient (see data from Booij, 1989)
- increasing *W* and *L* together (keeping *W*/*L* constant) tends to increase *k* coefficient (see data from Altai & Chu, 1997).
- no clear tendency exists regarding the impact of U_m on the exchange coefficient (see data from Altai & Chu, 1997).
- as *h* increases, *k* also seems to increase (see data from Altai & Chu, 1997)

1.3 *Objectives of chapter V*

The data of exchange coefficients from the literature is limited to a few configurations from several authors and thus no clear conclusion can be sorted in terms of the influence of the flow cavity characteristics on the coefficients. The aim of the present work is then to perform a more exhaustive experimental work in order to identify the influence of the following parameters on the exchange coefficient *k*. As seen in previous chapters, dimensional analysis indicate the dimensionless parameters that rule the flow and *k* should be so that:

$$k=k(W/L, h/L, Re)$$

where *W/L* is the aspect ratio of the cavity, *h/L* the relative water depth, *Re* is the upstream Reynolds number based on the hydraulic diameter. The influence of the Froude number is neglected as in the experiments, this parameter was always smaller than 0.23 (Table V.1).

2 SCALAR EXCHANGE FOR THE REFERENCE FLOW CONFIGURATION

For the reference configuration, the inlet discharge is fixed to 3.5L/s and the water depth is fixed to h=7cm (±0.15 mm) at the connection between the cavity and the main stream. As detailed above, two types of measurement are considered herein to estimate the exchange coefficients: velocity measurements using PIV and mass transfer measurements using measured colorant concentration.

2.1 Estimation of k_{veloc} using PIV

Regarding the estimation of k_{veloc}, the rapid video camera is located above the mixing layer in order to record the particle motion over 3000 consecutive images of 1280x960 pixels each, with an average spatial resolution of 0.3mm per pixel, at a frequency equal to 30Hz.

In Figure V.1, the time-average x-profile of absolute transverse velocity component $\overline{|v(x)|}$ measured at z/h=0.71 is plotted for the reference flow configuration with 3 aspect ratios of the cavity (W/L=1, 2 and 3), corresponding to the 3 first cases of series 1 in Table 2. This parameter appears to be minimum near the upstream corner of the cavity where the transverse velocity signal is thus of limited amplitude and to increase towards the downstream corner with a maximum amplitude of the transverse velocity signal obtained near x/L=2/3 (in agreement with data from Tuna *et al*. 2013). Moreover, the shape and intensity of the profile remains similar for the three plotted configurations W/L=1, 2,3,4 and 5.

Assuming a 2D-flow with not variation along z, V_{ex} can be computed as (see eq. 7):

$$V_{ex} = \frac{1}{2L}\int_{x=0}^{x=L} \overline{|v(x,t)|}dx \qquad (8)$$

and finally $k_{veloc}=V_{ex}/U_m$. Consequently, in our case, V_{ex} is simply half the average of Figure 1 curves. For instance, for W/L=1, this average equals 8.10^{-3}m/s, and thus $V_{ex}=4x10^{-3}$m/s and k_{veloc}=0.024 (as U_m=0.166m/s for the reference configuration). These data are indicated in the upper part of Table V.2. For all tested configurations with the same flow parameters but varying cavity geometry (W/L=1 to 5), all k_{veloc} coefficients appear to remain similar, equal to about 0.025. This approach based on PIV measurements thus indicates that the aspect ratio of the cavity does not impact the exchange coefficient.

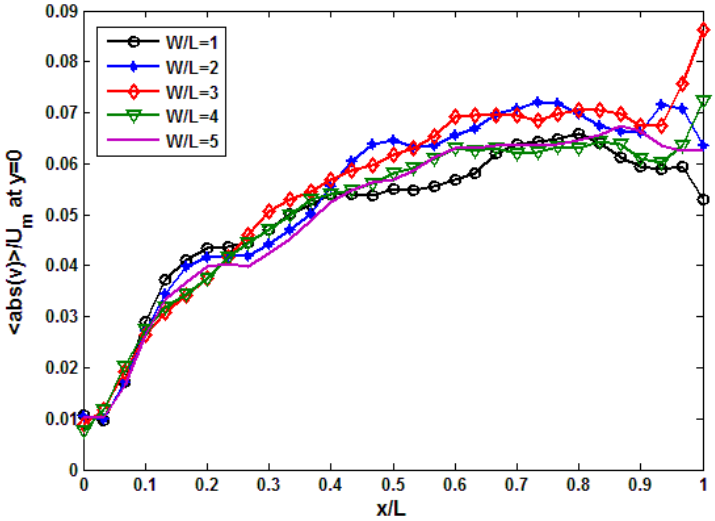

Figure V.1:Mean velocity transverse to the interface between the main stream and the cavity along x axis for W/L=1, 2 ,3,4 and 5.

2.2 Estimation of kconc using dye release

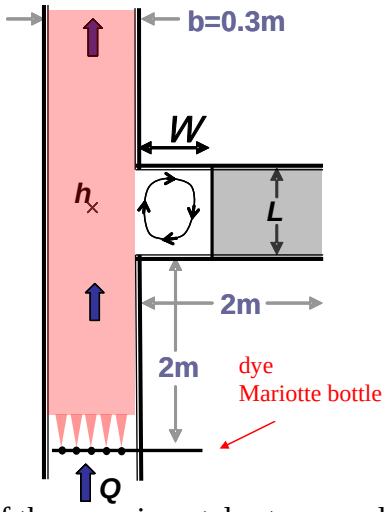

Figure V.2:Scheme of the experimental set-up used for k_{conc} estimation.

Regarding mass transfer measurement, the methodology used herein is similar to that proposed by Weitbrecht *et al*. (2008) except that in our case the dye is injected in the main stream and not in the cavity (see Figure. V.2). The whole set-up is introduced below a dark tent and a controlled and repeatable ambient light is located within the tent above the free surface.

Step1: Calibrations: Previous to experiments, the cavity is closed and filled with 9 consecutive controlled volumes of water with well-known dye concentrations so that the water depth remains exactly equal to 7 cm (equal to the water depth of the reference configuration). A high resolution photograph (4000-4000 pixels) of the cavity and intersection is taken from above the free surface for each concentration. Using the light intensity of each pixel, a calibration curve of light intensity *vs* dye concentration is finally established for each pixel as presented in Figure V.3.

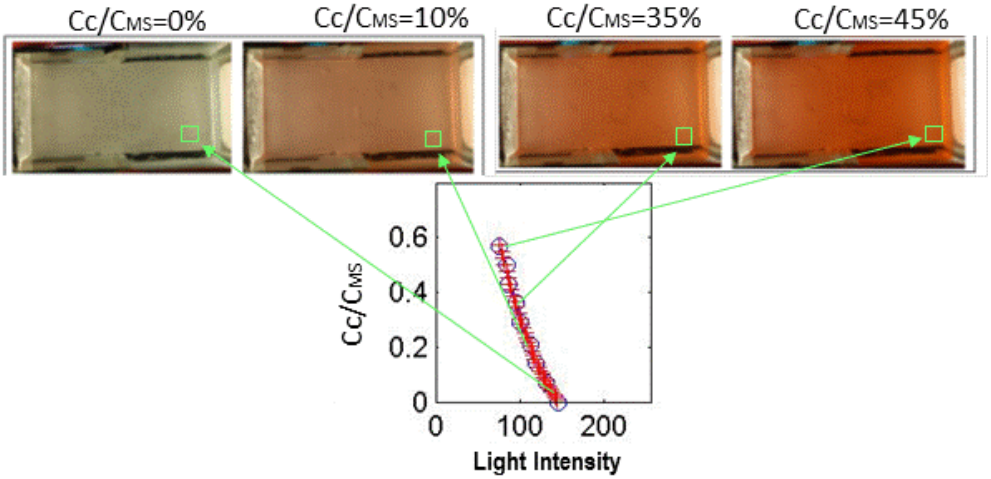

Figure V.3:Calibration = establishing for one pixel the relation between light intensity and scalar concentration

Step 2: Measurements: Initially, a steady-state flow is produced both in the main stream and the cavity with clear water. A constant discharge (two orders of magnitude lower than the water discharge) of dye is then injected using a Mariotte Bottle. The multipoint injection is located at the upstream end of the inlet channel (see Fig. 2) so that complete mixing is achieved before reaching the cavity. Time when the dye reaches the intersection is set as t=0. Similar photos as for the calibration are taken every 5 seconds. These photos and the calibration curves finally permit to compute the concentration map of $C(x,y,t)/C_{MS}$ every 5 seconds. The main limit of such approach,

used in the literature (*e.g.* Babarutsi and Chu, 1991) is the assumption that the concentration field is 2D with no evolution along the vertical axis. This methodology is applied to three configurations: W/L=1, 3 and 5 and on Figures 4-5-6 only a few times are selected for presentation.

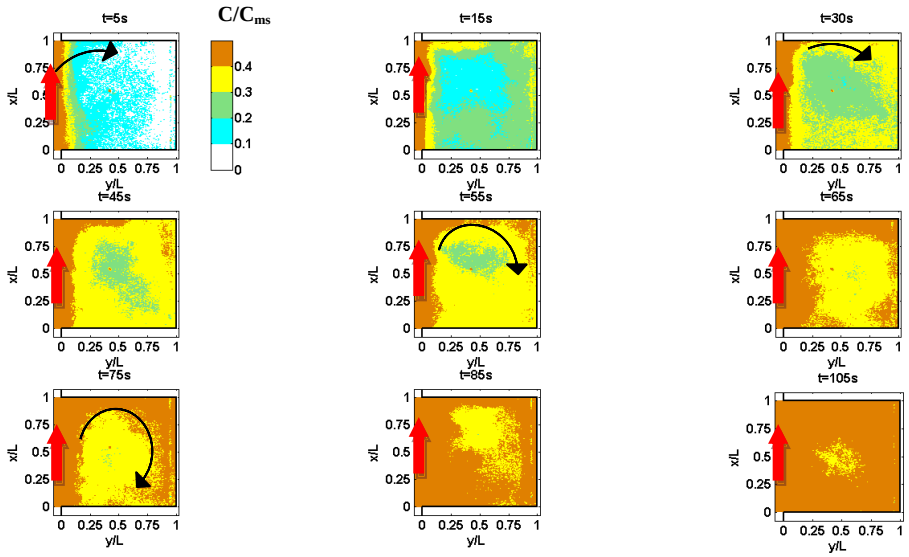

Figure V.4: Time-evolution of dye concentration maps for configurations with W/L=1, red arrows refer to the mean flow direction in the mainstream.

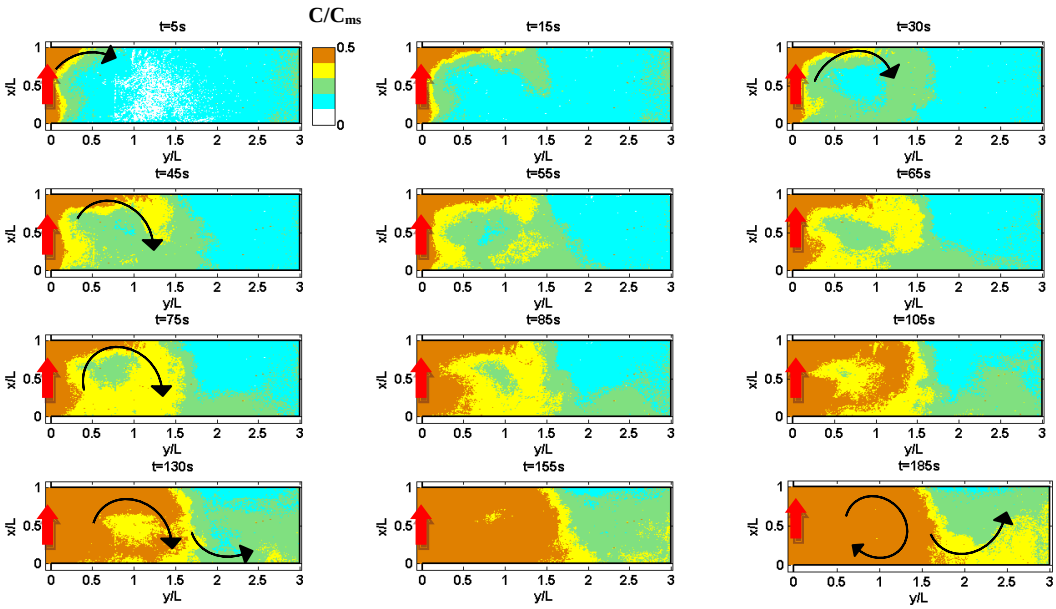

Figure V.5:Time-evolution of dye concentration maps for configurations with W/L=3.

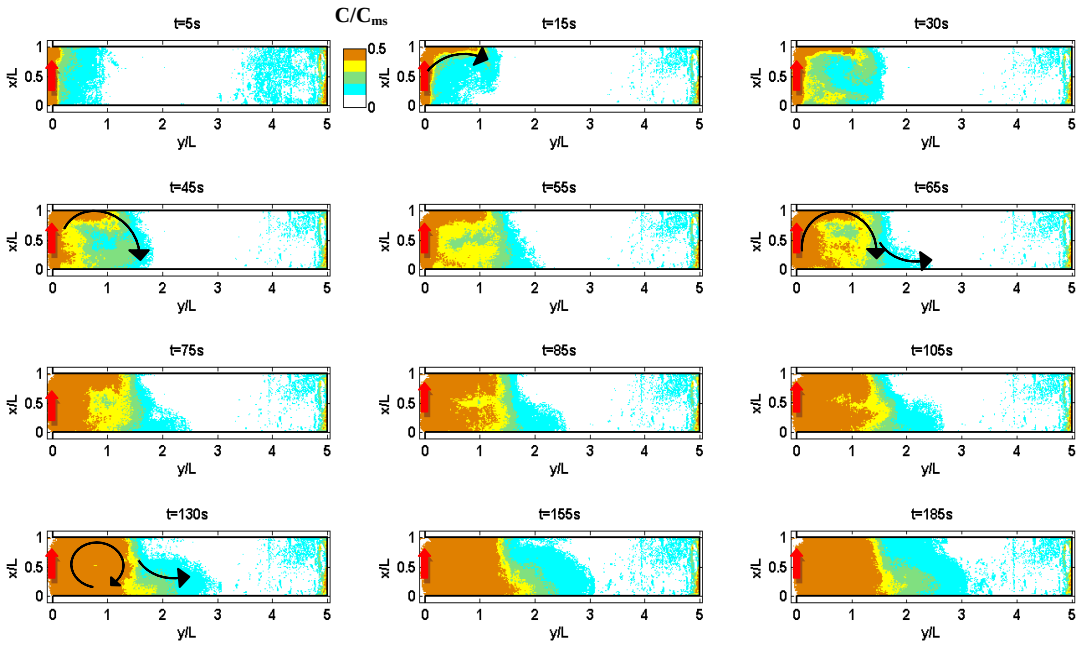

Figure V.6:Time-evolution of dye concentration maps for configurations with W/L=5.

At initial times (t=5-55s in Figures 4-5-6), exchange processes are similar for all configurations. Dye is introduced into the cavity through turbulent diffusion across the interface between the main stream and the cavity. Then, this scalar located on the cavity side is transported by the first cell towards the downstream corner (see black arrows at t=5s). Then, advection due to the mean flow in the first cell of the cavity permits to transport the scalar all around the first cell, which becomes completely "colored". Moreover, turbulent diffusion within the first cell transports dye for the outer layer towards the center of the cell, increasing the dye concentration over the whole surface of the first cell. Nevertheless, at t=30s the concentration map starts to differ for W/L=1, 3 and 5:

- For W/L=1, the first cell in the cavity is bounded by a wall at y=300mm. The cavity is short so that advection all around the first cell is rapid and diffusion distance from the outer layer to the center of the cell is short; consequently, the concentration in the first cell increases rapidly.

- For W/L=3 and 5, the first cell is more elongated along y axis, and both advection along the outer layer of the first cell and diffusion towards its center take more time. Finally, even if the exchange velocity V_{ex} is similar to case W/L=1 (according to Table 1), the concentration in the first cell remains lower at a given time (such as 55s in Figures 4-5-6).

For larger times (t>55s), the processes strongly differ between the distinct cavity geometries:
- For W/L=1, the same initial process continues: more dye is introduced in the cavity, is advected by the cavity mean flow and diffuses towards the center of the cell, so that the dye concentration rapidly increases everywhere in the cavity.
- For W/L=3 and 5 an additional process appears: part of the dye from the outer layer of the cell near x=400-500mm is advected towards the second cell (see Figures V.5- V.6). Consequently, the concentration increase in the first cell is delayed and the concentration in the second cell slowly increases.

Once the concentration maps such as plotted in Figures V.4-5-6 are obtained, the spatial averaging of dye concentration C over the cavity area leads to C_c in Equation 6. The term $\log_{10}\{[C_{MS}-C_C(t)]/C_{MS}\}=f(t)$ is finally plotted in Figure V.7. As the initial slope equals $-kU/(W.\ln(10))$, see Equation 6, estimation of k_{conc} is finally obtained. Note that the increasing absolute slope as W

decreases is coherent with a constant *k* value as for a given main stream flow, the slope being proportional to $-k/W$ for a given main stream flow.

However, it appears that the absolute value of the slope decreases with time due to the fact that the constant k is valid only as long as the concentration of scalar next to the mixing layer on the cavity side is null. As, after some time (20s to 30s here), the concentration of scalar rotates along the first cell of the cavity and reaches the mixing layer (on the cavity side), the coefficient *k* (and thus the slope of the curve in Figure V.7) is no longer constant. Thus, the value of the slope strongly depends on the time range over which the slope is estimated. For instance, for W/L=1, the slope equals $-80\text{x}10^{-4}\text{s}^{-1}$ if the three first points (t=5-15s) are considered and equals $-54\text{x}10^{-4}\text{s}^{-1}$ if the five first points (t=5-25s) are considered. As proposed by the literature, it is decided to consider the maximum exchange capacity, that is only the first data points of Figure V.7. These slopes respectively equal $-80\text{x}10^{-4}\text{s}^{-1}$, $-17\text{x}10^{-4}\text{s}^{-1}$ and $-12.4\text{x}10^{-4}\text{s}^{-1}$ leading to the k_{conc} values included in Table 2.

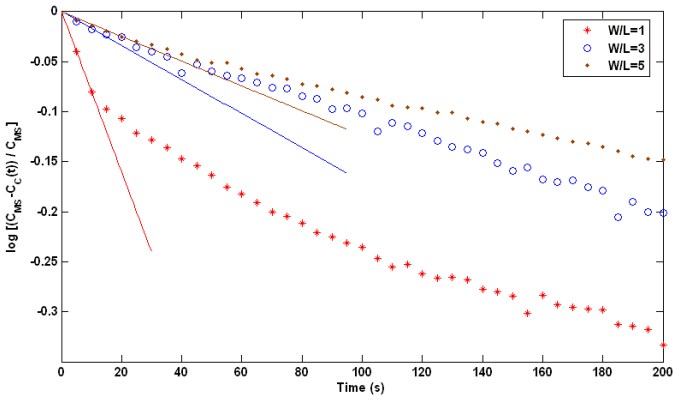

Figure V.7:Time-evolution of spatially averaged dye concentration in the cavity for W/L=1, 3 and 5.

3 IMPACT OF FLOW PARAMETERS ON THE SCALAR EXCHANGE COEFFICIENT

In order to identify the influence of the three identified parameters(from previous chapter): *W/L*, *Re* and *h/L*, Table 2 summarizes the exchange coefficients *k* obtained in our experiments using velocity (k_{veloc}) and concentration (k_{conc}) methodologies. In series 1 and 2, the main stream is kept constant and only the aspect ratio of the cavity (W/L) is modified. In series 3 and 4 the geometry of the cavity is kept constant and only the velocity of the main stream is modified is series 3 and only the water depth is modified in series 4. These configurations are the same as in Chapter III.

For most flow configurations in Table V.2, only k_{veloc} is estimated. However, for 5 configurations, kconc is also estimated using the dye release methodology. Table 2 reveals that both estimates of k coefficients are in fair agreement, with a mean difference of about 20%, that is about the same difference as obtained by Weitbrecht et al. (2008) in a groyne field (average error of 16.6%).

Table V.2:Flow and geometrical configurations along with k estimations from the literature with *W* and *L* the cavity width and length, *h* the water depth in the cavity and main stream in front of the cavity, U_m the bulk velocity, *Re* and *Fr* corresponding Reynolds and Froude numbers in the mainstream, z_{meas} the altitude at which the velocity profile is measured using the 2D PIV, k_{veloc} and k_{conc} both estimates of the exchange coefficient.

	W (m)	*L* (m)	*h* (cm)	U_m (m/s)	*W/L*	*h/L*	*Re*	*Fr*	z_{meas}/h	k_{veloc}	k_{conc}
Series 1	0.3	0.3	7	0.167	1	0.23	9.71E+04	0.20	0.71	0.025	0.033
	0.6	0.3	7	0.167	2	0.23	9.71E+04	0.20	0.71	0.027	
	0.9	0.3	7	0.167	3	0.23	9.71E+04	0.20	0.71	0.028	0.021
	1.2	0.3	7	0.167	4	0.23	9.71E+04	0.20	0.71	0.026	
	1.5	0.3	7	0.167	5	0.23	9.71E+04	0.20	0.71	0.026	0.026
Series 2	0.3	0.3	7	0.119	1	0.23	6.98E+04	0.15	0.71	0.030	
	0.6	0.3	7	0.119	2	0.23	6.98E+04	0.15	0.71	0.031	
	0.9	0.3	7	0.119	3	0.23	6.98E+04	0.15	0.71	0.029	
	1.2	0.3	7	0.119	4	0.23	6.98E+04	0.15	0.71	0.030	
	1.5	0.3	7	0.119	5	0.23	6.98E+04	0.15	0.71	0.029	
Series 3	0.3	0.3	7	0.048	1	0.23	2.77E+04	0.06	0.71	0.032	
	0.3	0.3	7	0.060	1	0.23	3.46E+04	0.07	0.71	0.031	
	0.3	0.3	7	0.071	1	0.23	4.14E+04	0.09	0.71	0.033	
	0.3	0.3	7	0.083	1	0.23	4.84E+04	0.10	0.71	0.031	
	0.3	0.3	7	0.095	1	0.23	5.53E+04	0.12	0.71	0.029	
	0.3	0.3	7	0.107	1	0.23	6.23E+04	0.13	0.71	0.029	
	0.3	0.3	7	0.119	1	0.23	6.92E+04	0.14	0.71	0.030	0.031
	0.3	0.3	7	0.131	1	0.23	7.62E+04	0.16	0.71	0.028	
	0.3	0.3	7	0.143	1	0.23	8.31E+04	0.17	0.71	0.027	
	0.3	0.3	7	0.155	1	0.23	9E+04	0.19	0.71	0.026	0.029
	0.3	0.3	7	0.167	1	0.23	9.7E+04	0.20	0.71	0.026	
	0.3	0.3	7	0.179	1	0.23	10.4E+04	0.22	0.71	0.026	
	0.3	0.3	7	0.190	1	0.23	11.1E+04	0.23	0.71	0.026	
Series 4	0.3	0.3	3	0.119	1	0.10	67350	0.22	0.71	0.028	
	0.3	0.3	4	0.119	1	0.13	68170	0.19	0.71	0.026	
	0.3	0.3	5	0.119	1	0.17	68660	0.17	0.71	0.028	
	0.3	0.3	6	0.119	1	0.20	69000	0.16	0.71	0.026	
	0.3	0.3	7	0.119	1	0.23	69240	0.14	0.71	0.028	
	0.3	0.3	8	0.119	1	0.27	69420	0.13	0.71	0.028	
	0.3	0.3	9	0.119	1	0.30	69560	0.13	0.71	0.029	
	0.3	0.3	10	0.119	1	0.33	69680	0.12	0.71	0.028	
	0.3	0.3	11	0.119	1	0.37	69770	0.11	0.71	0.029	
	0.3	0.3	12	0.119	1	0.40	69850	0.11	0.71	0.030	
	0.3	0.3	13	0.119	1	0.43	69910	0.11	0.71	0.031	
	0.3	0.3	14	0.119	1	0.47	69970	0.10	0.71	0.030	

3.1 Analysis of Series 1 and 2: impact of the aspect ratio W/L

PIV and concentration approaches for two flow configurations detailed in series 1 and 2 reveal that the exchange coefficients *k* remain constant when increasing the width of the cavity *W* and thus the aspect ratio *W/L* which seems consistent with data from Booij (1989).

This result may appear unexpected at first glance but becomes obvious when comparing the velocity magnitude of the first cell in Chapter II for the five measured configurations of series 1 (reference flow configuration). Indeed, *k* depends on the characteristics of the mixing layer (between the main stream and the cavity) which itself is mainly dependent on the velocity gradient between both regions (main stream and cavity). The velocity in the main stream is kept constant,

(*U*=16.6 cm/s, see Table 2) and Chapter II and Figure 8 reveal that the velocity magnitude of the first cell on the side of the mixing layer equals about 2.2cm/s for *W*/*L*=1, 1.5cm/s for *W*/*L*=2 and 3, 1.25cm/s for *W*/*L*=4 and 5. Thus the velocity difference across the mixing layer respectively equals about 14.5 cm/s for *W*/*L*=1, 15cm/s for *W*/*L*=2 and 3, 15.3 cm/s for *W*/*L*=4 and 5 (difference of only about 6%). These three mixing layers are thus very similar (see Figures III.16-20-23-24 of Chapter III) and it becomes obvious that the exchange velocity and thus the exchange coefficient should be similar, as revealed by Table 2.

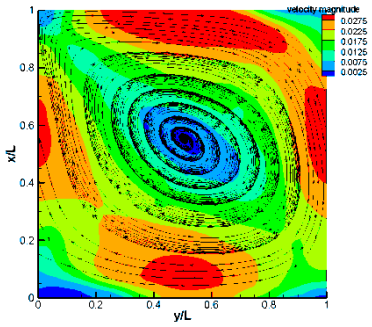

W/L=1

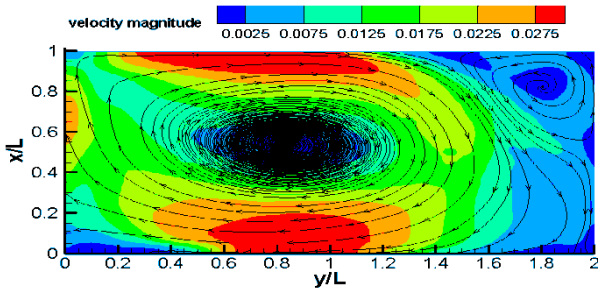

W/L=2

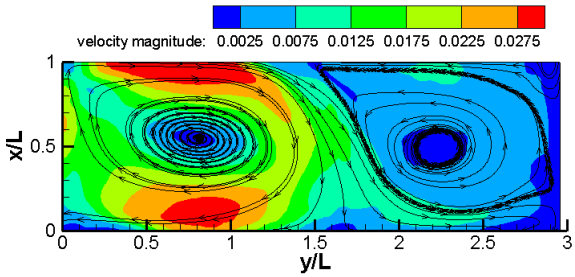

W/L=3

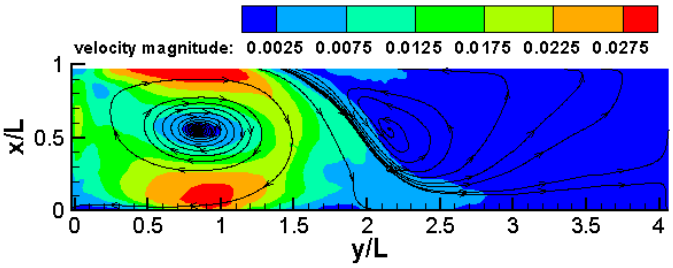

W/L=4

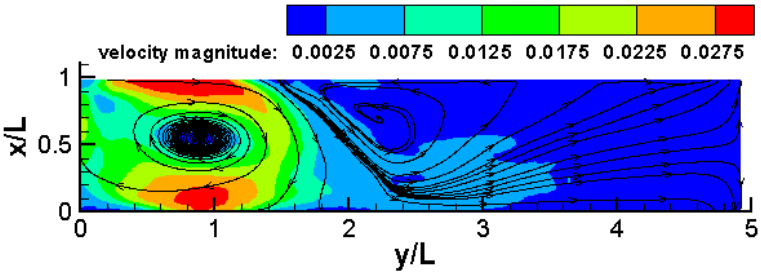

W/L=5

Figure V.8:Time-averaged 2D velocity field for W/L=1, 2, 3, 4 and 5.

3.2 Analysis of Series 3: impact of the mainstream Reynolds number Re

In series 3, the impact of *Re* is studied by varying main stream bulk velocity U_m whilst keeping *W*, *L* and *h* constant. Table V.2 and Figure V.9 indicate that for the range of velocity considered herein (U_m=0.05-0.23m/s *i.e.* *Re*=9200-36000), increasing *Re* results in decreasing the exchange coefficient *k*. Note that no main stream velocity larger than 0.2m/s is considered herein as the quality of PIV measurements near the downstream corner of the cavity becomes too low for higher values.

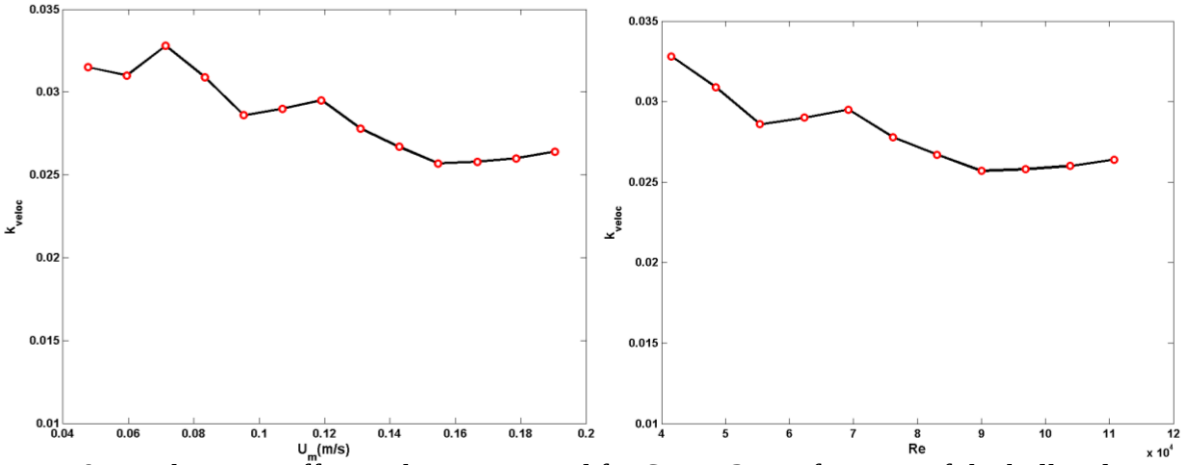

Figure V.9: Exchange coefficient k_{veloc} estimated for Series 3 as a function of the bulk velocity and Froude number of the inflow

In order to get deeper information on the origin of this tendency, the profile of the term $\overline{|v(x)|}/U_m$ (time average of the absolute transverse velocity component along *x* divided by the main stream bulk velocity, see Equation 8 and Figure V.1) along *x* is plotted in Figure 10. Remember that k_{veloc} equals the streamwise integral of this term dived by 2*L*. The figure reveals that all streamwise profiles are of same trend already described for Figure V.1. Nevertheless, is appears that as *Re* increases, the magnitude of the curve slightly decreases along most of the profile, leading to a decreasing value of the corresponding integral value and thus a decreasing exchange coefficient value *k*, as sketched previously by Figure V. 9.

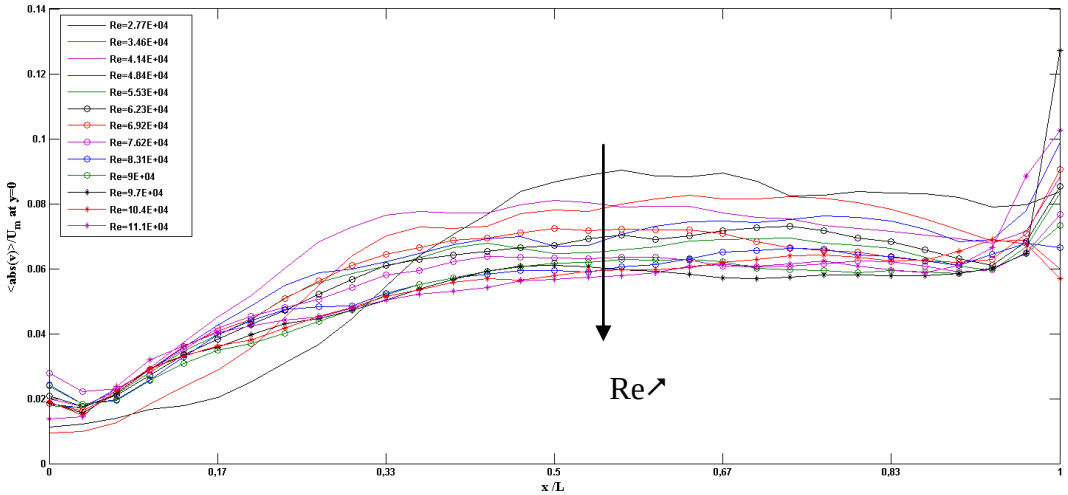

Figure V.10:Mean velocity transverse to the interface between the main stream and the cavity along *x* axis for Series 3

3.3 Analysis of Series 4: impact of the dimensionless water depth h/L

In series 4, the impact of the water depth *h* is studied by keeping *W*, *L* and U_m constant. Results are included in Table V.2 and Figure V.11. It appears that as *h*/*L* increases from 0.1 to 0.5 (*h* being multiplied by almost 5 from the shallowest to the deepest case), *k* increases very slowly from about 0.027 to about 0.03, that is by about 10%. Note that keeping *W*, *L* and U_m constant allow keeping *W/L* constant but not *Re* which increases when increasing *h*. Despites this increase of *Re*, *k* increases, showing thus that the effect of the dimensionless water depth is clearly to increase *k* as *h/L* increases.

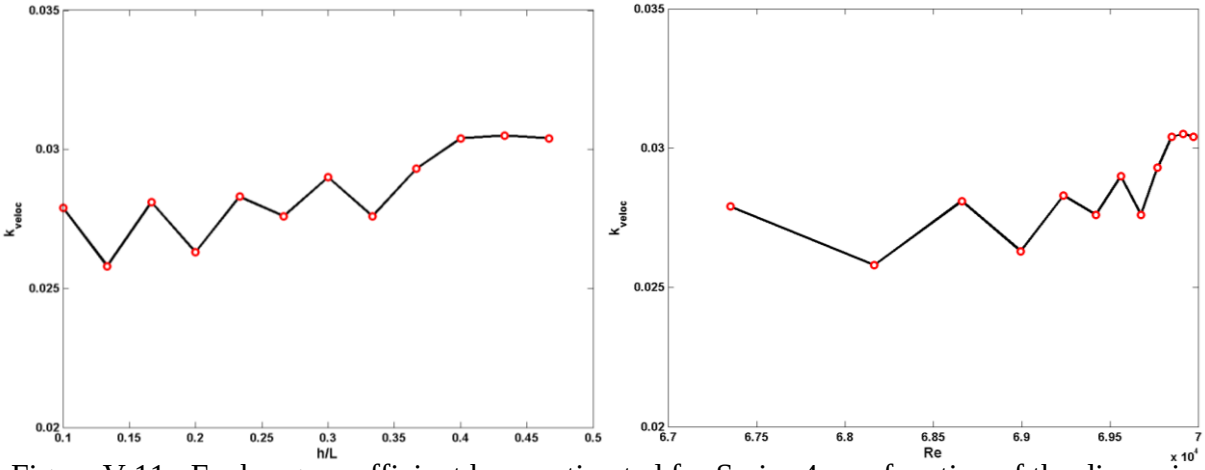

Figure V.11: Exchange coefficient k_{veloc} estimated for Series 4 as a function of the dimensionless water depth and Reynolds number of the inflow

As for section 3.2, the term $\overline{|v(x)|}/U_m$ along *x* is plotted in Figure V.12. As for Figure V.10, all tendencies remain similar and it appears that as *h/L* increases, the magnitude of this term increases all along the mixing layer length, leading to an increased *k* coefficient.

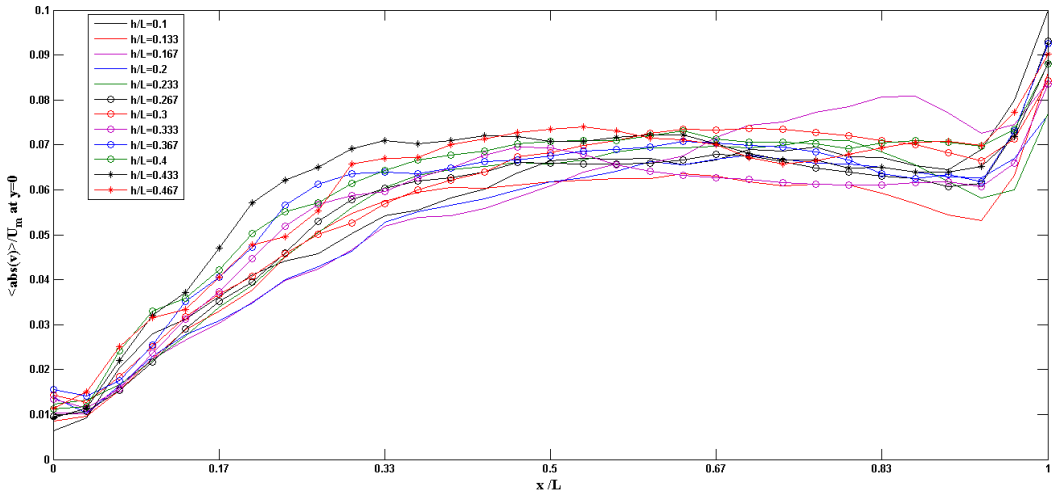

Figure V.12:Mean velocity transverse to the interface between the main stream and the cavity along x axis for Series 4

3.4 Exchange coefficient using the morphometric parameter

For groyne field configurations, Weitbrecht *et al*. (2008) proposed to relate the exchange coefficient *k* to a parameter named morphometric coefficient, equal to the cavity surface *WL* divided by the water depth and half the perimeter of the cavity as: $R_d = WL/[h(W+L)]$. The authors obtained a linear trend included in Figure V.13 as dashed line which is in fair agreement with groyne field data from

the literature. In the figure, data for lateral cavities k coefficients are included: from the literature and from present data. Agreement of lateral cavity data with the fitting curve from Weitbrecht *et al*. (2008) remains poor, which confirms the differences between a lateral cavity and a groyne field.

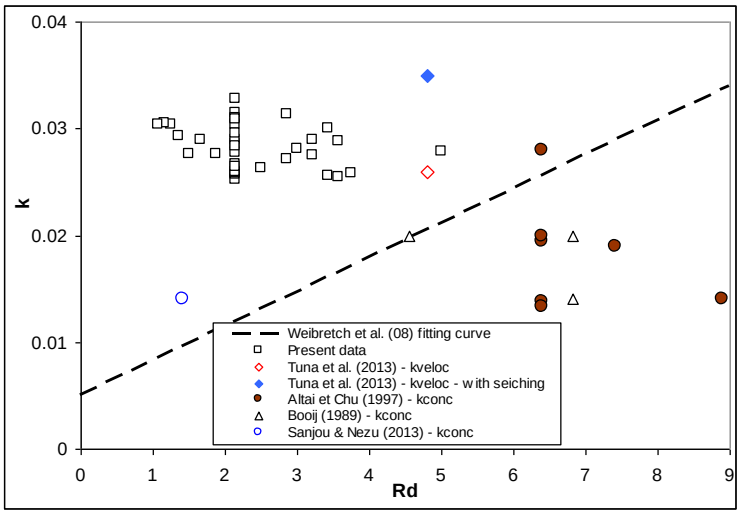

Figure V.13: Exchange coefficient as a function of the morphometric parameter from Weitbrecht *et al*. (2008).

3.5 Conclusion regarding the exchange coefficient k

We showed in sections 1 and 2 that two methodologies exist for the estimation of the exchange coefficient *k*: the velocity approach which permits to estimate k_{veloc} and the dye release approach which permits to estimate k_{conc}. In the present study, we mainly used the velocity approach due to a much higher experimental simplicity. We showed that this coefficient (k_{veloc}) does not evolve much within our range of varying parameters: k_{veloc} ranges between 0.025 and 0.033. Nevertheless, we observed that this coefficient is enhanced by decreasing upstream Reynolds numbers and by increasing relative water depth *h/d*.

4 CONCLUSION OF CHAPTER V

The exchange coefficient is an indicator of the capacity to exchange passive scalar between the main stream and the lateral cavity. The first aim of the present study was to characterize this exchange coefficient in lateral cavities, which was performed through i) velocity measurement and ii) dye concentration measurement. These two methodologies appear to be in fair agreement, as already observed in groyne fields. The second aim of the paper was to investigate the influence of the flow and cavity parameters on this coefficient. It appears that:

- increasing only the cavity width does not impact the obtained exchange coefficient,
- increasing the water depth tends to increase this coefficient,
- increasing the Reynolds number *Re* tends to decrease this coefficient,
- the linear trend between exchange the coefficient and the morphometric parameter proposed in the literature for groyne fields does not apply to the present configuration.

Future work should be devoted to analyze the influence of *h/L* alone and potentially of the Froude number. Moreover, the present experimental set-up was well suited to make vary the aspect ratio, with Reynolds numbers values comparable to the ones reported in part of the literature. Nevertheless, these values remain small and additional experiments in a larger set-up, i.*e.* for higher values of the Reynolds number, should be undertaken.

Conclusions

The objective of this thesis was to get more information on the open-channel lateral cavity flows. The choice was made to use an experimental approach in a small-scale channel with a simplified geometry. As the velocity of the flow within the cavity is much lower than that in the main flow, a mixing layer develops between the two regions. This mixing layer is able to transfer momentum from the main flow towards the cavity, which sets the flow in motion and also to transfer passive scalar between both regions. The thesis was then organized along three chapters dedicated to the investigation of the flow pattern in the cavity, the characteristics of the mixing layer and finally the transfer of passive scalar from the main flow towards the cavity.

Firstly, regarding the flow pattern in the cavity, the method selected was to keep a constant main flow and to gradually increase the aspect ratio (*W/L*= width/length ratio) of the cavity in the direction perpendicular to the main flow. For each of the 20 geometries, the 2D horizontal flow was measured at a given elevation using horizontal PIV. The patterns reported in the literature– *i.e.* two cells aligned in the streamwise direction for a cavity aligned with the main flow, and then one cell occupying the whole cavity for a cavity typically square– were reproduced. The pattern with two cells aligned in the crosswise direction was observed for different aspect ratio. Finally, the development of a third zone where the flow is three-dimensional was measured for the highest aspect ratios. Moreover, the transition from a one to a two-cell pattern aligned in the crosswise direction could be explained by analyzing the time-evolution of the instantaneous flow fields. This transition is due both to the increasing size and to the unstable behavior of the secondary cells located in the back corners for the shortest cavities that merge to form the second main cell for the wider cavities. It was also reported that the first cell characteristics are hardly modified by the appearance of the second cell and so by the increase of the cavity aspect ratio (*W/L*). Finally, velocity measurements show that the characteristic velocities decrease considerably from the main stream towards the first cell and from one cell to the next one when going away from the main stream.

Then, the mixing layer was analyzed in detail firstly for a given flow configuration and then the impact of the geometry and of the main flow characteristics on these characteristics was studied. The specificity of the present mixing layer, in comparison with more typical mixing layers is that in the present case the centerline of the mixing layer extends from the upstream to the downstream corner of the cavity. This type of mixing layer can be referred to as “constrained mixing layer”. The specificity comes from the fact that the mixing layer tends to self-organize from upstream to downstream, reaching a maximum width and Reynolds stress magnitude at about 70% of its development length and then is damped when approaching the downstream corner. Regarding its organization, it was observed that a peak frequency tends to appear in the downstream part of the mixing layer and reaches a maximum amplitude at 70% of the development length. Moreover, the analysis of the transverse velocity motion reveals a very stable alternation of flow directed from the main stream towards the cavity and inversed flow. The corresponding frequency of this alternation equals to maximum frequency observed in the transverse velocity spectrum. Finally, when applying a Reynolds decomposition, clockwise and counter-clockwise cells are observed and can be followed along the centerline of the mixing layer. They appear in the upstream region, slightly away from the upstream corner and finally leave the interface region when approaching the downstream corner. They finally end up either in the mixing layer or in the main stream. Moreover, it appears that these cells are usually not located along the interface but rather deflected to either one of the two regions. Also, it was possible to estimate their average celerity which appears to exceed the mean flow locally.

Finally, the alternation of the clockwise and counter-clockwise cells appears to follow a quite regular alternation process of same frequency as the transverse velocity motions. At the end, it was

possible to construct a scenario in four phases: 1. a transverse flow motion from the main flow towards the cavity followed by 2. a counter-clockwise cell (or vortex), followed by 3. a transverse flow motion from the cavity towards the main flow and finally followed by 2. a clockwise cell (or vortex).

The second objective of the mixing layer analysis was to investigate the impact of the flow and geometry parameters on the characteristics of the mixing layer. This requires to set a dimensional analysis which reveals that for the present low Froude number subcritical and smooth simplified cavity configuration, the remaining parameters susceptible to impact the flow characteristics are: i) the geometric aspect ratio of the cavity (*W/L*), ii) the Reynolds number of the main flow (*Re*) and iii) the water depth normalized by the cavity or main stream width (*h/L* or *h/b*). It was observed that the characteristics of the mixing layer are actually very stable and do not evolve much as the parameters are modified. Firstly, a slight modification of the outer velocity difference or ratio is reported without clear tendency. Then the mixing layer width increasing coefficient appears to increase as Re decreases or as *h/L* increases. The impact on the normalized peak frequency appears to be negligibly small so as the celerity of the vortices normalized by the local mean velocity along the interface and the typical wave length in the mixing layer.

Finally, the last section of the thesis aimed at investigating the processes involved in the transfer of passive scalar from the main stream towards the cavity. Firstly, a method was copied from the literature which consists in introducing dye in the upstream main stream and measuring its introduction in the cavity along the time. These results permit to understand the introduction processes: firstly the dye crosses the turbulent mixing layer due to the alternating transverse velocity motion; then this dye within the cavity is advected towards the downstream corner region by the mean flow of the first cell in the cavity and then along the downstream wall and finally all around the outer layer of the cavity, following the first cell mean motion. Additionally, turbulent structures transfer the dye from the outer layer towards the center of the first cell. Then it was showed that for longer cavities where a second cell exists, the outer layer of the first cell transfers a part of the dye towards the second cell. Consequently, as the width of the cavity increases, the homogenization time increases.

Two methodologies were then used to estimate the dye transfer capacity coefficient *k*: the method described above using dye release and a method based on the velocity measurement along the interface. Both methods appear to give results in fair agreement with each other. Then 4 series of flow configurations were considered and permitted to observe that: i) the geometry of the cavity (*W/L*) hardly affects this coefficient value, ii) a decrease of the Reynolds number *Re* or an increase of the water depth *h/L* tend to increase the value of the exchange coefficient *k*.

Perspectives

For the future work dedicated to lateral cavities, several perspectives can be expressed:

First aspect would be to consider a more natural shape of the cavity with slopes in the cavity (as measured by Sanjou and Nezu, 2013) or with a more realistic shape of the mainstream section, with a non-rectangular geometry of the cavity *etc*. The main objective would then be to verify whether the characteristics of the cavity flow pattern are strongly affected by this more realistic geometry of the cavity. Measurements would then have to be compared with data in real field cavities, as measured by Jackson *et al*. (2013) or Lecoz *et al*. (2010).

Another aspect would be the investigation of the seiching caracteristics of the cavity as already performed by Miele or by Tuna *et al*. (2013). One aspect that is actually planned within the laboratory would be to investigate the retroactions of the water volume in oscillation and the mixing layer when the peak frequency is establishing itself.

Finally 3D advanced numerical calculations of the cavity flow (with and without seiching) is also in progress at the Catholic University of Chile, performed by our partner Cristian Escauriaza and should soon be ready for comparison with the present experimental data.

Appendix A

It was stated in Chapter II that estimating the exact uncertainty associated to PIV measurements is a difficult task. The aim of the present appendix is to evaluate *a-posteriori* these uncertainties based on an empirical method: the idea is to put together different information corresponding to all the chapters of the manuscript and discuss the quality of the data by analyzing how the various parameters deriving from the PIV measurements evolve as a function of: i. the spatial location in the cavity, ii. the time during a measurement, iii. a slight change in the geometry of the cavity, iv. a slight change in the flow characteristics. These four items correspond to the four sections below.

1. Spatial location

First, let's consider the evolution of some time-averaged parameters along the spatial location in the cavity for a given main stream and a given cavity geometry. Figure A.1 shows the evolution of a mean 2D velocity field at two elevations, revealing a fair agreement between these two measurements. Then Figure A.2 shows the evolution along the centerline of the mixing layer (from the upstream to the downstream corner) of mixing layer characteristics such as its width and velocity spectra. These evolutions appear to be gradual, that is that they evolve smoothly along the centerline of the mixing layer. When one records that in PIV, all local velocity measurements are independent from the other locations, this gives credit to a low uncertainty level.

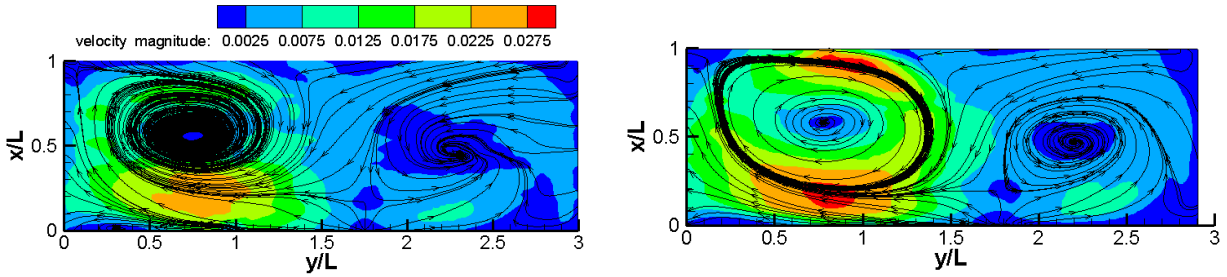

Figure A.1from figure III.33. Velocity fields at for *W/L*=3 for elevations z/h=0.07 (left) and 0.21 (right)

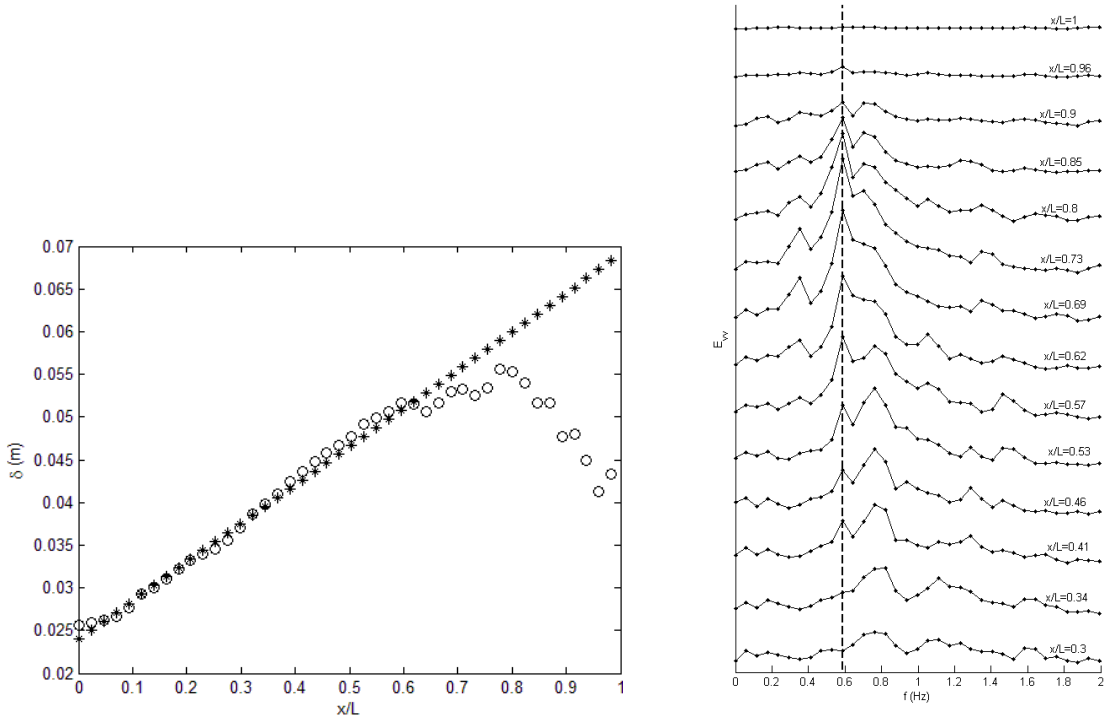

Figure A.2 from Figure III.4 and III.10: Evolution along the mixing layer of the mixing layer width and transverse velocity spectrum.

2. Time during a measurement

Now, let's consider the evolution of some parameters along the time during a PIV measurement. Figure A.3 shows the evolution along time of the velocity field averaged over 10 seconds. This time is not long enough to reach time convergence so that the flow patterns evolve from one estimate to the other. Nevertheless, these estimates appear to be in agreement with each other during the whole measurement time. Similarly, Figure A.4 shows the evolution along time of the detected coherent turbulent structures (vortices) and it appears that detecting each structure on each image is quite straightforward and that the trajectories of these structures can be is not chaotic at all, as confirmed on Figure A.5 where the abscise of the center of the structures increases gradually along time. These *a posteriori* observations also give credit to a low level of uncertainty: the estimation of the fluctuant part of the flow pattern is not chaotic and the velocity measurement seems to be fairly resolved at a time scale of about 1/7.5s.

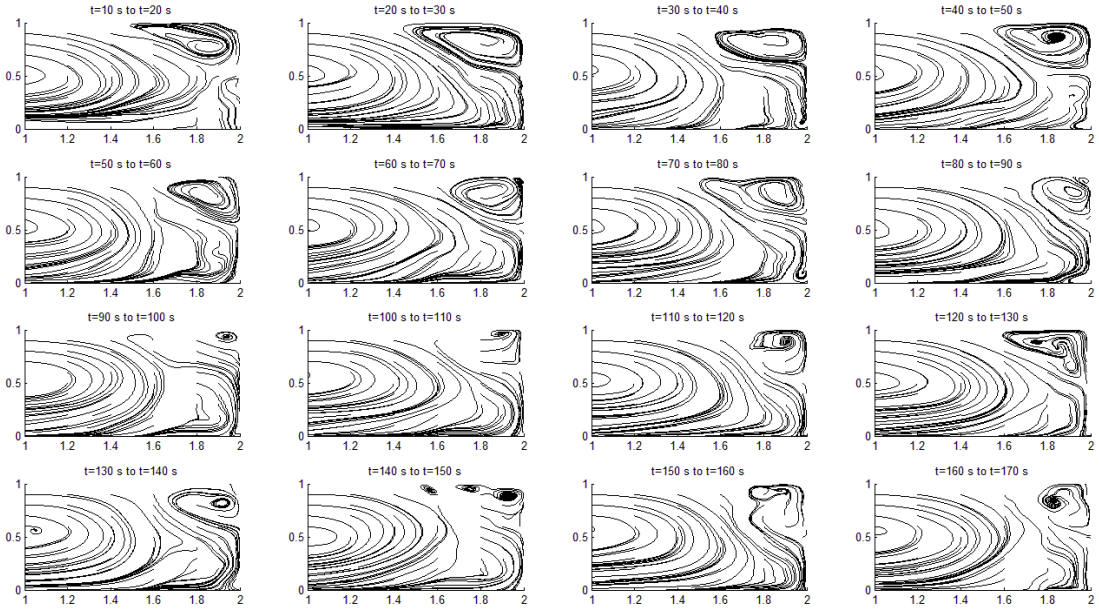

Figure A.3 from figure III.43:Streamlines of the flow averaged over 10 seconds, and plotted every 10 seconds for *W/L*=2 at *z/h*=0.71

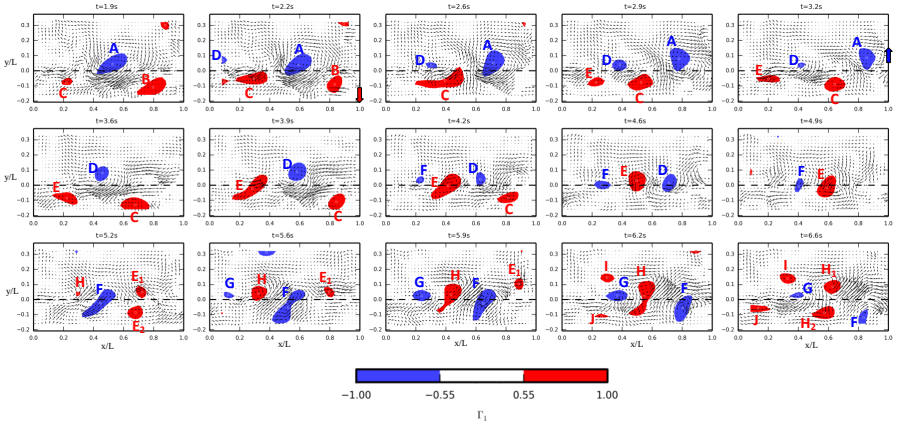

Figure A.4 from figure III.12: Detection of the coherent turbulent structures over time

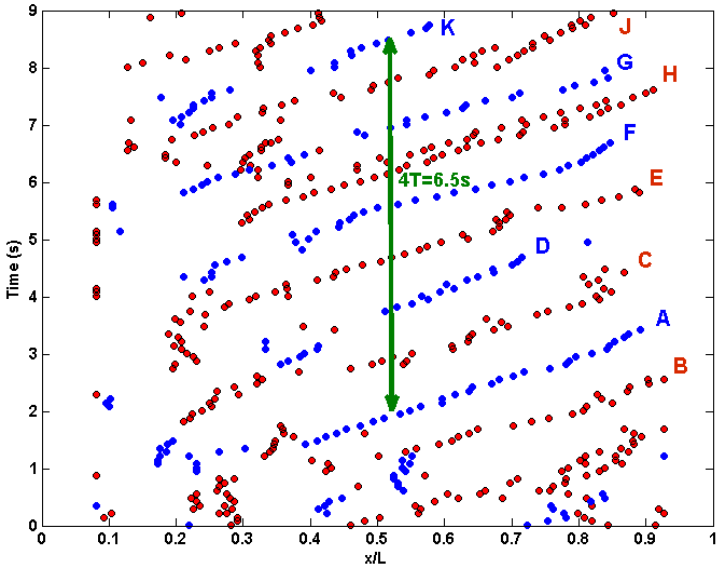

Figure A.5 from figure III.13:Time-evolution of the abscise of the coherent turbulent structures.

3. Change in the cavity geometry

In this section, characteristics of the 2D time-averaged flow field are estimated for several configurations for which the geometrical aspect ratio of the cavity is gradually increased while the characteristics of the main stream are kept constant. Figure. 1.6 reveals that the main characteristics of the flow pattern remains constant even though the aspect ratio increases from *W/L*=0.6 to 1.8: the typical mean velocity, the location of the maximum velocity, the asymmetry between $x<0$ and $x>0$ remain very stable as *W/L* increases. Then Figure. 1.7 shows, as an example, the evolution as *W/L* increases of the location along y of the first main cell. Once again, all these measurements are independent from each other and the evolution of these characteristics of the mean flow appear to evolve gradually with *W/L*. These observations give additional credit to a low level of uncertainty.

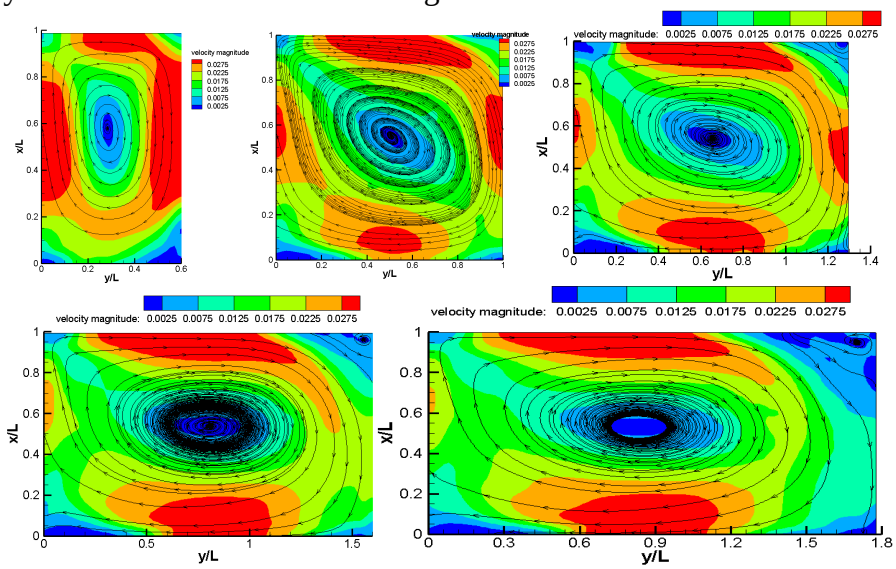

Figure A.6: Data from figures III.16-17-18-56, evolution of the mean 2D-PIV velocity field for increasing aspect ratio of the geometry of the cavity: *W/L* =0.6, 1, 1.3, 1.6, 1.8.

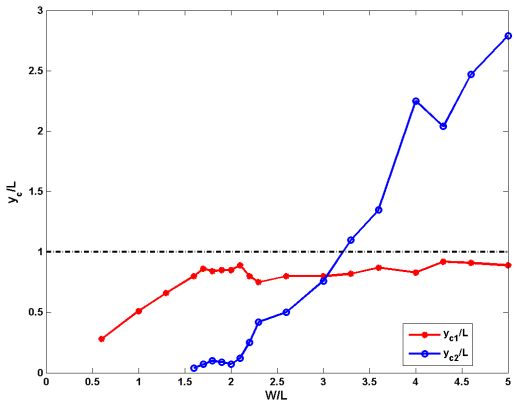

Figure A.7 from Figure III.30: *y*-position of the center of main cell for all configurations

4. Change of the flow characteristics

Finally, in the present section, the geometry of the cavity is kept constant and either the water depth of the bulk velocity of the main stream are gradually modified from one PIV measurement to the other. Figure A.8 shows for 12 values of dimensionless water depths *h/L* the evolution along the centerline of the mixing layer of its width δ, in a similar manner as in Fig. 1.2. It appears, on the one hand that the shape of the curves $\delta(x)$ is retrieved for all values of water depths and on the other hand that the magnitude of δ for all values of x increases quite regularly as *h/L* increases. On a complete other topic, the Figure A.9 exhibits the evolution of the ratio of the mean celerity of the vortices divided by the bulk velocity of the main stream as the velocity of the main stream increases (all parameters being kept constant) from about 4 to 19 cm/s. Figure A.9 reveals that this ratio remains quite constant and actually evolves between 0.56 and 0.63 with no tendency, that is a variation of about 10%. The method for estimating this celerity is strongly indirect (see section 4.2 of Chapter III) and thus this limited variation of 10% gives credit to a low level of uncertainty. Finally, Figure A.10 exhibits another indirect parameter obtained from the 2D-PIV measurement: the passive scalar exchange coefficient k and its evolution as the Reynolds number and the dimensionless water depth of the main stream increases. This figure reveals that the evolution as a function of these two parameters is smooth and gradual, giving credit to the low level of uncertainty of the velocity measurement.

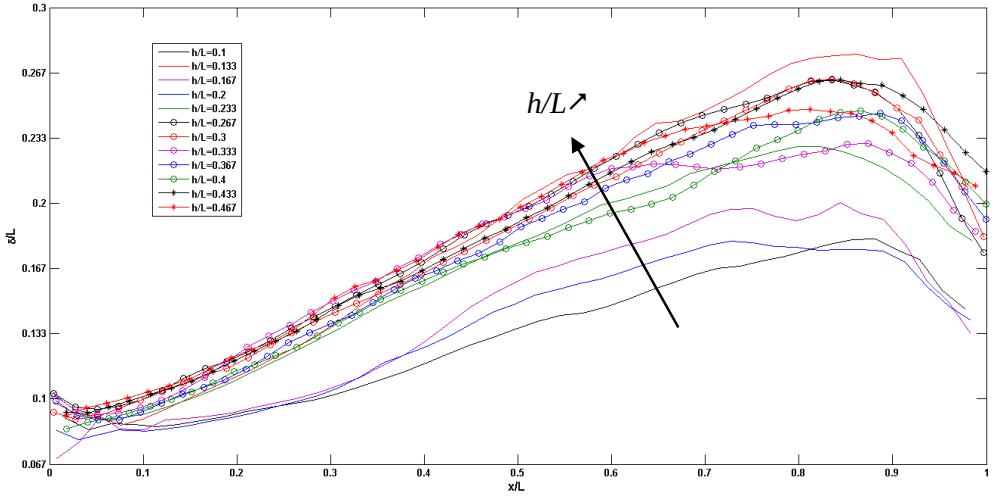

Figure A.8 from Figure III.20:Evolution of the mixing layer width $\delta(x)$ along the transverse direction as the dimensionless water depth *h/L* increases.

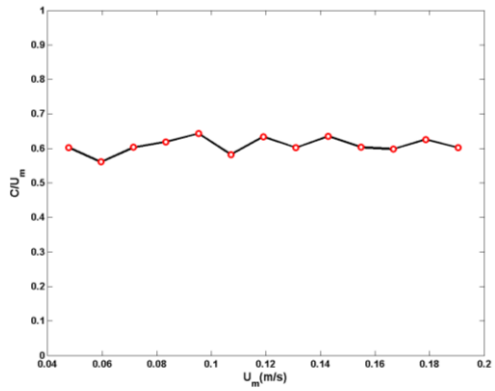

Figure A.9 from Figure III.27: Mean non-dimensional celerity of the vortices in the mixing layer for all configurations from series 3.

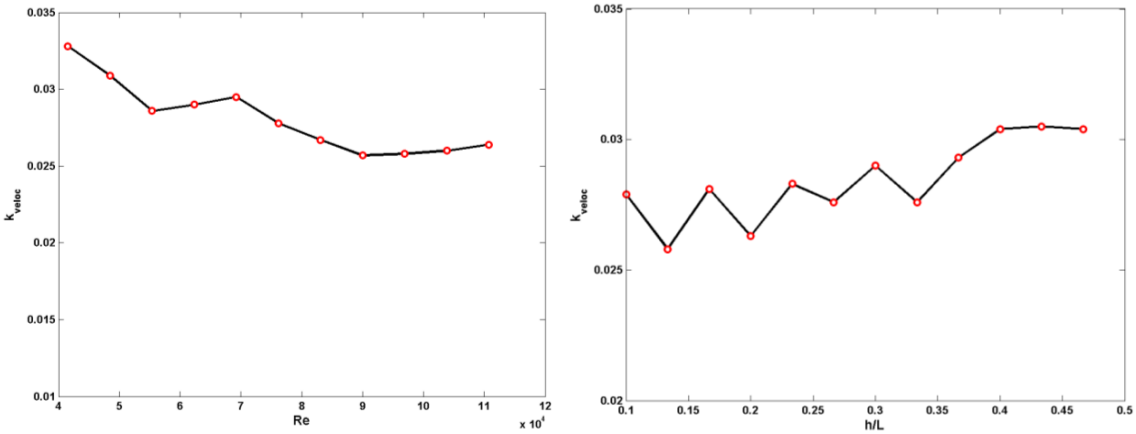

Figure A.10: Evolution of k_{veloc} coefficient from series as a function of *Re* (a) and of series 3 as a function of *h/L* (b).

To conclude, all these estimates and their smooth evolution along space, time and for varying geometry of the cavity and characteristics of the main stream permit to assume that the velocity field is actually measured with a reasonable accuracy. Nevertheless, this approach does not permit to conclude on some quantitative estimate of the measured velocity.

Referrences

Altai,W. and Chu, V. (1997). Retention time in recirculating flow. In *Environmental and Coastal Hydraulics: Protecting the Aquatic Habitat*, pages 9–14. ASCE.

Babarutsi, S., and Chu, V. H. (1991). Dye-concentration distribution in shallow recirculating flows. *Journal of Hydraulic Engineering*, 117(5), 643-659.

Babarutsi, S., Ganoulis, J., and Chu, V. (1989). Experimental investigation of shallow recirculating flows. *Journal of hydraulic engineering*. 115(7), 906–924.

Babarutsi, S., Nassiri, M., and Chu, V. (1996). Computation of shallow recirculating flow dominated by friction. *Journal of hydraulic engineering*,
122(7):367–372.

Biancofiore, L. (2014). Crossover between two- and three- dimensional turbulence in spatial mixing layers. Journal of Fluid Mechanics, 745:164–179.

Booij R., (1989) Exchange of mass in harbours, *Proc. 23rd IAHR Congress*, Delft, the Netherlands, D69-D74.

Booij, R. and Tukker, J. (2001). Integral model of shallow mixing layers. *J. Hydraulic Research*. 39(2), 169–179.

Bousmar, D. and Zech, Y.(1999). Momentum Transfer for Practical Flow Computation in Compound Channels. *J. Hydraul. Eng.*, 125(7), 696–706.

Brennen, Christopher E. (2005). Fundamentals of multiphase flow (Reprint. ed.). Cambridge [u.a.]: *Cambridge Univ. Pres,2005*.

ten Brinke, W. B. M., Kruit, N. M., Kroon, A., and van den Berg, J. H. 1999. "Erosion of sediments between groynes in the river Waal as a result of navigation traffic." *Special Publication No. 28, International Association of Sediment*, 147–160.

Brossard, C., Monnier, J.-C.. Principles and Applications of Particle Image Velocimetry. *Journal aerospacelab*, Issue 1 - December 2009.

Caton, F., Britter, R.E. & Dalziel, S. 2003. Dispersion mechanism in a street Canyon. *Atmospheric Environment* 37: 693-702.

Cai, W., Brosset, M., Mignot, E., Rivière, N., 2014. Measurement of mass exchange between a main flow and an adjacent lateral cavity. River Flow 014, Lausanne, Suisse, 3-5 septembre.

Cameron Tropea, Alexander Yarin, John Foss (ed.). Springer Handbook of Experimental Fluid Mechanics [M]. Springer Science & Business Media, 2007.

Chandrsuda, C., Bradshaw, P.. Turbulence structure of a reattaching mixing layer[J]. *Journal of Fluid Mechanics*, 1981, 110: 171-194.

Chen, D., Jirka, G.H., 1995. Experimental study of plane turbulent wakes in shallow water layer. *Fluid Dyn. Res.* 16 (1), 11–41.

Erpicum, S., Meile, T., Dewals, B. J., et al. 2D numerical flow modeling in a macro‐rough channel[J]. International journal for numerical methods in fluids, 2009, 61(11): 1227-1246.

Escauriaza C., Soto K. , Gonzalez C., Cai W., Mignot E., Riviere N., 2013, Vortex dynamics of rectangular lateral cavities in open channel flows: Effects of the aspect ratio on mass transport and residence times, Annual Meeting of the APS Division of Fluid Dynamics, Pittsburgh, USA.

Franca, M. J. 2005. Flow dynamics over a gravel riverbed. In *Proc. of the XXXI IAHR Congress*, Seoul, Korea.

Goring, G. and Nikora, V. (2002). Despiking acoustic doppler velocimeter data. J. *Hydraul. Eng*. 128(1), 117-126.

Graftieaux L, Michard M, Grosjean N. Combining PIV, POD and vortex identification algorithms for the study of unsteady turbulent swirling flows[J]. *Measurement Science and Technology*, 2001, 12(9): 1422.

Han, L. (2015), Recirculation à l'aval de l'élargissement brusque d'un écoulement à surface libre peu profond. PhD thesis, INSA-Lyon, Lyon, FRANCE.

Hattori, H., and Y. Nagano (2010), Investigation of turbulent boundary layer over forward-facing step via direct numerical simulation, *Int. J. of Heat and Fluid Flow*, 31, 284-294.

Hurther, D. and Lemmin, U. (2001). A correction method for turbulence measurements with a 3d acoustic doppler velocity profiler. Journal ofAtm*ospheric and Oceanic Technology*, 18(3):446–458.

Hinterberger C, Fröhlich J, Rodi W. Three-dimensional and depth-averaged large-eddy simulations of some shallow water flows[J]. *Journal of Hydraulic Engineering*, 2007, 133(8): 857-872.

Jackson, T.R., Haggerty, R., Apte S.V. & O'Connor B.L. 2013. A mean residence time relationship for lateral cavities in gravel-bed rivers and streams: Incorporating streambed roughness and cavity shape. *Water resources research*, 49:3642-3650.

James H. Bell and Rabindra D. Mehta. Development of a two-stream mixing layer from tripped and untripped boundary layers, *AIAA Journal*, Vol. 28, No. 12 (1990), pp. 2034-2042.

Jamieson, E. and Gaskin, S.J. (2007) Laboratory study of 3 dimensional characteristics of re-circulatingflow in a river embayment, *32nd Congress of IAHR*, July 1-6 2007, Venice, Italy.pp.1-9.

Kadotani K., Fujita I., Matsubara T., Tsubaki R. 2008. Analysis of water surface oscillation at open channel side cavity by image analysis and large eddy simulation. *ICHE conference*, Nagoya, Japan, sept. 9-12.

Klein, J. P., Maire, G., Exinger, F., Lutz, G., Sanchez-Perez, J.-M., Trémolières, M. et Junod, P. (1994). The restoration of former channels in the Rhine alluvial forest : the example of the Offendorf Nature Reserve (Alsace, France). *Water Sciences and Technology*, 29(3):301–305. 10

Kimura I. and Hosoda T. (1997). Fundamental Properties of Flows in Open Channels with Dead Zone.*J. Hydraul. Eng.*,123(2), 98–107.

Langendoen, E. J., Kranenburg, C., and Booij, R. (1994). Flow patterns and exchange of matter in

tidal harbours. *Journal of Hydraulic Research*, 32(2):259–270.

Lecordier B., Trinité M. . Accuracy assessment of image interpolation schemes for PIV from real images of particle. *13th Int. Symp. on Applications of Laser Techniques to Fluid Mechanics*, Lisbon, Portugal, June 26-29, 2006.

LeCoz J. 2007. Fonctionnement hydro-sédimentaire des bras mortsde rivière alluviale (Hydrosedimentary Processes in Abandoned Channels of Alluvial Rivers), PhD Thesis, Ecole centrale de Lyon.

Lesieur, M. (1997). Turbulence in Fluids. *Kluwer Academic*, Norwell, U.S.A.

Li, C.W. & Gu, J. 2002. 3D layered-integrated modelling of mass exchange in semi-enclosed water bodies. *Journal of Hydraulic Research* 39(4): 403-411.

Li, C.W. & Ip, K.W. 1999. Residence time in semi-enclosed water bodies. *Civil and Environmental Engineering Conference, 8-12 November 1999, Bangkok, Thailand*: VI.13–VI.16.

Li, X. and Djilali N. (1995), On the scaling of separation bubbles, J*SME Int. J. Series B*, 38 (4), 541-548.

Loucks, R. B. and Wallace, J. M. (2012). Velocity and velocity gradient based properties of a turbulent plane mixing layer. J*ournal of Fluid Mechanics*, 699:280–319.

Markides, C.N., Fokaides, P.A. & Neophytou, M.K. 2010. Flow and exchange processes in homogeneous urban street canyon geometries: an experimental study using particle image velocimetry. *International Congress on Mechanics, Limassol. Cyprius*.

McCoy A., Constantinescu G. and Weber L. J. 2008. Numerical Investigation of Flow Hydrodynamics in a Channel with a Series of Groynes. Journal of Hydraulic Engineering, 134(2), 157-172.

McLelland, S. J. and Nicholas, A. P. (2000). A new method for evaluating errors in high-frequency adv measurements. Hydrological Processes, 14(2):351–366.

Mignot, E., Barthelemy, E. and Hurther, D. (2009). Double averaging analysis and local flow characterization of near bed turbulence in gravel-bed channel flows. *J. Fluid Mech*. 618, 279–303.

Mignot E., Cai W., Escauriaza C., Riviere N. Analyse expérimentale et numérique du champ de vitesse dans des cavités latérales de différents rapports d'aspect, XXI° Congrès Français de la Mécanique 2013, Bordeaux, 26-30 Aout 2013.

Mignot E., Doppler D., Riviere N., Vinkovic I., Gence J.N., Simoens S. – 2014. Analysis of flow separation using a local frame-axis: application to the open-channel bifurcation, *Journal of Hydraulic Engineering*, 140 (3), 280-290.

Mignot, E., Hurther, D., and Barthelemy, E. (2011). Doubleaveraging turbulence characteristics in flows over a gravel bed. *Journal of Hydraulic Research*, 49(5):703–704.

Mignot, E., Vinkovic, I., Doppler, D., and Rivi`ere, N. (2014b). Mixing layer in open-channel junction flows. *Environmental Fluid Mechanics*. 14(5), 1027–1041.

Mizumura, K. and Hasatani, T. (2001). Geochemical Determinations of Geological Layers and Groundwater Flow Directions.*J. Hydrol. Eng.*, 6(3), 235–242.

Mizumura, K., Yamasaka, M.,and Adachi, J. (2003). Side Outflow from Supercritical Channel Flow.*J. Hydraul. Eng.*, 129(10), 769–776.

Mizumura, K. and Yamasaka, M. (2002). Flow in Open-Channel Embayments.*J. Hydraul. Eng.*, 128(12), 1098–1101.

Muto, Y., Imamoto, H. & Ishigaki, T. 2000. Velocity measurements in a straight open channel with a rectangular embayment. *Proc. 12th APD-IAHR, Bangkok, Thailand*: 353.

Nezu, I. and Nakagawa, H. (1993). Turbulence in open channel flows. In *IAHR monographs series*, Balkema, Rotterdam.

Nezu I, Onitsuka K. PIV Measurements of side-cavity open-channel flows—Wando model in rivers—[J]. *Journal of visualization*, 2002, 5(1): 77-84.

Peltier, Y., Riviere, N., Proust, S., Mignot, E., Paquier, A., and Shiono, K. (2013). Estimation of the error on the mean velocity and on the reynolds stress due to a misoriented adv probe in the horizontal plane: Case of experiments in a compound open-channel. Flow Measurement and Instrumentation, 34(0):34 – 41.

Peltier, Y., Erpicum, S., Archambeau, P., Pirotton, M., and Dewals, B. (2014). Meandering jets in shallow rectangular reservoirs: Pod analysis and identification of coherent structures. *Experiments in Fluids*, 55(6):1–16.

Plesniak M W, Mehta R D, Johnston J P. Curved two-stream turbulent mixing layers revisited[J]. *Experimental thermal and fluid scienc*e, 1996, 13(3): 190-205.

Pope, S. (2008). *Turbulence flows*. Cambridge University Press, Cambridge, United Kingdom.

Raupach M R, Finnigan J J, Brunei Y. Coherent eddies and turbulence in vegetation canopies: the mixing-layer analogy[J]. Boundary-Layer Meteorology, 1996, 78(3-4): 351-382.

Riviere, N., Garcia, M., Mignot, E. & Travin, G. 2010. Characteristics of the recirculation cell pattern in a lateral cavity. *International Conference on Fluvial Hydraulics* (River Flow 2010), Braunschweig, Germany: 673.

Salizzoni, P., Soulhac L. & Mejean, P. 2009. Street canyon ventilation and atmospheric turbulence. *Atmospheric Environment* 43 (32): 5056-5067.

Sanjou M. and Nezu I. 2013. Hydrodynamic characteristics and related mass-transfer properties in open-channel flows with rectangular embayment zone. *Environ Fluid Mech*. 13(6): 527-555.

Shakibainia A, Tabatabai M R M, Zarrati A R. Three-dimensional numerical study of flow structure in channel confluences[J]. Canadian Journal of Civil Engineering, 2010, 37(5): 772-781.

Shaw, R.H., Brunet, Y., Finnigan, J.J. & Raupach, M.R. 1995 A wind tunnel study of air flow in waving wheat: *Two-point velocity statistics. Boundary-Layer Meteorol*. 76, 349–376.

Soto K., Gonzalez C., Cai W., Mignot E., Riviere N., Escauriaza C. Dinámica del Flujo Turbulento en Cavidades Laterales: Estudio Experimental y Numérico de los Efectos sobre el Transporte y Dispersión de Contaminantes, XXI °Congreso Chileno de Ingeniería Hidraulica 2013, Concepcion, Chile, 21-25 Octubre, 2013.

Sukhodolov, A., Schnauder, I., and Uijttewaal,W. (2010). Dynamics of shallow lateral shear layers: experimental study in a river with a sandy bed. Water Resour. Res. 46, W11519.

Theunissen R., Scarano F., Riethmuller M.L.. Statistical adaptivity in PIV interrogation for mean flow estimation. *14th Int. Symp. on Applications of Laser Techniques to Fluid Mechanics*, Lisbon, Portugal, 07 -10 July 2008.

Tominaga A, Jong J. Effects of conjunction channel on water exchange in riverside embayment[J]. *Journal of Hydro-environment Research*, 2010, 4(2): 163-173.

Tuna, B. A.**,** Tinar, E., & Rockwell, D., 2013. Shallow flow past a cavity: globally coupled oscillations as a function of depth.*Experiments in Fluids*, 54(8), 1-20.

Uijttewaal W S J, Booij R. Effects of shallowness on the development of free-surface mixing layers[J]. Physics of Fluids (1994-present), 2000, 12(2): 392-402.

Uijttewaal, W., Lehmann, D., and Mazijk, A. (2001).Exchange Processes between a River and Its Groyne Fields: Model Experiments. *J. Hydraul. Eng.*, 127(11), 928–936.

Valentine E M, Wood I R. Longitudinal dispersion with dead zones[J]. *Journal of the Hydraulics Division*, 1977, 103(9): 975-990.

Valentine E M, Wood I R. Experiments in longitudinal dispersion with dead zones[J]. *Journal of the Hydraulics Division*, 1979, 105(8): 999-1016.

Van Prooijen B C, Uijttewaal W S J.. A linear approach for the evolution of coherent structures in shallow mixing layers[J]. *Physics of Fluids* (1994-present), 2002, 14(12): 4105-4114.

Vermaas, D. A., Uijttewaal, W. S. J., Hoitink, A. J. F. (2011) Lateral transfer of streamwise momentum caused by a roughness transition across a shallow channel, *Water Resources Res*. 47 (W02530).

Weitbrecht, V., Socolofsky, S., and Jirka, G. (2008). Experiments on Mass Exchange between Groin Fields and Main Stream in Rivers.*J. Hydraul. Eng.*,134(2), 173–183.

Westrich B. and Clad A. (1979), Mass and heat exchange in flows with recirculating zones, Proc. 18th IAHR Congress, Cagliari, Vol. 3, Subject Bb, pp. 269-276.

Westerweel J.. On velocity gradients in PIV interrogation. *Exp. Fluids*, Vol. 44, pp. 831-842, 2008.

Westerweel J..Theoretical analysis of the measurement precision in particle image velocimetry. *Exp. Fluids*, Vol. 29, N 7, pp. S3-S12, 2000.

White, B. and Nepf, H. (2007). Shear instability and coherent structures in shallow flow adjacent to a porous layer. Journal of Fluid Mechanics. 593, 1–32.

Wygnanski, I. and Fiedler, H. (1970). The two dimensional mixing region. Jou*rnal of Fluid Mechanics*. 41(2), 327–361.

Zhang, C., Shaw, R.H. & Paw, U.K.T. 1992 Spatial characteristics of turbulent coherent structures within and above an orchard canopy. in S. E. Schwartz and W. G. N. Slinn (eds.), *Precipitation Scavenging and Atmosphere-Surface Exchange, Hemisphere Publishing Co. Washington*, pp. 741-751 .